Научном већу

Института за физику у Београду

Предмет:

Покретање поступка за избор у звање научни сарадник

МОЛБА

Молим Научно веће Института за физику да покрене поступак за мој избор у звање научни сарадник. У прилогу достављам:

1. Мишљење руководиоца пројекта,
2. Стручну биографију,
3. Преглед научне активности,
4. Елементе за квалитативну анализу научног рада,
5. Елементе за квантитативну анализу научног рада,
6. Списак објављених радова,
7. Податке о цитираности,
8. Доказ о пострификацији дипломе,
9. Примерак докторске дисертације,
10. Копије објављених радова.

Са поштовањем,

Соња Прелић

др Соња Прелић

Научном већу Института за физику у Београду

Предмет: Мишљење руководиоца лабораторије о избору др Соње Предин у звање научни сарадник

Др Соња Предин је сарадник Лабораторије за примену рачунара у науци, у оквиру Националног центра изузетних вредности за изучавање комплексних система Института за физику у Београду. У истраживачком раду се бави темама из области физике кондензоване материје и статистичке физике. С обзиром да испуњава све предвиђене услове у складу са Правилником о поступку, начину вредновања и квантитативном исказивању научноистраживачких резултата истраживача МПНТР, сагласан сам са покретањем поступка за избор др Соње Предин у звање научни сарадник.

За састав комисије за избор др Соње Предин у звање научни сарадник предлажем:

(1) др Милица Миловановић, научни саветник, Институт за физику у Београду,
(2) др Ивана Васић, виши научни сарадник, Институт за физику у Београду,
(3) проф. др Марија Димитријевић-Ћирић, редовни професор Физичког факултета Универзитета у Београду.

др Антун Балаж
научни саветник
руководилац Лабораторије за
примену рачунара у науци

2. Биографски подаци кандидаткиње

Соња Предин је рођена у Београду 04.01.1986. Детињство је провела у Бечеју, где је завршила Основну школу "Здравко Гложански" и Гимназију као носилац Вукове дипломе. Дипломирала је 2012. године на смеру теоријска и експериментална физика са просечном оценом 9.12 (девет и 12/100) и оценом 10 (десет) на дипломском испиту. Дипломски рад, под називом "Коегзистенција тополошке суперпроводности и антиферомагнетизма", урадила је под руководством др Милице Миловановић на Институту за физику у Београду. Током студија, похађала је зимски семестар школске 2008./2009. године на Физичком факултету Универзитета у Грацу, Аустрија, као студент на размени студената и стипендиста Универзитета у Грацу.

По завршетку основних академских студија, Соња Предин уписала је докторске студије на Универзитету у Регензбургу из области теоријске физике. Докторску дисертацију под насловом "Entaglement spectrum of graphene systems" (Спектар квантне сплетености графенских система) урадила је под руководством prof. dr. John Schliemann-a и одбранила је 25.07.2017. Диплома докторских студија нострификована је у Републици Србији дана 22.01.2018., од стране Министарства просвете, науке и технолошког развоја Републике Србије, решењем број 612-01-03131/2017-06.

У периоду од 01.09.2012. до 31.03.2017., Соња Предин је радила као научни сарадник Факултета за физику Универзитета у Регензбургу, а од 01.04.2017. до 31.07.2017. била је ангажована као докторанткиња на поменутом факултету. На Универзитету у Регензбургу, Соња Предин се бавила научним радом у оквиру научних пројеката GRK 1570 "Electronic Properties of Carbon Based Nanostructures" и SFB 631 "Solid-State Based Quantum Information Processing" финансираних од стране Deutsche Forschungsgemeinschaft. Током докторских студија, од 2012. до 2016. била је стипендиста Фонда за младе таленте "Доситеја" Републике Србије за најбоље студенте у иностранству.

Од 01.08.2018. запослена је као научни сарадник на Институту за информационе системе у Хофу, Савезна Република Немачка. Од 2018. до 2020. била је ангожована на пројекту "Digital mobility of Hochfranken" (MobiDig), који је финансиран од стране Министарства саобраћаја и дигиталне инфраструктуре Савезне Републике Немачке. Након тога, од 2020. ангожавана је на пројекту "Shuttle-Modellregion Oberfranken"(SMO), који је већински финансиран од стране Министранства саобраћаја и дигиталне инфраструктуре Савезне Републике Немачке. За разлику од пројекта Mobidig, који је реализован искључиво од стране академских партнера и локалне самоуправе, на пројекту SMO укључена су и три индустријска партнера "Valeo Schalter und Sensoren GmbH", "REHAU AG + Co", "DB Regio Bus".

Као асистент на Факултету за физику Универзитета у Регензбургу, Соња Предин држала је теоријске вежбе сваког семестра из предмета Експериментална физика I: Механика и нелинеарна динамика, Теоријска механика, Квантни и таласи (Оптика), Квантна физика I, Квантна физика II на основним студијама. Такође, на мастер студијама држала је вежбе из Квантне теорије кондензоване материје. У летњем семестру школске 2019. године хонорално је држала предавања из Увода у квантне рачунаре на Факултету за информатику Високе школе у као доценткиња.

У тренутку подношења овог извештаја, Соња Предин је коаутор осам радова објављених у међународним часописима са ISI листе, од којих три у категорији M21, једног у категорији M22 и четири у категорији M34. Укупан број цитата је 30, односно 28 не рачунајући аутоцитате, са Хиршовим индексом 2. Соња Предин има сарадњу са групама у Регензбургу, Хофу, Минхену и Нинбергу.

3. ПРЕГЛЕД НАУЧНЕ АКТИВНОСТИ

Научна активност кандидаткиње може се поделити у две фазе. Прва фаза је реализована током израде дипломског рада у Лабораторији за примену рачунара у науци на Институту за физику у Београду, под менторством др Милице Миловановић и током докторских студија из теоријске физике на Факултету за физику Универзитета у Регензбургу у Савезној Републици Немачкој, под менторством проф. др John Schliemann-a. Уже научне области истраживања спроведеног током докторских студија су физика кондензоване материје и квантна информатика. Друга фаза обухвата кандидаткино постдокторско усавршавање на Институту за информатику у Хофу.

Током прве фазе истраживања кандидаткиња се бавила теоријским проучавањем спектра квантне сплетености различитих система кондензоване материје са посебним освртом на проучавање односа између енергетског спектра и спектра квантне сплетености. Досадашња научна активност кандидаткиње укључује проучавање следећих система кондензоване материје: графенског двослоја, суперпроводности и антиферомагнетизма на графену и Хајзенбергових спинских мердевина у временском зависном магнетном пољу.

Однос између енергетског спектра и спектра квантне сплетености био је фокус многих нумеричких и аналитичких студија. У свом раду кандидаткиња је користила пертурбациону теорију, разматрајући и дегенерисана и недегенерисана основна стања, у односу на претходне студије када су само недегенерисана стања била разматрана. Закључак претходних студија био је да у случају недегенерисаног основног стања када су испуњени одређени услови, Хамилтонијан спектра квантне сплетености може бити пропорционалан Хамилтонијану једног подсистема и на тај начин имати исте особине. Један од два услова који гарантују да су Хамилтонијани пропорционални у првој апроксимацији пертурбативне теорије је да непертурбативни Хамилтонијан спектра квантне сплетености има тривијални, недегенерисан спектар. Кандидаткиња је самостално током докторских студија, као једини аутор рада, проучавала спектар квантне сплетености Хајзенбергових мердевина у временском зависном магнетном пољу, користивши теорију пертурбације. У том случају, Хамилтонијан квантне сплетености је пропорционалан Хамилтонијану спинског ланца у првој апроксимацији, иако непертурбативни Хамилтонијан спектра квантне сплетености има нетривијални дегенерисан спектар. Резултати проучавања односа између Хамилтонијана спектра квантне сплетености Хајзенбергових мердевина у временски зависном магнетном пољу и Хамилтонијана подсистема, у овом случају једног спинског ланца, приказани су у раду

- **Sonja Predin**, Entanglement spectrum of the degenerative ground state of Heisenberg ladders in a time-dependent magnetic field, EPL 119, 57003 (2017).

Следећи рад се односи на графенски двослој и његов спектар квантне сплетености. У односу на претходне радове, кандидаткиња није разматрала само својствене вредности редуковане матрице густине (који чине спектар квантне сплетености), већ и њене својствене векторе. Од својствених вектора редуковане матрице густине конструисала је тополошке инваријанте, Беријеву кривину и Чернов број, да би проучавала тополошка својства спектра квантне сплетености. Такође, у односу на ранија проучавања графенског двослоја, кандидаткиња је извела аналитичке изразе својственог система за целу Брилуенову зону без апроксимација, када је узето у обзир и тригонално савијање енергетског спектра. Аналитичка студија спектра квантне сплетености графенског двослоја, када је тригонално савијање присутно у енергетском спектру приказана је у раду

- **Sonja Predin**, Paul Wenk, John Schliemann, Trigonal Warping in Bilayer Graphene: Energy versus Entanglement Spectrum, Phys. Rev. B **93**, 115106 (2016).

Кандидаткиња је овом раду показала да спектар квантне сплетености, који је добијен исецањем једног слоја, има нулте вредности између тачака где енергетски спектар поседује

три додатна Диракова конуса, која су узрокована тригоналним савијањем. Кандидаткиња је аналитички показала да спектар квантне сплетености може бити прекидна функција у односу на таласни вектор у овом систему. Тополошке особине спектра квантне сплетености графенског двослоја описане Беријевом кривином су у сагласности са тополошким особинама графенског једнослоја, иако се њихове геометријске особине јасно разликују.

Кандидаткиња је у дипломском раду дискутовала t-J-U модел на графену који има исти ниско-енергетски опис као графенски двослој, фокусирајући се на коегзистенију суперпроводних корелација и антифермогнетизма. Показано је да је тај модел релевантан за опис графенског двослоја. Такође, у присуству d + id Куперових корелација модел описује квадратну зависност енергетског процепа од магнетног поља, што је усагласности са експериметалним студијама. Анализе дате у дипломском раду су објављене у:

- M. V. Milovanović, **S. Predin**, On the coexistence of antiferromagnetism and d + id superconducting correlations in the graphene bilayer, Phys. Rev. B **86**, 195113 (2012).

Кандидаткиња је проучавала спектре квантне сплетености и у системима графена са основним стањима у којима су присутне суперпроводне корелације. Проучаване су s и d + id суперпроводне корелације. Кандидаткиња је да би аналитички проучавала спектар квантне сплетености, самостално извела изразе за својствену енергију и векторе спектра фермиона на графенској решетки у целој Брилуеновој зони у присуству суперпроводних корелација. Демонстрирала је да се тополошке особине Хамилтонијана квантне сплетености могу разликовати од истих особина Хамилтонијана подсистема. Резултати ових проучавања су публиковани у раду:

- **Sonja Predin**, John Schliemann, Entanglement spectra of superconductivity ground states on the honeycomb lattice, Eur. Phys. J. B (2017) 90: 239.

У другој фази истраживања, задатак кандидаткиње на пројекту Mobidig био је развој модела за оптимизацију и симулацију саобраћаја, првенствено градског саобраћаја у периферијским регионима Немачке. Периферијски региони у Немачкој нарочито су погођени демографским променама, старењем становништва, које је проузроковано негативним природним прираштајем и миграцијама ка атрактивним индустријским центрима. Градски превоз у оваквим условима је скуп за локалну самоуправу, а за грађене често је недовољно квалитетан, због дугачких временских интервала између вожњи и индиректних путања. Побољшање градског саобрћаја у оваквим регионима преставља један од приоритета Министраства саобраћаја и дигиталне инфраструктуре Савезне Републике Немачке.

Моделирање саобраћаја је један од најбољих алата за разумевање и развијање потреба градског саобраћаја, као и за предлагање нових линија градског саобраћаја. Симулациони модели су уобичајни алати за моделирање саобраћаја. Предходни симулациони модели су развијени на основу анкета становништва. Главни недостатак оваквог приступа је мали узорак на основу кога се развија симулација, а то доводи у питање и веродостојност саме симулације. Међутим, кандидаткиња је развила модел мобилности за регион Hochfranken (Горњу Франконију) користећи технике машинског учења у обради статистичких и GPRS података. Кандидаткиња је прво симулирала популацију града Хофа, поделивши популацију у групе према социо-демографским параметрима (старост, пол, занимање и брачно стање), користећи статистичке податке немачких државних институција. Људи се генеришу уз помоћ псеудо-случајних бројева на такав начин да се постигне стварна дистрибуција ових социо-демографских параметара у популацији. Овај поступак се понавља неколико пута како би се могао проверити утицај ове случајне дистрибуције на резултате симулације. Након тога, други случајни поступак користи се за стварање плана активности за сваку особу у популацији. Симулирала је помоћу програмског пакета MATSim у програмском језику Јава, за сваког

појединца све дневне активности, одлазак и повратак са посла, одлазак у куповину прехрабених намерница, у образовне институције и уставове прешколског образовања. У овом кораку кандидаткиња је узела у обзир да свака социо-демографска група има различите обрасце понашања. Приликом оваквог разматрања непознате су почетна и крајна тачка транспорта, време транспорта и превозно средство. У односу на друге ауторе, кандидаткиња је развила алгоритме машинског учења и користила методе статистичке анализе ради превиђања почетне и крајне тачке. Главни извори података у њеној студији за предвиђање почетне и крајне тачке транспорта су статистички подаци и подаци од GPRS уређаја. У даљем кораку, низ догађаја између појединих активности се утврђују за сваки план. У овом кораку неопходно је дефинисати изабрано возило или возила и тачну руту између активности. Да би симулирала тачне руте кретања између свих активности, кандидаткиња је развила мапу рута за сва возила, укључивајући и пешаке. У симулацији са програмским пакетом MATSim-ом, овај корак, одабир рута, плана активности и возила, је део процеса оптимизације. У ту сврху генерисана рута и избор возила се мења у различитим итерацијама симулације како би се постигао глобални оптимум. Функција процене, дневног плана сваког појединца, узима у обзир укупно време за одређену етапу, време потребно за пешачење, укупну удаљеност, трошкове и број промењених превозних средстава. Кандидаткиња је извршила калибрацију симулације користећи Бајесову статистичку методу. Тако развијен симулациони модел, кандидаткиња је користила да оптимизује постојеће линије градског саобраћаја, као и да понуди увођење нових линија. Нарочит бенефит оваког приступа се огледа у могућности разумевања и предвиђања стварних потреба за услугама градског превоза различитих демографских група.

Станице градског превоза у многим малим местима у Немачкој су често неприступачне многим потенцијалним путницима због велике удаљености. То значајно отежава употребу градског превоза, нарочито осетљивим социо-демографским групама, старијим особама и особама са инвалидитетом. Употреба конвенционалног линијског градског превоза обично није исплатива на кратким дистенацијама, или је чак и не могућа због инфраструктуре. Употреба аутономног шатл возила на таквим релацијима је предложено решење у овом истраживачком пројекту. Циљ пројекта је тестирање и даљи развој и унапређивање шатлова без возача као допунске и помоћне компоненте градског превоза. Задатак кандидаткиње на пројекту SMO је развој и унапређење алгоритама вештачке интелигеције аутономних шатл возила. Поред овога, одговорност кандидаткиње је мапирање потреба корисника градског превоза, како би се остварило поверење у аутономна возила у контексту интеракције човек-машина.

4. ЕЛЕМЕНТИ ЗА КВАЛИТАТИВНУ ОЦЕНУ НАУЧНОГ ДОПРИНОСА КАНДИДАТА

4.1 Квалитет научних резултата

4.1.1 Научни ниво и значај резултата, утицај научних радова

Најзначајни рад кандидаткиње је:

- **Sonja Predin**, Paul Wenk, John Schliemann, Trigonal Warping in Bilayer Graphene: Energy versus Entanglement Spectrum, Phys. Rev. B **93**, 115106 (2016), цитиран 11 пута.

У овом раду, приликом описивања графенске структуре графенског двослоја, кандидаткиња је разматрала и параметар кинетичке енергије између трећих суседа, који узрокује тригонално савијање. Овај параметар је у већини случаја био занемарен. Соња Предин је први аутор који је аналитички решио својствени проблем графенског двослоја за целу Брилуенову зону без апроксимација, укључујући и својствене вредности и својствене векторе. Ови резултати су

важни за разумевање физике графенског двослоја и могу мотивисати даља истраживања. Користећи овако добијене својствене векторе, кандидаткиња је аналитички конструисала спектар квантне сплетености графенског двослоја. Поред тога, кандидаткиња је у овом раду разматрала топологију спектра квантне сплетености и однос спектра квантне сплетености и Хамилтонијана одговарајућег подсистема. Да би проучавала топологију спектра квантне сплетености дефинисала је Чернов број и Беријеву кривину својствених вредности спектра квантне сплетености. Модел је омогућио да се прецизно испита утицај тригоналног савијања на физику графенског двослоја и спектар квантне сплетености, као и тополошке особине спектра квантне сплетености. Кандидаткиња је показала да тополошке особине спектра квантне сплетености могу бити исте као и спектра одговарајућег подсистема и када се њихове геометријске особине разликују.

4.1.2 Позитивна цитираност научних радова кандидата

Према подацима из базе Web of Knowledge на дан 07.12.2020., радови кандидаткиње цитирани су укупно 30, од чега 28 пута изузимајући аутоцитате. Хиршов индекс је 2.

4.1.3 Параметри квалитета часописа

Соња Предин је публиковала четири рада у међународним часописима и то:

- два рада у врхунском међународном часопису *Physical Review B* (IF2012 = 3.767, IF2016 = 3.836),
- један рад у истакнутом међународном часопису *European Physical Journal B* (IF2017 = 1.465) и
- један рад у врхунском међународном часопису EPL Journal (IF2017 = 1.957).

Библиометријски показатељи су сумирани у наредној табели:

	ИФ	М	СНИП
Укупно	11,025	29	3,92
Усредњено по чланку	2,756	7,25	0,98
Усредњено по аутору	5,853	17,167	2,143

4.1.4 Степен самосталности и степен учешћа у реализацији радова у научним центрима у земљи и иностранству

При изради своје докторске дисертације, Соња Предин је показала висок степен самосталности у свим корацима научног рада, укључујући поставку проблема, истраживање, обраду резултата, и припрему публикација за објављивање у часопису.

Кандидаткиња има изражену међународну сарадњу, што се посебно види по томе што је завршила докторске студије на Универзитету у Регензбургу, Немачка, а тренутно је запослена као научни сарадник на Институту за информационе системе у Хофу, Немачка. Током реализације пројекта Mobidig, кандидаткиња је остварила сарадњу са академским партнерима на пројекту, катедром за саобраћајни инжињеринг Техничког универзитета у Минхену и групом за Supply Chain Services Фраунхофер Института у Нинбергу.

4.2 Нормирање броја коауторских радова, патената и техничких решења

Имајући у виду да сва 4 рада имају највише 3 коаутора, сви радови се рачунају са пуном тежином.

4.3 Утицајност научних резултата

Утицајност научних резултата кандидаткиње је наведена у одељку 4.1 овог документа. Пун списак радова је дат у одељку 6, а подаци о цитираности са интернет странице *Web of Science* базе су дати након списка свих радова кандидаткиње.

4.4 Учешће у пројектима, подпројектима и пројектним задацима

Соња Предин до сада је учествовала на следећим пројектима:

- Graduiertenkolleg 1570 "Electronic Properties of Carbon Based Nanostructures", који је фининсиран од стране Deutsche Forschungsgemeinschaft (2012.-2014., 2015.-2016.),
- Collaborative Research Center SFB 631 "Solid-State Based Quantum Information Processing", који је фининсиран од стране Deutsche Forschungsgemeinschaft (2014.-2015.),
- "Digital mobility of Hochfranken", који је фининсиран од стране Немачког министарства за саобраћај и дигиталну инфраструктуру, укупни буџет пројекта је 2,97 милиона евра. Кандидаткиња је учествовала у реализацији пројекта у периоду од 2018.-2020.
- "Shuttle-Modellregion Oberfranken" (SMO). Овај пројекат је већински финансиран од стране Немачког министарства за саобраћај и дигиталну инфраструктуру са 12 милиона евра од укупно 15 милиона евра. Преостала 3 милиона евра финансирана су од индустријских партнера. Кандидактиња је активна на пројекту од 01.08.2020.

4.5. Активност у научним и научно-стручним друштвима

Током докторских студија кандидаткиња је била активни члан Немачког друштва физичара Deutsche Physikalische Gesellschaft.

Рецензије научних радова

Соња Предин је била рецензент једног рада у научном часопису *The European Physical Journal B*.

4.6. Конкретан допринос кандидата у реализацији радова у научним центрима у земљи и иностранству

Кандидаткиња је значајно допринела сваком раду у чијој је припреми учествовала.

Један рад објавила је током дипломских студија под менторством др Милице Миловановић. Резултати истраживања, које је реализовано на Универзитету у Регенсбургу, публиковани су у остала три рада. Дала је кључни допринос у свим радовима у којима је први аутор. Допринос кандидаткиње се огледа у изради прорачуна, добијању, интерпретацији и презентацији

резултата, писању радова и комуникацији са уредницима и рецензентима часописа.

5. ЕЛЕМЕНТИ ЗА КВАНТИТАТИВНУ ОЦЕНУ НАУЧНОГ ДОПРИНОСА КАНДИДАТА

Остварени резултати у периоду након одлуке Научног већа о предлогу за стицање претходног научног звања:

Категорија	**М бодова по раду**	**Број радова**	**Укупно М бодова**
M21	8	3	24
M22	5	1	5
M34	0,5	4	2
M70	6	1	6

Поређење са минималним квантитативним условима за избор у звање виши научни сарадник:

Минимални број М бодова		Остварено, М бодова без нормирања
Укупно	**16**	**37**
M10+M20+M31+M32+M33+M41+M42	**10**	**29**
M11+M12+M21+M22+M23	**6**	**29**

Према бази података *Web of Science* на дан 07.12.2020 године, радови кандиткиње су цитирани укупно 30 пута, односно 28 пута не рачунајући самоцитате. Према истој бази, Хиршов индекс кандидаткиње је 2.

6. СПИСАК РАДОВА ДР СОЊЕ ПРЕДИН

6.1 Радови у врхунским међународним часописима (М21)

1. M. V. Milovanovic, **S. Predin**, On the coexistence of antiferromagnetism and d + id superconducting correlations in the graphene bilayer, Phys. Rev. B **86**, 195113 (2012).
2. **Sonja Predin**, Paul Wenk, John Schliemann, Trigonal Warping in Bilayer Graphene: Energy versus Entanglement Spectrum, Phys. Rev. B **93**, 115106 (2016).
3. **Sonja Predin**, Entanglement spectrum of the degenerative ground state of Heisenberg ladders in a time-dependent magnetic field, EPL **119**, 57003 (2017).

6.2 Радови у истакнутим међународним часописима (М22)

4. **Sonja Predin**, John Schliemann, Entanglement spectra of superconductivity ground states on the honeycomb lattice, Eur. Phys. J. B 90: 239 (2017).

6.3 Саопштења са међународних скупова штампана у изводу (М34)

5. **Sonja Predin**, John Schliemann, Bilayer graphene: topological phases and entanglement spectrum, Deutsche Physikalische Gesellschaft (DPG) Spring Meeting, Dresden, Germany, 2014.
6. **Sonja Predin**, John Schliemann, An analytical study of the entanglement spectrum of graphene bilayers, Deutsche Physikalische Gesellschaft (DPG) Spring Meeting, Berlin, Germany, 2015.
7. **Sonja Predin**, John Schliemann, The effect of the trigonal warping on the energy and the entanglement spectrum of graphene bilayers, Simpozijum fizike kondenzovane materije, Beograd, 2015.
8. **Sonja Predin**, John Schliemann, Trigonal Warping in Bilayer Graphene: Energy versus Entanglement Spectrum, Deutsche Physikalische Gesellschaft (DPG) Spring Meeting, Regensburg, Germany, 2016.

6.4. Одбрањена докторска дисертација (М70):

9. **Sonja Predin**, Entanglement spectrum in graphene systems, 2017., Физички факултет, Универзитет у Регензбургу, Немачка.

Докторска дисертација кандидаткиње се може наћи на сајту:

- Националне библиотеке Немачке:
  http://d-nb.info/1139170767 и
- EPUB Универзитета у Регензбургу:
  https://epub.uni-regensburg.de/36119/

Република Србија
МИНИСТАРСТВО ПРОСВЕТЕ,
НАУКЕ И ТЕХНОЛОШКОГ РАЗВОЈА
Број: 612-01-03131/2017-06
Датум: 22.01.2018. године
Немањина 22-26
Београд
јк

На основу члана 133. став 4. Закона о високом образовању („Службени гласник РС", бр. 88/17), члана 136. став 1. Закона о општем управном поступку („Службени гласник РС", бр. 18/16) и члана 23. став 2. Закона о државној управи („Службени гласник РС", бр. 79/05, 101/07, 95/10 и 99/14), решавајући по захтеву Соње Предин из Београда, Република Србија, за признавање високошколске исправе издате у Савезној Републици Немачкој, ради запошљавања,

министар просвете, науке и технолошког развоја доноси

Р Е Ш Е Њ Е

1. Диплома коју је 25.07.2017. године на име Соња Предин издао Универзитет Регенсбург, Факултет за физику, Регенсбург, СР Немачка, о завршеним докторским студијама, студијски програм: Теоријска физика, звање/квалификација: Doktorin der Naturwissenschaften / Доктор природних наука (на основу превода овлашћеног судског тумача за немачки језик), **признаје се** као диплома докторских академских студија трећег степена високог образовања (180 ЕСПБ), у оквиру образовно-научног поља: Природно-математичке науке, научна, односно стручна област: Физичке науке, ради запошљавања.
2. Ово решење омогућава имаоцу општи приступ тржишту рада у Републици Србији, али га не ослобађа од испуњавања посебних услова за бављење професијама које су регулисане законом или другим прописом.
3. Превод звања/квалификације из тачке 1. диспозитива овог решења које је са оригиналне стране јавне исправе превео овлашћени судски тумач за немачки језик, не представља стручни, академски, научни односно уметнички назив који у складу са чланом 12. ставом 1. тачка 9. Закона о високом образовању, утврђује Национални савет за високо образовање.

О б р а з л о ж е њ е

Овом министарству обратила се Соња Предин из Београда, Република Србија, захтевом за признавање дипломе Универзитет Регенсбург, Факултет за физику, Регенсбург, СР Немачка, докторске студије високог образовања, студијски програм: Теоријска физика, звање/квалификација: Doktorin der Naturwissenschaften / Доктор природних наука, ради запошљавања.

Уз захтев, подносилац захтева доставио је:

1) оверену копију дипломе коју је 25.07.2017. године издао Универзитет Регенсбург, Факултет за физику, Регенсбург, СР Немачка, студијски програм: Теоријска физика, звање/квалификација: Doktorin der Naturwissenschaften;
2) оверену копију превода дипломе на српски језик судског тумача за немачки језик;
3) примерак докторске дисертације на изворном језику;
4) проширени апстракт рада на енглеском језику;
5) листу објављених радова;
6) радну биографију;
7) пријавни формулар;
8) доказ о уплати таксе за професионално признавање.

Одредбама члана 133. став 4. Закона о високом образовању прописано је да Министар доноси решење о професионалном признавању у року од 90 дана од дана пријема уредног захтева.

Одредбама члана 136. став 1. Закона о општем управном поступку прописано је да се решењем одлучује о праву, обавези или правном интересу странке.

Одредбама члана 23. став 2. Закона о државној управи прописано је да Министар представља Министарство, доноси прописе и решења у управним и другим појединачним стварима и одлучује о другим питањима из делокруга Министарства.

Одредбама члана 130. став 1. Закона о високом образовању, прописано је да признавање стране високошколске исправе јесте поступак којим се имаоцу те исправе утврђује право на наставак образовања, односно на запошљавање. Поступак признавања стране високошколске исправе спроводи се у складу са одредбама овог закона, ако међународним уговором није предвиђено другачије.

Чланом 131. став 1. Закон о високом образовању, прописано је да се вредновање страног студијског програма врши на основу врсте и нивоа постигнутих компетенција стечених завршетком студијског програма, узимајући у обзир систем образовања у земљи у којој је високошколска исправа стечена, услове уписа, права која проистичу из стране високошколске исправе у земљи у којој је стечена и друге релевантне чињенице,без разматрања формалних обележја и структуре студијског програма. Ставом 3. истог члана Закона о високом образовању прописано је да вредновање страног студијског програма ради запошљавања врши Национални центар за признавање страних високошколских исправа (у даљем тексту: ENIC/NARIC центар), као унутрашња организациона јединица Министарства.

У складу са чланом 131. став 4. Закона о високом образовању, комисија коју је именовао министар извршила је прво вредновање студијског програма на коме је стечена диплома из става 2. тачка 1) образложења овог решења, и дала предлог за признавање дипломе ради запошљавања.

Такса за решење по захтеву, по тарифном броју 172. тачка 4а) Закона о републичким административним таксама ("Службени гласник РС", бр. 43/03, 51/03-испр., 61/05, 101/05-др.закон, 5/09, 54/09, 50/11, 70/11- усклађени дин.изн., 55/12- усклађени дин.изн., 93/12, 47/13 - усклађени дин.изн, 65/13-др.закон, 57/14- усклађени дин.изн, 45/15- усклађени дин.изн, 83/15, 112/15, 50/16- усклађени дин.изн., 61/17- усклађени дин.изн., и 113/17), плаћена је и поништена.

Имајући у виду наведено, решено је као у диспозитиву овог решења.

Упутство о правном средству: Ово решење је коначно у управном поступку и против истог може се покренути управни спор. Тужба се подноси Управном суду у року од 30 дана од дана пријема овог решења.

Решење доставити:
- Соња Предин, ул. Поп-Стојанова бр. 17, 11000 Београд;
- Архива.

РЕПУБЛИКА СРБИЈА
МИНИСТАРСТВО ПРОСВЕТЕ, НАУКЕ И ТЕХНОЛОГИЈСКОГ РАЗВОЈА
БЕОГРАД

МИНИСТАР

Младен Шарчевић

Coexistence of antiferromagnetism and $d + id$ superconducting correlations in the graphene bilayer

M. V. Milovanović[1] and S. Predin[2]

[1]*Scientific Computing Laboratory, Institute of Physics Belgrade, University of Belgrade, Pregrevica 118, 11 080 Belgrade, Serbia*

[2]*Department of Physics, University of Belgrade, P.O. Box 368, 11001 Belgrade, Serbia*

(Received 18 May 2012; published 8 November 2012)

We discuss the t-J-U model on a honeycomb monolayer that has the same low-energy description of the kinetic term as the graphene bilayer, and in particular study coexistence of antiferromagnetism and superconducting correlations that originate from Cooper pairs without phase coherence. We show that the model is relevant for the description of the graphene bilayer and that the presence of the $d + id$ superconducting correlations with antiferromagnetism can lead to quadratic dependence in small magnetic fields of the gap of the effective monolayer consistent with the transport measurements of Velasco *et al.* on the graphene bilayer.

DOI: 10.1103/PhysRevB.86.195113 PACS number(s): 71.10.Pm

I. INTRODUCTION

The interaction effects are important for the physics of the graphene bilayer; recent experiments reveal gapped phase(s) in the undoped graphene bilayer which without interactions would represent a gapless system. In a recent experiment[1] with high quality samples, a completely insulating behavior was detected in transport measurements. Theoretical investigations, mean field, and renormalization group approaches[2–16] speak for a close competition of a few, mostly gapped, phases. One of the most prominent candidates for an explanation of the experiment in Ref. 1 is a layer antiferromagnetic (LAF) state. The main reason for the existence of this state would be an on-site Coulomb repulsion U; indeed as pointed out in Ref. 6, a Hubbard model on a honeycomb bilayer lattice would lead to the LAF state, both in weak and strong U limit. This may remind us of the behavior of the Hubbard model on the square lattice and the antiferromagnetic (AF) behavior due to nesting in the weak coupling limit. The Hubbard model on a square lattice is usually invoked as a model for cuprates in its strong coupling limit which forbids the double occupancy and leads to a "perfect" AF behavior at half-filling. On the other hand, the estimate for U is hard to know in the graphene bilayer and certainly depends on the computational scheme but it is expected to be stronger than both (inter and intralayer) hoppings. Due to the smallness of the gap revealed in the experiment in Ref. 1, we will not consider the large U limit (exclusion of double occupancy) when modeling the graphene bilayer. But we will keep the on-site repulsion as a main cause of the insulating behavior detected in the experiment. As expected from previous approaches this will lead to AF insulating behavior but seems insufficient to describe all phenomena detected in the experiment. An additional order parameter, besides the one that describes the antiferromagnetism, is necessary for the complete explanation of the transport data of the experiment.[1,8]

In this work we will look for the additional order parameter that can coexist with antiferromagnetism in the graphene bilayer at half-filling. We will argue that this is $d + id$ (broken time reversal symmetry)—wave superconducting order parameter. This $(d + id)$ order parameter and its coexistence with antiferromagnetism was already found at finite (nonzero) dopings in a numerical (Grassman tensor product) approach to the t-J (large U) model on the honeycomb monolayer in Ref. 17. Due to the assumed moderate (not large) value of U in our model of the graphene bilayer the AF and $d + id$ superconducting order parameter can coexist even at half-filling. Our model of the graphene bilayer can be described as a t-J-U model on an effective honeycomb lattice and, in the following, we will argue why this model is relevant for the description of graphene bilayer.

II. MODEL AND ITS MOTIVATION

The kinetic part of the Hamiltonian that describes the graphene bilayer on two honeycomb lattices, which are Bernal stacked, is

$$H_0 = -t \sum_{\vec{n},\sigma} \sum_{\vec{\delta}} (a^{\dagger}_{1,\vec{n},\sigma} b_{1,\vec{n}+\vec{\delta},\sigma} + a^{\dagger}_{2,\vec{n},\sigma} b_{2,\vec{n}-\vec{\delta},\sigma} + \text{H.c.}) + t_{\perp} \sum_{\vec{n},\sigma} (a^{\dagger}_{1,\vec{n},\sigma} a_{2,\vec{n},\sigma} + \text{H.c.}). \quad (1)$$

The index $i = 1,2$ denotes the layer index. In Fig. 1 the relative positions of two triangular sublattices $A1$ and $B1$ for lattice 1, and $A2$ and $B2$ for lattice 2 are illustrated. In Eq. (1) t is the hopping energy between nearest sites in each layer, and $t_{\perp}$ is the same energy for hopping between the layers. The on-site creation (annihilation) operators $a^{\dagger}_{i,\vec{n},\sigma}(a_{i,\vec{n},\sigma})$ are for the electrons in the sublattice Ai of the layer i with spin $\sigma = \uparrow,\downarrow$, and $b^{\dagger}_{i,\vec{n},\sigma}(b_{i,\vec{n},\sigma})$ for the electrons in the sublattice Bi. $\vec{\delta}$'s are defined as $\delta_1 = a(0, 1/\sqrt{3})$, $\delta_2 = a/2(1, -1/\sqrt{3})$, and $\delta_3 = a/2(-1, -1/\sqrt{3})$, and $a = \sqrt{3}\, a_{cc}$, a_{cc} is the distance between sites and a is the next to nearest neighbor distance.

The screening of the long-range part of the Coulomb interaction in two dimensions (2D), in the graphene bilayer,[18] is insufficient so this part can be neglected. Nevertheless, in the experiment we discuss,[1] two metallic gates are present and this must lead to an additional screening of the long-range part of the Coulomb interaction that will reduce the influence of the interaction to its short-range part. We will build our phenomenological model on the understanding based on the renormalization group method, as described in Refs. 5–10, of the influence of the short-range part in the context of the graphene bilayer. This understanding was successful in the explanation of the experiment of Mayorov *et al.*[19] Namely, the three most prominent instabilities of these studies are

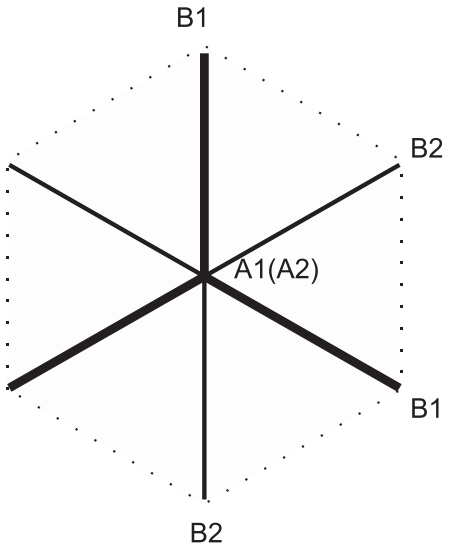

FIG. 1. A view of Bernal stacked honeycomb lattices 1 and 2 with corresponding sublattice sites $A1$ and $B1$, and $A2$ and $B2$.

antiferromagnetic (LAF), nematic, and anomalus Hall effect state. Also in mean field studies their close competition was observed and this indeed points out that the physics cannot be reduced to just (Hubbard) U, but must be extended to first and second near neighbors in an effective description. (This competition is not hard to understand in the graphene bilayer because the second near neighbors in the effective description belong to the same layer, while the first neighbors belong to opposite layers, see below.) But because the (edge) conductance of order e^2/h was not observed in the experiment,[1] we will neglect the influence of the second near neighbor interaction ($B1-B1, B2-B2$ in Fig. 1) that (according to the Haldane model[20,21]) would lead to the anomalous Hall effect.

Thus, according to the results of renormalization group approaches[5–10] and on phenomenological grounds (i.e., on the basis of the experiments[1,19]), the antiferromagnetic (LAF) state and a nematic state are the main instabilities that may arise due to interactions in the graphene bilayer. The nematic state is a result of an ordering in the particle-hole channel that can be described by a nonzero expectation value of the hopping (bond) operator

$$\sum_{\sigma} b^{\dagger}_{1,\vec{n}+\vec{\delta}_1,\sigma} b_{2,\vec{n}-\vec{\delta}_2,\sigma}, \tag{2}$$

where $\vec{n}+\vec{\delta}_1$ and $\vec{n}-\vec{\delta}_2$ denote sites that are near neighbors on the honeycomb lattice that make sublattices $B1$ and $B2$, as shown in Fig. 1. On the same lattice the antiferromagnetic ordering can occur which describes the LAF state.

The nematic, that is, bond ordering as described in Ref. 7, can be thought as a $d_{x^2-y^2}$ CDW (or a $d+id$ CDW as described in Ref. 5—see below Eq. (13) for the definition of the $d_{x^2-y^2}$ and $d+id$ ordering) in the language of Ref. 22. In the same reference this instability ("hidden order" on a square lattice) was proposed for cuprates. Just as in the case of the square lattice and cuprates, this ordering, in the graphene bilayer, can be thought as the result of short-range interactions and superexchange processes. These interactions and processes can also lead to the LAF state. The effective Heisenberg interaction on the $B1$ and $B2$ honeycomb of neighboring sites i and j ($\vec{n}+\vec{\delta}$ and $\vec{n}-\vec{\delta}'$) can be rewritten in terms of the hopping operators [Eq. (2)] as

$$\vec{S}_i\vec{S}_j = -\frac{1}{2}\left(\sum_{\sigma} b^{\dagger}_{1i\sigma} b_{2j\sigma}\right)\left(\sum_{\sigma} b^{\dagger}_{2j\sigma} b_{1i\sigma}\right) - \frac{1}{4}, \tag{3}$$

and should be a part of an effective description of the graphene bilayer. According to Refs. 6 and 10, the only instability in the weak coupling limit of the Hubbard model on the graphene bilayer is antiferromagnetism. Thus, on phenomenological grounds, we will assume that the value of J is an independent parameter in the effective description, favorable for both instabilities, nematic and antiferromagnetic.

With respect to cuprates the on-site repulsion U is not that strong to preclude the double occupancy on the graphene bilayer. Therefore we will explicitly include this interaction in our model Hamiltonian, which can be described as

$$H = H_{\mathrm{J}} + H_{\mathrm{H}}, \tag{4}$$

where

$$H_{\mathrm{J}} = J\sum_{\vec{n}}\sum_{\vec{\delta}_1,\vec{\delta}_2} \vec{S}_{b1}(\vec{n}+\vec{\delta}_1)\ \vec{S}_{b2}(\vec{n}-\vec{\delta}_2), \tag{5}$$

and the summation is over the near neighbors, and

$$H_{\mathrm{H}} = -\sum_{k\in IBZ} t_{\mathrm{eff}}\ \gamma_k^2 b^{\dagger}_{1k}\ b_{2k} + \mathrm{H.c.} + \sum_{i=1,2}\sum_{\vec{n}_i} U\hat{n}_{\uparrow\vec{n}_i}\hat{n}_{\downarrow\vec{n}_i}, \tag{6}$$

with $\gamma_k = \sum_{\vec{\delta}} \exp\{i\vec{k}\vec{\delta}\}$, $\vec{n}_1 \equiv \vec{n}+\vec{\delta}_1$, and $\vec{n}_2 \equiv \vec{n}-\vec{\delta}_2$. The kinetic term (written above in the momentum space) in real space, on the effective honeycomb monolayer of $B1$ and $B2$ sites, describes near-neighbor and two times weaker third-neighbor hopping. It can be recovered in the case of the noninteracting honeycomb bilayer by taking interlayer hopping to be large. In that case $t_{\mathrm{eff}} = \frac{t^2}{t_{\perp}}$. In the small momentum limit the kinetic term in Eq. (6) becomes the one of the graphene bilayer, that is, $t_{\mathrm{eff}}\ \gamma_k^2 \to \frac{t^2}{t_{\perp}}(k_x \mp ik_y)^2$ near K points: $K_{\pm} = \pm\frac{2\pi}{a}(\frac{2}{3},0)$.[23,24] Because we look for the low energy properties we will keep the two-band extension with γ_k^2 throughout the Brillouin zone.

This model is similar to the t-J-U model defined on the square lattice and known from previous investigations. The t-J-U model appeared also in the context of gossamer superconductivity,[25–29] the superconductivity that can exist even at half-filling.

III. MEAN FIELD APPROACH

In order to apply a mean field approach we can use the identity

$$\vec{S}_i\vec{S}_j = -\tfrac{1}{2}(b_{i\uparrow}b_{j\downarrow} - b_{i\downarrow}b_{j\uparrow})(b^{\dagger}_{j\downarrow}b^{\dagger}_{i\uparrow} - b^{\dagger}_{j\uparrow}b^{\dagger}_{i\downarrow}) + \tfrac{1}{4}. \tag{7}$$

We will define the superconducting order parameter,

$$\Delta_{\vec{\delta}} = \langle b_{1i\uparrow}b_{2i+\vec{\delta}\downarrow} - b_{2i+\vec{\delta}\uparrow}b_{1i\downarrow}\rangle, \tag{8}$$

where $\vec{\delta}$ can be any of the near-neighbor vectors on the honeycomb lattice, and

$$m = \langle n_{i\uparrow} - n_{i\downarrow}\rangle, \tag{9}$$

the antiferromagnetic order parameter. In the following we will use the following notation: $t \equiv t_{\rm eff}$, and apply to the Hamiltonian in Eq. (4) the mean field ansatzes. We will generalize the derivation of Ref. 30 to the case with the antiferromagnetic order parameter.

If we use spinors,

$$\Psi_k = [b_{1k\uparrow}\ \ b_{2k\uparrow}\ \ b^\dagger_{1-k\downarrow}\ b^\dagger_{2-k\downarrow}]^T, \tag{10}$$

we can write the mean field Hamiltonian as

$$H_{\rm MF} = \Psi^\dagger_k \mathcal{H} \Psi_k + \frac{1}{2} NJ \sum_{\vec\delta} |\Delta_{\vec\delta}|^2 + U\frac{m^2}{2}N, \tag{11}$$

where N is the number of unit cells,

$$\mathcal{H} = \begin{bmatrix} \frac{U}{2}m & -t\gamma_k^2 & 0 & -\frac{J}{2}\Delta(k) \\ -t\gamma_k^{*2} & -\frac{U}{2}m & -\frac{J}{2}\Delta(-k) & 0 \\ 0 & -\frac{J}{2}\Delta^*(-k) & \frac{U}{2}m & t\gamma_{-k}^{*2} \\ -\frac{J}{2}\Delta^*(k) & 0 & t\gamma_{-k}^2 & -\frac{U}{2}m \end{bmatrix}, \tag{12}$$

and $\Delta(k) = \sum_{\vec\delta} \Delta_{\vec\delta} \exp\{i\vec k\vec\delta\}$. The symmetry analysis of the order parameter on a honeycomb lattice, first done in Ref. 31, concluded that there are three possibilities,

$$\Delta_{\vec\delta}: \begin{matrix} \Delta\ (1,\ \ 1,\ \ 1) \\ \Delta\ (2,\ -1,\ -1) \\ \Delta\ (0,\ \ 1,\ -1) \end{matrix} \tag{13}$$

that span the space of order parameter. The last two possibilities belong to a two-dimensional subspace of irreducible representation of $\mathcal{S}_3$, permutation group.[32] The s-wave $\Delta_\delta = \Delta(1,1,1)$ has nodes at K points because $\Delta_k = \Delta\gamma_k$. For $d_{x^2-y^2}$ wave $\Delta_\delta = \Delta(2,-1,-1)$ near $K_\pm$ points we have $\Delta_1(K_\pm + k) = \Delta[3 \pm \frac{\sqrt3}{2}(k_x \pm ik_y)]$, and for d_{xy} wave $\Delta_\delta = \Delta(0,1,-1)$ the expansions are $\Delta_2(K_\pm + k) = \Delta i[\pm\sqrt3 - \frac{1}{2}(k_x \pm ik_y)]$. Therefore if the $d+id$ combination $\Delta_1(k) \pm i\sqrt3\Delta_2(k)$ is taken near one of the K points the order parameter is a constant (6Δ) and at the other K point is linear in k_x and k_y. Therefore, instead of having the coefficients of the same absolute magnitude with $b^\dagger_{1k\uparrow}b^\dagger_{2-k\downarrow}$ and $b^\dagger_{2k\uparrow}b^\dagger_{1-k\downarrow}$ (and $b_{2-k\downarrow}b_{1k\uparrow}$ and $b_{1-k\downarrow}b_{2k\uparrow}$) for a fixed valley point $d+id$ singles out one spin projection (up or down) to be associated with sites on layer 1 and the opposite one to be associated with sites on layer 2. Thus it favors pairing (Cooper pairs) in which the layer index is associated with definite spin projection just as in an antiferromagnetically ordered state, that is, LAF state described above.

$d+id$ wave and s wave can coexist, as rotationally symmetric states, with the LAF state although only for certain values of J and U parameters. One can show that for the coexistence of the LAF state and s-wave $J \gg U$, which cannot be the case in the graphene bilayer. For the $d+id$ wave, on the other hand, one can find an interval for couplings J and U for which the LAF state and $d+id$-wave pairing can coexist. Expanding the mean field equations to fourth order in the ratio of superconducting and antiferromagnetic order parameter and in the weak coupling limit that is, $t > J,U$, we find $\frac{4}{3} - \frac{1}{4}Jw < \frac{J}{U} < \frac{4}{3} + \frac{1}{4}Jw$, with $w = \frac{1}{\sqrt3\pi t}$. We expect that the interval will broaden when the short-range correlations (due to U) are properly taken into account that will renormalize (reduce) the effective value of t. This was worked out for the square lattice in Ref. 27 in a comprehensive (renormalized mean field) study of the t-J-U model, and a interval of couplings was identified for which antiferromagnetism and superconducting correlations can coexist at half-filling. Furthermore, in Ref. 28 a variational Monte Carlo method was applied to the same system, and a finite value of the pairing amplitude (Δ) was found in the antiferromagnetic region (with no superconducting phase coherence). We expect a similar situation in our case.

As in the case of honeycomb monolayer in Ref. 31, we can diagonalize the free part of the above Hamiltonian and come to the following expressions for order parameters:

$$C_{\vec k} = \sum_{\vec\delta} \Delta_{\vec\delta} \cos\{\vec k\vec\delta - 2\phi_{\vec k}\}$$

and

$$S_{\vec k} = \sum_{\vec\delta} \Delta_{\vec\delta} \sin\{\vec k\vec\delta - 2\phi_{\vec k}\},$$

where $\phi_{\vec k} = \arg[\gamma(k)]$. Due to the expansion of Δ_k around K points in the case of the $d+id$ wave we have

$$C_{K_\pm+k} \sim S_{K_\pm+k} \sim \frac{(k_x \pm ik_y)^2}{|k|^2}, \tag{14}$$

where the last sign is independent of K points. Thus we recovered the basic signatures of $d+id$ pairing: (a) The order parameter is an eigenfunction of orbital angular momentum with eigenvalue equal to two, and (b) due to the same sign (chirality) at both K points this wave is a time reversal symmetry breaking wave on the bilayer honeycomb lattice. Therefore in analyzing this wave we can keep the leading behavior in $\Delta_1(k)$ and $\Delta_2(k)$ as this effectively captures the basic phenomenology of the $d+id$ wave. Thus we take

$$\mathcal{H}_{d-id} = \begin{bmatrix} \frac{U}{2}m & -t\gamma_k^2 & 0 & -J3\Delta \\ -t\gamma_k^{*2} & -\frac{U}{2}m & 0 & 0 \\ 0 & 0 & \frac{U}{2}m & t\gamma_{-k}^{*2} \\ -J3\Delta & 0 & t\gamma_{-k}^2 & -\frac{U}{2}m \end{bmatrix} \tag{15}$$

in the case of $\Delta(k) = \Delta_1(k) - i\sqrt3\Delta_2(k)$ combination, or

$$\mathcal{H}_{d+id} = \begin{bmatrix} \frac{U}{2}m & -t\gamma_k^2 & 0 & 0 \\ -t\gamma_k^{*2} & -\frac{U}{2}m & -J3\Delta & 0 \\ 0 & -J3\Delta & \frac{U}{2}m & t\gamma_{-k}^{*2} \\ 0 & 0 & t\gamma_{-k}^2 & -\frac{U}{2}m \end{bmatrix} \tag{16}$$

in the case when $\Delta(k) = \Delta_1(k) + i\sqrt3\Delta_2(k)$.

In the same low-momentum limit $\gamma_{K_\pm+k} \approx \mp a\frac{\sqrt3}{2}(k_x \mp ik_y)$. We will use redefinitions $\frac{U}{2}m \equiv m$, $J3\Delta \equiv \Delta$, and $ta^2\frac{3}{4} \equiv t$ in the following.

We take Δ to be purely real and without the phase [$U(1)$] degree of freedom, that is, phase coherence[33] that would lead to supercurrents proportional to the gradient of this phase that would screen a magnetic field that may be present. We assume that supercurrents cannot develop in the antiferromagnetic, insulating background.

The Bogoliubov spectrum is the same irrespective whether we ask for energy eigenvalues in the case defined by Eq. (15) or (16), and with the introduced redefinitions the eigenvalues are

$$E = \pm\sqrt{m^2 + \left[\frac{\Delta}{2} \pm \sqrt{t^2k^4 + \left(\frac{\Delta}{2}\right)^2}\right]^2}. \tag{17}$$

Therefore the two different chirality states of the d wave are equally likely in the presence of the antiferromagnetic ordering.

IV. PRESENCE OF SMALL MAGNETIC FIELD

In the presence of magnetic field, due to the minimal prescription, we may introduce a pair of creation and annihilation operators and express the resulting Hamiltonian matrix around K_+ point as

$$\mathcal{H}^o_{+(d-id)B} = \begin{bmatrix} m & -\omega_c(a^\dagger)^2 & 0 & -\Delta \\ -\omega_c(a)^2 & -m & 0 & 0 \\ 0 & 0 & m & \omega_c(a^\dagger)^2 \\ -\Delta & 0 & \omega_c(a)^2 & -m \end{bmatrix}. \tag{18}$$

Here we introduced $\omega_c = \frac{eB}{mc}$, where B is the magnetic field and m is the effective mass of the graphene bilayer $\frac{1}{m} = 2t$. The eigenvectors can be expressed as 4-spinor coefficients of eigenvectors Ψ_n of $a^\dagger a$ operator $a^\dagger a\Psi_n = n\Psi_n$ classified by integer eigenvalues n: 0,1,2, ... In the presence of small magnetic field we will look for the eigenstates in the form

$$\Psi_n = [c_1\ c_2\ c_3\ c_4]^T|n\rangle, \quad n = 0,1,2,\ldots. \tag{19}$$

The Nambu-Gorkov formalism with 4-spinors artificially doubles the degrees of freedom. This appears in spectra as doubling of energy levels ($\pm E$). Thus when solving the $\mathcal{H}_{+(d-id)B}$ we have to keep levels that are continuously related to energy levels with no superconducting instability ($\Delta \neq 0$) and are pertinent to the 2×2 upper, left block of the Hamiltonian matrix.

The Hamiltonian in Eq. (18) we will consider under the approximation of a small magnetic field and rewrite it as

$$\mathcal{H}^o_{+(d-id)B} = H_0 + V, \tag{20}$$

where

$$H_0 = \begin{bmatrix} m & 0 & 0 & -\Delta \\ 0 & -m & 0 & 0 \\ 0 & 0 & m & 0 \\ -\Delta & 0 & 0 & -m \end{bmatrix}, \tag{21}$$

and V denotes the perturbation

$$V = \begin{bmatrix} 0 & -\omega_c(a^\dagger)^2 & 0 & 0 \\ -\omega_c(a)^2 & 0 & 0 & 0 \\ 0 & 0 & 0 & \omega_c(a^\dagger)^2 \\ 0 & 0 & \omega_c(a)^2 & 0 \end{bmatrix}. \tag{22}$$

Taking as solutions only values that are connected continuously in the limit $\Delta \to 0$ to the upper 2×2 left part of H_0 we get for the eigenvalues and eigenvectors of H_0:

$$E_1^n = -m, \quad \Psi_1 = [0,\ 1,\ 0,\ 0]^T|n\rangle,$$
$$E_2^n = \sqrt{m^2 + \Delta^2}, \quad \Psi_2 = c[m + E,\ 0,\ 0,\ -\Delta]^T|n\rangle,$$

where $E = \sqrt{m^2 + \Delta^2}$ and $c = \frac{1}{\sqrt{2E(E+m)}}$. Considering the small magnetic field to second order as perturbation we get $E_1^n = -m - \frac{(n+2)(n+1)}{2}\frac{\omega_c^2}{E}$ and $E_2^n = E + \frac{n(n-1)}{2}\frac{\omega_c^2}{E}$. Considering the same problem at $K' \equiv -K$ point we get $\tilde{E}_1^n = m + \frac{(n+2)(n+1)}{2}\frac{\omega_c^2}{E}$ and $\tilde{E}_2^n = -E - \frac{n(n-1)}{2}\frac{\omega_c^2}{E}$.

Thus, by analyzing the spectra of both K points together, we can conclude that with the inclusion of small magnetic fields the gap changes from $E_g = 2m$ value to $E_g = 2m + 2\frac{\omega_c^2}{E}$ in the presence of $d - id$ correlations. Without the correlations or with $d + id$ correlations the gap will not have the correction quadratic in small magnetic field, which direction is fixed in Eq. (18). $d - id$ correlations minimize the energy of the system by shifting also the energy levels closest to the Fermi point. In the Appendix we compare the energies of the states with $d + id$ and $d - id$ correlations, and show that $d - id$ are indeed of the lower energy.

The energy minimization, when the direction of perpendicular magnetic field is opposite, requires that the superconducting correlations are of $d + id$ kind. Thus the change in the direction of magnetic field is followed by the change in the chirality of the superconducting instability, that is, $B \to -B$ followed by $d - id \to d + id$, as one would expect from the superconducting instability that has orbital and therefore magnetic moment. This amounts to just switching of the previously found spectra between K and K' points. The gap is the same irrespective of the direction of the magnetic field although with the inclusion of superconducting correlations linear in k [on the diagonal in Eqs. (15) and (16)] leads to an asymmetry which may be related to the asymmetry detected in the transport measurements of Ref. 1 with respect to the change in the direction of the external field.

V. DISCUSSION AND CONCLUSION

In the literature we find several proposals[34–36] for the explanation of the data of Ref. 1. See also Ref. 37 for further experimental investigations on the same system and possible explanations based on anomalous quantum Hall physics. Reference 34 by Kharitonov introduces an additional order parameter to the Néel order parameter, but the resulting gap dependence does not have a minimum at B(magnetic field) = 0—compare Fig. 3 in Ref. 34, in contrast to what can be seen from the transport measurements—compare Fig. 3 in Ref. 1. Reference 35 by Zhu, Aji, and Varma with the interesting proposal of taking into account the full four band structure, still gives linear dependence on B of the gap—compare with Fig. 6 in Ref. 35, in contrast to the quadratic dependence on small B as seen in the experiment. Reference 36 by Roy does describe the quadratic dependence based on a mean field treatment of spin magnetism, where a phenomenological ferromagnetic interaction next to the Néel ordering among the spins of electrons is introduced which existence (with a precise magnitude) is necessary to obtain a correspondence to the experimental data.

Our approach is also mean field and phenomenological, though clearly motivated microscopically by the physics of the t-J-U model, as we introduce orbital magnetism of superconducting correlations. This leads to the quadratic dependence of the gap on small B as observed in the experiment. Thus we demonstrated a possibility that the quadratic dependence on small magnetic field observed in the experiment of Ref. 1 may be due to the time reversal symmetry breaking d-wave superconducting correlations that coexist with antiferromagnetism.

The $d+id$ wave superconductivity and antiferromagnetism at high dopings of the graphene monolayer were studied in Refs. 38 and 39. It was shown[39] that both instabilities are connected with the existence of the on-site repulsion U.

The last and important question we would like to discuss is how our proposal can explain the behavior of the system gap in strong (and moderate) magnetic fields. In other words, the question is how does the antiferromagnetic ground state with $d+id$ superconducting correlations evolve in the many-body state of half-filled zero-energy Landau level, which is eightfold degenerate due to flavor [spin and valley (layer)] and orbital ($n=0,1$ Landau index) degrees of freedom. We expect a gradual formation of a QHFM (quantum Hall ferromagnet)[40] due to many-body correlations and the spontaneous ferromagnetic ordering of the spin degree of freedom. Thus we will fix the valley and orbital degree of freedom in the following and discuss how from two (spin up and spin down) Landau levels we can have effectively a single filled Landau level and ferromagnetic ordering. $d+id$ wave Cooper pairs, described in the long distance with the following Cooper pair wave function:[41]

$$f(\vec{r}_{1\uparrow}-\vec{r}_{2\downarrow})\sim\frac{\bar{z}_{1\uparrow}-\bar{z}_{2\downarrow}}{z_{1\uparrow}-z_{2\downarrow}}, \tag{23}$$

in the presence of the magnetic flux will be modified by flux (vortex) attachment due to the particles of opposite spin as in

$$f(\vec{r}_{1\uparrow}-\vec{r}_{2\downarrow})\sim\frac{\bar{z}_{1\uparrow}-\bar{z}_{2\downarrow}}{z_{1\uparrow}-z_{2\downarrow}}\prod_i(z_{1\uparrow}-z_{i\downarrow})^2\prod_j(z_{2\downarrow}-z_{j\uparrow})^2. \tag{24}$$

This will lead to the following many-body state

$$\mathrm{Det}\left(\frac{\bar{z}_{i\uparrow}-\bar{z}_{j\downarrow}}{z_{i\uparrow}-z_{j\downarrow}}\right)\prod_{i,j}(z_{i\uparrow}-z_{j\downarrow})^2=\prod_{i,j}(z_{i\uparrow}-z_{j\downarrow})\chi_2, \tag{25}$$

where Det denotes the determinant of the antisymmetrized product of Cooper pair wave functions, and χ_2 denotes the filled second Landau level wave function in the Jain notation. The identity used in Eq. (25) was proved in Ref. 42. The topological properties of the wave function in Eq. (25) (or the low energy properties of the system described with the wave function as discussed in Ref. 43) are equivalent to the Halperin (1,1,1) state or QHFM, that is, the following state:

$$\prod_{i<j}(z_{i\uparrow}-z_{j\uparrow})\prod_{p<q}(z_{p\downarrow}-z_{q\downarrow})\prod_{l,m}(z_{l\uparrow}-z_{m\downarrow}) \tag{26}$$

for fixed valley and orbital index, and thus lead to the QHFM state with the effective filling factor $\nu_{\mathrm{eff}}=4$. It was shown in Ref. 44 that this state would lead to the gap with linear dependence on the (strong) magnetic field as observed in Ref. 1. Thus we described a possible route from antiferromagnetic state with $d+id$ superconducting correlations to the spin QHFM state consistent with the experiment.

ACKNOWLEDGMENTS

M.V.M. thanks M. Goerbig, D. Tanasković, and J. Vučićević for previous collaboration. The authors are supported by the Serbian Ministry of Education and Science under project No. ON171017.

APPENDIX: ENERGY MINIMIZATION

To find whether $d-id$ or $d+id$ SC correlations coexist with antiferromagnetism in the presence of the magnetic field, which direction is defined as in Eq. (18), we should compare the two ground state energies,

$$E^{d-id}=\sum_{n=0}^{n'}[-m-(n+1)(n+2)\delta]+\sum_{n=0}^{n''}[-E-n(n-1)\delta] \tag{A1}$$

and

$$E^{d+id}=\sum_{n=0}^{\bar{n}'}[-E-(n+1)(n+2)\delta]+\sum_{n=0}^{\bar{n}''}[-m-n(n-1)\delta], \tag{A2}$$

where $\delta=\frac{\omega_c^2}{2E}$, and the bounds for the summations are determined by the lower cutoff $-E_c$, that is, we have in the $d-id$ case

$$(n'+2)(n'+1)=\frac{E_c-m}{\delta}, \tag{A3}$$

$$n''(n''-1)=\frac{E_c-E}{\delta}, \tag{A4}$$

$$(\bar{n}'+2)(\bar{n}'+1)=\frac{E_c-E}{\delta}, \tag{A5}$$

and

$$\bar{n}''(\bar{n}''-1)=\frac{E_c-m}{\delta} \tag{A6}$$

in the $d+id$ case. After a few steps of simple algebra we get

$$E^{d-id}-E^{d+id}=2(m-E). \tag{A7}$$

Because $E>m$, the energy minimization favors $d-id$ SC correlations for the fixed direction of the magnetic field [Eq. (18)].

[1] J. Velasco, Jr., L. Jing, W. Bao, Y. Lee, P. Kratz, V. Aji, M. Bockrath, C. N. Lau, C. Varma, R. Stillwell, D. Smirnov, F. Zhang, J. Jung, and A. H. MacDonald, Nat. Nanotechnol. **7**, 156 (2012).
[2] H. Min, G. Borghi, M. Polini, and A. H. MacDonald, Phys. Rev. B **77**, 041407(R) (2008).
[3] R. Nandkishore and L. Levitov, Phys. Rev. Lett. **104**, 156803 (2010); Phys. Rev. B **82**, 115124 (2010).
[4] F. Zhang, H. Min, M. Polini, and A. H. MacDonald, Phys. Rev. B **81**, 041402(R) (2010).
[5] O. Vafek and K. Yang, Phys. Rev. B **81**, 041401(R) (2010).
[6] O. Vafek, Phys. Rev. B **82**, 205106 (2010).
[7] Y. Lemonik, I. L. Aleiner, C. Toke, and V. I. Falko, Phys. Rev. B **82**, 201408 (2010).
[8] R. E. Throckmorton and O. Vafek, Phys. Rev. B **86**, 115447 (2012).
[9] Y. Lemonik, I. L. Aleiner, and V. I. Falko, Phys. Rev. B **85**, 245451 (2012).
[10] V. Cvetkovic, R. E. Throckmorton, and O. Vafek, Phys. Rev. B **86**, 075467 (2012).
[11] F. Zhang, J. Jung, G. A. Fiete, Q. Niu, and A. H. MacDonald, Phys. Rev. Lett. **106**, 156801 (2011).
[12] J. Jung, F. Zhang, and A. H. MacDonald, Phys. Rev. B **83**, 115408 (2011).
[13] F. Zhang and A. H. MacDonald, Phys. Rev. Lett. **108**, 186804 (2012).
[14] M. M. Scherer, S. Uebelacker, and C. Honerkamp, Phys. Rev. B **85**, 235408 (2012).
[15] E. V. Gorbar, V. P. Gusynin, V. A. Miransky, and I. A. Shovkovy, Phys. Rev. B **86**, 125439 (2012).
[16] F. Zhang, H. Min, and A. H. MacDonald, Phys. Rev. B **86**, 155128 (2012).
[17] Z.-C. Gu, H.-C. Jiang, D. N. Sheng, H. Yao, L. Balents, and X.-G. Wen, arXiv:1110.1183.
[18] E. H. Hwang and S. Das Sarma, Phys. Rev. Lett. **101**, 156802 (2008); T. Ando, A. B. Fowler, and F. Stern, Rev. Mod. Phys. **54**, 437 (1982).
[19] A. S. Mayorov, D. C. Elias, M. Mucha-Kruczynski, R. V. Gorbachev, T. Tudorovskiy, A. Zhukov, S. V. Morozov, M. I. Katsnelson, V. I. Fal'ko, A. K. Geim, and K. S. Novoselov, Science **333**, 860 (2011).
[20] F. D. M. Haldane, Phys. Rev. Lett. **61**, 2015 (1988).
[21] S. Raghu, X.-L. Qi, C. Honerkamp, and S.-C. Zhang, Phys. Rev. Lett. **100**, 156401 (2008).
[22] S. Chakravarty, R. B. Laughlin, D. K. Morr, and C. Nayak, Phys. Rev. B **63**, 094503 (2001).
[23] E. McCann and V. I. Falko, Phys. Rev. Lett. **96**, 086805 (2006).
[24] K. S. Novoselov, E. McCann, S. V. Morozov, V. I. Falko, M. I. Katsnelson, U. Zeitler, D. Jiang, F. Schedin, and A. K. Geim, Nat. Phys. **2**, 177 (2006).
[25] H. Heiselberg, Phys. Rev. A **79**, 063611 (2009).
[26] F. C. Zhang, Phys. Rev. Lett. **90**, 207002 (2003).
[27] F. Yuan, Q. Yuan, and C. S. Ting, Phys. Rev. B **71**, 104505 (2005).
[28] S. Guertler, Q. H. Wang, and F. C. Zhang, Phys. Rev. B **79**, 144526 (2009).
[29] R. B. Laughlin, arXiv:cond-mat/0209269.
[30] J. Vučićević, D. Tanasković, M. O. Goerbig, and M. V. Milovanović, arXiv:1202.3375.
[31] A. M. Black-Schaffer and S. Doniach, Phys. Rev. B **75**, 134512 (2007).
[32] D. Poletti, C. Miniatura, and B. Gremaud, Europhys. Lett. **93**, 37008 (2011).
[33] R. Nandkishore, Phys. Rev. B **86**, 045101 (2012).
[34] M. Kharitonov, arXiv:1109.1553.
[35] L. Zhu, V. Aji, and C. M. Varma, arXiv:1202.0821.
[36] B. Roy, arXiv:1203.6340.
[37] W. Bao, J. Velasco, F. Zhang, L. Jing, B. Standley, D. Smirnov, M. Bockrath, A. MacDonald, and C. N. Lau, Proc. Nat. Acad. Sci. USA **109**, 10802 (2012).
[38] R. Nandkishore, L. Levitov, and A. Chubukov, Nat. Phys. **8**, 158 (2012); R. Nandkishore and A. V. Chubukov, Phys. Rev. B **86**, 115426 (2012).
[39] M. Kiesel, C. Platt, W. Hanke, D. A. Abanin, and R. Thomale, Phys. Rev. B **86**, 020507 (2012).
[40] Y. Barlas, R. Cote, K. Nomura, and A. H. MacDonald, Phys. Rev. Lett. **101**, 097601 (2008).
[41] N. Read and D. Green, Phys. Rev. B **61**, 10267 (2000). Note that in this case the antiferromagnetic background will play the role of chemical potential and lead to weak pairing. This can be explicitly shown in the long-distance limit of the Bogoliubov problem [Eq. (15) or (16)].
[42] N. Moran, A. Sterdyniak, I. Vidanović, N. Regnault, and M. V. Milovanović, Phys. Rev. B **85**, 245307 (2012).
[43] N. Read, Phys. Rev. Lett. **65**, 1502 (1990)
[44] R. Nandkishore and L. Levitov, arXiv:1002.1966.

Trigonal warping in bilayer graphene: Energy versus entanglement spectrum

Sonja Predin, Paul Wenk, and John Schliemann
Institute for Theoretical Physics, University of Regensburg, D-93040 Regensburg, Germany
(Received 21 December 2015; revised manuscript received 10 February 2016; published 2 March 2016)

We present a mainly analytical study of the entanglement spectrum of Bernal-stacked graphene bilayers in the presence of trigonal warping in the energy spectrum. Upon tracing out one layer, the entanglement spectrum shows qualitative geometric differences to the energy spectrum of a graphene monolayer. However, topological quantities such as Berry-phase-type contributions to Chern numbers agree. The latter analysis involves not only the eigenvalues of the entanglement Hamiltonian but also its eigenvectors. We also discuss the entanglement spectra resulting from tracing out other sublattices. As a technical basis of our analysis, we provide closed analytical expressions for the full eigensystem of bilayer graphene in the entire Brillouin zone with a trigonally warped spectrum.

DOI: 10.1103/PhysRevB.93.115106

I. INTRODUCTION

Although first considered as a source of quantum corrections to the entropy of black holes [1], entanglement entropy, in particular von Neumann entropy, evolved into a tool in the field of many-body systems. This brought along connections between seemingly unrelated research areas. In condensed matter, the entanglement entropy serves, e.g., as a geometrical interpretation for the boundary between local quantum many-body systems. This connection has its origin in the *area laws* [2].

However, Li and Haldane have shown that the related entanglement spectrum contains more information than the single number expressed by the entanglement entropy [3]. This spectrum is determined by the Schmidt decomposition of the ground state of a bipartite system, and the reduced density matrix obtained by tracing out one of the subsystems can always be formulated as

$$\rho_{\mathrm{red}} = \frac{e^{-\mathcal{H}_{\mathrm{ent}}}}{Z} \tag{1}$$

with an entanglement Hamiltonian $\mathcal{H}_{\mathrm{ent}}$ encoding the entanglement spectrum, and a partition function $Z = \mathrm{tr}(e^{-\mathcal{H}_{\mathrm{ent}}})$. Following the Li-Haldane conjecture [3], in a gapped phase, the entanglement spectrum can be directly related to the spectrum of edge excitations as shown for the fractional quantum Hall system [4–6]. This relation to edge excitations can also be seen analytically in the case of noninteracting particles. It can be shown by mapping the free fermionic system $\mathcal{H}$ onto a *flatband* Hamiltonian $\mathcal{H}_{\mathrm{flat}}$ [7]. Now, the eigenenergies e_i of the latter are related to the eigenenergies of the corresponding entanglement energies ε_i as $e_i \sim \tanh(\varepsilon_i/2)/2 + \mathrm{const}$ [8]. Thereby, the eigenstates of both $\mathcal{H}_{\mathrm{flat}}$ and $\mathcal{H}$ are the same. Thus, if $\mathcal{H}$ contains topologically protected surface states, the same holds for the entanglement Hamiltonian.

This is why the entanglement spectrum, beyond the related entropy, is considered a *tower of states* and is used as a fingerprint for topological order. However, this is not true in general, as shown recently by Chandran *et al.* [9].

As a result of a multitude of studies, there is a plethora of revisited effects in the context of an entanglement spectrum, such as the Kondo effect, many-body localization, or disordered quantum spin systems; for recent reviews, see Refs. [10,11].

A particular situation arises if the edge comprises the entire remaining subsystem, as is the case for spin ladders [12–21] and various bilayer systems [22–24]. A typical observation in such scenarios is, in the regime of strongly coupled subsystems, a proportionality between the energy Hamiltonian of the remaining subsystem and the appropriately defined entanglement Hamiltonian. We note that the entanglement Hamiltonian entering the reduced density matrix (1) is only determined up to multiples of the unit operator, which has consequences regarding thermodynamic relations between the entanglement entropy and the subsystem energy [22–24].

On the other hand, such a close relation between energy and the entanglement Hamiltonian is not truly general, as shown in Ref. [18], where a spin ladder of clearly nonidentical legs was studied. In the present work, we provide another counterexample given by graphene bilayers in the presence of trigonal warping [25,26]. As we shall see in the following, the geometric properties of the entanglement spectrum of an undoped graphene bilayer and the energy spectrum of a monolayer clearly differ qualitatively. However, certain topological quantities such as Berry-phase-type contributions to Chern numbers agree. The latter analysis involves not only the eigenvalues of the entanglement Hamiltonian (i.e., the entanglement spectrum) but also its eigenvectors.

This paper is organized as follows. In Sec. II, we discuss the full eigensystem of the tight-binding model of bilayer graphene in the presence of trigonal warping; a full account of the technical details is given in Appendixes A and B. To enable analytical progress, we neglect here terms breaking particle-hole symmetry. On the other hand, our calculation considers the entire first Brillouin zone and avoids the Dirac cone approximation usually employed in studies of trigonal warping in graphene bilayers [27–35]. We compare our results for the full four-band model with an effective Hamiltonian acting on the two central bands [27,34,35]. The entanglement spectrum obtained from the ground state of undoped graphene bilayers is analyzed in Sec. III. We discuss the case of one layer being traced out as well as the situation in which the trace is performed over two other out of four sublattices. We close with a summary and an outlook in Sec. IV.

II. ENERGY SPECTRUM OF GRAPHENE BILAYERS: TRIGONAL WARPING AND TOPOLOGICAL INVARIANTS

The standard tight-binding Hamiltonian for graphene bilayers in Bernal stacking can be formulated as [25,26]

$$\begin{aligned} H = &-t\sum_{\vec{k}}(\gamma(\vec{k})a^{\dagger}_{1\vec{k}}b_{1\vec{k}} + \gamma(\vec{k})a^{\dagger}_{2\vec{k}}b_{2\vec{k}} + \text{H.c.}) \\ &+ t_{\perp}\sum_{\vec{k}}(b^{\dagger}_{1\vec{k}}a_{2\vec{k}} + a^{\dagger}_{2\vec{k}}b_{1\vec{k}}) \\ &- t_3\sum_{\vec{k}}(\gamma(\vec{k})b^{\dagger}_{2\vec{k}}a_{1\vec{k}} + \gamma^{*}(\vec{k})a^{\dagger}_{1\vec{k}}b_{2\vec{k}}) \\ &+ t_4\sum_{\vec{k}}[\gamma(\vec{k})(a^{\dagger}_{1\vec{k}}a_{2\vec{k}} + b^{\dagger}_{1\vec{k}}b_{2\vec{k}}) + \text{H.c.}], \end{aligned} \tag{2}$$

where $a^{\dagger}_{i\vec{k}}$ ($a_{i\vec{k}}$) and $b^{\dagger}_{i\vec{k}}$ ($b_{i\vec{k}}$) create (annihilate) electrons with wave vector $\vec{k}$ in layers $i = 1,2$ on sublattices A and B, respectively. Moreover, $\gamma(\vec{k}) = \sum_{l=1}^{3}\exp(i\vec{k}\cdot\vec{\delta}_l)$, where the $\vec{\delta}_l$ are the vectors connecting a given carbon atom with its nearest neighbors on the other sublattice in a graphene monolayer. In what follows, we will use coordinates with

$$\vec{\delta}_{1,2} = \frac{a}{2}(-1,\pm\sqrt{3}), \quad \vec{\delta}_3 = a(1,0), \tag{3}$$

where $a = 1.42$ Å is the distance between neighboring carbon atoms, such that the two inequivalent corners of the first Brillouin zone can be given as

$$\vec{K}_{\pm} = \frac{2\pi}{3\sqrt{3}a}(\sqrt{3},\pm 1). \tag{4}$$

The parameter t describes hopping within each layer between the sublattices while $t_{\perp}$ parametrizes the vertical hopping between the two sublattices in different layers lying on top of each other. The additional hopping processes described by the skew parameters t_3,t_4 lead to trigonal warping of the spectrum and electron-hole asymmetry, respectively. Experimentally established values [36] for these quantities are $t = 3.16$ eV, $t_{\perp} = 0.381$ eV, $t_3 = 0.38$ eV, and $t_4 = 0.14$ eV. The geometry of the first Brillouin zone is visualized in Fig. 1 along with a color plot of the modulus $|\gamma(\vec{k})|$.

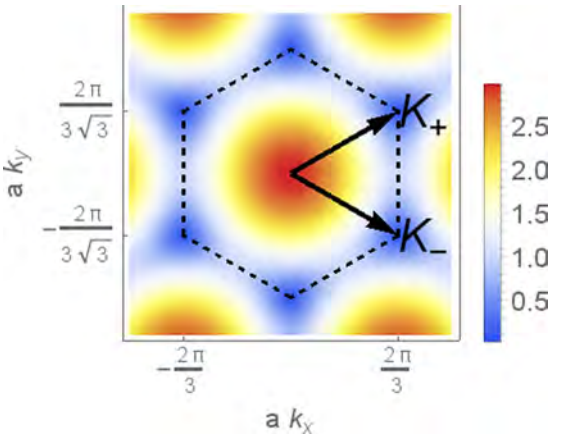

FIG. 1. Brillouin zone with a density plot of $|\gamma(\vec{k})|$.

The presence of all four couplings in the Hamiltonian Eq. (2) makes its explicit diagonalization in terms of analytical expressions a particularly cumbersome task. As the present study chiefly relies on analytical calculations rather than resorting to numerics, we will drop the contributions proportional to the smallest parameter t_4 in order to achieve an analytically manageable situation.

Setting $t_4 = 0$, the full eigensystem of the Hamiltonian (2) can be obtained in a closed analytical fashion as detailed in Appendix A. The four dispersion branches $[\pm E_1(\vec{k})]$,$[\pm E_2(\vec{k})]$ form a symmetric spectrum with

$$E_{1/2} = \sqrt{\tfrac{1}{2}\left(t_{\perp}^2 + t_3^2|\gamma(\vec{k})|^2 + 2t^2|\gamma(\vec{k})|^2 \pm \sqrt{4t^2|\gamma(\vec{k})|^2\left(t_{\perp}^2 + t_3^2|\gamma(\vec{k})|^2 - 2t_{\perp}t_3|\gamma(\vec{k})|\cos(3\phi_{\vec{k}})\right) + \left(t_{\perp}^2 - t_3^2|\gamma(\vec{k})|^2\right)^2}\right)} \tag{5}$$

and $\gamma(\vec{k}) = |\gamma(\vec{k})|e^{i\phi_{\vec{k}}}$. The two outer branches $[\pm E_1(\vec{k})]$ are separated from the inner ones $[\pm E_2(\vec{k})]$ by gaps determined essentially by the hopping parameter $t_{\perp}$. The result Eq. (5) generalizes the energy spectrum given in Ref. [27] within the Dirac cone approximation to the full Brillouin zone. Moreover, in Appendix A we also give the complete data of the corresponding eigenvectors. Figure 2 concentrates on the vicinity of a given K point using realistic parameters.

The inner branches $[\pm E_2(\vec{k})]$ dominate the low-energy physics of the system near half-filling and meet at zero energy for

$$\gamma(\vec{k}) = 0 \tag{6}$$

corresponding to the two inequivalent corners $K_{\pm}$ of the first Brillouin zone, and for

$$\cos(3\phi_{\vec{k}}) = -1 \quad \wedge \quad |\gamma(\vec{k})| = \frac{t_{\perp}t_3}{t^2}. \tag{7}$$

The latter condition defines three additional satellite Dirac cones around each K point, two of which lie on the edges (faces) of the Brillouin zone connecting $K_{\pm}$. The third satellite Dirac cone lies formally outside the Brillouin zone but is equivalent to a satellite cone on the edge around an equivalent K point. Indeed, the quantity $\gamma(\vec{k})$ has a constant phase $\phi_{\vec{k}} \in \{-\pi/3,\pi/3,\pi\}$ on each face: As an example, consider the edge connecting the two inequivalent K points given in Eq. (4), where one finds

$$\gamma\left(\frac{2\pi}{3a},k_y\right) = e^{-i\pi/3}\left[2\cos\left(\frac{\sqrt{3}}{2}k_y a\right) - 1\right] \tag{8}$$

with the parentheses being non-negative for k_y ranging between $[\pm 2\pi/(3\sqrt{3}a)]$. Thus, solving for k_y, the satellite

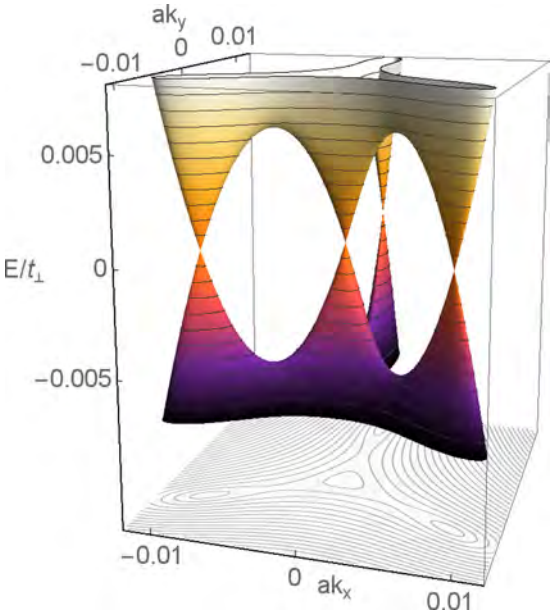

FIG. 2. The central energy bands $[\pm E_2(\vec{k})]$ plotted around a given K point for $t_\perp = 0.1t$, $t_3 = 0.15t$. The dispersions show a central Dirac cone accompanied by three satellites. The components of the wave vector are measured relative to the K point.

Dirac cones on that edge lie at

$$\vec{k} = \left(\frac{2\pi}{3a}, \pm\frac{2}{\sqrt{3}a}\arccos\left[\frac{1}{2}\left(1+\frac{t_\perp t_3}{t^2}\right)\right]\right), \tag{9}$$

and the other satellite cones are located at positions being equivalent under reciprocal-lattice translation and/or hexagonal rotation. Note that for $t_\perp t_3/t^2 = 1$, the satellite cones merge in the M points (centers of the faces) and they vanish for even larger values of that ratio. In Fig. 3 we present a sketch of the situation in the entire Brillouin zone for moderate values of $t_\perp$ and t_3.

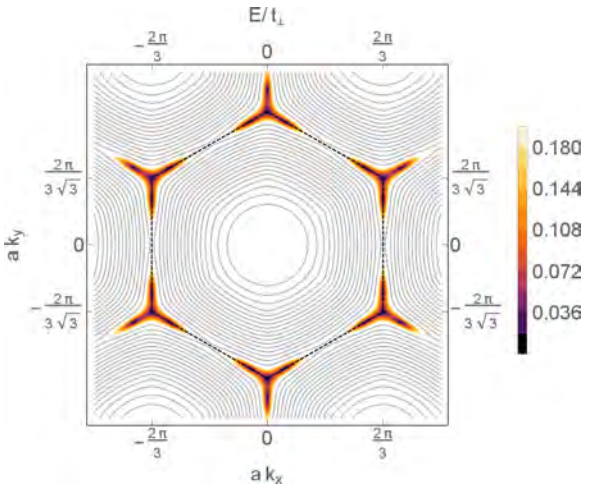

FIG. 3. Contour plot of the energy band $[+E_2(\vec{k})]$ plotted for $t_\perp = t$, $t_3 = 0.5t$. The contour of the colored region indicates $E = 0.2/t_\perp$. The edge of the first Brillouin zone is marked by dashed lines.

For $t_3 = 0$, the two energy bands $[\pm E_2(\vec{k})]$ touch only at the K points where they have a quadratic dispersion. Finite $t_3 \neq 0$ causes a splitting into a total of four Dirac cones with linear dispersion, an effect known as trigonal warping [25,34].

As a further important property, the eigenvectors corresponding to $[\pm E_2(\vec{k})]$ are discontinuous as a function of wave vector at the degeneracy points defined by Eq. (7); for more technical details, we refer the reader to Appendix B. As a simplistic toy model mimicking such an effect, one can consider the Hamiltonian $H = -k\sigma^z$ with a one-dimensional wave number k and the Pauli matrix σ^z describing some internal degree of freedom: In the many-body ground state of zero Fermi energy all occupied states with $k > 0$ have spin up, while for all states with $k < 0$ the spin points downward, resulting in a discontinuity of the occupied eigenvectors at $k = 0$. As we shall see below, in the present case of graphene bilayers this discontinuity is also reflected in the entanglement spectrum.

An effective Hamiltonian providing an approximate description of the central bands $[\pm E_2(\vec{k})]$ can be given following Ref. [27]. In up to linear order in $1/t_\perp$, one finds

$$H = -\begin{pmatrix} 0 & \frac{t^2}{t_\perp}(\gamma^*(\vec{k}))^2 + t_3\gamma(\vec{k}) \\ \frac{t^2}{t_\perp}(\gamma(\vec{k}))^2 + t_3\gamma^*(\vec{k}) & 0 \end{pmatrix} \tag{10}$$

with respect to the basis $(b^\dagger_{2\vec{k}}, a^\dagger_{1\vec{k}})|0\rangle$. The eigenstates read

$$|\chi_\pm\rangle = \frac{1}{\sqrt{2}}\begin{pmatrix} 1 \\ \mp e^{i\psi_{\vec{k}}} \end{pmatrix} \tag{11}$$

with

$$e^{i\psi_{\vec{k}}} = \frac{\frac{t^2}{t_\perp}(\gamma(\vec{k}))^2 + t_3\gamma^*(\vec{k})}{\left|\frac{t^2}{t_\perp}(\gamma(\vec{k}))^2 + t_3\gamma^*(\vec{k})\right|}. \tag{12}$$

Note that the Hamiltonian (10) vanishes if and only if the conditions (6) or (7) are fulfilled, implying that the positions of the central and satellite Dirac cones are the same as for the full Hamiltonian (2). Moreover, $\psi_{\vec{k}}$ is a smooth and well-defined function of the wave vector except for the locations of Dirac cones. Accordingly, the Berry curvature

$$F(\vec{k}) = \frac{\partial A_y}{\partial k_x} - \frac{\partial A_x}{\partial k_y} \tag{13}$$

arising from the Berry connection

$$\vec{A}(\vec{k}) = i\langle\chi_\pm(\vec{k})|\frac{\partial}{\partial\vec{k}}|\chi_\pm(\vec{k})\rangle = -\frac{1}{2}\frac{\partial\psi_{\vec{k}}}{\partial\vec{k}} \tag{14}$$

vanishes everywhere outside the Dirac cones where contributions in terms of δ functions arise. Integrating the Berry connection along a closed path in $\vec{k}$ space leads to geometrical quantities often referred to as Berry phases, although no contact to adiabaticity is made here. Moreover, if the Berry curvature has only nonzero contributions in terms of δ functions (as is the case here and in the following), these geometrical phases are indeed topological, i.e., they are invariant under continuous variations of the paths as long as the support of the δ functions is not touched.

As discussed in Refs. [31,33,34], integrating along a closed path around the central Dirac cones at $K_\pm$ yields a Berry phase of $(\mp\pi)$, while each of the accompanying satellite cones gives a contribution of $(\pm\pi)$. Thus, the total Berry phase arising at and around each K point is, as in the absence of trigonal warping, $(\pm 2\pi)$, and the integral over the whole Brillouin zone of the Berry connection (i.e., the Chern number) vanishes. Naturally, our present analysis going beyond the Dirac cone approximation confirms these results.

III. ENTANGLEMENT SPECTRA

For systems of free fermions such as those studied here, the entanglement Hamiltonian can be formulated as a single-particle operator [23,37,38],

$$H_{\text{ent}} = \sum_\lambda \xi_\lambda d_\lambda^\dagger d_\lambda. \tag{15}$$

Here the $d_\lambda^\dagger$ generate eigenstates of the correlation matrix

$$C_{\alpha\beta} = \langle\Psi| c_\alpha^\dagger c_\beta |\Psi\rangle, \tag{16}$$

where $|\Psi\rangle$ is the ground state of the composite system, and single-particle operators c_α, c_β act on its remaining part after tracing out a subsystem. The entanglement levels ξ_λ are related to the eigenvalues η_λ of the correlation matrix via

$$\xi_\lambda = \ln\left(\frac{1-\eta_\lambda}{\eta_\lambda}\right) = 2\,\text{artanh}\,(1-2\eta_\lambda). \tag{17}$$

In particular, the entanglement Hamiltonian and the correlation matrix share the same system of eigenvectors.

A. Tracing out one layer

We now consider the ground state of the undoped graphene bilayer such that all states with negative energies $[-E_1(\vec{k})]$, $[-E_2(\vec{k})]$ are occupied while all others are empty. Tracing out layer 1 leads to the correlation matrix

$$C(\vec{k}) = \begin{pmatrix} \frac{1}{2} & u(\vec{k}) \\ u^*(\vec{k}) & \frac{1}{2} \end{pmatrix} \tag{18}$$

where an explicit expression for $u(\vec{k})$ is given in Appendix C. The entanglement levels corresponding to the eigenvalues $\eta_\pm(\vec{k}) = 1/2 \mp |u(\vec{k})|$ are

$$\xi_\pm(\vec{k}) = \pm 2\,\text{artanh}(2|u(\vec{k})|). \tag{19}$$

The modulus $|u|$ can be formulated as

$$|u| = \frac{1/2}{\sqrt{1+\{d/[t|\gamma(\vec{k})|]\}^2}}\sqrt{\frac{1}{2}\left(1-\frac{\epsilon_1\epsilon_2+b^2}{E_1E_2}\right)} \tag{20}$$

with [cf. Eqs. (A14) and (A15)]

$$d = \frac{\left(t_\perp^2 - t_3^2|\gamma(\vec{k})|^2\right)/2}{\sqrt{t_\perp^2 + t_3^2|\gamma(\vec{k})|^2 - 2t_\perp t_3|\gamma(\vec{k})|\cos(3\phi_{\vec{k}})}}, \tag{21}$$

$$b = \frac{t_\perp t_3|\gamma(\vec{k})||\sin(3\phi_{\vec{k}})|}{\sqrt{t_\perp^2 + t_3^2|\gamma(\vec{k})|^2 - 2t_\perp t_3|\gamma(\vec{k})|\cos(3\phi_{\vec{k}})}}, \tag{22}$$

and [cf. Eq. (A21)]

$$\epsilon_{1,2} = t|\gamma(\vec{k})| \pm \sqrt{\left(t_\perp^2 + t_3^2|\gamma(\vec{k})|^2 - 2t_\perp t_3|\gamma(\vec{k})|\cos(3\phi_{\vec{k}})\right)^2/4 + d^2} \tag{23}$$

implying

$$E_{1,2} = \sqrt{\epsilon_{1,2}^2 + b^2}. \tag{24}$$

The right-hand side of Eq. (20) becomes zero if the radicand vanishes. According to the discussion in Appendixes B and C, this is the case when $\cos(3\phi_{\vec{k}}) = -1$ leading to $b = 0$ and $E_1 = \epsilon_1 \geqslant 0, E_2 = |\epsilon_2|$ such that

$$|u| \propto \sqrt{\frac{1}{2}\left(1-\frac{\epsilon_2}{|\epsilon_2|}\right)}. \tag{25}$$

Now Eq. (B2) shows that $|u(\vec{k})| = 0$ is equivalent to

$$\cos(3\phi_{\vec{k}}) = -1 \quad \wedge \quad |\gamma(\vec{k})| \in [0, t_\perp t_3/t^2], \tag{26}$$

where the end point of the above interval defines according to condition (7) the location of the satellite Dirac cones. As a result, the entanglement levels (19) vanish along segments of the faces of the first Brillouin zone bounded by the positions of the central Dirac cones and their satellites. At the satellite Dirac cones, the entanglement spectrum is discontinuous as a function of wave vector. In Fig. 4, we plotted the entanglement spectrum $\xi_+(\vec{k})$ for the whole Brillouin zone. For a better visualization, large hopping parameters have been chosen. The contour of the colored region connects all three satellite Dirac cones. As discussed in Appendix B, this discontinuity is inherited from a discontinuity in the eigenvectors of the occupied single-particle states. The entanglement spectrum in the entire Brillouin zone is illustrated in Fig. 4, whereas Fig. 5 focuses on a given K point.

Moreover, apart from the eigenvalues of the entanglement Hamiltonian, let us also consider its eigenvector, which

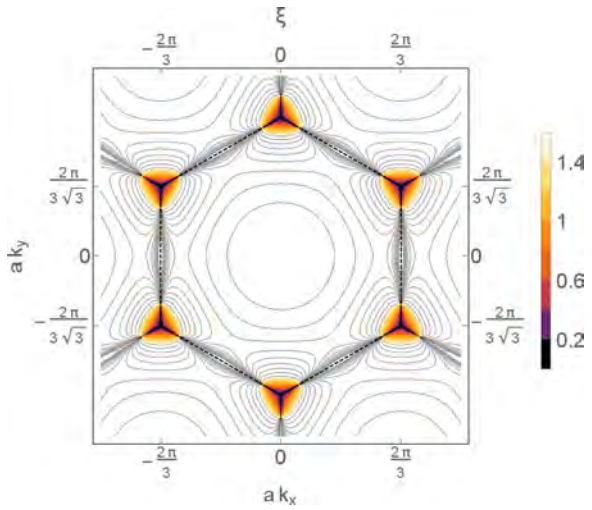

FIG. 4. Contour plot of the entanglement spectrum $\xi_+(\vec{k})$ plotted for $t_\perp = t$, $t_3 = 0.5t$. The contour of the colored region indicates $\xi = 1.5$. The dashed line delineates the first Brillouin zone.

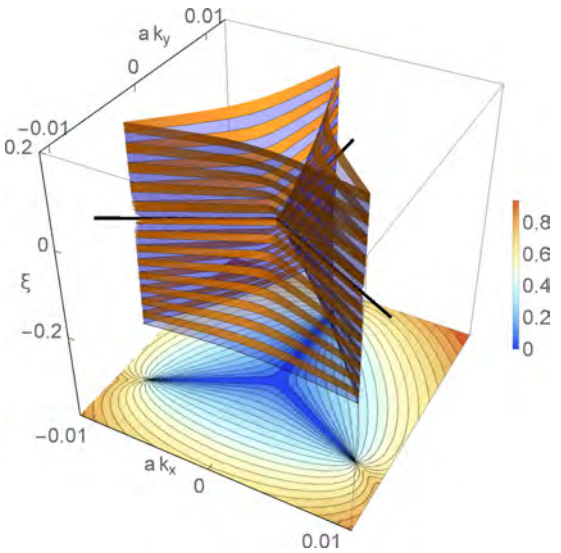

FIG. 5. The entanglement spectrum (19) plotted around a given K point for the same parameters as in Fig. 2. The density plot shows the upper entanglement level. Zero eigenvalues of the entanglement Hamiltonian occur along lines connecting the K point with the locations of satellite Dirac cones of the energy spectrum (thick black lines). The components of the wave vector are measured relative to the K point.

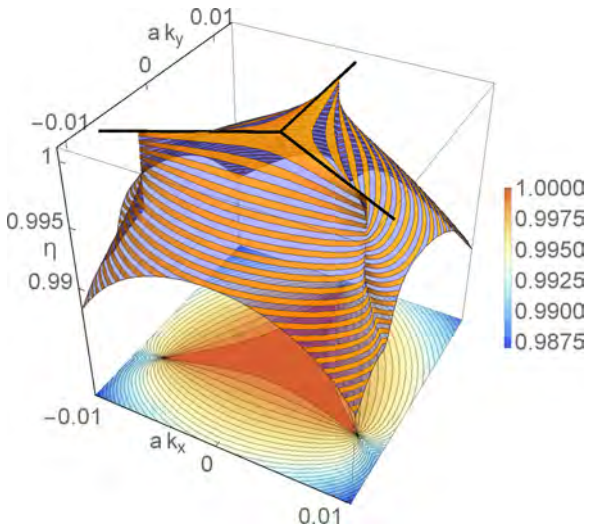

FIG. 6. Eigenvalues $\eta_-(\vec{k}) = 1/2 + |v(\vec{k})|$ of the correlation matrix plotted around a given K point for $t_\perp = 0.1t$, $t_3 = 0.15t$. The thick black lines correspond to the one in Fig. 5, and the components of the wave vector are again measured relatively to the K point.

coincides with the eigenvectors of the correlation matrix (18). As discussed in Appendix C, the complex function $u(\vec{k})$ entering the correlation matrix becomes singular at the K points and the positions of the accompanying satellite Dirac cones of the energy spectrum, leading again to δ-function-type contributions to the Berry curvature that vanishes otherwise. Combining symbolic computer algebra techniques and numerical calculations, we find here a Berry phase of $(\mp\pi/2)$ around the corners $K_\pm$ of the Brillouin zone, and $(\pm\pi/2)$ for the corresponding satellite positions. For the central positions, the above calculations can also be done fully analytically by expanding the eigensystem data around $K_\pm$. For the satellite locations, such an expansion is not possible due to the discontinuity of the eigenvectors.

Thus, the total Berry phase contribution from each K point $K_\pm$ is $(\pm\pi)$ and agrees with the Berry phase around the Dirac cones in monolayer graphene. As a result, although the entanglement spectrum of graphene bilayers generated by tracing out one layer shows obvious differences from the energy spectrum of monolayer graphene regarding qualitative geometrical properties, the topological Berry phases obtained from the corresponding eigenvectors still coincide at each K point.

B. Tracing out other sublattices

Now, we will consider the entanglement spectrum obtained by tracing out sublattices A1 and B2 (or A2 and B1) lying in different layers. In the former case, one finds

$$C(\vec{k}) = \begin{pmatrix} \frac{1}{2} & v(\vec{k}) \\ v^*(\vec{k}) & \frac{1}{2} \end{pmatrix}, \tag{27}$$

where an explicit expression for $v(\vec{k})$ is given in Appendix C. The above correlation matrix has eigenvalues $\eta_\pm(\vec{k}) = 1/2 \mp |v(\vec{k})|$ leading to the entanglement levels

$$\xi_\pm(\vec{k}) = \pm 2\,\mathrm{artanh}(2|v(\vec{k})|)\,. \tag{28}$$

In Fig. 6, we plotted the eigenvalues $\eta_-(\vec{k}) = 1/2 + |v(\vec{k})|$ of the correlation matrix around a given K point. The modulus $|v(\vec{k})|$ reads more explicitly

$$|v(\vec{k})| = \frac{1}{2}\sqrt{1 - \frac{t^2|\gamma(\vec{k})|^2}{t^2|\gamma(\vec{k})|^2 + d^2}\frac{1}{2}\left(1 - \frac{\epsilon_1\epsilon_2 + b^2}{E_1E_2}\right)} \tag{29}$$

$$= \tfrac{1}{2}\sqrt{1 - 4|u(\vec{k})|^2} \tag{30}$$

and has a structure similar to $|u(\vec{k})|$ given in Eq. (20). In particular, $|v(\vec{k})| = 1/2 \Leftrightarrow |u(\vec{k})| = 0$ if the conditions (26) are fulfilled. In this case, $\eta_+ = 0$ and $\eta_- = 1$, indicating that the remaining subsystem is unentangled with the system traced out.

Regarding Berry phases generated from the eigenstates of the correlation matrix (27), we note that the off-diagonal element $v(\vec{k})$ does not vanish anywhere. As a consequence, the Berry curvature defined analogously as in Eqs. (11)–(14) is zero throughout the Brillouin zone, which in turn holds for all Berry phases. The nonvanishing of $v(\vec{k})$ follows from the fact that $|v(\vec{k})| = 0$ would require $|u(\vec{k})| = 1/2$ such that the entanglement (19) would diverge, which is, as seen in Sec. III A, not the case.

Finally, the correlation matrix obtained by tracing over the sublattices A1 and A2 (or B1 and B2) is proportional to the unit matrix,

$$C(\vec{k}) = \begin{pmatrix} \frac{1}{2} & 0 \\ 0 & \frac{1}{2} \end{pmatrix}, \tag{31}$$

indicating that these sublattices are maximally entangled with the part traced out.

IV. CONCLUSIONS AND OUTLOOK

We have studied the entanglement properties of the ground state of Bernal stacked graphene bilayers in the presence of trigonal warping. Our analysis includes both the eigenvalues of the reduced density matrix (giving rise to the entanglement spectrum) as well as its eigenvectors. When tracing out one layer, the entanglement spectrum shows qualitative geometric differences to the energy spectrum of a graphene monolayer, while topological quantities such as Berry-phase-type contributions to Chern numbers agree. The latter finding is in contrast to the reduced density matrix resulting from tracing out other sublattices of the bilayer system. Here, all corresponding Berry phase integrals yield trivially zero. Thus, our study provides an example for common topological properties of the eigensystem of the energy Hamiltonian of a subsystem (here a graphene monolayer) and the entanglement Hamiltonian, while the geometrical shape of both spectra grossly differs. Our investigations are based on closed analytical expressions for the full eigensystem of bilayer graphene in the entire Brillouin zone with a trigonally warped spectrum.

Future work might address bilayer systems of other geometrical structures such as the Kagome lattice, the influence of a static perpendicular magnetic field [23,39], and the effect of time-periodic in-plane electric fields [40].

Note added in proof. Recently, we became aware of Ref. [41] where also Chern numbers calculated from the eigenstates of entanglement Hamiltonians are studied. Most recent work building upon this concept is reported on in Ref. [42].

ACKNOWLEDGMENTS

This work was supported by Deutsche Forschungsgemeinschaft via GRK1570.

APPENDIX A: DIAGONALIZATION OF THE BILAYER HAMILTONIAN

Setting $t_4 = 0$ and fixing a wave vector $\vec{k}$, the Hamiltonian (2) reads with respect to the basis $(a^\dagger_{2\vec{k}}, b^\dagger_{1\vec{k}}, b^\dagger_{2\vec{k}}, a^\dagger_{1\vec{k}})|0\rangle$

$$H = \begin{pmatrix} 0 & t_\perp & -t\gamma(\vec{k}) & 0 \\ t_\perp & 0 & 0 & -t\gamma^*(\vec{k}) \\ -t\gamma^*(\vec{k}) & 0 & 0 & -t_3\gamma(\vec{k}) \\ 0 & -t\gamma(\vec{k}) & -t_3\gamma^*(\vec{k}) & 0 \end{pmatrix}. \tag{A1}$$

Using $\gamma(\vec{k}) = |\gamma(\vec{k})|e^{i\phi_{\vec{k}}}$, we apply the transformation

$$U_1 = \frac{1}{\sqrt{2}} \begin{pmatrix} 1 & 1 & 0 & 0 \\ 0 & 0 & e^{i\phi_{\vec{k}}} & e^{-i\phi_{\vec{k}}} \\ 0 & 0 & e^{i\phi_{\vec{k}}} & -e^{-i\phi_{\vec{k}}} \\ 1 & -1 & 0 & 0 \end{pmatrix} \tag{A2}$$

such that in

$$H_1 = U_1 H U_1^\dagger = \begin{pmatrix} t_\perp & -t|\gamma(\vec{k})| & 0 & 0 \\ -t|\gamma(\vec{k})| & -t_3|\gamma(\vec{k})|\cos(3\phi_{\vec{k}}) & it_3|\gamma(\vec{k})|\sin(3\phi_{\vec{k}}) & 0 \\ 0 & -it_3|\gamma(\vec{k})|\sin(3\phi_{\vec{k}}) & t_3|\gamma(\vec{k})|\cos(3\phi_{\vec{k}}) & -t|\gamma(\vec{k})| \\ 0 & 0 & -t|\gamma(\vec{k})| & -t_\perp \end{pmatrix} \tag{A3}$$

all information on the phase $\phi_{\vec{k}}$ is contained in the matrix elements being proportional to the skew parameter t_3. Proceeding now with the transformation

$$U_2 = \frac{1}{\sqrt{2}} \begin{pmatrix} 1 & -1 & 0 & 0 \\ 1 & 1 & 0 & 0 \\ 0 & 0 & 1 & -1 \\ 0 & 0 & 1 & 1 \end{pmatrix}, \tag{A4}$$

we find

$$H_2 = U_2 H_1 U_2^\dagger = \frac{1}{2} \begin{pmatrix} e_1 & c & -is & -is \\ c & e_2 & is & is \\ is & -is & -e_2 & c \\ is & -is & c & -e_1 \end{pmatrix} \tag{A5}$$

with

$$e_1 = \quad 2t|\gamma(\vec{k})| + t_\perp - t_3|\gamma(\vec{k})|\cos(3\phi_{\vec{k}}), \tag{A6}$$

$$e_2 = -2t|\gamma(\vec{k})| + t_\perp - t_3|\gamma(\vec{k})|\cos(3\phi_{\vec{k}}), \tag{A7}$$

$$c = t_\perp + t_3|\gamma(\vec{k})|\cos(3\phi_{\vec{k}}), \tag{A8}$$

$$s = t_3|\gamma(\vec{k})|\sin(3\phi_{\vec{k}}). \tag{A9}$$

Here it is useful to split the above matrix as $H_2 = H_2^{'} + H_2^{''}$, where

$$H_2^{'} = \frac{1}{2}\begin{pmatrix} e_1 & 0 & -is & 0 \\ 0 & e_2 & 0 & is \\ is & 0 & -e_2 & 0 \\ 0 & -is & 0 & -e_1 \end{pmatrix}, \quad H_2^{''} = \frac{1}{2}\begin{pmatrix} 0 & c & 0 & -is \\ c & 0 & is & 0 \\ 0 & -is & 0 & c \\ is & 0 & c & 0 \end{pmatrix}. \tag{A10}$$

$H_2^{'}$ is diagonalized by

$$U_3 = \begin{pmatrix} \alpha_+ & 0 & -i\sigma\alpha_- & 0 \\ 0 & -i\sigma\alpha_+ & 0 & \alpha_- \\ -i\sigma\alpha_- & 0 & \alpha_+ & 0 \\ 0 & \alpha_- & 0 & -i\sigma\alpha_+ \end{pmatrix} \tag{A11}$$

with $\sigma = \text{sign}\,(\sin[3\phi(\vec{k})])$ and

$$\alpha_\pm = \sqrt{\frac{1}{2}\left(1 \pm \frac{t_\perp - t_3|\gamma(\vec{k})|\cos(3\phi_{\vec{k}})}{\sqrt{t_\perp^2 + t_3^2|\gamma(\vec{k})|^2 - 2t_\perp t_3|\gamma(\vec{k})|\cos(3\phi_{\vec{k}})}}\right)} \tag{A12}$$

such that

$$H_3 = U_3 H_2 U_3^\dagger = \begin{pmatrix} \zeta_1 & id\sigma & 0 & b \\ -id\sigma & \zeta_2 & b & 0 \\ 0 & b & -\zeta_2 & id\sigma \\ b & 0 & -id\sigma & -\zeta_1 \end{pmatrix}, \tag{A13}$$

where

$$d = \frac{\left(t_\perp^2 - t_3^2|\gamma(\vec{k})|^2\right)/2}{\sqrt{t_\perp^2 + t_3^2|\gamma(\vec{k})|^2 - 2t_\perp t_3|\gamma(\vec{k})|\cos(3\phi_{\vec{k}})}}, \tag{A14}$$

$$b = \frac{t_\perp t_3|\gamma(\vec{k})||\sin(3\phi_{\vec{k}})|}{\sqrt{t_\perp^2 + t_3^2|\gamma(\vec{k})|^2 - 2t_\perp t_3|\gamma(\vec{k})|\cos(3\phi_{\vec{k}})}}, \tag{A15}$$

and $\pm\zeta_1$ and $\pm\zeta_2$ are eigenvalues of $H_2^{'}$ given by

$$\zeta_{1/2} = \tfrac{1}{2}\big(\pm 2t|\gamma(\vec{k})| + \sqrt{t_\perp^2 + t_3^2|\gamma(\vec{k})|^2 - 2t_\perp t_3|\gamma(\vec{k})|\cos(3\phi_{\vec{k}})}\big). \tag{A16}$$

Splitting now H_3 in the form

$$H_3 = \begin{pmatrix} \zeta_1 & id & 0 & 0 \\ -id & \zeta_2 & 0 & 0 \\ 0 & 0 & -\zeta_2 & id \\ 0 & 0 & -id & -\zeta_1 \end{pmatrix} + \begin{pmatrix} 0 & 0 & 0 & b \\ 0 & 0 & b & 0 \\ 0 & b & 0 & 0 \\ b & 0 & 0 & 0 \end{pmatrix}, \tag{A17}$$

the first part is diagonalized by

$$U_4 = \begin{pmatrix} -i\sigma\tau\beta_+ & \beta_- & 0 & 0 \\ \beta_- & -i\sigma\tau\beta_+ & 0 & 0 \\ 0 & 0 & -i\sigma\tau\beta_+ & \beta_- \\ 0 & 0 & \beta_- & -i\sigma\tau\beta_+ \end{pmatrix} \tag{A18}$$

with $\tau = \text{sign}(d)$ and

$$\beta_\pm = \sqrt{\frac{1}{2}\left(1 \pm \frac{\zeta_1 - \zeta_2}{\sqrt{(\zeta_1 - \zeta_2)^2 + 4d^2}}\right)} \tag{A19}$$

while the second part is left unchanged by U_4, resulting in

$$H_4 = U_4 H_3 U_4^\dagger = \begin{pmatrix} \epsilon_1 & 0 & 0 & b \\ 0 & \epsilon_2 & b & 0 \\ 0 & b & -\epsilon_2 & 0 \\ b & 0 & 0 & -\epsilon_1 \end{pmatrix} \tag{A20}$$

with the diagonal elements given in terms of

$$\epsilon_{1/2} = \tfrac{1}{2}(\zeta_1 + \zeta_2 \pm \sqrt{(\zeta_1 - \zeta_2)^2 + 4d^2}). \tag{A21}$$

Finally, H_4 is brought into diagonal form via

$$U_5 = \begin{pmatrix} \gamma_+^{(1)} & 0 & 0 & \gamma_-^{(1)} \\ 0 & \gamma_+^{(2)} & \gamma_-^{(2)} & 0 \\ 0 & \gamma_-^{(2)} & -\gamma_+^{(2)} & 0 \\ \gamma_-^{(1)} & 0 & 0 & -\gamma_+^{(1)} \end{pmatrix} \tag{A22}$$

with

$$\gamma_\pm^{(1)} = \sqrt{\frac{1}{2}\left(1 \pm \frac{\epsilon_1}{E_2}\right)}, \quad \gamma_\pm^{(2)} = \sqrt{\frac{1}{2}\left(1 \pm \frac{\epsilon_2}{E_2}\right)}, \tag{A23}$$

and

$$E_{1/2} = \sqrt{\epsilon_{1,2}^2 + b^2} \tag{A24}$$

$$= \sqrt{\tfrac{1}{2}\left(t_\perp^2 + t_3^2|\gamma(\vec{k})|^2 + 2t^2|\gamma(\vec{k})|^2 \pm \sqrt{4t^2|\gamma(\vec{k})|^2\left(t_\perp^2 + t_3^2|\gamma(\vec{k})|^2 - 2t_\perp t_3|\gamma(\vec{k})|\cos(3\phi_{\vec{k}})\right) + \left(t_\perp^2 - t_3^2|\gamma(\vec{k})|^2\right)^2}\right)}. \tag{A25}$$

Thus,

$$U_5 H_4 U_5^\dagger = \mathrm{diag}(E_1, E_2, -E_2, -E_1), \tag{A26}$$

and the matrix elements of the corresponding total transformation $U = U_5U_4U_3U_2U_1$ can be expressed as

$$U_{11} = \tfrac{1}{2}(\alpha_- - i\sigma\alpha_+)(\tau\beta_+ + \beta_-)(\gamma_+^{(1)} - i\sigma\gamma_-^{(1)}), \tag{A27}$$

$$U_{12} = \tfrac{1}{2}(\alpha_+ - i\sigma\alpha_-)(\tau\beta_+ + \beta_-)(\gamma_-^{(1)} - i\sigma\gamma_+^{(1)}), \tag{A28}$$

$$U_{13} = -\frac{e^{i\phi_{\vec{k}}}}{2}(\alpha_- - i\sigma\alpha_+)(\tau\beta_+ - \beta_-)(\gamma_+^{(1)} + i\sigma\gamma_-^{(1)}), \tag{A29}$$

$$U_{14} = \frac{e^{-i\phi_{\vec{k}}}}{2}(\alpha_- + i\sigma\alpha_+)(\tau\beta_+ - \beta_-)(\gamma_+^{(1)} - i\sigma\gamma_-^{(1)}), \tag{A30}$$

and

$$U_{21} = -\tfrac{1}{2}(\alpha_+ + i\sigma\alpha_-)(\tau\beta_+ - \beta_-)(\gamma_+^{(2)} - i\sigma\gamma_-^{(2)}), \tag{A31}$$

$$U_{22} = -\tfrac{1}{2}(\alpha_+ - i\sigma\alpha_-)(\tau\beta_+ - \beta_-)(\gamma_+^{(2)} + i\sigma\gamma_-^{(2)}), \tag{A32}$$

$$U_{23} = -\frac{e^{i\phi_{\vec{k}}}}{2}(\alpha_+ + i\sigma\alpha_-)(\tau\beta_+ + \beta_-)(\gamma_+^{(2)} + i\sigma\gamma_-^{(2)}), \tag{A33}$$

$$U_{24} = -\frac{e^{-i\phi_{\vec{k}}}}{2}(\alpha_+ - i\sigma\alpha_-)(\tau\beta_+ + \beta_-)(\gamma_+^{(2)} - i\sigma\gamma_-^{(2)}), \tag{A34}$$

which are the complex conjugates of the components of the eigenvectors of the conduction-band states with positive energies $E_1(\vec{k}), E_2(\vec{k})$, while

$$U_{31} = \tfrac{1}{2}(\alpha_- - i\sigma\alpha_+)(\tau\beta_+ - \beta_-)(\gamma_+^{(2)} - i\sigma\gamma_-^{(2)}), \tag{A35}$$

$$U_{32} = \tfrac{1}{2}(\alpha_- + i\sigma\alpha_+)(\tau\beta_+ - \beta_-)(\gamma_+^{(2)} + i\sigma\gamma_-^{(2)}), \tag{A36}$$

$$U_{33} = -\frac{e^{i\phi_{\vec{k}}}}{2}(\alpha_+ + i\sigma\alpha_-)(\tau\beta_+ + \beta_-)(\gamma_-^{(2)} - i\sigma\gamma_+^{(2)}), \tag{A37}$$

$$U_{34} = -\frac{e^{-i\phi_{\vec{k}}}}{2}(\alpha_+ - i\sigma\alpha_-)(\tau\beta_+ + \beta_-)(\gamma_-^{(2)} + i\sigma\gamma_+^{(2)}), \tag{A38}$$

and

$$U_{41} = \tfrac{1}{2}(\alpha_+ + i\sigma\alpha_-)(\tau\beta_+ + \beta_-)(\gamma_+^{(1)} - i\sigma\gamma_-^{(1)}), \tag{A39}$$

$$U_{42} = -\tfrac{1}{2}(\alpha_- + i\sigma\alpha_+)(\tau\beta_+ + \beta_-)(\gamma_-^{(1)} - i\sigma\gamma_+^{(1)}), \tag{A40}$$

$$U_{43} = \frac{e^{i\phi_{\vec{k}}}}{2}(\alpha_+ + i\sigma\alpha_-)(\tau\beta_+ - \beta_-)(\gamma_+^{(1)} + i\sigma\gamma_-^{(1)}), \tag{A41}$$

$$U_{44} = \frac{e^{-i\phi_{\vec{k}}}}{2}(\alpha_- + i\sigma\alpha_+)(\tau\beta_+ - \beta_-)(\gamma_-^{(1)} + i\sigma\gamma_+^{(1)}), \tag{A42}$$

correspond to the valence-band states with negative energies $[-E_2(\vec{k})],[-E_1(\vec{k})]$. Note that all factors involving $\alpha_\pm,\gamma_\pm^{(1)},\gamma_\pm^{(2)}$ in the above expressions have modulus 1, i.e., they are phase factors.

APPENDIX B: CONTINUITY PROPERTIES

The eigenvectors corresponding to the energy branches $[\pm E_2(\vec{k})]$ are discontinuous at wave vectors determined by the condition (7). This comes about as follows: The matrix elements $U_{2,n}(\vec{k}),U_{3,n}(\vec{k}),n \in \{1,2,3,4\}$ contain the quantities $\gamma_\pm^{(2)}$ defined in Eqs. (A23), whereas the $U_{1,n}(\vec{k}),U_{4,n}(\vec{k})$ corresponding to $[\pm E_1(\vec{k})]$ involve $\gamma_\pm^{(1)}$. Fixing now $\cos(\phi_{\vec{k}}) = -1$, we have $b = 0$ such that $E_1 = \epsilon_1 \geqslant 0$ and $E_2 = |\epsilon_2|$ such that $\gamma_\pm^{(1)}$ remain continuous while $\gamma_\pm^{(2)}$ become

$$\gamma_\pm^{(2)} = \sqrt{\frac{1}{2}\left(1 \pm \frac{\epsilon_2}{|\epsilon_2|}\right)}. \tag{B1}$$

Inspection of Eq. (A21) now shows that for $\cos(\phi_{\vec{k}}) = -1$,

$$\epsilon_2(\vec{k})\begin{cases} > 0 & |\gamma(\vec{k})| < t_\perp t_3/t^2, \\ < 0 & |\gamma(\vec{k})| > t_\perp t_3/t^2, \end{cases} \tag{B2}$$

such that $\epsilon_2(\vec{k})$ changes sign for $|\gamma(\vec{k})| = t_\perp t_3/t^2$, i.e., $\gamma_\pm^{(2)}$ is discontinuous at wave vectors given by the condition (7). This discontinuity is inherited by the correlation matrix and, in turn, by the entanglement spectrum.

The technical reason for this discontinuity in the eigenvectors is of course the fact that the dispersions $[\pm E_2(\vec{k})]$ become degenerate at wave vectors fulfilling (7). In fact, the eigenvectors can also be considered as continuous functions of the wave vector by appropriately relabeling the dispersion branches. In the ground state of the undoped bilayer system, however, only the lower branch $[-E_2(\vec{k})]$ is occupied, which makes the discontinuity unavoidable.

To circumvent this discontinuity, one can open an energy gap between the upper and lower central band such that the corresponding eigenstates are necessarily continuous for all wave vectors. Among the various mechanisms producing such a gap, only a few allow for a still halfway convenient analytical treatment of the Hamiltonian. These include introducing identical mass terms in both layers, i.e., $H \mapsto H + H'$, with

$$H' = \mathrm{diag}(m,-m,-m,m), \tag{B3}$$

or applying a bias voltage Λ between the layers,

$$H' = \mathrm{diag}(-\Lambda/2,\Lambda/2,-\Lambda/2,\Lambda/2). \tag{B4}$$

In the former case, the four dispersion branches $[\pm E_1(\vec{k})]$, $[\pm E_2(\vec{k})]$ are given by

$$\begin{aligned} E_{1/2}(\vec{k}) = \big[&m^2 + \tfrac{1}{2}\big(t_\perp^2 + t_3^2|\gamma(\vec{k})|^2 + 2t^2|\gamma(\vec{k})|^2\big) \\ &\pm \tfrac{1}{2}\sqrt{4t^2|\gamma(\vec{k})|^2\big(t_\perp^2 + t_3^2|\gamma(\vec{k})|^2 - 2t_\perp t_3|\gamma(\vec{k})|\cos(3\phi_{\vec{k}})\big) + \big(t_\perp^2 - t_3^2|\gamma(\vec{k})|^2\big)^2}\big]^{1/2} \end{aligned} \tag{B5}$$

while for a bias voltage one finds [27]

$$\begin{aligned} E_{1/2}(\vec{k}) = \Bigg[&\frac{\Lambda^2}{4} + \frac{1}{2}\big(t_\perp^2 + t_3^2|\gamma(\vec{k})|^2 + 2t^2|\gamma(\vec{k})|^2\big) \\ &\pm \frac{1}{2}\sqrt{4t^2|\gamma(\vec{k})|^2\big(t_\perp^2 + t_3^2|\gamma(\vec{k})|^2 - 2t_\perp t_3|\gamma(\vec{k})|\cos(3\phi_{\vec{k}}) + \Lambda^2\big) + \big(t_\perp^2 - t_3^2|\gamma(\vec{k})|^2\big)^2}\Bigg]^{1/2}. \end{aligned} \tag{B6}$$

In both cases, the central energy bands $[\pm E_2(\vec{k})]$ are separated by a gap, and the spectrum can still be given in terms of comparably simple closed expressions since the characteristic polynomial of the 4×4 Hamiltonian matrix is a second-order polynomial in the energy squared leading to a spectrum being symmetric around zero. Also, the corresponding eigenvectors can

be obtained in closed analytical forms by procedures analogous to (but in detail somewhat more complicated than) the one given in Appendix A [43].

Note that applying a bias voltage as well as introducing a mass term in each layer discriminates the layers against each other. The latter circumstance is due to the fact that $t_\perp$ couples sublattices in different layers for which the mass term has a different sign. As a result, when tracing out, say, one layer of an undoped (i.e., half-filled) bilayer system, the remaining layer will not be half-filled, which obscures somewhat the comparison with an undoped graphene monolayer.

APPENDIX C: CORRELATION MATRICES

Upon tracing out layer 1 from the ground state of the undoped bilayer system, the correlation matrix reads in the basis $(a^\dagger_{2\vec{k}}, b^\dagger_{2\vec{k}})|0\rangle$

$$C(\vec{k}) = \begin{pmatrix} U_{31}U_{31}^* + U_{41}U_{41}^* & U_{31}U_{33}^* + U_{41}U_{43}^* \\ U_{33}U_{31}^* + U_{43}U_{41}^* & U_{33}U_{33}^* + U_{43}U_{43}^* \end{pmatrix} = \begin{pmatrix} \frac{1}{2} & u(\vec{k}) \\ u^*(\vec{k}) & \frac{1}{2} \end{pmatrix} \tag{C1}$$

with

$$u(\vec{k}) = \frac{e^{-i\phi_{\vec{k}}}}{4}(\beta_+^2 - \beta_-^2)((\gamma_+^{(1)} - i\sigma\gamma_-^{(1)})^2 - (\gamma_+^{(2)} - i\sigma\gamma_-^{(2)})^2). \tag{C2}$$

This quantity becomes singular at the corners of the Brillouin zone where $\gamma(\vec{k})$ is zero such that its phase is ill-defined, and at the positions of the satellite Dirac cones of the energy spectrum where, as discussed in Appendix B, $\gamma_\pm^{(2)}$ is discontinuous.

Tracing out the sublattices A1 and B2, one finds in the basis $(a^\dagger_{2\vec{k}}, b^\dagger_{1\vec{k}})|0\rangle$

$$C(\vec{k}) = \begin{pmatrix} U_{31}U_{31}^* + U_{41}U_{41}^* & U_{31}U_{32}^* + U_{41}U_{42}^* \\ U_{32}U_{31}^* + U_{42}U_{41}^* & U_{32}U_{32}^* + U_{42}U_{42}^* \end{pmatrix} = \begin{pmatrix} \frac{1}{2} & v(\vec{k}) \\ v^*(\vec{k}) & \frac{1}{2} \end{pmatrix} \tag{C3}$$

with

$$v(\vec{k}) = \frac{(\alpha_- - i\sigma\alpha_+)^2}{4}((\tau\beta_+ - \beta_-)^2(\gamma_+^{(2)} - i\sigma\gamma_-^{(2)})^2 + (\tau\beta_+ + \beta_-)^2(\gamma_+^{(1)} - i\sigma\gamma_-^{(1)})^2). \tag{C4}$$

Note that the expressions (C2) and (C4) obey the interesting sum rule

$$|u(\vec{k})|^2 + |v(\vec{k})|^2 = \tfrac{1}{4}, \tag{C5}$$

which is fulfilled whenever the coefficients involved satisfy

$$\alpha_+^2 + \alpha_-^2 = \beta_+^2 + \beta_-^2 = (\gamma_+^{(1/2)})^2 + (\gamma_-^{(1/2)})^2 = 1, \tag{C6}$$

which is the case here by construction.

Finally, the correlation matrix obtained by tracing out the sublattices A1 and A2 is proportional to the unit matrix,

$$C(\vec{k}) = \begin{pmatrix} U_{32}U_{32}^* + U_{42}U_{42}^* & U_{32}U_{33}^* + U_{42}U_{43}^* \\ U_{33}U_{32}^* + U_{43}U_{42}^* & U_{33}U_{33}^* + U_{43}U_{43}^* \end{pmatrix} = \begin{pmatrix} \frac{1}{2} & 0 \\ 0 & \frac{1}{2} \end{pmatrix}, \tag{C7}$$

implying that the remaining subsystem is maximally entangled with the subsystem traced out.

[1] L. Bombelli, R. K. Koul, J. Lee, and R. D. Sorkin, Phys. Rev. D **34**, 373 (1986).
[2] J. Eisert, M. Cramer, and M. B. Plenio, Rev. Mod. Phys. **82**, 277 (2010).
[3] H. Li and F. D. M. Haldane, Phys. Rev. Lett. **101**, 010504 (2008).
[4] A. M. Läuchli, E. J. Bergholtz, J. Suorsa, and M. Haque, Phys. Rev. Lett. **104**, 156404 (2010).
[5] R. Thomale, D. P. Arovas, and B. A. Bernevig, Phys. Rev. Lett **105**, 116805 (2010).
[6] A. Chandran, M. Hermanns, N. Regnault, and B. A. Bernevig, Phys. Rev. B **84**, 205136 (2011).
[7] A. Kitaev, Ann. Phys. (NY) **321**, 2 (2006).
[8] A. M. Turner, Y. Zhang, and A. Vishwanath, Phys. Rev. B **82**, 241102 (2010).
[9] A. Chandran, V. Khemani, and S. L. Sondhi, Phys. Rev. Lett. **113**, 060501 (2014).
[10] N. Regnault, arXiv:1510.07670.
[11] N. Laflorencie, arXiv:1512.03388.
[12] D. Poilblanc, Phys. Rev. Lett. **105**, 077202 (2010).
[13] J. I. Cirac, D. Poilblanc, N. Schuch, and F. Verstraete, Phys. Rev. B **83**, 245134 (2011).
[14] I. Peschel and M.-C. Chung, Europhys. Lett. **96**, 50006 (2011).
[15] A. M. Läuchli and J. Schliemann, Phys. Rev. B **85**, 054403 (2012).

[16] J. Schliemann and A. M. Läuchli, J. Stat. Mech. (2012) P11021.
[17] S. Tanaka, R. Tamura, and H. Katsura, Phys. Rev. A **86**, 032326 (2012).
[18] R. Lundgren, V. Chua, and G. A. Fiete, Phys. Rev. B **86**, 224422 (2012).
[19] R. Lundgren, Y. Fuji, S. Furukawa, and M. Oshikawa, Phys. Rev. B **88**, 245137 (2013).
[20] X. Chen and E. Fradkin, J. Stat. Mech. (2013) P08013.
[21] R. Lundgren, arXiv:1412.8612.
[22] J. Schliemann, Phys. Rev. B **83**, 115322 (2011).
[23] J. Schliemann, New J. Phys. **15**, 053017 (2013); **15**, 079501(E) (2013).
[24] J. Schliemann, J. Stat. Mech. (2014) P09011.
[25] E. McCann and M. Koshino, Rep. Prog. Phys. **76**, 056503 (2013).
[26] A. V. Rozhkov, A. O. Sboychakov, A. L. Rakhmanov, and F. Nori, arXiv:1511.06706.
[27] E. McCann and V. I. Falko, Phys. Rev. Lett. **96**, 086805 (2006).
[28] J. Nilsson, A. H. Castro Neto, N. M. R. Peres, and F. Guinea, Phys. Rev. B **73**, 214418 (2006).
[29] M. Koshino and T. Ando, Phys. Rev. B **73**, 245403 (2006).
[30] K. Kechedzhi, V. I. Falko, E. McCann, and B. L. Altshuler, Phys. Rev. Lett. **98**, 176806 (2007).
[31] J. L. Manes, F. Guinea, and M. A. H. Vozmediano, Phys. Rev. B **75**, 155424 (2007).
[32] J. Cserti, A. Csordás, and G. Dávid, Phys. Rev. Lett. **99**, 066802 (2007).
[33] G. P. Mikitik and Y. V. Sharlai, Phys. Rev. B **77**, 113407 (2008).
[34] E. Mariani, A. J. Pearce, and F. von Oppen, Phys. Rev. B **86**, 165448 (2012).
[35] D. A. Cosma and V. I. Falko, Phys. Rev. B **92**, 165412 (2015).
[36] A. B. Kuzmenko, I. Crassee, D. van der Marel, P. Blake, and K. S. Novoselov, Phys. Rev. B **80**, 165406 (2009).
[37] I. Peschel, J. Phys. A **36**, L205 (2003).
[38] S.-A. Cheong and C. L. Henley, Phys. Rev. B **69**, 075111 (2004).
[39] N. Nemec and G. Cuniberti, Phys. Rev. B **75**, 201404 (2007).
[40] Y.-X. Wang and F. Li, arXiv:1511.01972.
[41] T. Fukui and Y. Hatsugai, J. Phys. Soc. Jpn. **83**, 113705 (2014).
[42] H. Araki, T. Kariyado, T. Fukui, and Y. Hatsugai, arXiv:1602.02910.
[43] S. Predin, P. Wenk, and J. Schliemann (unpublished).

LETTER

Entanglement spectrum of the degenerative ground state of Heisenberg ladders in a time-dependent magnetic field

To cite this article: Sonja Predin 2017 *EPL* **119** 57003

A Letters Journal Exploring the Frontiers of Physics

September 2017

EPL, **119** (2017) 57003 www.epljournal.org
doi: 10.1209/0295-5075/119/57003

Entanglement spectrum of the degenerative ground state of Heisenberg ladders in a time-dependent magnetic field

Sonja Predin

Institute for Theoretical Physics, University of Regensburg - D-93040 Regensburg, Germany

received 26 May 2017; accepted in final form 17 October 2017
published online 14 November 2017

PACS 75.10.Jm – Quantized spin models, including quantum spin frustration
PACS 03.67.-a – Quantum information
PACS 05.30.-d – Quantum statistical mechanics

Abstract – We investigate the relationship between the entanglement and subsystem Hamiltonians in the perturbative regime of strong coupling between subsystems. One of the two conditions that guarantees the proportionality between these Hamiltonians obtained by using the nondegenerate perturbation theory within the first order is that the unperturbed ground state has a trivial entanglement Hamiltonian. Furthermore, we study the entanglement Hamiltonian of the Heisenberg ladders in a time-dependent magnetic field using the degenerate perturbation theory, where couplings between legs are considered as a perturbation. In this case, when the ground state is twofold degenerate, and the entanglement Hamiltonian is proportional to the Hamiltonian of a chain within first-order perturbation theory, even then also the unperturbed ground state has a nontrivial entanglement spectrum.

Introduction. – Quantum entanglement, primarily a source of quantum information, has developed into one of the most studied subfields of many-body physics. In the last decade, quantum entanglement has mainly been used to study the phase structure in condensed-matter physics [1]. The entanglement spectrum of a bipartite system of subsystems A and B is defined in terms of the Schmidt decomposition of its ground state $|\psi\rangle$ as

$$|\psi\rangle = \sum_n e^{-\frac{\xi_n}{2}} |\psi_n^A\rangle |\psi_n^B\rangle \tag{1}$$

where the states $|\psi_n^A\rangle$ ($|\psi_n^B\rangle$) are orthonormal states of the subsystem A (B), respectively, and the non-negative quantities ξ_n represent the levels of the entanglement spectrum. Further, Haldane and Li in ref. [2] have reported a remarkable relationship between the excitation spectrum and the edges separating the subsystems, considering the entanglement spectrum of the fractional quantum Hall system obtained using a spatial cut. This connection between the edge spectrum and entanglement spectrum is observed in many condensed-matter systems including ladders systems [3–5]. In many previous studies, the proportionality between the energetic Hamiltonian of the subsystem A $\mathcal{H}_A$ and the entanglement Hamiltonian $\mathcal{H}_{ent}$ in the strong coupling regime [6–12] has been observed. However, this does not hold in general, even in the strong coupling limit which is illustrated by counterexamples in ref. [13] where four spin terms of the Kugel-Khomskii model are considered in ref. [11], in which anisotropic spin ladders of arbitrary spin length were considered, where even the unperturbed nondegenerate ground state has a nontrivial entanglement spectrum.

Here we study the entanglement spectrum of the Heisenberg spin ladders in a time-dependent magnetic field via the degenerate perturbation theory, where couplings between legs are considered as a perturbation. The entanglement Hamiltonian is, within the first-order perturbation theory, proportional to the energy Hamiltonian of a chain in the magnetic field when the ground state is degenerate. This holds, although the entanglement spectrum of the unperturbed ground state has a nontrivial entanglement spectrum.

Motivation. – We consider a bipartite system consisting of two subsystems described by the Hamiltonians $\mathcal{H}_A$ of subsystem A and $\mathcal{H}_B$ of subsystem B, which are coupled by the Hamiltonian $\mathcal{H}_0$. We assume that the Hamiltonians $\mathcal{H}_A$ and $\mathcal{H}_B$ are small compared to $\mathcal{H}_0$, and it will be treated as a small perturbation. This problem can be illustrated by two leg spin ladders, where the interaction between rungs is considered as a small perturbation (see fig. 1).

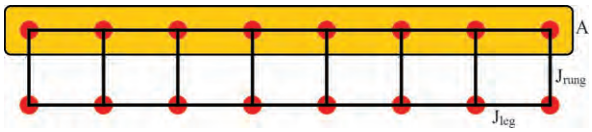

Fig. 1: (Colour online) Illustration of the two leg spin ladder considered in this paper. The entanglement spectrum is performed by tracing out subsystem A.

The projector onto the subsystem orthogonal to the nondegenerative ground state $|\psi_0\rangle$ is defined as

$$Q_l = 1 - |\psi_0\rangle\langle\psi_0| = \sum_{l\neq 0} |\psi_l\rangle\langle\psi_l|. \tag{2}$$

Then, the first correlation $|\psi_l^{(1)}\rangle$ of the nondegenerative ground state $|\psi_0\rangle$ reads

$$|\psi_l^{(1)}\rangle = |\psi_0\rangle + \frac{1}{E_0 - \mathcal{H}_0} Q_l \left((\mathcal{H}_A + \mathcal{H}_B) - \langle\psi_0| (\mathcal{H}_A + \mathcal{H}_B) |\psi_0\rangle \right) |\psi_l\rangle, \tag{3}$$

where $E_0 = \langle\psi_0|\mathcal{H}_0|\psi_0\rangle$. We also use that $\frac{1}{E_0-\mathcal{H}_0} Q_l = \sum_{l\neq 0} \frac{|\psi_l\rangle\langle\psi_l|}{E_0-E_l}$, where $E_l = \langle\psi_l|\mathcal{H}_0|\psi_l\rangle$ and the fact that $\frac{1}{E_0-\mathcal{H}_0} Q_l|\psi_0\rangle = 0$ by definition. In the following, we will assume that $\frac{1}{E_0-E_l}$ is equal for every l. This allows us to rewrite eq. (3) as

$$|\psi_l^{(1)}\rangle = |\psi_0\rangle + \frac{1}{E_0 - E_l} (\mathcal{H}_A + \mathcal{H}_B)|\psi_0\rangle. \tag{4}$$

The density matrix within the first order of the perturbation theory has the following form:

$$\rho = |\psi_l^{(1)}\rangle\langle\psi_l^{(1)}|, \quad \rho = |\psi_0\rangle\langle\psi_0| + \frac{1}{E_0 - E_l} ((\mathcal{H}_A + \mathcal{H}_B)|\psi_0\rangle\langle\psi_0| + |\psi_0\rangle\langle\psi_0|(\mathcal{H}_A + \mathcal{H}_B)). \tag{5}$$

Owing to the fact that, here, the Hamiltonian $\mathcal{H}_A$ acts only on the subsystem A, the reduced density matrix can be calculated by tracing out the subsystem B:

$$\rho_{red} = \rho_1 + \frac{1}{E_0 - E_l} \left(\mathcal{H}_A \rho_1 + \rho_1 \mathcal{H}_A \right), \tag{6}$$

where $\rho_1 = tr_2|\psi_0\rangle\langle\psi_0|$ is the reduced density matrix within the zeroth order of the perturbation theory. When the two subsystems are maximally entangled, ρ_1 is proportional to the unit matrix. In this case, we obtain

$$\rho_{red} = \rho_1 \left(1 - \frac{2}{E_0 - E_l} \mathcal{H}_A \right). \tag{7}$$

The reduced density matrix can be reformulated as

$$\rho_{red} = \frac{1}{Z} \exp(-\mathcal{H}_{ent}^{(1)}), \tag{8}$$

where the entanglement Hamiltonian $\mathcal{H}_{ent}$ is the entanglement Hamiltonian, and the partition function Z is $Z = \mathrm{tr}(\exp(-\mathcal{H}_{ent}^{(1)}))$. The entanglement Hamiltonian

$$\mathcal{H}_{ent} = \frac{2}{E_0 - E_l} \mathcal{H}_A \tag{9}$$

is proportional to the Hamiltonian of subsystem A, with the proportionality factor $\beta = \frac{2}{E_0-E_l}$ interpreted as an inverse temperature.

To conclude, we assume that

1) $\frac{1}{E_0-E_l}$ is equal for every l, and

2) ρ_1 is proportional to the unit matrix.

These two assumptions directly lead to the proportionality between the entanglement and subsystem Hamiltonians in the strong coupling limit within the first order of the perturbation theory, when the ground state is nondegenerate.

In ref. [6], Poilblanc stressed a remarkable similarity between the chain-chain entanglement spectrum in the two-leg spin-1/2 ladders and the energy spectrum of a single spin-1/2 Heisenberg chain. Läuchli and Schliemann [10] analytically showed that the entanglement Hamiltonian of the two coupled anisotropic XXZ chains is proportional to the energy Hamiltonian of the single chain with renormalized anisotropy in the first order of the perturbation theory in the strong coupling limit. There, the first assumption (1) is not valid. In the case of the isotropic Heisenberg ladders, both assumptions (1) and (2) are valid, and for that reason, they found that the entanglement spectrum is directly proportional to the energy of the single chain. The authors in ref. [11] generalized this observation for the isotropic Heisenberg ladders to the case of the arbitrary spin length S. They found that for arbitrary spin, the entanglement spectrum of the isotropic Heisenberg ladders is proportional to the energy of the single chain within the first-order perturbation theory. This is also a consequence of the fact that both assumptions (1) and (2) hold. However, they found that there is no proportionality between the entanglement Hamiltonian of anisotropic spin ladders of arbitrary spin length. Since here, the reduced density matrix in zeroth order of the perturbation theory is not proportional to the unit matrix, there is no mention of proportionality.

Model. – We investigate the Hamiltonian of the Heisenberg spin-1/2 ladder in a time-dependent circularly polarized magnetic field B described by the Hamiltonian

$$\tilde{H} = J_{rung} \sum_i \vec{S}_{2i}\vec{S}_{2i+1} + B \sum_i (S_i^x \cos\omega t - S_i^y \sin\omega t) + J_{leg} \sum_i \vec{S}_{2i}\vec{S}_{2i+2} + J_{leg} \sum_i \vec{S}_{2i+1}\vec{S}_{2i+3}. \tag{10}$$

where ω is the angular velocity of the rotation of the magnetic field. The sites on the first (second) leg are denoted by even (odd) labels, such that the i-th rung consists of

sites $2i$ and $2i+1$. All spin-1/2 operators are taken to be dimensionless, such that the couplings along the rungs J_{rung} and the legs J_{leg} have the dimensions of energy. We will consider antiferromagnetic coupling when $J_{rung} > 0$.

This time-dependent Hamiltonian can be factorized to a time-independent Hamiltonian by unitary transformations that represent a rotation around the z-axis $R(t) = \exp(-iS_z\omega t/\hbar)$ [14]. Since

$$\begin{aligned} R(t)S_xR^{-1}(t) &= S_x\cos\omega t + S_y\sin\omega t, \\ R(t)S_yR^{-1}(t) &= -S_x\sin\omega t + S_y\cos\omega t, \\ R(t)S_zR^{-1}(t) &= S_z, \end{aligned} \tag{11}$$

the Hamiltonian equation (10) can be transformed into a time-independent Hamiltonian:

$$\widehat{H} = R(t)\tilde{H}(t)R(t)^{-1}, \tag{12}$$

$$\widehat{H} = J_{rung}\sum_i \vec{S}_{2i}\vec{S}_{2i+1} + B\sum_i S_i^x + J_{leg}\sum_i \vec{S}_{2i}\vec{S}_{2i+2} + J_{leg}\sum_i \vec{S}_{2i+1}\vec{S}_{2i+3}. \tag{13}$$

Defining the propagator that confirms

$$\frac{\partial}{\partial t}K(t,t_0) = -\frac{i}{\hbar}\tilde{H}(t)K(t,t_0), \tag{14}$$

$$\frac{\partial}{\partial t}K(t,t_0) = -\frac{i}{\hbar}R_{-1}(t)\widehat{H}(t)R(t)K(t,t_0), \tag{15}$$

we find

$$\frac{\partial}{\partial t}\left(R(t)K(t,t_0)R^{-1}(t_0)\right) = -\frac{i}{\hbar}H\left(R(t)K(t,t_0)R^{-1}(t_0)\right).$$

Then, the Hamiltonian becomes

$$H = J_{rung}\sum_i \vec{S}_{2i}\vec{S}_{2i+1} + B\sum_i S_i^x + \omega\sum_i S_i^z + J_{leg}\sum_i \vec{S}_{2i}\vec{S}_{2i+2} + J_{leg}\sum_i \vec{S}_{2i+1}\vec{S}_{2i+3}, \tag{16}$$

where the propagator is

$$K(t,t_0) = \exp\left(\frac{i}{\hbar}S_z\omega t\right)\exp\left(-\frac{i}{\hbar}H(t-t_0)\right)\exp\left(-\frac{i}{\hbar}S_z\omega t_0\right). \tag{17}$$

In order to use the perturbation theory, we will rewrite the Hamiltonian equation (16) as $H = H_0 + H_1$, where

$$H_0 = J_{rung}\sum_i \vec{S}_{2i}\vec{S}_{2i+1} + B\sum_i S_i^x + \omega\sum_i S_i^z \tag{18}$$

and

$$H_1 = J_{leg}\sum_i \vec{S}_{2i}\vec{S}_{2i+2} + J_{leg}\sum_i \vec{S}_{2i+1}\vec{S}_{2i+3} \tag{19}$$

and consider H_1 as a small perturbation. The Hamiltonian equation (18) is independent of the direction of the magnetic field and it can be considered as the isotropic Heisenberg chain in the magnetic field $\sqrt{B^2+\omega^2}$

$$H_0 = J_{rung}\sum_i \vec{S}_{2i}\vec{S}_{2i+1} + \sqrt{B^2+\omega^2}\sum_i S_i^z \tag{20}$$

and

$$H_1 = J_{leg}\sum_i \vec{S}_{2i}\vec{S}_{2i+2} + J_{leg}\sum_i \vec{S}_{2i+1}\vec{S}_{2i+3}. \tag{21}$$

The energies of a rung of the singlet and triplet states are

$$E_{s_i} = -\frac{3}{4}J_{rung}, \tag{22}$$

$$E_{t_i^+} = \frac{1}{4}J_{rung} + \sqrt{B^2+\omega^2}, \tag{23}$$

$$E_{t_i^0} = \frac{1}{4}J_{rung}, \tag{24}$$

$$E_{t_i^-} = \frac{1}{4}J_{rung} - \sqrt{B^2+\omega^2}. \tag{25}$$

The ground state changes from the spin singlet $|s_i\rangle$ to the triplet state $|t_i^-\rangle$ by increasing the value of $\sqrt{B^2+\omega^2}$. When $J_{rung} = \sqrt{\omega^2+B^2}$, the ground state is twofold degenerate, since the singlet states $|s_i\rangle$ and triplet states $|t_i^-\rangle$ have the same eigenenergy. The situation when the ground state is twofold degenerate is quite interesting and it will be considered in the following section.

Entanglement spectrum. – When $J_{rung} = \sqrt{\omega^2+B^2}$, it is necessary to use the degenerate perturbation theory, while any combination of eigenstates $|s_i\rangle$ and $|t_i^-\rangle$ can be taken as the ground state $|\psi_0\rangle$. In order to achieve an analytically manageable situation, we will assume a finite number of rungs $i = 4$. Let us suppose that the unperturbed ground state $|psi_0\rangle$ of the Hamiltonian $\mathcal{H}_0$ is an unknown combination of eigenvectors $|s_i\rangle$ and $|t_i^-\rangle$. In the following, we will note eigenvectors of the ground state $|\psi_0\rangle$ as $\{|\overline{n}\lambda\rangle|, \lambda = 1,\ldots,4\}$, where

$$\begin{aligned} |\overline{n}1\rangle &= |s_1\rangle|s_2\rangle|s_3\rangle|s_4\rangle, & |\overline{n}2\rangle &= |s_1\rangle|s_2\rangle|s_3\rangle|t_4^-\rangle, \\ |\overline{n}3\rangle &= |s_1\rangle|s_2\rangle|t_3^-\rangle|s_4\rangle, & |\overline{n}4\rangle &= |s_1\rangle|t_2^-\rangle|s_3\rangle|s_4\rangle, \\ |\overline{n}5\rangle &= |t_1^-\rangle|s_2\rangle|s_3\rangle|s_4\rangle, & |\overline{n}6\rangle &= |t_1^-\rangle|t_2^{-1}\rangle|s_3\rangle|s_4\rangle, \\ |\overline{n}7\rangle &= |t_1^{-1}\rangle|s_2\rangle|t_3^{-1}\rangle|s_4\rangle, & |\overline{n}8\rangle &= |t_1^{-1}\rangle|s_2\rangle|s_3\rangle|t_4^{-1}\rangle, \\ |\overline{n}9\rangle &= |s_1\rangle|t_2^{-1}\rangle|t_3^{-1}\rangle|s_4\rangle, & |\overline{n}10\rangle &= |s_1\rangle|t_2^{-1}\rangle|s_3\rangle|t_4^{-1}\rangle, \\ |\overline{n}11\rangle &= |s_1\rangle|s_2\rangle|t_3^{-1}\rangle|t_4^{-1}\rangle, & |\overline{n}12\rangle &= |t_1^{-1}\rangle|t_2^{-1}\rangle|t_3^{-1}\rangle|s_4\rangle, \\ |\overline{n}13\rangle &= |t_1^{-1}\rangle|t_2^{-1}\rangle|s_3\rangle|t_4^{-1}\rangle, & |\overline{n}14\rangle &= |t_1^{-1}\rangle|s_2\rangle|t_3^{-1}\rangle|t_4^{-1}\rangle, \\ |\overline{n}15\rangle &= |s_1\rangle|t_2^{-1}\rangle|t_3^{-1}\rangle|t_4^{-1}\rangle, & |\overline{n}16\rangle &= |t_1^{-1}\rangle|t_2^{-1}\rangle|t_3^{-1}\rangle|t_4^{-1}\rangle. \end{aligned} \tag{26}$$

The projector $P_n^{(0)}$ of $\mathcal{H}_0$ projects on the subspace, and is defined by the eigenvalue $E_{\overline{n}}^{(0)} = -\frac{3}{4}J_{rung}$ of the Hamiltonian $\mathcal{H}_0$. Furthermore, the projector $P_n^{(0)}$ satisfies

$$P_n^{(0)}\mathcal{H}^{'}P_n^{(0)}|\psi_0\rangle = E^{(1)}|\psi_0\rangle, \tag{27}$$

where $E^{(1)}$ is the eigenvalue of $P_n^{(0)}\mathcal{H}^{'}P_n^{(0)}$ for eigenvector $|\psi_0\rangle$. In order to find the eigenvalue $E^{(1)}$ of the perturbation $\mathcal{H}^{'}$ and the ground state $|\psi_0\rangle$, it is sufficient to

diagonalize a 16×16 matrix

$$\begin{bmatrix} \langle\overline{n}1|\mathcal{H}'|\overline{n}1\rangle & \cdots & \langle\overline{n}1|\mathcal{H}'|\overline{n}16\rangle \\ \cdots & \cdots & \cdots \\ \langle\overline{n}16|\mathcal{H}'|\overline{n}1\rangle & \cdots & \langle\overline{n}16|\mathcal{H}'|\overline{n}16\rangle \end{bmatrix}. \tag{28}$$

By elementary calculations, one finds the uniquely determined ground state $|\psi_0\rangle$ and the first correction of the energy $E^{(1)}$.

The unperturbed density matrix is constructed from this ground state and is given, after simplification, by

$$\rho^{(0)} = \textstyle\sum_{\lambda}^{16} |\overline{n}\lambda\rangle\langle\overline{n}\lambda|. \tag{29}$$

By again tracing out one leg, we obtain the reduced unperturbed density matrix

$$\rho^{(0)}_{red} = \frac{1}{2^4} \bigotimes_{i=1}^{4} \left(1 - S^z_{2i+1}\right). \tag{30}$$

It is obvious that this reduced density matrix is not proportional to the unitary matrix and possesses a nontrivial entanglement spectrum. The first corrections to the ground state in the degenerate perturbation theory are defined by

$$|1\rangle = \sum_{n\neq\overline{n}} |n\lambda\rangle \frac{\langle n\lambda|H_1|\psi_0\rangle}{E^{(0)}_{\overline{n}} - E^{(0)}_{n}}, \tag{31}$$

$$|1'\rangle = \sum_{n\neq\overline{n},n'} \sum_{\lambda'} |\overline{n}\lambda\rangle \frac{\langle\overline{n}\lambda|H_1|n'\lambda\rangle}{E^{(1)} - E^{(1)}_{\lambda}} \frac{\langle n'\lambda|H_1|\psi_0\rangle}{E^{(0)}_{\overline{n}} - E^{(0)}_{n'}}. \tag{32}$$

One finds the reduced density matrix to the first order

$$\rho^{(1)}_{red} = \frac{1}{2^4} \bigotimes_{i=1}^{4} \left(1 - S^z_{2i+1}\right) - \frac{J_{leg}}{8J_{rung}} \Big((1 - S^z_1)(1 - S^z_3)\vec{S}_5\vec{S}_7 + (1 - S^z_1)\vec{S}_3\vec{S}_5(1 - S^z_7) + \vec{S}_1\vec{S}_3(1 - S^z_5)(1 - S^z_7) \Big). \tag{33}$$

The reduced density matrix can be rewritten as

$$\rho_{red} = \frac{1}{Z} \exp(-\mathcal{H}^{(1)}_{ent}), \tag{34}$$

where the partition function Z is $Z = \mathrm{tr}\exp(-\mathcal{H}^{(1)}_{ent})$ and the entanglement Hamiltonian within the first order of the perturbation theory has the following form:

$$\mathcal{H}^{(1)}_{ent} = \frac{1}{J_{rung}} \sum_{i=0}^{3} \Big(2J_{leg}\vec{S}_{2i+1}\vec{S}_{2i+3} + J_{rung}S_{2i+1} \Big). \tag{35}$$

The entanglement Hamiltonian is simply proportional to the Hamiltonian of a chain in the magnetic field with the proportional factor $\beta = \frac{1}{J_{rung}}$ defined as an inverse temperature.

The system of the Heisenberg chain in the longitudinal magnetic field is exactly solvable by the Bethe ansatz. The ground state becomes the spin-liquid one and gapless up to when $\frac{\sqrt{B^2+\omega^2}}{J_{leg}} = 2$, where the phase transition of the Pokrovsky-Talapov type takes place and the ground state becomes a completely ordered gapped ferromagnetic state. One of the most important features of the energy spectra of spin chains is the absence of an excitation gap over the ground state for the integer spin length. We restrict ourselves to the case when the two chains are strongly coupled; therefore, $\frac{\sqrt{B^2+\omega^2}}{J_{leg}} \gg 1$ and the Hamiltonian of a subsystem stays gapless in this region. The entanglement spectrum eq. (35) remains gapless owing to the proportionality to the energy spectrum.

Summary. – Here we investigated the entanglement spectrum of Heisenberg ladders in a time-dependent magnetic field using the degenerate perturbation theory, where couplings between legs are taken as a small perturbation. When the ground state is not degenerate, the existence of the trivial entanglement Hamiltonian in the zeroth order of the perturbation theory is identified as an important condition that guarantees the proportionality between the entanglement and subsystem Hamiltonians. We find that although the entanglement spectrum of the unperturbed ground state has a nontrivial entanglement spectrum, the entanglement Hamiltonian of Heisenberg ladders in a time-dependent magnetic field, within the first-order perturbation theory, is proportional to the energy Hamiltonian of a chain in the magnetic field when the ground state is degenerate.

* * *

The author kindly acknowledges John Schliemann.

REFERENCES

[1] Amico Luigi, Fazio Rosario, Osterloh Andreas and Vedral Vlatko, *Rev. Mod. Phys.*, **80** (2008) 517.

[2] Li H. and Haldane F. D. M., *Phys. Rev. Lett.*, **101** (2008) 010504.

[3] Qi Xiao-Liang, Katsura Hosho and Ludwig Andreas W. W., *Phys. Rev. Lett.*, **108** (2012) 196402.

[4] Chen Xiao and Fradkin Eduardo, *J. Stat. Mech.* (2013) P08013.

[5] Lundgren Rex, Fuji Yohei, Furukawa Shunsuke and Oshikawa Masaki, *Phys. Rev. B*, **88** (2013) 245137.

[6] Poilblanc D., *Phys. Rev. Lett.*, **105** (2010) 077202.

[7] Cirac J. I., Poilblanc D., Schuch N. and Verstraete F., *Phys. Rev. B*, **83** (2011) 245134.

[8] Schliemann J., *Phys. Rev. B*, **83** (2011) 115322.

[9] Peschel Ingo and Chung Ming-Chiang, *EPL*, **96** (2011) 50006.

[10] Läuchli A. M. and Schliemann J., *Phys. Rev. B*, **85** (2012) 054403.

[11] Schliemann J. and Luchli A. M., *J. Stat. Mech.* (2012) P11021.

[12] Schliemann J., *New J. Phys*, **15** (2013) 053017.

[13] Lundgren R., Chua V. and Fiete G. A., *Phys. Rev. B*, **86** (2012) 224422.

[14] Dittrich Thomas, Hänggi Peter, Ingold Gert-Ludwig, Kramer Bernhard, Schön Gerd and Zwerger Wilhelm, *Quantum Transport and Dissipation* (Wiley-VCH Weinheim) 1998.

Eur. Phys. J. B (2017) 90: 239
DOI: 10.1140/epjb/e2017-80304-4

THE EUROPEAN PHYSICAL JOURNAL B

Regular Article

Entanglement spectra of superconductivity ground states on the honeycomb lattice

Sonja Predin[a] and John Schliemann

Institute for Theoretical Physics, University of Regensburg, D-93040 Regensburg, Germany

Received 29 May 2017 / Received in final form 20 September 2017
Published online 11 December 2017 –

Abstract. We analytically evaluate the entanglement spectra of the superconductivity states in graphene, primarily focusing on the s-wave and chiral $d_{x^2-y^2}+id_{xy}$ superconductivity states. We demonstrate that the topology of the entanglement Hamiltonian can differ from that of the subsystem Hamiltonian. In particular, the topological properties of the entanglement Hamiltonian of the chiral $d_{x^2-y^2}+id_{xy}$ superconductivity state obtained by tracing out one spin direction clearly differ from those of the time-reversal invariant Hamiltonian of noninteracting fermions on the honeycomb lattice.

1 Introduction

In graphene, the sixfold symmetry of the honeycomb lattice favors the degenerate $d_{x^2-y^2}$- and d_{xy}-wave superconductivity states. Recent theoretical studies have shown that a s-wave superconductivity state [1] and a chiral $d_{x^2-y^2}\pm id_{xy}$ superconducting state emerges from electron–electron interactions in graphene doped to the vicinity of the van-Hove singularity point [2–7], and in lower doped bilayer graphene [8–10] (for a recent review, see Ref. [11]). Below the superconducting transition temperature T_C, this degeneracy yields the time-reversal symmetry-breaking $d_{x^2-y^2}\pm id_{xy}$ state [11,12]. In the past two years, considerable experimental progress has been made regarding the observation of superconductivity in graphene. Evidence of superconductivity has been experimentally observed on Ca-intercalated bilayer graphene and graphene laminates at 4 [13] and 6.4 K [14], respectively. Furthermore, additional experimental progress has been made regarding evidence of superconductivity in Li-decorated monolayer graphene with a transition temperature of approximately 5.9 K [15].

The discovery of topological phases, which possess topological order and cannot be classified by a broken symmetry, has revealed the urgent need for a tool for characterization of these phases. It has been proven that the entanglement entropy obtained from the reduced density matrix can be an indicator of the topology in a system [16–18]. Further, Haldane and Li [19] have suggested that the entanglement spectrum of a system (the full set of eigenvalues of the reduced density matrix) contains more information about that system than the entanglement entropy, a single number. They have reported a remarkable relationship between the excitation spectrum and the edges separating the subsystems, considering the entanglement spectrum of the fractional quantum Hall system obtained using a spatial cut. It has been suggested that the entanglement spectrum constitutes a *tower of states*, which can be regarded as a fingerprint of the topological order [20–36] (for recent reviews, see Refs. [37,38]). The relationship between the entanglement, which can be calculated from the ground state, and the edge states, which are excited states of the Hamiltonian in a sample with boundaries, has been explored in this context. However, this relationship is not valid in general, as shown in references [39–41], in which the various entanglement spectra fail to describe the topological phase transitions.

The relationship between the entanglement spectrum obtained by tracing out one subsystem and the energy spectrum of the remaining subsystem is attracting considerable research attention. Particular focus has been placed on various spin ladder systems [42–50] and on bilayer systems [51–53], where a proportionality between the entanglement and subsystem Hamiltonians is realized by the strong coupling limit. However, this relationship is not valid in general, as indicated in reference [54], in which spin ladders of clearly nonidentical legs are studied, and in the case of graphene bilayers in the presence of trigonal warping [55].

In a two-dimensional topological superconductor with broken time-reversal symmetry, the topology can be characterized by a Chern number, which is an integral of the Berry curvature over the Brillouin zone. The entanglement Chern number C, i.e., the Chern number of the entanglement Hamiltonian obtained from the eigenvectors of that Hamiltonian, has been suggested to be a topological invariant of the entanglement Hamiltonian [55–57]. Note that some investigation of the relationship between the energetic and entanglement Hamiltonian topologies has already been performed [55].

[a] e-mail: sonja.predin@physik.uni-regensburg.de

In this paper, we present a fully analytical study of the entanglement spectrum of the fermionic ground state on a graphene honeycomb lattice, in the presence of superconductivity instability and as obtained by tracing out a single spin direction. We investigate the relationship between the entanglement and energy spectra of the remaining noninteracting part, placing a special focus on the correlation between their topologies. We show that the entanglement Hamiltonian obtained by tracing out one of the subsystems and the Hamiltonian of the remaining subsystem can have completely different topologies. This difference is due to the fact that the entanglement Hamiltonian is a ground-state property. That is, the $d_{x^2-y^2} + id_{xy}$ superconductivity state breaks the time-reversal symmetry of the superconductivity Hamiltonian; this behavior is reflected in the ground state of the composite superconductivity Hamiltonian. Further, the entanglement Hamiltonian is constructed from that ground state. We also discuss the case of sublattices B is traced out.

This paper is organized as follows: In Section 2, we introduce the model Hamiltonian and discuss the different superconductivity paired states that can arise on the honeycomb lattice. Classification of the topological phases of the superconductivity states on the honeycomb lattice based on their different symmetries is also performed in this section. The entanglement spectrum obtained from the Bardeen-Cooper-Schrieffer ground state by tracing out a single spin direction is analyzed in Section 3. Our primary interest in this section is to explore the relationship between the geometrical and topological properties of the entanglement Hamiltonian and the remaining noninteracting Hamiltonian. We close with a summary and an overview of the future research outlook, which is presented in Section 4. Some technical details on the analytical derivation of the full eigenstates of the noninteracting fermionic system on the honeycomb lattice in the presence of superconductivity instabilities are presented, along with correlation matrix calculations, in Appendices A and B.

2 Model Hamiltonian

The tight-binding Hamiltonian for free fermions on a graphene honeycomb lattice with a single $2p_z$ orbital per carbon (C) atom is

$$H_0 = -t\sum_{\langle ij\rangle}\sum_{\sigma=\uparrow,\downarrow}\left(a^\dagger_{i,\sigma}b_{j,\sigma} + h.c.\right) - \mu\sum_{i,\sigma}\left(a^\dagger_{i,\sigma}a_{i,\sigma} + b^\dagger_{i,\sigma}b_{i,\sigma}\right), \quad (1)$$

where t is the hopping energy between the nearest-neighbor C atoms, μ is the chemical potential and $a_{i,\sigma}$ ($a^\dagger_{i,\sigma}$) and $b_{i,\sigma}$ ($b^\dagger_{i,\sigma}$) are the onsite annihilation (creation) operators for electrons on sublattices A and B, respectively, with spin $\sigma =\uparrow,\downarrow$. Diagonalization of equation (1) yields the energy spectrum $\pm E_\pm$, with

$$E_\pm = \pm t|\gamma(\boldsymbol{k})| - \mu, \quad (2)$$

where $\gamma(\boldsymbol{k}) = \sum_{\boldsymbol{\delta}}\exp(i\boldsymbol{k}\cdot\boldsymbol{\delta})$ and $\boldsymbol{\delta}$ is a nearest-neighbor vector. In what follows, we use coordinates with

$$\boldsymbol{\delta}_1 = a\left(0, \frac{1}{\sqrt{3}}\right), \quad (3)$$

$$\boldsymbol{\delta}_{2,3} = \frac{a}{2}\left(\pm 1, -\frac{1}{\sqrt{3}}\right), \quad (4)$$

where $a = 1.42$ Å is the distance between neighboring C atoms, such that the two inequivalent corners of the first Brillouin zone can be expressed as

$$\boldsymbol{K}_\pm = \pm\left(\frac{4\pi}{3a}, 0\right). \quad (5)$$

The energy spectrum of the free fermions over the first Brillouin zone is visualized in Figure 1.

In order to apply the mean-field approximation, we define the superconductivity order parameter as a three-component complex vector

$$\overrightarrow{\Delta} \equiv (\Delta_{\boldsymbol{\delta}_1}, \Delta_{\boldsymbol{\delta}_2}, \Delta_{\boldsymbol{\delta}_3}), \quad (6)$$

where the components are defined by

$$\Delta_{\boldsymbol{\delta}} = \langle a_{i\uparrow}b_{i+\boldsymbol{\delta}\downarrow} - a_{i\downarrow}b_{i+\boldsymbol{\delta}\uparrow}\rangle. \quad (7)$$

We study the superconductivity pairing arising from the nearest-neighbor attractive interaction

$$H_{int} = \sum_{i,\boldsymbol{\delta}}\Delta_{\boldsymbol{\delta}}\left(a^\dagger_{i\uparrow}b^\dagger_{i+\boldsymbol{\delta}\downarrow} - a^\dagger_{i\downarrow}b^\dagger_{i+\boldsymbol{\delta}\uparrow}\right), \quad (8)$$

with the limit of strong onsite interaction. The resulting mean-field Hamiltonian can be expressed in momentum space as

$$H_{MF} = -t\sum_{\boldsymbol{k}\sigma}\left(\gamma(\boldsymbol{k})a^\dagger_{\boldsymbol{k}\sigma}b_{\boldsymbol{k}\sigma} + h.c.\right) - \mu\sum_{\boldsymbol{k}\sigma}\left(a^\dagger_{\boldsymbol{k}\sigma}a_{\boldsymbol{k}\sigma} + b^\dagger_{\boldsymbol{k}\sigma}b_{\boldsymbol{k}\sigma}\right) - J\sum_{\boldsymbol{k},\boldsymbol{\delta}}\left(\Delta_{\boldsymbol{\delta}}e^{i\boldsymbol{k}\boldsymbol{\delta}}\left(a^\dagger_{\boldsymbol{k}\uparrow}b^\dagger_{-\boldsymbol{k}\downarrow} - a^\dagger_{\boldsymbol{k}\downarrow}b^\dagger_{-\boldsymbol{k}\uparrow}\right) + h.c.\right), \quad (9)$$

where J is the effective pairing potential arising from the electron–electron interaction. The kinetic part of the previous Hamiltonian can be diagonalized by introducing the following transformations

$$c_{\boldsymbol{k},\sigma} = \frac{1}{\sqrt{2}}(a_{\boldsymbol{k},\sigma} - e^{i\cdot\phi_{\boldsymbol{k}}}b_{\boldsymbol{k},\sigma}),$$
$$d_{\boldsymbol{k},\sigma} = \frac{1}{\sqrt{2}}(a_{\boldsymbol{k},\sigma} + e^{i\cdot\phi_{\boldsymbol{k}}}b_{\boldsymbol{k},\sigma}), \quad (10)$$

where the phase $\phi_{\boldsymbol{k}}$ is defined as $\phi_{\boldsymbol{k}} = \arg(\gamma_{\boldsymbol{k}})$. Note that $c^\dagger_{\boldsymbol{k},\boldsymbol{\sigma}}$ and $d^\dagger_{\boldsymbol{k},\boldsymbol{\sigma}}$ create an electron in the upper and lower Bogoliubov bands, respectively.

Thus, introducing the energy basis, the Hamiltonian becomes

$$H_{MF} = -t\sum_{\boldsymbol{k},\sigma}|\gamma_{\boldsymbol{k}}|(d^{\dagger}_{\boldsymbol{k},\sigma}d_{\boldsymbol{k},\sigma} - c^{\dagger}_{\boldsymbol{k},\sigma}c_{\boldsymbol{k},\sigma}) - \mu\sum_{\boldsymbol{k},\sigma}(d^{\dagger}_{\boldsymbol{k},\sigma}d_{\boldsymbol{k},\sigma} + c^{\dagger}_{\boldsymbol{k},\sigma}c_{\boldsymbol{k},\sigma}) - J\sum_{\boldsymbol{k}}\sum_{\boldsymbol{\delta}}\Big(\Delta_{\boldsymbol{\delta}}\Big(\cos(\boldsymbol{k\delta}-\phi_{\boldsymbol{k}})(d^{\dagger}_{\boldsymbol{k},\uparrow}d^{\dagger}_{-\boldsymbol{k},\downarrow} - c^{\dagger}_{\boldsymbol{k},\uparrow}c^{\dagger}_{-\boldsymbol{k},\downarrow}) + i\sin(\boldsymbol{k\delta}-\phi_{\boldsymbol{k}})(c^{\dagger}_{\boldsymbol{k},\uparrow}d^{\dagger}_{-\boldsymbol{k},\downarrow} - d^{\dagger}_{\boldsymbol{k},\uparrow}c^{\dagger}_{-\boldsymbol{k},\downarrow})\Big) + h.c.\Big). \quad (11)$$

The third line in this Hamiltonian is the intraband pairing, containing an order parameter that is even in k-space and corresponding to the spin-singlet pairing. The fourth line is the interband pairing, containing an order parameter that is odd in k-space and corresponding to the spin-triplet pairing. We use the definitions

$$C_{\boldsymbol{k}} = J\sum_{\boldsymbol{\delta}}\Delta_{\boldsymbol{\delta}}\cos(\boldsymbol{k\delta}-\phi_{\boldsymbol{k}}), \quad (12)$$

and

$$S_{\boldsymbol{k}} = J\sum_{\boldsymbol{\delta}}\Delta_{\boldsymbol{\delta}}\sin(\boldsymbol{k\delta}-\phi_{\boldsymbol{k}}). \quad (13)$$

The corresponding span of the superconducting order parameter is

$$\overrightarrow{\Delta} = \begin{cases} \Delta(1,1,1), \\ \Delta(2,-1,-1), \\ \Delta(0,-1,1), \end{cases} \quad (14)$$

where Δ is the self-consistent superconductivity order parameter. In what follows, we use the redefinition $J\Delta \equiv \Delta$. The linearized self-consistence equations of the order parameter are invariant with respect to the hexagonal group C_{6v} [2], i.e., the symmetry group of the honeycomb lattice. The first solution corresponds to the s-wave, $\overrightarrow{\Delta} = \Delta(1,1,1)$, belonging to the natural A1 irreducible representation of the C_{6v} group of the honeycomb lattice. The A1 irreducible representation is spanned by the vector $\boldsymbol{u}_1 = (1,1,1)$. The final two solutions, $\overrightarrow{\Delta} = \Delta(2,-1,-1)$ and $\overrightarrow{\Delta} = \Delta(0,-1,1)$, belong to the two-dimensional subspace of the S_3 group [58], the span of which is $\boldsymbol{u}_2 = (2,-1,-1)$ and $\boldsymbol{u}_3 = (0,-1,1)$. The second (corresponding to the $d_{x^2-y^2}$ wave) and third (corresponding to the d_{xy} wave) solutions belong to the E1 and E2 irreducible representations of the S_3 group, respectively. From the symmetry perspective, it is noteworthy that every combination of the $d_{x^2-y^2}$ and d_{xy} waves is possible. However, it has been shown that the $d_{x^2-y^2} \pm id_{xy}$-wave superconductivity state with an order parameter

$$\overrightarrow{\Delta}_{d_{x^2-y^2}\pm id_{xy}} = \frac{1}{\sqrt{3}}\Delta\begin{pmatrix} 1 \\ e^{\pm\frac{2i\pi}{3}} \\ e^{\mp\frac{2i\pi}{3}} \end{pmatrix}, \quad (15)$$

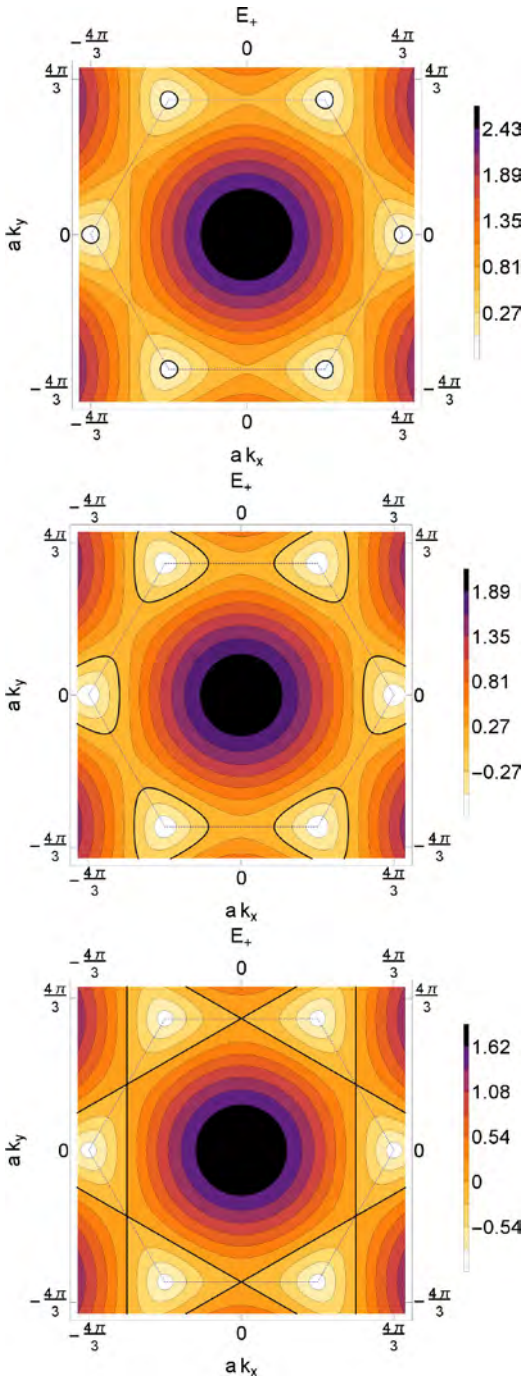

Fig. 1. Brillouin zone with density plot of $|\gamma(\boldsymbol{k})| - \frac{\mu}{t}$ for: (a) $\frac{\mu}{t} = 0.2$; (b) $\frac{\mu}{t} = 0.8$; and (c) $\frac{\mu}{t} = 1$. The edge of the first Brillouin zone is marked by dashed blue lines.

is preferred in graphene below T_C for a superconductivity coupling strength J that is not excessively large, and for doping up to and in the vicinity of the van-Hove singularity point [2].

The s-wave superconductivity order parameter is given by $\Delta(\boldsymbol{k}) = \gamma(\boldsymbol{k})$, while the $d_{x^2-y^2} + id_{xy}$-wave superconductivity order parameter is

$$\Delta_{d\pm id}(\boldsymbol{k}) = \cos\left(\frac{\pi}{3}\right)\Delta_{d_{x^2-y^2}}(\boldsymbol{k}) \pm \sin\left(\frac{\pi}{3}\right)\Delta_{d_{xy}}(\boldsymbol{k}), \quad (16)$$

with

$$\Delta_{d_{x^2-y^2}}(\boldsymbol{k}) = 2\Delta\left(e^{iak_x} - e^{-i\frac{a}{2}k_x}\cos(\frac{a\sqrt{3}}{2}k_y)\right), \quad (17)$$

$$\Delta_{d_{xy}}(\boldsymbol{k}) = -2i\Delta\sin\left(\frac{a\sqrt{3}}{2}k_y\right)e^{-i\frac{a}{2}k_x}. \quad (18)$$

Introducing the spinor

$$\varphi^\dagger_{\boldsymbol{k}} = \left(a^\dagger_{\boldsymbol{k}\uparrow}, b^\dagger_{\boldsymbol{k}\uparrow}, a^\dagger_{\boldsymbol{k}\downarrow}, b^\dagger_{\boldsymbol{k}\downarrow}, a_{-\boldsymbol{k}\uparrow}, b_{-\boldsymbol{k}\uparrow}, a_{-\boldsymbol{k}\downarrow}, b_{-\boldsymbol{k}\downarrow}\right), \quad (19)$$

the Hamiltonian of equation (9) can be expressed as

$$H_{MF} = \frac{1}{2}\sum_{\boldsymbol{k}}\varphi^\dagger_{\boldsymbol{k}}\mathcal{M}_{\boldsymbol{k}}\varphi_{\boldsymbol{k}}, \quad (20)$$

where

$$\mathcal{M}_{\boldsymbol{k}} = \begin{pmatrix} \zeta(\boldsymbol{k}) & 0 & 0 & -\overline{\Delta}(\boldsymbol{k}) \\ 0 & \zeta(\boldsymbol{k}) & \overline{\Delta}(\boldsymbol{k}) & 0 \\ 0 & \overline{\Delta}^*(-\boldsymbol{k}) & -\zeta^*(-\boldsymbol{k}) & 0 \\ -\overline{\Delta}^*(-\boldsymbol{k}) & 0 & 0 & -\zeta^*(-\boldsymbol{k}) \end{pmatrix}, \quad (21)$$

with

$$\zeta(\boldsymbol{k}) = \begin{pmatrix} -\mu & -t\gamma(\boldsymbol{k}) \\ -t\gamma^*(\boldsymbol{k}) & -\mu \end{pmatrix}, \quad (22)$$

$$\overline{\Delta}(\boldsymbol{k}) = \begin{pmatrix} 0 & \Delta(\boldsymbol{k}) \\ \Delta(-\boldsymbol{k}) & 0 \end{pmatrix}. \quad (23)$$

The resultant Hamiltonian indicates that the spin-singlet superconductivity state without spin-orbit coupling is invariant under the spin SU(2) rotation. Hence, we obtain the condition

$$[J_i, \mathcal{M}(\boldsymbol{k})] = 0, \quad J_i = \begin{pmatrix} s_i & 0 \\ 0 & -s_i^* \end{pmatrix}, \ (i = x, y, z). \quad (24)$$

As a result of the spin SU(2) rotation, it is sufficient to use the spinor $\Psi^\dagger_{\boldsymbol{k}} = (a^\dagger_{\boldsymbol{k}\uparrow}, b^\dagger_{\boldsymbol{k}\uparrow}, a_{-\boldsymbol{k}\downarrow}, b_{-\boldsymbol{k}\downarrow})$ in order to express the Hamiltonian of the superconductivity state on the honeycomb lattice in the form

$$H_{MF} = \sum_{\boldsymbol{k}}\Psi^\dagger_{\boldsymbol{k}}h(\boldsymbol{k})\Psi_{\boldsymbol{k}}, \quad (25)$$

where

$$h(\boldsymbol{k}) = \begin{pmatrix} -\mu & -t\gamma(\boldsymbol{k}) & 0 & -\Delta(\boldsymbol{k}) \\ -t\gamma^*(\boldsymbol{k}) & -\mu & -\Delta(-\boldsymbol{k}) & 0 \\ 0 & -\Delta^*(-\boldsymbol{k}) & \mu & t\gamma^*(-\boldsymbol{k}) \\ -\Delta^*(\boldsymbol{k}) & 0 & t\gamma(-\boldsymbol{k}) & \mu \end{pmatrix}. \quad (26)$$

When the superconductivity order parameter is pure real the Hamiltonian $h(\boldsymbol{k})$ satisfies

$$Th(\boldsymbol{k})T^{-1} = h(-\boldsymbol{k}), \quad (27)$$

where $T = K$ mimics time-reversal symmetry. The condition given in equation (27) can satisfy a real superconductivity order parameter only. The $d_{x^2-y^2} + id_{xy}$-wave superconductivity order parameter given by equation (16) breaks the time-reversal symmetry. It appertains to the CI-class in the Altland-Zirnbauer classification of topological insulators and superconductors [59–61]. Furthermore, it is possible to classify two-dimensional C-class superconductors using the Chern number C. Note that the nontrivial topology of the $d_{x^2-y^2} + id_{xy}$-wave superconductivity state is denoted by the Chern number $C = 2$.

3 Entanglement spectra

A method for analytically calculating the entanglement spectrum of a free-fermion system is given in references [52,62,63]. Here, we generalize this method to superconductivity systems, using an approach similar to that described in references [64,65].

The entanglement Hamiltonian can be constructed as a single-particle operator in a quadratic matrix [52,62,63], as it is completely determined by any correlation matrix of operators acting on the remaining part after the subsystem has been traced out. Our system consists of two subsystems, A and B. The reduced density matrix for subsystem A, defined as $\rho_A = \mathrm{tr}_B\rho$, can be formulated as in the free fermion case, such that $\rho_A = \frac{1}{Z}e^{-H_{\mathrm{ent}}}$, using the entanglement spectrum H_{ent} and the partition function $Z = \mathrm{tr}\left(e^{-H_{\mathrm{ent}}}\right)$. Furthermore, the average $\langle\mathcal{O}\rangle$ of a local operator in subsystem A can be calculated as $\langle\mathcal{O}\rangle = \mathrm{tr}(\rho_A\mathcal{O}_A)$.

By tracing out a single spin direction, e.g., the negative spin ↓, from the ground state on the honeycomb lattice in the presence of the s-wave and chiral $d + id$-wave superconductivity, the correlation matrix can be formulated as

$$C(\boldsymbol{k}) = \begin{pmatrix} \langle a^\dagger_{\boldsymbol{k}\uparrow}a_{\boldsymbol{k}\uparrow}\rangle & \langle a^\dagger_{\boldsymbol{k}\uparrow}b_{\boldsymbol{k}\uparrow}\rangle \\ \langle b^\dagger_{\boldsymbol{k}\uparrow}a_{\boldsymbol{k}\uparrow}\rangle & \langle b^\dagger_{\boldsymbol{k}\uparrow}b_{\boldsymbol{k}\uparrow}\rangle \end{pmatrix}. \quad (28)$$

For more technical details of the analytical calculations of the correlation matrix, we refer the reader to Appendix B. Here, one can show that the eigenvalues of the correlation matrix η_l are related to the entanglement spectrum ξ_l, such that

$$\xi_l = \ln\left(\frac{1-\eta_l}{\eta_l}\right). \quad (29)$$

3.1 s-wave scenario

The s-wave superconductivity order parameter corresponds to the bond-independent superconductivity state; thus, $S_{\boldsymbol{k}}$ is identically zero.

We analytically obtain the entanglement levels (Eq. (29))

$$\xi_1(\boldsymbol{k}) = -2\mathrm{arcsinh}\left(\frac{t|\gamma(\boldsymbol{k})| + \mu}{|C_{\boldsymbol{k}}|}\right) \quad (30)$$

and

$$\xi_2(\boldsymbol{k}) = 2\text{arcsinh}\left(\frac{t|\gamma(\boldsymbol{k})| - \mu}{|C_{\boldsymbol{k}}|}\right). \tag{31}$$

The entanglement Hamiltonian has the form

$$\mathcal{H}_{ent} = \sum_{\boldsymbol{k}} \left(\xi_1 e^{\dagger}_{\boldsymbol{k},+} e_{\boldsymbol{k},+} + \xi_2 f^{\dagger}_{\boldsymbol{k},+} f_{\boldsymbol{k},+}\right), \tag{32}$$

where $e_{\boldsymbol{k},+}$ and $f_{\boldsymbol{k},+}$ are Bogoliubov transformations given in Appendix B by equations (B.1) and (B.2). The entanglement levels for different values of μ, with $t = 2.5\,\text{eV}$, and $\Delta = 3\,\text{eV}$ are shown in Figure 2.

The undoped graphene is a gapless semi-metal and is not a superconductor at low temperatures. However, when the system is at half-filling (with $\mu = 0$), the entanglement levels are

$$\xi_{1,2}(\boldsymbol{k}) = \pm 2\text{arcsinh}\left(\frac{t}{\Delta}\right), \tag{33}$$

being constant over the entire Brillouin zone. In the strong coupling regime, when $\Delta \gg t$, one finds

$$\xi_{1,2}(\boldsymbol{k}) \approx \pm 2\frac{t}{\Delta}. \tag{34}$$

The canonical entanglement Hamiltonian at half-filling is independent of the inverse temperature [53] $\beta = k_E/\Delta$, such that

$$\mathcal{H}_{can} = \sum_{i=1}^{2} \frac{1}{k_E}\left(e^{\dagger}_{\boldsymbol{k},+} e_{\boldsymbol{k},+} + f^{\dagger}_{\boldsymbol{k},+} f_{\boldsymbol{k},+}\right), \tag{35}$$

where k_E is a constant. In general, there is no proportionality between the entanglement Hamiltonian and the energy Hamiltonian of free fermions, because the coupling between subsystems $C_{\boldsymbol{k}}$ is $\boldsymbol{k}$-dependent in the Brillouin zone. When $C_{\boldsymbol{k}} = 0$, at the Dirac points, the entanglement levels are not entangled. However, at finite doping, the maximally entangled states, when the entanglement levels are zero, correspond to the zero-energy state of the noninteracting fermions. To provide a superior visualization, a thick black line is used to connect the zero-energy states in Figure 1 and the maximally entangled states in Figure 2.

3.2 Chiral d-wave scenario

To enable analytical calculations, we diagonalize the Hamiltonian (26)

$$H_{MF} = \sum_{\boldsymbol{k}} E_\alpha (o^{\dagger}_{\boldsymbol{k},+} o_{\boldsymbol{k},+} + o^{\dagger}_{-\boldsymbol{k},-} o_{-\boldsymbol{k},-}) + \sum_{\boldsymbol{k}} E_\beta (p^{\dagger}_{\boldsymbol{k},+} p_{\boldsymbol{k},+} + p^{\dagger}_{-\boldsymbol{k},-} p_{-\boldsymbol{k},-}), \tag{36}$$

by the Bogoliubov quasiparticles $o_{\boldsymbol{k},+}, o_{-\boldsymbol{k},-}, p_{\boldsymbol{k},+}$ and $p_{-\boldsymbol{k},-}$ given in Appendix A with equations (A.30) and (A.31). The energies of the Bogoliubov quasiparticles are $\pm E_\alpha$ and $\pm E_\beta$, where

$$E_\alpha = \sqrt{t^2|\gamma(\boldsymbol{k})|^2 + \mu^2 + (|S_{\boldsymbol{k}}|^2 + |C_{\boldsymbol{k}}|^2) + 2\sqrt{u+v}}, \tag{37}$$

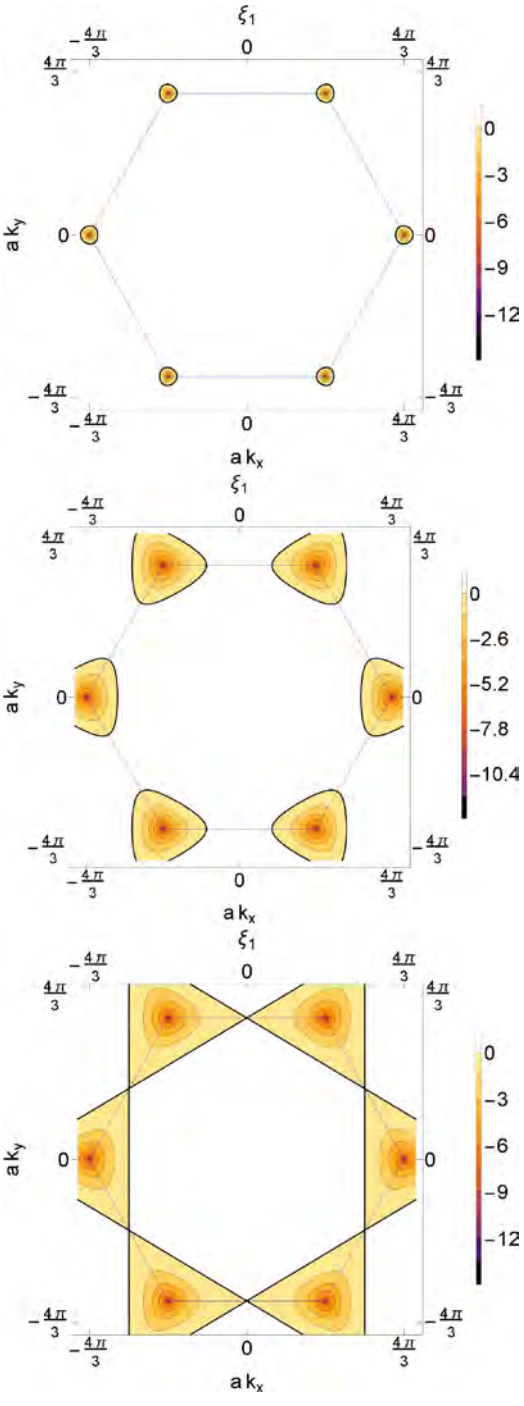

Fig. 2. Contour plot of entanglement level $\xi_1(\boldsymbol{k})$ of s-wave superconductivity state on honeycomb lattice plotted for $\frac{J}{t} = 3$ and: (a) $\frac{\mu}{t} = 0.2$; (b) $\frac{\mu}{t} = 0.8$; and (c) $\frac{\mu}{t} = 1$. The thin blue dashed and thick black lines represent the first Brillouin zone and connect the zero energy states, respectively.

and

$$E_\beta = \sqrt{t^2|\gamma(\boldsymbol{k})|^2 + \mu^2 + (|S_{\boldsymbol{k}}|^2 + |C_{\boldsymbol{k}}|^2) - 2\sqrt{u+v}} \quad (38)$$

with

$$u = \left(\mu^2 + |S_{\boldsymbol{k}}|^2\right) t^2|\gamma(\boldsymbol{k})|^2, \quad (39)$$

and

$$v = \left(\mathrm{Re}(C_{\boldsymbol{k}})\mathrm{Im}(S_{\boldsymbol{k}}) - \mathrm{Re}(S_{\boldsymbol{k}})\mathrm{Im}(C_{\boldsymbol{k}})\right)^2. \quad (40)$$

When the superconductivity order parameters $\Delta_{\boldsymbol{\delta}}$ are pure real, i.e., when no time-reversal symmetry breaking occurs, v vanishes.

From analytical calculations, one obtains the correlation matrix at $T = 0$

$$C(\boldsymbol{k}) = \begin{pmatrix} C_{11}(\boldsymbol{k}) & C_{12}(\boldsymbol{k}) \\ C_{12}^*(\boldsymbol{k}) & C_{22}(\boldsymbol{k}) \end{pmatrix}, \quad (41)$$

where

$$\begin{aligned} C_{11} &= \langle a_{\boldsymbol{k}\uparrow}^\dagger a_{\boldsymbol{k}\uparrow}\rangle \\ &= \frac{1}{2} + \frac{1}{4}\frac{\mu}{\sqrt{\mu^2 + |S_{\boldsymbol{k}}|^2}}(\epsilon_1 + m) \\ &\quad \times \frac{1}{E_\alpha}\left(1 - \frac{m}{\sqrt{t^2|\gamma(\boldsymbol{k})|^2 + m^2}}\right) \\ &\quad + \frac{1}{4}\frac{\mu}{\sqrt{\mu^2 + |S_{\boldsymbol{k}}|^2}}(\epsilon_2 + m) \\ &\quad \times \frac{1}{E_\beta}\left(1 + \frac{m}{\sqrt{t^2|\gamma(\boldsymbol{k})|^2 + m^2}}\right), \end{aligned} \quad (42)$$

$$\begin{aligned} C_{22} &= \langle b_{\boldsymbol{k}\uparrow}^\dagger b_{\boldsymbol{k}\uparrow}\rangle \\ &= \frac{1}{2} + \frac{1}{4}\frac{\mu}{\sqrt{\mu^2 + |S_{\boldsymbol{k}}|^2}}(\epsilon_1 - m) \\ &\quad \times \frac{1}{E_\alpha}\left(1 + \frac{m}{\sqrt{t^2|\gamma(\boldsymbol{k})|^2 + m^2}}\right) \\ &\quad + \frac{1}{4}\frac{\mu}{\sqrt{\mu^2 + |S_{\boldsymbol{k}}|^2}}(\epsilon_2 - m) \\ &\quad \times \frac{1}{E_\beta}\left(1 - \frac{m}{\sqrt{t^2|\gamma(\boldsymbol{k})|^2 + m^2}}\right), \end{aligned} \quad (43)$$

$$\begin{aligned} C_{12} &= \langle a_{\boldsymbol{k}\uparrow}^\dagger b_{\boldsymbol{k}\uparrow}\rangle \\ &= \frac{1}{4}e^{-i\phi_{\boldsymbol{k}}}\left(\left(\frac{\epsilon_1}{E_\alpha} - \frac{\epsilon_2}{E_\beta}\right) - in\left(\frac{1}{E_\alpha} - \frac{1}{E_\beta}\right)\right) \\ &\quad \times \frac{t|\gamma(\boldsymbol{k})|}{\sqrt{t^2|\gamma(\boldsymbol{k})|^2 + m^2}} \end{aligned} \quad (44)$$

with

$$\epsilon_{1,2} = \sqrt{\mu^2 + |S_{\boldsymbol{k}}|^2} \pm \sqrt{t^2|\gamma(\boldsymbol{k})|^2 + m^2}, \quad (45)$$

while

$$m = \frac{\mathrm{Re}(\mathrm{C}_{\boldsymbol{k}}) \cdot \mathrm{Im}(\mathrm{S}_{\boldsymbol{k}}) - \mathrm{Im}(\mathrm{C}_{\boldsymbol{k}}) \cdot \mathrm{Re}(\mathrm{S}_{\boldsymbol{k}})}{\sqrt{\mu^2 + |S_{\boldsymbol{k}}|^2}}, \quad (46)$$

and

$$n = \frac{\mathrm{Re}(C_{\boldsymbol{k}})\mathrm{Re}(S_{\boldsymbol{k}}) + \mathrm{Im}(C_{\boldsymbol{k}})\mathrm{Im}(S_{\boldsymbol{k}})}{\sqrt{\mu^2 + |S_{\boldsymbol{k}}|^2}}. \quad (47)$$

Thus, the entanglement spectrum obtained from the eigenvalues of the correlation matrix given in equation (29) consists of entanglement levels ξ_1 and ξ_2 where:

$$\begin{aligned} \xi_{1,2} = &-2\mathrm{arctanh} \\ &\times(C_{11} + C_{22} - 1 \pm \sqrt{(C_{11} - C_{22})^2 + 4|C_{12}|^2}). \end{aligned} \quad (48)$$

As the d-wave spin-singlet superconductivity order parameter involves both $C_{\boldsymbol{k}}$ and $S_{\boldsymbol{k}}$, there is no relationship between states with the zero-value states of the entanglement spectrum and the zero-energy states of the free fermions. At the van-Hove singularity point, i.e., when $\mu = t$, both the entanglement spectrum and the energy spectrum of the free fermions are zero at the M point. The results of our analytical calculations of the entanglement spectrum of the $d_{x^2-y^2} + id_{xy}$-wave superconductivity on the honeycomb lattice are presented in Figure 3.

As we have discussed above, the $d_{x^2-y^2}$- and d_{xy}-wave superconductivity order parameters preserve the time-reversal symmetry (Eq. (27)). Based on the time-reversal symmetry and provided $\Psi_{\boldsymbol{k}}$ are the eigenstates of the Hamiltonian given in equation (26), we can state that

$$\Psi_{\boldsymbol{k}}^* = \Psi_{-\boldsymbol{k}}, \quad (49)$$

where the $\Psi_{-\boldsymbol{k}}^*$ are also eigenstates of the Hamiltonian of equation (26). This yields

$$\Phi_{\boldsymbol{k}}^* = \Phi_{-\boldsymbol{k}}. \quad (50)$$

Hence, the real d-wave superconductivity order parameter preserves the time-reversal symmetry in the correlation matrix, which is constructed from the $\Phi_{\boldsymbol{k}}$ as $C(\boldsymbol{k}) = \langle\Phi_{\boldsymbol{k}}^\dagger\Phi_{\boldsymbol{k}}\rangle$. The entanglement Hamiltonian satisfies:

$$T_E\mathcal{H}_{ent}(\boldsymbol{k})T_E^{-1} = \mathcal{H}_{ent}(-\boldsymbol{k}), \quad (51)$$

with $T_E = K$.

When the $d_{x^2-y^2} + id_{xy}$-wave superconductivity order parameter is considered, $C_{\boldsymbol{k}}$ and $S_{\boldsymbol{k}}$ are complex functions. Then, the m and n terms are non-zero. Hence, the average occupancy number at site A, $C_{11}(\boldsymbol{k})$, and the average occupancy number at site B, $C_{22}(\boldsymbol{k})$, are not equal and the off-diagonal element of the correlation matrix $C_{12}(\boldsymbol{k})$ is complex. Because $S_{\boldsymbol{k}}$ is an odd

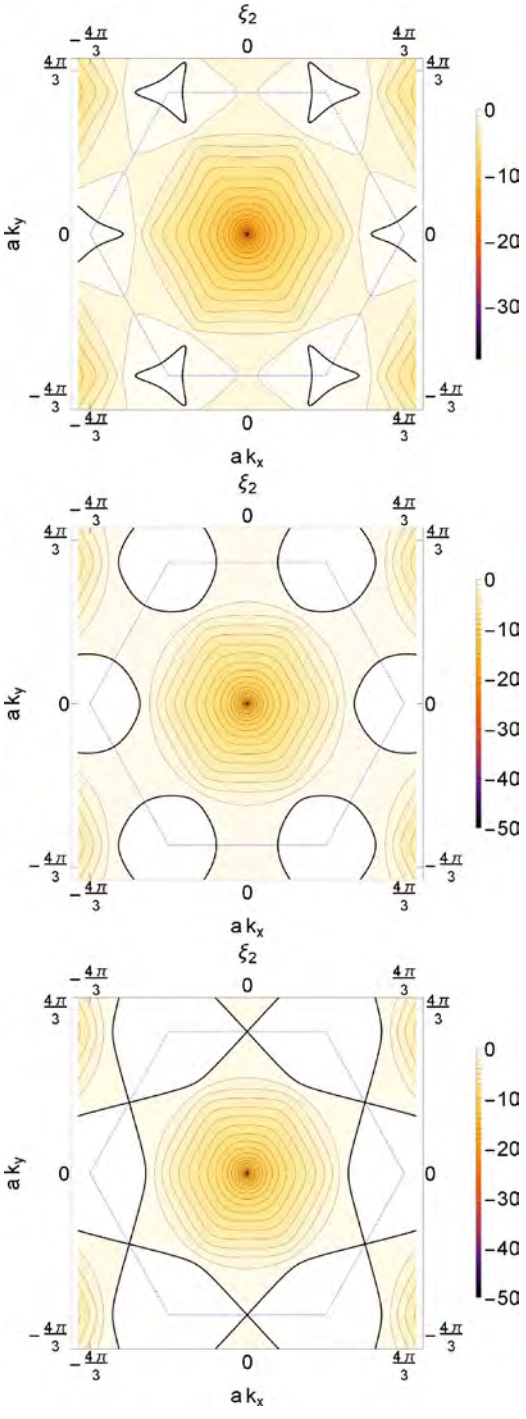

Fig. 3. Contour plot of the entanglement level $\xi_1(\boldsymbol{k})$ of $d_{x^2-y^2}+id_{xy}$-wave superconductivity state on the honeycomb lattice plotted for $\frac{J}{t}=3$ and (a) $\frac{\mu}{t}=0.2$, (b) $\frac{\mu}{t}=0.8$ and (c) $\frac{\mu}{t}=1$. The dashed blue line delineates the first Brillouin zone, while the thick black line shows maximally entangled states.

function in the momentum space, while $C_{\boldsymbol{k}}$ is a even function, it can be shown that elements of the correlation matrix $C_{11}(\boldsymbol{k})$, $C_{22}(\boldsymbol{k})$, and $C_{12}(\boldsymbol{k})$ are constrained as $C_{11}(-\boldsymbol{k})=C_{22}(\boldsymbol{k})$ and $C^*_{12}(-\boldsymbol{k})=C_{12}(\boldsymbol{k})$. Therefore, it follows that the complex $d_{x^2-y^2}+id_{xy}$-wave superconductivity order parameter breaks the time-reversal symmetry in the entanglement Hamiltonian. The topology of the entanglement Hamiltonian in two-dimension with broken time-reversal symmetry is characterized by the entanglement Chern number.

For further analysis of the topological properties of the entanglement Hamiltonian, we require not only its eigenvalues, but also its eigenstates. The eigenstates of the correlation matrix are identical to the eigenstates of the entanglement Hamiltonian and can be expressed as

$$q_{\boldsymbol{k}\uparrow}=\delta_+(\boldsymbol{k})a_{\boldsymbol{k}\uparrow}+\delta_-(\boldsymbol{k})b_{\boldsymbol{k}\uparrow}, \tag{52}$$
$$r_{\boldsymbol{k}\uparrow}=\delta_+(-\boldsymbol{k})a_{\boldsymbol{k}\uparrow}-\delta^*_-(-\boldsymbol{k})b_{\boldsymbol{k}\uparrow}, \tag{53}$$

where explicit expressions for $\delta_+(\boldsymbol{k})$ and $\delta_-(\boldsymbol{k})$ are given in Appendix B by equation (B.17). Using these eigenstates, we can calculate the Berry curvature

$$F(\boldsymbol{k})=\frac{\partial A_y}{\partial k_x}-\frac{\partial A_x}{\partial k_y} \tag{54}$$

and the Berry connection

$$\boldsymbol{A}(\boldsymbol{k})=i\langle r(\boldsymbol{k})|\frac{\partial}{\partial \boldsymbol{k}}|r(\boldsymbol{k})\rangle, \tag{55}$$

which vanish everywhere outside the Dirac points where quantized "monopole" sources of the δ-function type exist.

Through numerical integrations of the Berry curvature along the Brillouin zone, we find that the entanglement Chern number is $C=1$, in the case of the chiral $d_{x^2-y^2}+id_{xy}$-wave superconductivity state. In the presence of $SU(2)$ rotation and broken time-reversal symmetry, as in the case of an energetic Hamiltonian, the Chern number C can have even values only. For the entanglement Hamiltonian, it is possible to obtain an odd value for the Chern number, as it is not invariant to the $SU(2)$ rotation. As a result, the topology of the entanglement Hamiltonian, which is obtained by tracing out the spin-down subsystem of the ground state of the chiral $d_{x^2-y^2}+id_{xy}$-wave superconductivity state on the honeycomb lattice, clearly differs from the topology of the energetic Hamiltonian of free fermions without the superconductivity instabilities.

3.3 Tracing out B sublattices

3.3.1 s-wave scenario

We will now consider the ground state of interacting fermions on the honeycomb lattice in the presence of the s-wave superconductivity instability. Upon tracing out B sublattices the entanglement levels:

$$\xi_\pm=\pm 2\text{arctanh}\left(\frac{t^2|\gamma(\boldsymbol{k})|^2-\mu^2+\Delta^2|\gamma(\boldsymbol{k})|^2}{E_\alpha E_\beta}\right), \tag{56}$$

where $E_\alpha=\sqrt{\left(t|\gamma(\boldsymbol{k})|-\mu\right)^2+\Delta^2|\gamma(\boldsymbol{k})|^2}$ and $E_\beta=\sqrt{\left(t|\gamma(\boldsymbol{k})|+\mu\right)^2+\Delta^2|\gamma(\boldsymbol{k})|^2}$. When system is at half-filling the subsystems are maximally entangled. The entanglement levels are plotted at Figure 4.

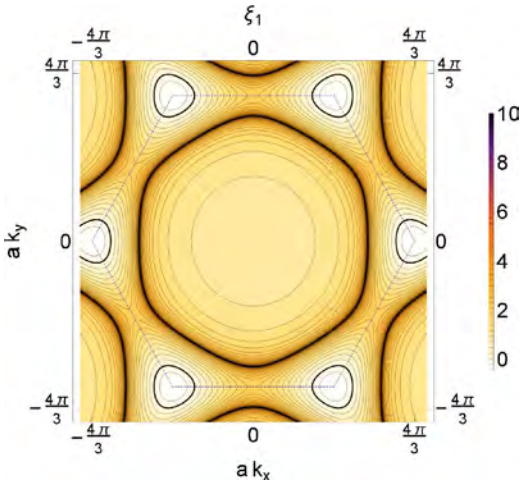

Fig. 4. Contour plot of entanglement level $\xi_1(\boldsymbol{k})$ of s-wave superconductivity state on honeycomb lattice plotted for $\frac{J}{t}=3$ and $\frac{\mu}{t}=0.8$. The first Brillouin zone is border by the dashed blue line, while the thick line connects maximally entangled states.

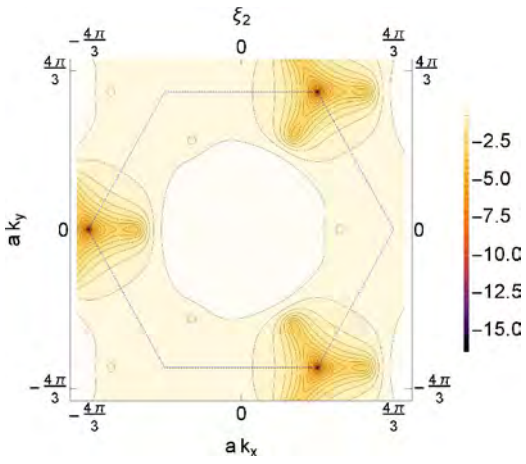

Fig. 5. Contour plot of entanglement level $\xi_2(\boldsymbol{k})$ of $d_{x^2-y^2}+id_{xy}$ superconductivity state on honeycomb lattice plotted for $\frac{J}{t}=3$ and $\frac{\mu}{t}=0.8$. The thin blue dashed and thick black lines represent the first Brillouin zone and connect the zero energy states, respectively.

3.3.2 Chiral d-wave scenario

Upon tracing out B sublattices, the entanglement spectrum of d-wave superconductivity state on the honeycomb lattice is completely determined by the correlation matrix:

$$C(\boldsymbol{k})=\begin{pmatrix} C_{11}(\boldsymbol{k}) & C_{13}(\boldsymbol{k}) \\ C_{13}^{*}(\boldsymbol{k}) & C_{33}(\boldsymbol{k}) \end{pmatrix}, \tag{57}$$

where C_{11}, C_{33} and C_{13} are given in Appendix B. The eigenvalues $\eta_{1,2}$ of the correlation matrix

$$\eta_{1,2}=\frac{1}{2}\left((C_{11}+C_{33}+\pm\sqrt{(C_{11}-C_{33})^2+4|C_{13}|^2}\right). \tag{58}$$

are related to the entanglement levels $\xi_{1,2}=\ln\left(\frac{\eta_{\pm}}{1-\eta_{pm}}\right)$. At finite doping the entanglement levels never vanish. Here, space inversion symmetry of the entanglement spectrum is broken and the entanglement levels satisfy $\xi_{\pm}(-\boldsymbol{k})=-\xi_{\mp}(\boldsymbol{k})$. The entanglement level $\xi_2(\boldsymbol{k})$ is visualized in Figure 5. The broken time-reversal symmetry in the entanglement Hamiltonian leads to the entanglement Chern number $C=1$.

4 Conclusion and outlook

We analytically evaluated the entanglement spectra of the superconductivity states on the graphene honeycomb lattice, primarily focusing on the s-wave and chiral $d_{x^2-y^2}+id_{xy}$ superconductivity states. When one spin direction was traced out, exact correspondence between the maximally entangled states of the s-wave superconductor and the zero energies of the noninteracting fermionic honeycomb lattice at finite doping was observed. The relationship between the topologies of the entanglement and subsystem Hamiltonians was found to depend on the coupling between the subsystems. Further, the chiral $d_{x^2-y^2}+id_{xy}$ superconductivity order parameter breaks the time-reversal symmetry in the entanglement Hamiltonian. The topological properties of the entanglement Hamiltonian, characterized by the topological nontrivial entanglement Chern number $C=1$, clearly differ from those of the time-reversal invariant Hamiltonian of the noninteracting fermions on the honeycomb lattice. The investigations presented herein are based on closed analytical expressions for the full eigensystems of the s- and d-wave superconductivity states on the honeycomb lattice over the entire Brillouin zone. The method used to examine these eigensystems may constitute a useful tool for new studies of superconductivity in graphene. Future work may investigate the relationship between the topologies of the entanglement and subsystem Hamiltonians through the topological phase transition; for example, in the coexistence region between antiferromagnetism and $d_{x^2-y^2}+id_{xy}$ superconducting correlations in graphene [66] and graphene bilayers [8].

The authors kindly acknowledge Milica V. Milovanović. This work was supported by Deutsche Forschungsgemeinschaft via GRK1570.

Appendix A: Derivation of the eigensystem

In this appendix we present analytical diagonalization of the Hamiltonian of the chiral $d+id$-wave superconductivity state on the honeycomb lattice. Complexity of the order parameter makes the analytical approach more difficult. The starting point of our analysis is the Bardeen-Cooper-Schrieffer mean-field Hamiltonian in

$$H_1(\boldsymbol{k}) = \begin{pmatrix} t|\gamma(\boldsymbol{k})| - \mu & 0 & C_{\boldsymbol{k}} & -iS_{\boldsymbol{k}} \\ 0 & -t|\gamma(\boldsymbol{k})| - \mu & iS_{\boldsymbol{k}} & -C_{\boldsymbol{k}} \\ C^*_{\boldsymbol{k}} & -iS^*_{\boldsymbol{k}} & -t|\gamma(\boldsymbol{k})| + \mu & 0 \\ iS^*_{\boldsymbol{k}} & -C^*_{\boldsymbol{k}} & 0 & t|\gamma(\boldsymbol{k})| + \mu \end{pmatrix} \tag{A.4}$$

$$H_1^{'}(\boldsymbol{k}) = \begin{pmatrix} t|\gamma(\boldsymbol{k})| - \mu & 0 & 0 & -iS_{\boldsymbol{k}} \\ 0 & -t|\gamma(\boldsymbol{k})| - \mu & iS_{\boldsymbol{k}} & 0 \\ 0 & -iS^*_{\boldsymbol{k}} & -t|\gamma(\boldsymbol{k})| + \mu & 0 \\ iS^*_{\boldsymbol{k}} & 0 & 0 & t|\gamma(\boldsymbol{k})| + \mu \end{pmatrix} \tag{A.5}$$

momentum space

$$\begin{aligned} H_{MF}(\boldsymbol{k}) &= -t\sum_{\boldsymbol{k}} \left(\gamma(\boldsymbol{k}) a^\dagger_{\boldsymbol{k}\sigma} b_{\boldsymbol{k}\sigma} + h.c.\right) \\ &- \mu \sum_{\boldsymbol{k}} \left(a^\dagger_{\boldsymbol{k}\sigma} a_{\boldsymbol{k}\sigma} + b^\dagger_{\boldsymbol{k}\sigma} b_{\boldsymbol{k}\sigma}\right) \\ &- J\sum_{\boldsymbol{k},\boldsymbol{\delta}} \left(\Delta_{\boldsymbol{\delta}} e^{i\boldsymbol{k}\boldsymbol{\delta}} \left(a^\dagger_{\boldsymbol{k}\uparrow} b^\dagger_{-\boldsymbol{k}\downarrow} - a^\dagger_{\boldsymbol{k}\downarrow} b^\dagger_{-\boldsymbol{k}\uparrow}\right) + h.c.\right), \end{aligned} \tag{A.1}$$

where we define the superconductivity order parameter

$$\Delta(\boldsymbol{k}) = \sum_{\boldsymbol{\delta}} \Delta_{\boldsymbol{\delta}} e^{i\boldsymbol{k}\boldsymbol{\delta}}, \tag{A.2}$$

as a combination of the $d_{x^2-y^2}$ and d_{xy}-wave superconductivity state $\Delta_{d\pm id}(\boldsymbol{k}) = \cos\left(\frac{\pi}{3}\right)\Delta_{d^2_x-y^2}(\boldsymbol{k}) \pm \sin\left(\frac{\pi}{3}\right)\Delta_{d_{xy}}(\boldsymbol{k})$ which minimalizes a free energy.

We apply the transformations

$$\begin{aligned} c_{\boldsymbol{k},\sigma} &= \frac{1}{\sqrt{2}}(a_{\boldsymbol{k},\sigma} - e^{i\cdot\phi_{\boldsymbol{k}}} b_{\boldsymbol{k},\sigma}), \\ d_{\boldsymbol{k},\sigma} &= \frac{1}{\sqrt{2}}(a_{\boldsymbol{k},\sigma} + e^{i\cdot\phi_{\boldsymbol{k}}} b_{\boldsymbol{k},\sigma}), \end{aligned} \tag{A.3}$$

such that in

see equation (A.4) above

diagonalize the kinetic part of the Hamiltonian. $C_{\boldsymbol{k}} = J\sum_{\boldsymbol{\delta}} \boldsymbol{\Delta}_{\boldsymbol{\delta}} \cos(\boldsymbol{k}\boldsymbol{\delta} - \phi_{\boldsymbol{k}})$ and $S_{\boldsymbol{k}} = J\sum_{\boldsymbol{\delta}} \boldsymbol{\Delta}_{\boldsymbol{\delta}} \sin(\boldsymbol{k}\boldsymbol{\delta} - \phi_{\boldsymbol{k}})$ are complex functions.

Here it is useful to split this Hamiltonian as $H_1 = H_1^{'} + H_1^{''}$ where

see equation (A.5) above

and

$$H_1^{''}(\boldsymbol{k}) = \begin{pmatrix} 0 & 0 & C_{\boldsymbol{k}} & 0 \\ 0 & 0 & 0 & -C_{\boldsymbol{k}} \\ C^*_{\boldsymbol{k}} & 0 & 0 & 0 \\ 0 & -C^*_{\boldsymbol{k}} & 0 & 0 \end{pmatrix}. \tag{A.7}$$

$H_1^{'}$ is diagonalized by

$$e_{\boldsymbol{k}+} = i\alpha^*_- c_{\boldsymbol{k}\uparrow} + \alpha_+ d^\dagger_{-\boldsymbol{k}\downarrow} \tag{A.8}$$

$$f_{\boldsymbol{k}+} = -i\alpha^*_- d_{\boldsymbol{k}\uparrow} + \alpha_+ c^\dagger_{-\boldsymbol{k}\downarrow} \tag{A.9}$$

with

$$\begin{aligned} \alpha_+ &= \sqrt{\frac{1}{2}\left(1 + \frac{\mu}{\sqrt{\mu^2 + |S_{\boldsymbol{k}}|^2}}\right)} \\ \alpha_- &= \frac{S_{\boldsymbol{k}}}{\sqrt{2\sqrt{\mu^2 + |S_{\boldsymbol{k}}|^2}\left(\mu + \sqrt{\mu^2 + |S_{\boldsymbol{k}}|^2}\right)}}. \end{aligned} \tag{A.10}$$

This leads to

$$H_2 = U_2 H_1 U_2^\dagger = \begin{pmatrix} e_1 & m & -l & 0 \\ m & e_2 & 0 & l \\ -l^* & 0 & -e_1 & m \\ 0 & l^* & m & -e_2 \end{pmatrix} \tag{A.11}$$

with

$$m = \frac{\mathrm{Re}(\mathrm{C}_{\boldsymbol{k}}) \cdot \mathrm{Im}(\mathrm{S}_{\boldsymbol{k}}) - \mathrm{Im}(\mathrm{C}_{\boldsymbol{k}}) \cdot \mathrm{Re}(\mathrm{S}_{\boldsymbol{k}})}{\sqrt{\mu^2 + |S_{\boldsymbol{k}}|^2}} \tag{A.12}$$

and

$$l = \alpha_+^2 C^*_{\boldsymbol{k}} + (\alpha^*_-)^2 C_{\boldsymbol{k}} \tag{A.13}$$

and $\pm e_1$ and $\pm e_2$ are eigenenergies of the Hamiltonian $H_1^{'}$ given by

$$e_1 = t|\gamma(\boldsymbol{k})| + \sqrt{\mu^2 + |S_{\boldsymbol{k}}|^2} \tag{A.14}$$

and

$$e_2 = -t|\gamma(\boldsymbol{k})| + \sqrt{\mu^2 + |S_{\boldsymbol{k}}|^2}. \tag{A.15}$$

We can now split this Hamiltonian as $H_2 = H_2^{'} + H_2^{''}$ where

$$H_2^{'} = \begin{pmatrix} e_1 & m & 0 & 0 \\ m & e_2 & 0 & 0 \\ 0 & 0 & -e_1 & m \\ 0 & 0 & m & -e_2 \end{pmatrix},$$
$$H_2^{''} = \begin{pmatrix} 0 & 0 & -l & 0 \\ 0 & 0 & 0 & l \\ -l^* & 0 & 0 & 0 \\ 0 & l^* & 0 & 0 \end{pmatrix}. \quad \text{(A.16)}$$

Proceeding now with the transformations

$$g_{\boldsymbol{k}+} = \beta_+ e_{\boldsymbol{k}+} + \sigma\beta_- f_{\boldsymbol{k}+} \quad \text{(A.17)}$$
$$h_{\boldsymbol{k}+} = \sigma\beta_- e_{\boldsymbol{k}+} - \beta_+ f_{\boldsymbol{k}+} \quad \text{(A.18)}$$

where $\sigma = \text{sign}(m)$ and

$$\beta_\pm = \sqrt{\frac{1}{2}\left(1 \pm \frac{t|\gamma(\boldsymbol{k})|}{\sqrt{t^2|\gamma(\boldsymbol{k})|^2 + m^2}}\right)} \quad \text{(A.19)}$$

we diagonalize first part of the Hamiltonian $H_2^{'}$ and we get

$$H_3 = U_3 H_2 U_3^\dagger = \begin{pmatrix} \epsilon_1 & 0 & 0 & -l \\ 0 & \epsilon_2 & -l & 0 \\ 0 & -l^* & -\epsilon_2 & 0 \\ -l^* & 0 & 0 & -\epsilon_1 \end{pmatrix} \quad \text{(A.20)}$$

where $\pm\epsilon_1$ and $\pm\epsilon_2$ are eigenenergies of the Hamiltonian $H_2^{'}$

$$\epsilon_1 = \sqrt{\mu^2 + |S_{\boldsymbol{k}}|^2} + \sqrt{t^2|\gamma(\boldsymbol{k})|^2 + m^2} \quad \text{(A.21)}$$

and

$$\epsilon_2 = \sqrt{\mu^2 + |S_{\boldsymbol{k}}|^2} - \sqrt{t^2|\gamma(\boldsymbol{k})|^2 + m^2}. \quad \text{(A.22)}$$

Finally, this Hamiltonian is brought to the diagonalized form with transformations

$$o_{\boldsymbol{k}+} = \gamma_+^{(1)} g_{\boldsymbol{k}+} - \gamma_-^{(1)} g_{\boldsymbol{k}-}^\dagger \quad \text{(A.23)}$$
$$p_{\boldsymbol{k}+} = \gamma_+^{(2)} h_{\boldsymbol{k}+} - \gamma_-^{(2)} h_{\boldsymbol{k}-}^\dagger \quad \text{(A.24)}$$

with

$$\gamma_+^{(1)} = \sqrt{\frac{1}{2}\left(1 + \frac{\epsilon_1}{E_\alpha}\right)},\ \gamma_-^{(1)} = \frac{l}{\sqrt{2E_\alpha\left(E_\alpha + \epsilon_1\right)}} \quad \text{(A.25)}$$

and

$$\gamma_+^{(2)} = \sqrt{\frac{1}{2}\left(1 + \frac{\epsilon_2}{E_\beta}\right)},\ \gamma_-^{(2)} = \frac{l}{\sqrt{2E_\beta\left(E_\beta + \epsilon_2\right)}} \quad \text{(A.26)}$$

and

$$E_\alpha = \sqrt{t^2|\gamma(\boldsymbol{k})|^2 + \mu^2 + |S_{\boldsymbol{k}}|^2 + |C_{\boldsymbol{k}}|^2 + 2\sqrt{u+v}} \quad \text{(A.27)}$$

and

$$E_\beta = \sqrt{t^2|\gamma(\boldsymbol{k})|^2 + \mu^2 + |S_{\boldsymbol{k}}|^2 + |C_{\boldsymbol{k}}|^2 - 2\sqrt{u+v}} \quad \text{(A.28)}$$

where

$$u = \left(\mu^2 + |S_{\boldsymbol{k}}|^2\right) t^2|\gamma(\boldsymbol{k})|^2$$
$$v = \left(\text{Re}C_{\boldsymbol{k}}\text{Im}S_{\boldsymbol{k}} - \text{Re}S_{\boldsymbol{k}}\text{Im}C_{\boldsymbol{k}}\right)^2. \quad \text{(A.29)}$$

Bogoliubov transformations $o_{\boldsymbol{k}+}$ and $p_{\boldsymbol{k}+}$ in the basis $a_{\boldsymbol{k}\uparrow}, b_{\boldsymbol{k},\uparrow}$

$$\begin{aligned} o_{\boldsymbol{k}+} = &-\frac{1}{\sqrt{2}}\left(\alpha_+\gamma_-^{(1)} - i\alpha_-^*\gamma_+^{(1)}\right)\left(\beta_+ - \sigma\beta_-\right)a_{\boldsymbol{k}\uparrow} \\ &-\frac{1}{\sqrt{2}}e^{i\phi_{\boldsymbol{k}}}\left(\alpha_+\gamma_-^{(1)} + i\alpha_-^*\gamma_+^{(1)}\right)\left(\beta_+ + \sigma\beta_-\right)b_{\boldsymbol{k}\uparrow} \\ &+\frac{1}{\sqrt{2}}\left(\alpha_+\gamma_+^{(1)} + i\alpha_-\gamma_-^{(1)}\right)\left(\beta_+ + \sigma\beta_-\right)a_{-\boldsymbol{k}\downarrow}^\dagger \\ &+\frac{1}{\sqrt{2}}e^{i\phi_{\boldsymbol{k}}}\left(\alpha_+\gamma_+^{(1)} - i\alpha_-\gamma_-^{(1)}\right)\left(\beta_+ - \sigma\beta_-\right)b_{-\boldsymbol{k}\downarrow}^\dagger \end{aligned} \quad \text{(A.30)}$$

$$\begin{aligned} p_{\boldsymbol{k}+} = &-\frac{1}{\sqrt{2}}\left(\alpha_+\gamma_-^{(2)} + i\alpha_-^*\gamma_+^{(2)}\right)\left(\beta_+ + \sigma\beta_-\right)a_{\boldsymbol{k}\uparrow} \\ &+\frac{1}{\sqrt{2}}e^{i\phi_{\boldsymbol{k}}}\left(\alpha_+\gamma_-^{(2)} - i\alpha_-^*\gamma_+^{(2)}\right)\left(\beta_+ - \sigma\beta_-\right)b_{\boldsymbol{k}\uparrow} \\ &+\frac{1}{\sqrt{2}}\left(\alpha_+\gamma_+^{(2)} - i\alpha_-\gamma_-^{(2)}\right)\left(\beta_+ - \sigma\beta_-\right)a_{-\boldsymbol{k}\downarrow}^\dagger \\ &-\frac{1}{\sqrt{2}}e^{i\phi_{\boldsymbol{k}}}\left(\alpha_+\gamma_+^{(2)} + i\alpha_-\gamma_-^{(2)}\right)\left(\beta_+ + \sigma\beta_-\right)a_{-\boldsymbol{k}\downarrow}^\dagger \end{aligned} \quad \text{(A.31)}$$

Appendix B: Correlation martix

B.1 s-wave scenario

The Hamiltonian equation (26) for s-wave superconductivity state in graphene can be diagonalized by using Bogoluibov transformations

$$\begin{aligned} e_{\boldsymbol{k}+} = &\alpha_+\frac{1}{\sqrt{2}}(a_{\boldsymbol{k},\uparrow} - e^{i\cdot\phi_{\boldsymbol{k}}}b_{\boldsymbol{k},\uparrow}) \\ &+\alpha_-\frac{1}{\sqrt{2}}(a_{-\boldsymbol{k},\downarrow}^\dagger - e^{i\cdot\phi_{\boldsymbol{k}}}b_{-\boldsymbol{k},\downarrow}^\dagger) \end{aligned} \quad \text{(B.1)}$$

$$\begin{aligned} f_{\boldsymbol{k}+} = &\beta_-\frac{1}{\sqrt{2}}(a_{\boldsymbol{k},\uparrow} + e^{i\cdot\phi_{\boldsymbol{k}}}b_{\boldsymbol{k},\uparrow}) \\ &-\beta_+\frac{1}{\sqrt{2}}(a_{-\boldsymbol{k},\downarrow}^\dagger + e^{i\cdot\phi_{\boldsymbol{k}}}b_{-\boldsymbol{k},\downarrow}^\dagger) \end{aligned} \quad \text{(B.2)}$$

where $\alpha_+ = \sqrt{\frac{1}{2}\left(1+\frac{t|\gamma(\boldsymbol{k})|-\mu}{\sqrt{(t|\gamma(\boldsymbol{k})|-\mu)^2+|C_{\boldsymbol{k}}|^2}}\right)}$, $\alpha_- = \frac{C_{\boldsymbol{k}}}{\sqrt{2E_\alpha(E_\alpha+t|\gamma(\boldsymbol{k})|-\mu)}}$, $\beta_+ = \sqrt{\frac{1}{2}\left(1+\frac{t|\gamma(\boldsymbol{k})|+\mu}{\sqrt{(t|\gamma(\boldsymbol{k})|+\mu)^2+|C_{\boldsymbol{k}}|^2}}\right)}$, and $\beta_- = \frac{C_{\boldsymbol{k}}}{\sqrt{2E_\beta(E_\beta+t|\gamma(\boldsymbol{k})|+\mu)}}$ with E_α and E_β are energies of Bogoliubov quasi-particles

$$E_\alpha = \sqrt{(t|\gamma(\boldsymbol{k})|-\mu)^2+|C_{\boldsymbol{k}}|^2} \tag{B.3}$$

and

$$E_\beta = \sqrt{(t|\gamma(\boldsymbol{k})|+\mu)^2+|C_{\boldsymbol{k}}|^2}. \tag{B.4}$$

The e (f) sections are determined by equations (B.1) and (B.2), respectively. These sections are decoupled in Bogoliubov description and we are allowed than to obtain their contributions to the ground state separative. We can demand $e_{\boldsymbol{k}+}|G\rangle = 0$ and $e^\dagger_{\boldsymbol{k}-}|G\rangle = 0$ where $|G\rangle$ is the ground state. The e section contributes to the ground state as:

$$\prod_{\boldsymbol{k}\in IBZ}\left(\alpha_+(\boldsymbol{k})-\alpha_-(\boldsymbol{k})c^\dagger_{\boldsymbol{k}\uparrow}c^\dagger_{-\boldsymbol{k}\downarrow}\right)|0\rangle \tag{B.5}$$

where $|0\rangle$ is the vacuum state. Similar, the contribution of the f section to the ground state:

$$\prod_{\boldsymbol{k}\in IBZ}\left(\beta_-(\boldsymbol{k})+\beta_+(\boldsymbol{k})d^\dagger_{\boldsymbol{k}\uparrow}d^\dagger_{-\boldsymbol{k}\downarrow}\right)|0\rangle \tag{B.6}$$

the ground state $|G\rangle$ is determined by conditions: $f_{\boldsymbol{k}+}|G\rangle = 0$ and $f^\dagger_{\boldsymbol{k}-}|G\rangle = 0$. This leads to the complete ground state vector:

$$\begin{aligned}&\prod_{\boldsymbol{k}\in IBZ}\left(\alpha_+(\boldsymbol{k})-\alpha_-(\boldsymbol{k})c^\dagger_{\boldsymbol{k}\uparrow}c^\dagger_{-\boldsymbol{k}\downarrow}\right)\\&\prod_{\boldsymbol{q}\in IBZ}\left(\beta_-(\boldsymbol{q})+\beta_+(\boldsymbol{q})d^\dagger_{\boldsymbol{q}\uparrow}d^\dagger_{-\boldsymbol{q}\downarrow}\right)|0\rangle.\end{aligned} \tag{B.7}$$

Similar findings are obtained for the ground state of the p-wave superconductivity state in graphene [67].

This ground state leads to the correlation matrix when spin ↓ is traced out:

$$C(\boldsymbol{k}) = \begin{pmatrix}\frac{1}{2}\left(|\alpha_-|^2+|\beta_+|^2\right) & \frac{1}{2}e^{-i\phi_{\boldsymbol{k}}}\left(|\beta_+|^2-|\alpha_-|^2\right)\\ \frac{1}{2}e^{i\phi_{\boldsymbol{k}}}\left(|\beta_+|^2-|\alpha_-|^2\right) & \frac{1}{2}\left(|\alpha_-|^2+|\beta_+|^2\right)\end{pmatrix}. \tag{B.8}$$

B.2 Chiral d-wave scenario

Using

$$\begin{aligned}a_{\boldsymbol{k}\uparrow} =& -\frac{1}{\sqrt{2}}\left(\alpha_+\left(\gamma^{(1)}_-\right)^*+i\alpha_-\gamma^{(1)}_+\right)\left(\beta_+-\sigma\beta_-\right)o_{\boldsymbol{k},+}\\&-\frac{1}{\sqrt{2}}\left(\alpha_+\left(\gamma^{(2)}_-\right)^*+i\alpha_-\gamma^{(2)}_+\right)\left(\beta_++\sigma\beta_-\right)p_{\boldsymbol{k},+}\\&+\frac{1}{\sqrt{2}}\left(\alpha_+\gamma^{(2)}_+-i\alpha_-\gamma^{(2)}_-\right)\left(\beta_++\sigma\beta_-\right)p^\dagger_{-\boldsymbol{k},-}\\&+\frac{1}{\sqrt{2}}\left(\alpha_+\gamma^{(1)}_+-i\alpha_-\gamma^{(1)}_-\right)\left(\beta_+-\sigma\beta_-\right)o^\dagger_{-\boldsymbol{k},-}\end{aligned} \tag{B.9}$$

we can calculate the mean occupancy at cite A:

$$\begin{aligned}\langle a^\dagger_{\boldsymbol{k}\uparrow}a_{\boldsymbol{k}\uparrow}\rangle =& \frac{1}{2}\left(\alpha_+^2(\gamma^{(1)}_+)^2+|\alpha_-|^2|\gamma^{(1)}_-|^2\right.\\&\left.-i\,\alpha_+\gamma^{(1)}_+\left(\alpha_-\gamma^{(1)}_--\alpha^*_-\left(\gamma^{(1)}_-\right)^*\right)\right)\left(\beta_+-\sigma\beta_-\right)^2\\&+\frac{1}{2}\left(\alpha_+^2(\gamma^{(2)}_+)^2+|\alpha_-|^2|\gamma^{(2)}_-|^2-i\alpha_+\gamma^{(2)}_+\left(\alpha_-\gamma^{(2)}_-\right.\right.\\&\left.\left.-\alpha^*_-\left(\gamma^{(2)}_-\right)^*\right)\right)\left(\beta_++\sigma\beta_-\right)^2.\end{aligned} \tag{B.10}$$

After basic algebra we find that the correlation matrix obtained by tracing out spin ↓ at $T = 0$ reads

$$C(\boldsymbol{k}) = \begin{pmatrix}C_{11}(\boldsymbol{k}) & C_{12}(\boldsymbol{k})\\ C^*_{12}(\boldsymbol{k}) & C_{22}(\boldsymbol{k})\end{pmatrix} \tag{B.11}$$

with

$$\begin{aligned}C_{11}(\boldsymbol{k}) =& \frac{1}{2}\left(\alpha_+^2(\gamma^{(1)}_+)^2+|\alpha_-|^2|\gamma^{(1)}_-|^2-\alpha_+\gamma^{(1)}_+\right.\\&\left.\times\left(\alpha_-\gamma^{(1)}_--\alpha^*_-\left(\gamma^{(1)}_-\right)^*\right)\right)\left(\beta_+-\sigma\beta_-\right)^2\\&+\frac{1}{2}\left(\alpha_+^2(\gamma^{(2)}_+)^2+|\alpha_-|^2|\gamma^{(2)}_-|^2-i\alpha_+\gamma^{(2)}_+\right.\\&\left.\times\left(\alpha_-\gamma^{(2)}_--\alpha^*_-\left(\gamma^{(2)}_-\right)^*\right)\right)\left(\beta_++\sigma\beta_-\right)^2\\=&\frac{1}{2}+\frac{1}{4}\frac{\mu}{\sqrt{\mu^2+|S_{\boldsymbol{k}}|^2}}(\epsilon_1+m)\\&\times\frac{1}{E_\alpha}\left(1-\frac{m}{\sqrt{t^2|\gamma(\boldsymbol{k})|^2+m^2}}\right)\\&+\frac{1}{4}\frac{\mu}{\sqrt{\mu^2+|S_{\boldsymbol{k}}|^2}}(\epsilon_2+m)\\&\times\frac{1}{E_\beta}\left(1+\frac{m}{\sqrt{t^2|\gamma(\boldsymbol{k})|^2+m^2}}\right),\end{aligned} \tag{B.12}$$

$$
\begin{aligned}
C_{22}(\boldsymbol{k}) = & \frac{1}{2}\left(\alpha_+^2(\gamma_+^{(1)})^2 + |\alpha_-|^2|\gamma_-^{(1)}|^2 + i\alpha_+\gamma_+^{(1)}\right. \\
& \left.\times\left(\alpha_-\gamma_-^{(1)} - \alpha_-^*\left(\gamma_-^{(1)}\right)^*\right)\right)(\beta_+ + \sigma\beta_-)^2 \\
& + \frac{1}{2}\left(\alpha_+^2(\gamma_+^{(2)})^2 + |\alpha_-|^2|\gamma_-^{(2)}|^2 + i\alpha_+\gamma_+^{(2)}\right. \\
& \left.\times\left(\alpha_-\gamma_-^{(2)} - \alpha_-^*\left(\gamma_-^{(2)}\right)^*\right)\right)(\beta_+ - \sigma\beta_-)^2 \\
= & \frac{1}{2} + \frac{1}{4}\frac{\mu}{\sqrt{\mu^2 + |S_{\boldsymbol{k}}|^2}}(\epsilon_1 - m) \\
& \times \frac{1}{E_\alpha}\left(1 + \frac{m}{\sqrt{t^2|\gamma(\boldsymbol{k})|^2 + m^2}}\right) \\
& + \frac{1}{4}\frac{\mu}{\sqrt{\mu^2 + |S_{\boldsymbol{k}}|^2}}(\epsilon_2 - m) \\
& \times \frac{1}{E_\beta}\left(1 - \frac{m}{\sqrt{t^2|\gamma(\boldsymbol{k})|^2 + m^2}}\right), \qquad \text{(B.13)}
\end{aligned}
$$

and

$$
\begin{aligned}
C_{12}(\boldsymbol{k}) = & \frac{1}{2}e^{-i\phi_{\boldsymbol{k}}}\left(\alpha_+^2(\gamma_+^{(1)})^2 - |\alpha_-|^2|\gamma_-^{(1)}|^2 - i\alpha_+\gamma_+^{(1)}\right. \\
& \left.\times\left(\alpha_-^{(1)}\gamma_-^{(1)} + \left(\alpha_-^{(1)}\right)^*\left(\gamma_-^{(1)}\right)^*\right)\right)(\beta_+^2 - \beta_-^2) \\
& - \frac{1}{2}e^{-i\phi_{\boldsymbol{k}}}\left(\alpha_+^2(\gamma_+^{(2)})^2 - |\alpha_-|^2|\gamma_+^{(2)}|^2 - i\alpha_+\gamma_+^{(2)}\right. \\
& \left.\times\left(\alpha_-^{(1)}\gamma_-^{(2)} + \left(\alpha_-^{(1)}\right)^*\left(\gamma_-^{(2)}\right)^*\right)\right)(\beta_+^2 - \beta_-^2) \\
= & \frac{1}{4}e^{-i\phi_{\boldsymbol{k}}}\left(\left(\frac{\epsilon_1}{E_\alpha} - \frac{\epsilon_2}{E_\beta}\right)\right. \\
& \left. - i\,n\left(\frac{1}{E_\alpha} - \frac{1}{E_\beta}\right)\right)\frac{t|\gamma(\boldsymbol{k})|}{\sqrt{t^2|\gamma(\boldsymbol{k})|^2 + m^2}} \qquad \text{(B.14)}
\end{aligned}
$$

where $n = \frac{\mathrm{Re}(C_{\boldsymbol{k}})\mathrm{Re}(S_{\boldsymbol{k}}) + \mathrm{Im}(C_{\boldsymbol{k}})\mathrm{Im}(S_{\boldsymbol{k}})}{\sqrt{\mu^2 + |S_{\boldsymbol{k}}|^2}}$. Here, one should notice that $C_{11}(-\boldsymbol{k}) = C_{22}(\boldsymbol{k})$ and $C_{12}(\boldsymbol{k}) = (C_{12}(-\boldsymbol{k}))^*$.

Eigenvectors of the correlation matrix

$$
q_{\boldsymbol{k}\uparrow} = \delta_+(\boldsymbol{k})a_{\boldsymbol{k}\uparrow} + \delta_-(\boldsymbol{k})b_{\boldsymbol{k}\uparrow} \qquad \text{(B.15)}
$$

$$
r_{\boldsymbol{k}\uparrow} = \delta_+(-\boldsymbol{k})a_{\boldsymbol{k}\uparrow} - \delta_-^*(-\boldsymbol{k})b_{\boldsymbol{k}\uparrow} \qquad \text{(B.16)}
$$

where:

$$
\begin{aligned}
\delta_+(\boldsymbol{k}) &= \sqrt{\frac{1}{2}\left(1 + \frac{C_{11} - C_{22}}{\sqrt{(C_{11} - C_{22})^2 + 4|C_{12}|^2}}\right)} \\
\delta_-(\boldsymbol{k}) &= \frac{2C_{12}}{\sqrt{2\sqrt{(C_{11} - C_{22})^2 + 4|C_{12}|^2}w}} \qquad \text{(B.17)}
\end{aligned}
$$

with $w = (C_{11} - C_{22} + \sqrt{(C_{11} - C_{22})^2 + 4|C_{12}|^2})$.

Finally, we find that the correlation matrix obtained by tracing out one sublattice, B for example

$$
C(\boldsymbol{k}) = \begin{pmatrix} C_{11}(\boldsymbol{k}) & C_{13}(\boldsymbol{k}) \\ C_{13}^*(\boldsymbol{k}) & C_{33}(\boldsymbol{k}) \end{pmatrix} \qquad \text{(B.18)}
$$

with

$$
\begin{aligned}
C_{11}(\boldsymbol{k}) = & \frac{1}{2}\left(\alpha_+^2(\gamma_+^{(1)})^2 + |\alpha_-|^2|\gamma_-^{(1)}|^2 - i\alpha_+\gamma_+^{(1)}\right. \\
& \left.\times\left(\alpha_-\gamma_-^{(1)} - \alpha_-^*\left(\gamma_-^{(1)}\right)^*\right)\right)(\beta_+ - \sigma\beta_-)^2 \\
& + \frac{1}{2}\left(\alpha_+^2(\gamma_+^{(2)})^2 + |\alpha_-|^2|\gamma_-^{(2)}|^2 - i\alpha_+\gamma_+^{(2)}\right. \\
& \left.\times\left(\alpha_-\gamma_-^{(2)} - \alpha_-^*\left(\gamma_-^{(2)}\right)^*\right)\right)(\beta_+ + \sigma\beta_-)^2 \\
= & \frac{1}{2} + \frac{1}{4}\frac{\mu}{\sqrt{\mu^2 + |S_{\boldsymbol{k}}|^2}}(\epsilon_1 + m) \\
& \times \frac{1}{E_\alpha}\left(1 - \frac{m}{\sqrt{t^2|\gamma(\boldsymbol{k})|^2 + m^2}}\right) \\
& + \frac{1}{4}\frac{\mu}{\sqrt{\mu^2 + |S_{\boldsymbol{k}}|^2}}(\epsilon_2 + m) \\
& \times \frac{1}{E_\beta}\left(1 + \frac{m}{\sqrt{t^2|\gamma(\boldsymbol{k})|^2 + m^2}}\right), \qquad \text{(B.19)}
\end{aligned}
$$

$$
\begin{aligned}
C_{33}(\boldsymbol{k}) = & \frac{1}{2}\left(\alpha_+^2(\gamma_-^{(1)})^2 + |\alpha_-|^2|\gamma_+^{(1)}|^2 - i\alpha_+\gamma_+^{(1)}\right. \\
& \left.\times\left(\alpha_-\gamma_-^{(1)} - \alpha_-^*\left(\gamma_-^{(1)}\right)^*\right)\right)(\beta_+ + \sigma\beta_-)^2 \\
& + \frac{1}{2}\left(\alpha_+^2(\gamma_-^{(2)})^2 + |\alpha_-|^2|\gamma_+^{(2)}|^2 - i\alpha_+\gamma_+^{(2)}\right. \\
& \left.\times\left(\alpha_-\gamma_-^{(2)} - \alpha_-^*\left(\gamma_-^{(2)}\right)^*\right)\right)(\beta_+ - \sigma\beta_-)^2 \\
= & \frac{1}{2} - \frac{1}{4}\frac{\mu}{\sqrt{\mu^2 + |S_{\boldsymbol{k}}|^2}}(\epsilon_1 - m) \\
& \times \frac{1}{E_\alpha}\left(1 + \frac{m}{\sqrt{t^2|\gamma(\boldsymbol{k})|^2 + m^2}}\right) \\
& - \frac{1}{4}\frac{\mu}{\sqrt{\mu^2 + |S_{\boldsymbol{k}}|^2}}(\epsilon_2 - m) \\
& \times \frac{1}{E_\beta}\left(1 - \frac{m}{\sqrt{t^2|\gamma(\boldsymbol{k})|^2 + m^2}}\right), \qquad \text{(B.20)}
\end{aligned}
$$

and

$$
\begin{aligned}
C_{13}(\boldsymbol{k}) = & \frac{1}{2}\left(\alpha_+^2\left(\gamma_+^{(1)}\gamma_-^{(1)} - \gamma_+^{(2)}\gamma_-^{(2)}\right) - \left(\alpha_-^*\right)^2\left(\gamma_+^{(1)}\right.\right. \\
& \left.\left.\times(\gamma_-^{(1)})^* - \gamma_+^{(2)}(\gamma_-^{(2)})^*\right)\right)(\beta_+^2 - \beta_-^2) \\
= & \frac{1}{4}\left(\frac{1}{E_\alpha} - \frac{1}{E_\beta}\right)\frac{\mu}{\sqrt{\mu^2 + |S_{\boldsymbol{k}}|^2}} \\
& \times \frac{t|\gamma(\boldsymbol{k})|}{\sqrt{t^2|\gamma(\boldsymbol{k})|^2 + m^2}}C_{\boldsymbol{k}}^*. \qquad \text{(B.21)}
\end{aligned}
$$

References

1. B. Uchoa, A.H. Castro Neto, Phys. Rev. Lett. **98**, 146801 (2007)
2. A.M. Black-Schaffer, S. Doniach, Phys. Rev. B **75**, 134512 (2007)
3. C. Honerkamp, Phys. Rev. Lett. **100**, 146404 (2008)
4. S. Pathak, V.B. Shenoy, G. Baskaran, Phys. Rev. B **81**, 085431 (2010)
5. R. Nandkishore, L.S. Levitov, A.V. Chubukov, Nat. Phys. **8**, 158 (2011)
6. M. Kiesel, C. Platt, W. Hanke, D.A. Abanin, R. Thomale, Phys. Rev. B **86**, 020507(R) (2012)
7. W. S. Wang, Y.Y. Xiang, Q.-H. Wang, F. Wang, F. Yang, D.-H. Lee, Phys. Rev. B **85**, 035414 (2012)
8. M.V. Milovanović, S. Predin, Phys. Rev. B **86**, 195113 (2012)
9. J. Vučičević, M.O. Goerbig, M.V. Milovanović, Phys. Rev. B **86**, 214505 (2012)
10. O. Vafek, J.M. Murray, V. Cvetkovic, Phys. Rev. Lett. **112**, 147002 (2014)
11. A.M. Black-Schaffer, C. Honerkamp, J. Phys.: Condens. Matter **26**, 423201 (2014)
12. C. Platt, W. Hanke, R. Thomale, Adv. Phys. **62**, 453 (2013)
13. S. Ichinokura, K. Sugawara, A. Takayama, T. Takahashi, S. Hasegawa, ACS Nano **10**, 2761 (2016)
14. J. Chapman, Y. Su, C.A. Howard, D. Kundys, A.N. Grigorenko, F. Guinea, A.K. Geim, I.V. Grigorieva, R.R. Nair, Sci. Rep. **6**, 23254 (2016)
15. B.M. Ludbrook, G. Levy, P. Nigge, M. Zonno, M. Schneider, D.J. Dvorak, C.N. Veenstra, S. Zhdanovich, D. Wong, P. Dosanjh, C. Straßer, A. Stöhr, S. Forti, C.R. Ast, U. Starke, A. Damascelli, Proc. Natl. Acad. Sci. **112**, 11795 (2015)
16. M. Levin, X.-G. Wen, Phys. Rev. Lett. **96**, 110405 (2006)
17. A. Kitaev, J. Preskill, Phys. Rev. Lett. **96**, 110404 (2006)
18. H.-C. Jiang, Z. Wang, L. Balents, Nat. Phys. **8**, 902 (2012)
19. H. Li, F.D.M. Haldane, Phys. Rev. Lett. **101**, 010504 (2008)
20. N. Bray-Ali, L. Ding, S. Haas, Phys. Rev. B **80**, 180504 (2009)
21. A.M. Läuchli, E.J. Bergholtz, J. Suorsa, M. Haque, Phys. Rev. Lett. **104**, 156404 (2010)
22. H. Yao, X.-L. Qi, Phys. Rev. Lett. **105**, 080501 (2010)
23. E. Prodan, T.L. Hughes, B.A. Bernevig, Phys. Rev. Lett. **105**, 115501 (2010)
24. R. Thomale, A. Sterdyniak, N. Regnault, B.A. Bernevig, Phys. Rev. Lett. **104**, 180502 (2010)
25. A.M. Turner, Y. Zhang, A. Vishwanath, Phys. Rev. B **82**, 241102 (2010)
26. L. Fidkowski, Phys. Rev. Lett. **104**, 130502 (2010)
27. F. Pollmann, A.M. Turner, E. Berg, M. Oshikawa, Phys. Rev. B **81**, 064439 (2010)
28. M. Kargarian, G.A. Fiete, Phys. Rev. B **82**, 085106 (2010)
29. M. Hermanns, A. Chandran, N. Regnault, B.A. Bernevig, Phys. Rev. B **84**, 121309 (2011)
30. J. Dubail, N. Read, Phys. Rev. Lett. **107**, 157001 (2011)
31. N. Regnault, B.A. Bernevig, Phys. Rev. X **1**, 021014 (2011)
32. Z. Papić, B.A. Bernevig, N. Regnault, Phys. Rev. Lett. **106**, 056801 (2011)
33. T.L. Hughes, E. Prodan, B.A. Bernevig, Phys. Rev. B **83**, 245132 (2011)
34. X.-L. Qi, H. Katsura, A.W.W. Ludwig, Phys. Rev. Lett. **108**, 196402 (2012)
35. D. Poilblanc, N. Schuch, D. Perez-Garcia, J.I. Cirac, Phys. Rev. B **86**, 014404 (2012)
36. B. Swingle, T. Senthil, Phys. Rev. B **86**, 045117 (2012)
37. N. Regnault, arXiv:1510.07670 (2015)
38. N. Laflorencie, Phys. Rep. **643**, 1 (2016)
39. A. Chandran, V. Khemani, S.L. Sondhi, Phys. Rev. Lett. **113**, 060501 (2014)
40. H. Braganca, E. Mascarenhas, G.I. Luiz, C. Duarte, R.G. Pereira, M.F. Santos, M.C.O. Aguiar, Phys. Rev. B **89**, 235132 (2014)
41. R. Lundgren, J. Blair, M. Greiter, A. Läuchli, G.A. Fiete, R. Thomale, Phys. Rev. Lett. **113**, 256404 (2014)
42. D. Poilblanc, Phys. Rev. Lett. **105**, 077202 (2010)
43. J.I. Cirac, D. Poilblanc, N. Schuch, F. Verstraete, Phys. Rev. B **83**, 245134 (2011)
44. I. Peschel, M.-C. Chung, Europhys. Lett. **96**, 50006 (2011)
45. A.M. Läuchli, J. Schliemann, Phys. Rev. B **85**, 054403 (2012)
46. J. Schliemann, A.M. Läuchli, J. Stat. Mech. **2012**, P11021 (2012)
47. S. Tanaka, R. Tamura, H. Katsura, Phys. Rev. A **86**, 032326 (2012)
48. R. Lundgren, Y. Fuji, S. Furukawa, M. Oshikawa, Phys. Rev. B **88**, 245137 (2013)
49. X. Chen, E. Fradkin, J. Stat. Mech. **2013**, P08013 (2013)
50. R. Lundgren, Phys. Rev. B **93**, 125107 (2016)
51. J. Schliemann, Phys. Rev. B **83**, 115322 (2011)
52. J. Schliemann, New J. Phys. **15** 053017 (2013), Corrigendum: **15**, 079501 (2013)
53. J. Schliemann, J. Stat. Mech. **2014**, P09011 (2014)
54. R. Lundgren, V. Chua, G.A. Fiete, Phys. Rev. B **86**, 224422 (2012)
55. S. Predin, P. Wenk, J. Schliemann, Phys. Rev. B **93**, 115106 (2016)
56. T. Fukui, Y. Hatsugai, J. Phys. Soc. Jpn. **83**, 113705 (2014)
57. H. Araki, T. Kariyado, T. Fukui, Y. Hatsugai, arXiv:1602.02910 (2016)
58. D. Poletti, C. Miniatura, B. Gremaud, Europhys. Lett. **93**, 37008 (2011)
59. M. Sato, S. Fujimoto, J. Phys. Soc. Jpn. **85**, 072001 (2016)
60. A. Altland, M.R. Zirnbauer, Phys. Rev. B, **55**, 1142 (1997)
61. A.P. Schnyder, S. Ryu, A. Furusaki, A.W.W. Ludwig, Phys. Rev. B **78**, 195125 (2008)
62. I. Peschel, J. Phys. A: Math. Gen. **36**, L205 (2003)
63. S.-A. Cheong, C.L. Henley, Phys. Rev. B **69**, 075111 (2004)
64. J. Borchmann, A. Farrell, S. Matsuura, T. Pereg-Barnea, Phys. Rev. B **90**, 235150 (2014)
65. E.H. Kim, J. Phys.: Condens. Matter **26**, 205602 (2014)
66. A.M. Black-Schaffer, K. Le Hur, Phys. Rev. B **92**, 140503(R) (2015)
67. M.V. Milovanović, arXiv:1102.2576 (2011)

HL 83: Poster: Graphene (with MA/O)

Time: Wednesday 17:00–20:00 Location: P1

HL 83.1 Wed 17:00 P1

Semi-empirical phonon calculations for graphene on different substrates — •Henrique Miranda, Alejandro Molina-Sanchez, and Ludger Wirtz — Physics and Materials Science Research Unit, UNIVERSITÉ DU LUXEMBOURG, Luxembourg

We investigate the graphene-substrate interaction via changes in the phonon dispersion of graphene. Ab-initio calculations on these systems are of high computational cost due to the non-commensurability of the unit cells of graphene and the substrate. This leads to the formation of Moiré patterns with accordingly large supercell sizes. We use a semi-empirical force constant model for the calculation of phonons of graphene on different metallic and insulating substrates. The interaction of graphene with the substrate is described via suitably chosen spring constants. The phonon dispersion in the primitive unit cell of graphene is obtained via an "unfolding procedure" similar to the ones used for the discussion of ARPES (angular resolved photo-emission spectroscopy) of graphene on incommensurate substrates.

HL 83.2 Wed 17:00 P1

Bilayer graphene: topological phases and entanglement spectrum — •Sonja Predin and John Schliemann — Institute for Theoretical Physics,University of Regensburg, D-93040 Regensburg, Germany

We present a calculation of the entanglement spectrum of fermions in bilayer graphene. In particular, a non-trivial topological order of the Abelian phase of the time-reversal symmetry breaking d-wave state is studied. We show that the entanglement spectrum is gapped, additionally we show that edge excitations in the entanglement spectrum form doublet Dirac fields around every K point.

HL 83.3 Wed 17:00 P1

Ultrafast dynamics and photoluminescence of hot carriers in graphene — •Thomas Danz, Andreas Neff, Reiner Bormann, Sascha Schäfer, and Claus Ropers — IV. Physical Institute, University of Göttingen, 37077 Göttingen, Germany

The ultrafast dynamics of optically excited carriers in graphene can be monitored by pump-probe spectroscopy [1,2]. Furthermore, it was recently shown that the thermalization of hot carriers leads to photoluminescence at wavelengths far away from the exciting pump [3,4]. Here, we present the implementation of an experimental setup which combines transient spectroscopy with sub-15-fs temporal resolution with hot carrier photoluminescence detection under the same excitation conditions. With this approach, we aim at a comprehensive picture of the ultrafast carrier response and the disentanglement of the timescales underlying different relaxation pathways. First experimental results will be presented.

[1] J. M. Dawlaty *et al.*, Appl. Phys. Lett. **92**, 042116 (2008)
[2] M. Breusing *et al.*, Phys. Rev. B. **83**, 153410 (2011)
[3] C. H. Lui *et al.*, Phys. Rev. Lett. **105**, 127404 (2010)
[4] W. Liu *et al.*, Phys. Rev. B. **82**, 081408 (2010)

HL 83.4 Wed 17:00 P1

Electron spin resonance of ion-irradiation induced single vacancies on monolayer graphene characterized by scanning tunneling spectroscopy — •Sven Just[1], Stephan Zimmermann[2], Vladislav Kataev[2], Marco Pratzer[1], Bernd Büchner[2], and Markus Morgenstern[1] — [1]II. Physikalisches Institut B, RWTH Aachen — [2]Leibniz-Institut für Festkörper- und Werkstoffforschung, Dresden

Single vacancies with densities of $0.003/\mathrm{nm}^2 - 3/\mathrm{nm}^2$ are prepared on HOPG and on single layer graphene on SiO_2 produced by chemical vapour deposition using Ar ions with 50 eV kinetic energy. The vacancies exhibit a peak at E_F in scanning tunneling spectroscopy, which survives 3 h of air exposure, afterwards a small broadening of the peak is observed. Electron spin resonance shows a peak corresponding to g = 2.0022, if the defect density is above $0.3/\mathrm{nm}^2$, and a peak width of 10 G with an anisotropy below 0.5 G between in-plane and out-of-plane magnetic field. The peak width hardly depends on temperature, while the peak intensity decreases with increasing temperature in the range of 4 K - 20 K.

HL 83.5 Wed 17:00 P1

Enhancing the Raman signal of graphene on SiC(0001) by using a solid immersion lens in *top-down* geometry — •Felix Fromm[1], Martin Hundhausen[2], Michl Kaiser[3], Julia Krone[1], and Thomas Seyller[1] — [1]TU Chemnitz, Institut für Physik — [2]FAU Erlangen-Nürnberg, Lehrstuhl für Laserphysik — [3]FAU Erlangen-Nürnberg, Lehrstuhl für Werkstoffwissenschaften

We present a study of epitaxial graphene by recording Raman spectra from the backside through the silicon carbide (SiC) substrate. In that *top-down* geometry we profit from the fact, that the graphene layer emits approximately 96 % of the Raman intensity into the SiC [1]. However, we only observe an intensity enhancement of approximately a factor of 4 compared to the conventional *top-up* geometry. This is because the solid angle of detection is decreased by refraction at the SiC/air interface and is limited by the total internal reflection. To further improve the detection efficiency, we use a high refractive index solid immersion lens (SIL) made of cubic zirconia combined with a suitable immersion liquid. By that, the angle of total internal reflection, as well as the solid angle of detection are increased. We eventually observe an increase of the detected Raman intensity towards the *top-up* geometry to a factor of 25. As an additional advantage, the background signal of the two-phonon Raman modes of the SiC is suppressed to a large extent.

[1] F. Fromm et al., New J. Phys. 15, 113006 (2013)

HL 83.6 Wed 17:00 P1

Growth of graphene on 6H-SiC(0001) under ammonia/argon atmosphere — •Christian Raidel, Felix Fromm, Samir Mammadov, Martina Wanke, and Thomas Seyller — TU Chemnitz, Insitut für Physik, Germany

In this work we investigated the nitrogen incorporation into epitaxial grown monolayer graphene by using ammonia as process gas within argon flow during thermal decomposition of SiC. The growth parameters as temperature and ammonia concentration were studied by various surface sensitive methods as XPS, LEED, RAMAN, AFM, and STM. ARPES shows that the ammonia grown graphene shows more p-type doped graphene than undoped graphene on SiC(0001). Due to the dissociation of ammonia during the growth process etch pits are produced. Vacancy associated nitrogen incorporation was observed by XPS and STM.

HL 83.7 Wed 17:00 P1

Characterization and transfer of 2D dichalcogenides produced by anodic bonding — •Philipp Nagler, Gerd Plechinger, Christian Schüller, and Tobias Korn — Institut für Experimentelle und Angewandte Physik, Universität Regensburg, 93040 Regensburg, Germany

Atomically thin MoS_2 and WS_2 structures have attracted growing attention as promising 2D semiconductors. As monolayers, both materials exhibit a direct bandgap and therefore are suitable candidates for future opto-electronical devices. We produced singlelayer MoS_2 and WS_2 by means of anodic bonding. In this process, the material is bonded by electrostatic forces on a borosilicate glass substrate. Compared to mechanical exfoliation, this technique usually yields larger flakes. Anodic bonded MoS_2 flakes were characterized by Raman and photoluminescence (PL) spectroscopy. Performing low-temperature PL measurements, we observed similar behaviour as in SiO_2-supported MoS_2. Furthermore, PL measurements for anodic bonded WS_2 are presented. By applying the wedging transfer technique, we transferred anodic bonded monolayer WS_2 from the glass to a SiO_2 substrate. Additionally, using this method, heterostructures consisting of various 2D materials could be produced and characterized.

HL 83.8 Wed 17:00 P1

Graphene nanostructures produced from transfered layers — •Christopher Belke, Dmitri Smirnov, Johannes C. Rode, Hennrik Schmidt, and Rolf J. Haug — Institut für Festkörperphysik, Leibniz Universität Hannover, D-30167 Hannover, Germany

Graphene consists of carbon atoms, which are arranged in a two-dimensional honeycomb lattice. It has unique electronic properties, which can be examined in high quality samples [1]. These are often

prepared by mechanical exfoliation on a silicon wafer with silicon dioxide on top. This substrate has a strong influence on the transport properties due to charge traps and surface roughness [2]. To reduce these effects or to produce novel complexe layersystems, graphene sheets can be stacked by a transfer methode e. g. onto other substrates or one upon the other to fabricate twisted flakes. The latter has been done and was under examination with magnetotransport measurements. Graphene is exfoliated on a thin PMMA layer, which can be detached from the silicon wafer. This layer is then placed on another graphene mono- or bilayer flakes. The samples were characterized at low temperatures and in dependence of a magnetic field. Magnetic field independent oscillations could be observed in a multilayer system.

[1] K. S. Novoselov et al. Science **306**, 666 (2004)
[2] P. Barthold et al. NJP **13**, 0433020 (2011)

HL 83.9 Wed 17:00 P1

Twisted graphene bilayers, folded via atomic force microscope — •Johannes C. Rode, Dmitri Smirnov, Christopher Belke, and Rolf J. Haug — Institut für Festkörperphysik, Leibniz Universität Hannover

Naturally occurring double-layer graphene consists of two hexagonal lattices in Bernal stacking. We investigate the folding of single-layer graphene via atomic force microscope (AFM) and the electronic properties of thusly created bilayers. The crystal lattices of these are twisted against each other which affects the interlayer coupling, giving rise to interesting electronic properties like a screening effect and reduced Fermi velocities at higher twist angles. Furthermore, the influence of a moiré-superlattice or twist induced van-Hove-singularities can be expected at lower twist angles. Our samples are obtained by micromechanical cleavage of natural graphite and placed on a silicon substrate with a top layer of silicon dioxide. The atomic force microscope then serves as a tool to mechanically manipulate the sample by programmed tip movements. We show AFM-induced folding of graphene on a μm-scale which can afterwards be contacted via e-beam lithography. Magnetotransport measurements over the folded areas show interesting signatures like multiple origins of landau fans in the charge carrier concentration.

HL 83.10 Wed 17:00 P1

The Effect of the Chemical Potential of Graphene on THz Detection — •Markus Göthlich[1], Fathi Gouider[1], André Müller[2], Yuri B. Vasilyev[3], and Georg Nachtwei[1] — [1]Institut für Angewandte Physik, Technische Universität Braunschweig, Mendelssohnstraße 2, D-38106 Braunschweig — [2]Physikalisch Technische Bundesanstalt, Bundesallee 100, D-38116 Braunschweig — [3]A.F.Ioffe Physical Technical Institute, RU-194021 St.Petersburg, Russia

One particular fact about graphene is its remarkable Landau quantization $E_n = \mathrm{sgn}(n)\sqrt{\Delta^2 + 2\hbar e v_F^2 |n|B}$ with n being the Landau level (LL) index. This would allow a transition at 2.4 THz (corresponding to an energy of about 10 meV) to happen at a magnetic field as low as 0.2 T. But theoretical investigations show the opening of a bandgap and a high chemical potential in epitaxial graphene on Si-face SiC due to graphene–substrate interactions. On the other hand our calculations—based on Gusynin et al. Phys. Rev. Lett. 98, 157402 (2007)—show that at high chemical potential the photoresponse can only be observed at higher magnetic fields of some Tesla. Gating is difficult due to the insolating behaviour of SiC substrate on the one hand and THz intransparency of top gates on the other hand. Therefore our aim is to design a new sample geometry that allows the manipulation of the chemical potential of the graphene while not blocking the THz radiation before reaching the detector.

HL 83.11 Wed 17:00 P1

Gate-controlled STM study of magnetic impurities on a graphene surface — •Paul Punke[1], Christian Dette[1], Roberto Urcuyo[1], Christopher Kley[1], Sören Krotzky[1], Rico Gutzler[1], Marko Burghard[1], Soon Jung Jung[1], and Klaus Kern[1,2] — [1]Max-Planck-Institute for Solid State Research, Heisenbergstr. 1, 70569 Stuttgart, Germany — [2]Institut de Physique de la Matière Condensée, Ecole Polytechnique Fédérale de Lausanne, CH-1015 Lausanne, Switzerland

Graphene has been regarded as an ideal material for post silicon electronic application due to its unique electronic properties. To realize a field effect transistor for logic applications out of graphene, there has been a lot of effort to understand the gating effect on the charge-carrier-density-dependent properties of graphene, such as electronic scattering, spin based phenomena and collective excitations. We have designed a gatable low temperature scanning tunneling microscope (STM) by adding contacts to the sample holder. To prepare the gate-tunable graphene devices, we use graphene grown by chemical vapor deposition (CVD), transferred with or without a supporting layer of polymethylmethacrylate (PMMA) or polystyrene (PS), on an insulating layer of SiO2 or hexagonal boron nitride (h-BN) on SiO2. We also grow the graphene on h-BN directly on Ni substrate by CVD method. The quality of these samples will be compared by means of optical microscopy, atomic force microscopy (AFM), Raman spectroscopy and STM. Finally, we will present the gate-controlled electronic structure of graphene.

HL 83.12 Wed 17:00 P1

Ion Implantation of Graphene - Toward IC Compatible Technologies — •H. Hofsäss[1], U. Bangert[2,3], W. Pierce[2], D. M. Kepaptsoglou[3], Q Ramasse[3], R Zan[1], M. H. Gass[3,4], J.A. van den Berg[5], C. Boothroyd[6], and J Amani[1] — [1]II. Physikalisches Institut, Georg-August-Universität Göttingen, Göettingen, Germany — [2]School of Materials, The University of Manchester, Manchester, United Kingdom — [3]SuperSTEM Laboratory, Daresbury, United Kingdom — [4]AMEC, Walton House, 404 The Quadrant, Birchwood, United Kingdom — [5]School of Computing, Science and Engineering, University of Salford, Salford, United Kingdom — [6]Ernst Ruska-Centre for Microscopy and Spectroscopy, Juelich Research Centre, Juelich, Germany

Doping of graphene via ultra low energy ion implantation could open possibilities for fabrication of nanometer-scale patterned graphene-based devices as well as for graphene functionalization compatible with large-scale integrated semiconductor technology. Using advanced electron microscopy/spectroscopy methods, we show for the first time directly that graphene can be doped with B and N via ion implantation of mass selected ions at energies of 20 - 30 eV and that the retention is in good agreement with predictions from calculation-based literature values. Atomic resolution high-angle dark field imaging (HAADF) combined with single-atom electron energy loss (EEL) spectroscopy reveals that for sufficiently low implantation energies ions are predominantly substitutionally incorporated into the graphene lattice with a very small fraction residing in defect-related sites.

TT 44: Transport: Graphene (Joint session of DS, DY, HL, MA, O and TT organized by TT)

Time: Wednesday 9:30–13:15 Location: H22

Invited Talk TT 44.1 Wed 9:30 H22

Ultrafast photo-thermoelectric currents in graphene — •Alexander Holleitner — Walter Schottky Institut and Physics Department, Technical University of Munich, Am Coulombwall 4a, D-85748 Garching, Germany.

We show that photo-thermoelectric currents occur on a picosecond time-scale in graphene [1]. To this end, we apply an on-chip pump/probe photocurrent spectroscopy [2,3] to double-gated junctions of graphene. Our experiments reveal the interplay of photogenerated hot electrons with so-called photovoltaic currents. Moreover, we demonstrate that hot electrons allow to read-out an ultrafast non-radiative energy transfer from fluorescent emitters, namely nitrogen-vacancy centers in nano-diamonds. The non-radiative energy transfer can be exploited as an ultrafast, electronic read-out process of the electron spin in nitrogen vacancy centers in the diamond nanocrystals. The detection gives access to fast energy transfer processes, which have not yet been observed by fluorescence measurements because of quenching of the optical signal for short transfer distances [4].

We thank A. Brenneis, F. Schade, L. Gaudreau, M. Seifert, H. Karl, M.S. Brandt, H. Huebl, J.A. Garrido, F.H.L. Koppens, for a very fruitful collaboration, and the ERC-grant 'NanoREAL' for financial support.

[1] A. Brenneis et al., (2016)
[2] L. Prechtel et al., Nature Comm. **3**, 646 (2012)
[3] C. Kastl et al. Nature Comm. **6**, 6617 (2015)
[4] A. Brenneis et al. Nature Nanotech. **10**, 135 (2015)

TT 44.2 Wed 10:00 H22

Double-logarithmic velocity renormalization at the Dirac points of graphene — •Peter Kopietz, Anand Sharma, and Carsten Bauer — Institut für Theoretische Physik, Universität Frankfurt, Max-von-Laue Str. 1, 60438 Frankfurt

Using a functional renormalization group approach with partial bosonization in the forward scattering channel we reconsider the effect of long-range Coulomb interactions on the quasi-particle velocity v_k close to the Dirac points of graphene. In contrast to calculations based on perturbation theory and field theoretical renormalization group methods, we find that v_k is proportional to $\ln[\kappa_k/k]$ where k is the deviation of the quasiparticle momentum from the Dirac points and the cutoff scale κ_k vanishes logarithmically for small k. We show that this double-logarithmic singularity is compatible with experiments and with the known three-loop expansion of v_k which contains terms of order $\ln k$ and $\ln^2 k$.

TT 44.3 Wed 10:15 H22

Dirac fermion wave packets in oscillating potential barriers — Walter Pötz[1], Sergey E. Savel'ev[2], Peter Hänggi[3], and •Wolfgang Häusler[3] — [1]Karl Franzens Univ. Graz, Inst. Phys., A-8010 Graz, Austria — [2]Department of Physics, Loughborough University, Loughborough LE11 3TU, United Kingdom — [3]Institut für Physik, Univ. Augsburg, 86135 Augsburg, Germany

We integrate the time-dependent (2+1)D Dirac equation for massless fermions in graphene or topological insulator surfaces. A recently developed staggered-grid leap-frog scheme is employed [1,2]. We consider an initial Gaussian wave packet which moves in the x-direction towards a potential barrier that is homogeneous along y and oscillates periodically in time. As for the x-dependence, we investigate square-well, sinusoidal, and linear-ramp potential profiles. Small transversal momentum components k_y of the wave packet were analyzed analytically [3] and predicted to generate non-zero current densities j_y, even at normal incidence $k_y = 0$ [4]. These findings are consistent with the present numerical studies of particle-, current-, and spin-density. We also investigate massive fermions: regarding some properties they resemble massless fermions, regarding other properties, however, peculiar intrinsic oscillations, reminiscent of Zitterbewegung, appear.

[1] R. Hammer and W. Pötz, PRB **88**, 235119 (2013)
[2] R. Hammer *et al.*, J. Comp. Phys. **265**, 50 – 70 (2014)
[3] S.E. Savel'ev, W. Häusler, and P. Hänggi, PRL **109**, 226602 (2012)
[4] S.E. Savel'ev, W. Häusler, and P. Hänggi, EPJB **86**, 433 (2013).

TT 44.4 Wed 10:30 H22

Electric and magnetic control of electron guiding in graphene — •Ming-Hao Liu and Klaus Richter — Institut für Theoretische Physik, Universität Regensburg

Electrons in graphene are known to behave like massless Dirac fermions, whose transport properties can be best revealed by experiments using ultra-clean graphene. Reliable quantum transport simulations for ballistic graphene is naturally a powerful tool for understanding and predicting high-quality transport experiments. In this talk we show gate-controlled electron guiding along electrically confined channels in suspended graphene, which is a combined work of our transport simulations and the experiment done by the Schönenberger group [1]. We have recently further applied our simulation (Green's function method within the scalable tight-binding model [2]) to revisit the transverse magnetic focusing experiment [3], where the guiding of the electrons is controlled by an external magnetic field, instead of electrical gates. Besides good agreement with the experiments [1,3], our simulations further allow for probing charge flow through an additional scanning probe tip.

[1] P. Rickhaus *et al.*, Nano Lett. **15**, 5819 (2015).
[2] M.-H. Liu *et al.*, Phys. Rev. Lett. **114**, 036601 (2015).
[3] T. Taychatanapat *et al.*, Nat. Phys. **9**, 225 (2013).

TT 44.5 Wed 10:45 H22

Current flow paths in deformed graphene: from quantum transport to classical trajectories in curved space — •Nikodem Szpak[1] and Thomas Stegmann[1,2] — [1]Fakultät für Physik, Universität Duisburg-Essen, Duisburg — [2]Instituto de Ciencias Fisicas, Universidad Nacional Autonoma de Mexico, Cuernavaca

We compare two contrasting approaches to the electronic transport in deformed graphene: a) the condensed matter approach in which current flow paths are obtained by applying the non-equilibrium Green's function (NEGF) method to the tight-binding model with local strain, b) the general relativistic approach in which classical trajectories of relativistic point particles moving in a curved surface with a pseudo-magnetic field are calculated. The connection between the two is established in the long-wave limit via an effective Dirac Hamiltonian in curved space. Geometrical optics approximation, applied to focused current beams, allows us to directly compare the wave and the particle pictures. We obtain very good numerical agreement between the quantum and the classical approaches for a fairly wide set of parameters. The presented method offers an enormous reduction of complexity from irregular tight-binding Hamiltonians defined on large lattices to geometric language for curved continuous surfaces. It facilitates a comfortable and efficient tool for predicting electronic transport properties in graphene nanostructures with complicated geometries, paving the way to new interesting transport phenomena such as bending or focusing (lensing) of currents depending on the shape of the deformation. It can be applied in designing ultrasensitive sensors or in nanoelectronics.

TT 44.6 Wed 11:00 H22

Trigonal Warping in Bilayer Graphene: Energy versus Entanglement Spectrum — •Sonja Predin, Paul Wenk, and John Schliemann — Institute for Theoretical Physics, University of Regensburg, D-93040 Regensburg, Germany

We present a mainly analytical study of the entanglement spectrum of Bernal-stacked graphene bilayers in the presence of trigonal warping in the energy spectrum. Upon tracing out one layer, the entanglement spectrum shows qualitative geometric differences to the energy spectrum of a graphene monolayer. However, topological quantities such as Berry phase type contributions to Chern numbers agree. The latter analysis involves not only the eigenvalues of the entanglement Hamiltonian but also its eigenvectors. We also discuss the entanglement spectra resulting from tracing out other sublattices.

15 min. break

TT 44.7 Wed 11:30 H22

Valley-based Cooper pair splitting via topologically confined channels in bilayer graphene — •Alexander Schroer[1], Peter G. Silvestrov[1], and Patrik Recher[1,2] — [1]Institut für Mathematische Physik, Technische Universität Braunschweig, D-38106

Braunschweig, Germany — [2]Laboratory for Emerging Nanometrology Braunschweig, D-38106 Braunschweig, Germany

Bilayer graphene hosts valley-chiral one-dimensional modes at domain walls between regions of different interlayer potential or stacking order. When such a channel is close to a superconductor, the two electrons of a Cooper pair, which tunnel into it, move in opposite directions because they belong to different valleys related by the time-reversal symmetry. This kinetic variant of Cooper pair splitting requires neither Coulomb repulsion nor energy filtering but is enforced by the robustness of the valley isospin in the absence of atomic-scale defects. We derive an effective normal/superconducting/normal (NSN) model of the channel in proximity to an *s*-wave superconductor, calculate the conductance of split and spin-entangled pairs, and interpret it as a result of *local* Andreev reflection, in contrast to the widespread identification of Cooper pair splitting with crossed Andreev reflection in an NSN geometry.

TT 44.8 Wed 11:45 H22

The decisive role of stacking faults for understanding transport in bilayer graphene — •Heiko B. Weber[1], Ferdinand Kisslinger[1], Christian Ott[1], and Sam Shallcross[2] — [1]Lehrstuhl für Angewandte Physik, FAU Erlangen-Nürnberg (FAU), Erlangen, Germany — [2]Lehrstuhl für Theoretische Festkörperphysik, FAU Erlangen-Nürnberg (FAU)

Charge transport in bilayer graphene provides rich low-temperature phenomena, often assigned to interaction-driven phase transitions. We will discuss charge transport in bilayer graphene in a single-particle picture, but including stacking faults. Such partial dislocations are unavoidable in bilayer graphene and were recently imaged [1]. Depending on details, partial dislocations can introduce improved conductance, fully insulating behaviour or linear magnetoresistance. The latter is reliably found in transport experiments at elevated temperatures [2].

[1] B. Butz, C. Dolle, F. Niekiel, K. Weber, D. Waldmann, H. B. Weber, B. Meyer, E. Spiecker, Nature **505**, 533 (2014)
[2] F. Kisslinger, C. Ott, C. Heide, E. Kampert, B. Butz, E. Spiecker, S. Shallcross, H. B. Weber, Nature Phys. **11**, 650 (2015).

TT 44.9 Wed 12:00 H22

Linear magnetoresistance in two-dimensional disordered conductors — •Ferdinand Kisslinger[1], Christian Ott[1], Erik Kampert[2], and Heiko B. Weber[1] — [1]Lehrstuhl für Angewandte Physik, FAU Erlangen-Nürnberg (FAU), Erlangen, Germany. — [2]Dresden High Magnetic Field Laboratory, Helmholtz-Zentrum Dresden-Rossendorf, Dresden, Germany.

The recent observation of linear magnetoresistance (MR) in large-area bilayer graphene gives a key to the understanding of this old and barely understood phenomenon [1]. In bilayer graphene, it can be traced back to mosaic-like pattern of a partial dislocation network [2]. In this talk we discuss how linear MR evolves in disordered samples, using a two dimensional resistor network model conceptually introduced by Parish and Littlewood [3]. This model is in the weak disorder regime dominated by boundary effects. We identified a new regime representing the bulk situation in a disordered conductor. We investigated different possible sources of disorder: mobility, charge carrier density and network structure. The slope of the MR turned out to be simply governed by the Hall resistance and therefore by the inverse of the charge carrier density. An equivalent circuit model finally gives a consistent explanation as to why the magnetoresistance is linear in mosaic like samples.

[1] F. Kisslinger et al., Nature Physics **11**, 650 (2015)
[2] B. Butz et al., Nature **505**, 533 (2014).
[3] M. M. Parish & P. B. Littlewood, Nature **426**, 162 (2003)

TT 44.10 Wed 12:15 H22

Mechanically strained graphene nanojunctions — •Seddigheh Nikipar[1], Dmitry Ryndyk[1], and Gianaurelio Cuniberti[1,2] — [1]Institute for Materials Science and Max Bergmann Center of Biomaterials, TU Dresden, Germany — [2]Dresden Center for Computational Materials Science (DCMS), TU Dresden, Germany

It has been demonstrated recently that mechanically strained graphene presents interesting electrical properties, which have great potential for novel applications in electronic devices. In particular, the strain in graphene nanoribbons can lead to substantial changes in its electronic properties. Besides, it provides a possibility to develop atomic point contacts and break junctions. The main purpose of this work is to investigate theoretically the influence of uniaxial mechanical strains on graphene nanojunctions in order to design graphene point contact.

To this aim, we developed the computational model by combining density functional theory and molecular dynamics methods. First, we investigated the change of the junction shape with increasing strain and the breaking with the formation of the nanogap. As expected, our theoretical model predicts the deformation of the break junction bottleneck into carbon chains before the rupture of the structure. we evaluated the electronic transmission function of graphene quantum junction by employing a coupled tight bonding and nonequilibrium green function methods. Interestingly it is found that graphene point contact can present resonance transmission in contrast to the conventional metallic point contacts with quantized conductance. This might be originated from influence of other parameters on transmission.

TT 44.11 Wed 12:30 H22

Graphene nanoribbons as effective spin ladders — •Cornelie Koop, Manuel J. Schmidt, and Stefan Wessel — Institut für Theoretische Festkörperphysik, RWTH Aachen University

Zigzag edges of graphene nanoribbons host particular, localized edge states. Since the density of states is strongly enhanced near the edges in graphene, interaction effects between the spins of these edge states become important. We can significantly simplify the analysis of such systems by means of an effective model that separates the edge and bulk states. Treating the effective interactions to first order proves sufficient in most cases, while second order corrections do not dramatically change the results. In many cases, the edge system can be reduced to a general spin ladder model, where the decay of the spin-spin interaction is determined by the shape of the edges. We examine these effective spin ladders at finite temperatures by means of quantum Monte Carlo simulations, using the stochastic series expansion method. Thereby, correlation functions and spin structure factors can be determined for realistically large graphene nanoribbons.

TT 44.12 Wed 12:45 H22

Edge State Structure of the $\nu = 0$ quantum Hall State in monolayer Graphene — •Angelika Knothe[1,2] and Thierry Jolicoeur[2] — [1]Physikalisches Institut, Albert-Ludwigs-Universität Freiburg, Hermann-Herder-Str. 3, 79104 Freiburg — [2]Université Paris 11, CNRS, LPTMS, UMR 8626, Orsay 91405 France

Single-layer graphene at neutrality under a magnetic field is a many-body insulator whose phase structure is under intense scrutiny. When tilting the applied magnetic field, there is a phase transition towards a conducting state [1]. A plausible description is to start from a SU(4) spin-valley symmetric quantum Hall ferromagnet and add some lattice-scale anisotropies in valley space [2]. In the manifold of ground states captured by this approach, it has been proposed that graphene undergoes a transition between a canted antiferromagnetic state and a ferromagnetic state. While this picture is clear in the bulk of the system, it remains to understand the effect of this phase change on the current-carrying edge states that are formed a the physical boundaries of a real sample [3]. We use an extended Hartree-Fock approach to describe a finite-size system with a simple model for the edge and extract the one-body spectrum. We then describe the current-carrying edge textures.

[1] A. F. Young et al., Nature (London) 505, 528 (2014) [2] M. Kharitonov, Phys. Rev. B 85, 155439 (2012) [3] M. Kharitonov, Phys. Rev. B 86, 075450 (2012); G. Murthy et al., Phys. Rev. B 90, 241410 (2014) and arXiv:1510.04255; A. Knothe and T. Jolicoeur, Phys. Rev. B 92, 165110 (2015)

TT 44.13 Wed 13:00 H22

Spin lifetimes exceeding 12 ns in graphene non-local spin valves at room temperature — •Christopher Franzen[1], Marc Drögeler[1], Frank Volmer[1], Tobias Pohlmann[1], Maik Wolter[1], Kenji Watanabe[2], Takashi Taniguchi[2], Christoph Stampfer[1], and Bernd Beschoten[1] — [1]2nd Institute of Physics and JARA-FIT, RWTH Aachen University, 52074 Aachen, Germany — [2]National Institute for Materials Science, 1-1 Namiki, Tsukuba, 305-0044, Japan

We present spin transport measurements on graphene non-local spin transport devices by fabricating the electrodes first and subsequently transfer graphene with hexagonal boron nitride on top [1]. We achieve spin lifetimes of 12.6 ns and a spin diffusion length as high as 30 μm at room temperature.

This improvement exceeds all current models for contact-induced spin dephasing which paves the way towards probing intrinsic spin properties of graphene. Furthermore, we investigate the contact properties

of our devices using scanning force microscopy (SFM) and conductive SFM. We discuss the importance of using large area hexagonal boron nitride for the transfer process and for achieving such high spin lifetimes and spin diffusion lengths.

[1] M. Drögeler *et al.* Nano Letters **14**, 6050 (2014).

TT 101: Low-Dimensional Systems: Topological Order 2 (jointly with DS, HL, MA, O)

Time: Thursday 15:00–18:30 Location: H 3010

TT 101.1 Thu 15:00 H 3010

Topological entropy in the classical toric code model — •Johannes Helmes and Simon Trebst — Institut für Theoretische Physik, Universität zu Köln, Germany

For interacting quantum many-body systems the study of entanglement entropies is well established to analyze the fundamental nature of their ground states. In particular, the O(1) correction to the prevalent boundary-law can be used to identify topological order. However, not only in quantum systems, but also in classical systems we can track topological contributions to the classical entropy by employing an analogous approach.

We report results for the classical toric code model in a magnetic field which has a topologically protected zero field degeneracy. We show, how the classical entropy tracks the break-down of the classical topological order upon increasing the external field or temperature. In more technical terms, we apply the replica technique to calculate Renyi entropies from classical Monte Carlo simulations using a newly developed update scheme for efficient loop-gas sampling.

TT 101.2 Thu 15:15 H 3010

Symmetry fractionalization in SU(2n) antiferromagnetic Heisenberg chains — •Andreas Weichselbaum[1] and Thomas Quella[2] — [1]Ludwig Maximilians University, Munich, Germany — [2]University of Cologne, Germany

We explore generalizations of the Affleck-Kennedy-Lieb-Tasaki (AKLT, 1987) model for spin-1 antiferromagnetic Heisenberg chains to higher-rank SU(2n) symmetries. In particular we show that by proper tuning of higher order spin interactions there also exist exact low-dimensional matrix-product ground states with fractionalized edge states. These states are adiabatically connected to the ground state of the plain SU(2n) Heisenberg model. The parameter space is explored using state of the art density matrix renormalization group (DMRG), explicitly utilizing SU(N) symmetry up to N=6 based on the QSpace tensor library.

TT 101.3 Thu 15:30 H 3010

Protection of topological phases by quantum deformed symmetries — •Thomas Quella — Universität zu Köln, Institut für Theoretische Physik, Köln, Germany

We show that topological phases of quantum spin systems may enjoy protection even in the absence of ordinary group symmetries. The relevant mechanism is explained in full detail for the example of 1D spin chains with quantum group (q-deformed) symmetry $SO_q(3)$. We also sketch the generalization to quantum deformations of other continuous Lie groups such as those associated with $SU(N)$ or $SO(N)$. Our results provide a complete classification of quantum group symmetry protected topological phases for real values of q.

TT 101.4 Thu 15:45 H 3010

Topological phase transition in the quench dynamics of a Fermi gas — •Pei Wang — Department of Physics, Zhejiang University of Technology, Hangzhou 310023, China and Institute for Theoretical Physics, University of Goettingen, German

We study the quench dynamics of a one-dimensional ultracold Fermi gas with synthetic spin-orbit coupling. At equilibrium, the ground state of the system can undergo a topological phase transition and become a topological superfluid with Majorana edge states. As the interaction is quenched near the topological phase boundary, we identify an interesting dynamical phase transition of the quenched state in the long-time limit, characterized by an abrupt change of the pairing gap at a critical quenched interaction strength. We further demonstrate the topological nature of this dynamical phase transition from edge-state analysis of the quenched states. Our findings provide interesting clues for the understanding of topological phase transitions in dynamical processes, and can be useful for the dynamical detection of Majorana edge states in corresponding systems.

TT 101.5 Thu 16:00 H 3010

Diagnosing the statistics of excitations from the dynamical structure factor — •Siddhardh Morampudi[1], Ari Turner[2], and Frank Pollmann[1] — [1]Max-Planck-Institut für Physik komplexer Systeme, Dresden, Germany — [2]Department of Physics and Astronomy, The Johns Hopkins University, Baltimore, Maryland

We show that the statistics of excitations in quantum spin liquids yield characteristic features in the dynamical structure factor. Quantum spin liquids are exotic phases of matter which fall beyond the traditional paradigm of symmetry breaking. Originally proposed by Anderson with regard to high temperature superconductivity, they are now widely believed to arise in frustrated spin systems such as the antiferromagnetic Heisenberg model on the kagome lattice. Recently, various theoretical methods to characterize spin liquids have been introduced, especially with regard to numerical simulations. In this work, we obtain results connecting the statistics of the excitations to features of the dynamical structure factor which can be obtained from neutron scattering. We furthermore demonstrate how the results can be used to distinguish different types of gapped spin liquids.

TT 101.6 Thu 16:15 H 3010

Dissipative Chern Insulators — •Jan Carl Budich[1,2], Peter Zoller[1,2], and Sebastian Diehl[3] — [1]Institute for Theoretical Physics, University of Innsbruck, 6020 Innsbruck, Austria — [2]Institute for Quantum Optics and Quantum Information, Austrian Academy of Sciences, 6020 Innsbruck, Austria — [3]Institute of Theoretical Physics, TU Dresden, D-01062 Dresden, Germany

Engineered dissipation can be employed to prepare interesting quantum many body states in a non-equilibrium fashion. The basic idea is to obtain the state of interest as the unique steady state of a quantum master equation, irrespective of the initial state. Due to a fundamental interference of topology and locality, the dissipative preparation of gapped topological phases with a non-vanishing Chern number has so far remained elusive. Here, we study the open quantum system dynamics of fermions on a two-dimensional lattice in the framework of a Lindblad master equation. In particular, we discover a novel mechanism to dissipatively prepare a topological steady state with non-zero Chern number by means of short-range system bath interaction. Quite remarkably, this gives rise to a stable topological phase in a non-equilibrium phase diagram. We demonstrate how our theoretical construction can be implemented in a microscopic model that is experimentally feasible with cold atoms in optical lattices.

TT 101.7 Thu 16:30 H 3010

Absence of an interaction driven Chern insulating phase on the honeycomb lattice — •Johannes Motruk, Adolfo G. Grushin, and Frank Pollmann — Max-Planck-Institut für Physik komplexer Systeme, Dresden, Deutschland

Mean field calculations in the literature have suggested the existence of an interaction-induced Chern insulator (CI) phase in a tight-binding model of spinless fermions on a honeycomb lattice with nearest- and next-nearest-neighbor interactions. The CI phase is an example of a state that breaks time-reversal symmetry spontaneously and possesses a quantized Hall conductance. However, it has been proven elusive in exact diagonalization (ED) studies of this system. Since ED is limited to small system sizes, the fate of this phase in the thermodynamic limit still remains unclear. Using the infinite density matrix renormalization group (iDMRG) algorithm we reach system sizes exceeding those accessible in ED calculations while keeping track of quantum fluctuations neglected in mean field studies. We map out the phase diagram as a function of both nearest- and next-nearest-neighbor interaction strengths for an infinite cylinder geometry and find different charge-ordered phases but no sign of the interaction driven Chern insulator phase.

15 min. break.

TT 101.8 Thu 17:00 H 3010

Quasiparticle interference patterns from different impurities on the surface of pyrochlore iridates: signatures of the Weyl phase — •Fabian Lambert[1], Andreas Schnyder[2], Roderich Moessner[3], and Ilya Eremin[1] — [1]Institut für Theoretische Physik III, Ruhr-Universität Bochum, D-44801 Bochum, Germany — [2]Max-Planck-Institut für Festkörperforschung, Heisenbergstrasse 1, D-70569 Stuttgart, Germany — [3]Max Planck Institute for the Physics of Complex Systems, D-01187 Dresden, Germany

Weyl semi-metals exhibit topologically protected surface Fermi arcs,

which pairwise connect projections of bulk band touchings in the surface Brillouin zone. The nontrival spin and orbital character of these topological surface states can be tested experimentally using quasiparticle interference (QPI) measurements. Here, we compute the QPI patterns for a Hubbard Hamiltonian on a pyrochlore lattice. For weak impurity potentials, the QPI patterns can be computed within the First Born approximation. To account for the antiferromangetic spin configuration of $R_2Ir_2O_7$, we treat the Hubbard interaction at the mean-field level. In the antiferromagnetic state the quadratic band touching of the model is split into eight linear band touchings, each of which carries a non-trivial Chern number, thereby realizing a Weyl phase with broken time- reversal symmetry. Using exact diagonalization, we compute the surface spectrum and quasiparticle interference patterns of this Weyl phase for various surface impurities. We show that the spin and orbital texture of the surface states can be inferred from the absence of certain backscattering processes and from the symmetries of the QPI features.

TT 101.9 Thu 17:15 H 3010

Interacting surface states of three-dimensional topological insulators — •Titus Neupert[1], Stephan Rachel[2], Ronny Thomale[3], and Martin Greiter[3] — [1]Princeton Center for Theoretical Science, Princeton University, Princeton, New Jersey 08544, USA — [2]Institute for Theoretical Physics, Technische Universitaet Dresden, 01171 Dresden, Germany — [3]Institute for Theoretical Physics, University of Wuerzburg, Am Hubland, D-97074 Wuerzburg, Germany

We numerically investigate the surface states of a strong topological insulator in the presence of strong electron-electron interactions. We choose a spherical topological insulator geometry to make the surface amenable to a finite size analysis. The single-particle problem maps to that of Landau orbitals on the sphere with a magnetic monopole at the center that has unit strength and opposite sign for electrons with opposite spin. Assuming density-density contact interactions, we find superconducting and anomalous (quantum) Hall phases for attractive and repulsive interactions, respectively, as well as chiral fermion and chiral Majorana fermion boundary modes between different phases. Our setup is preeminently adapted to the search for topologically ordered surface terminations that could be microscopically stabilized by tailored surface interaction profiles.

TT 101.10 Thu 17:30 H 3010

Resonant scattering in the topological Dirac semimetal Cd_3As_2 — Vladimir Gnezdilov[1,2], Azat Sharafeev[1], •Peter Lemmens[1], Raman Sankar[3], and Fangcheng Chou[3] — [1]IPKM, TU-BS, Braunschweig — [2]ILTPE NAS, Ukraine — [3]CCMS, National Taiwan Univ., Taipei, Taiwan

In the symmetry-broken topological Dirac semimetal with strong spin-orbit coupling, Cd_3As_2, a pronounced temperature evolution of quasielastic electronic Raman scattering and resonant effects are observed. These effects are then compared to observations in topological insulators, as Bi_2Se_3.

Work supported by RTG-DFG 1953/1, Metrology for Complex Nanosystems and the Laboratory for Emerging Nanometrology Braunschweig, TU Braunschweig.

TT 101.11 Thu 17:45 H 3010

Angle-resolved Photoemission Investigation of SmB_6 — •Peter Hlawenka[1], Oliver Rader[1], Konrad Siemensmeyer[1], Eugen Weschke[1], Andrei Varykhalov[1], Natalya Shitsevalova[2], Slavomir Gabani[3], Karol Flachbart[3], and Emile Rienks[1] — [1]Helmholtz-Zentrum Berlin — [2]Institute for Problems of Material Science, Kiev — [3]IEP, Slovak Academy of Science, Kosice

Recently the mixed valence compound SmB_6 has drawn great attention. Theoretically predicted surface states, which should result from a hybridisation of localised f-bands with conduction electrons and a band inversion, would make SmB_6 the first realisation of a so called topological Kondo insulator [1-2]. Conductivity and transport measurements, as well as spin-resolved photoemission spectroscopy seem to fortify the scenario of a topological nature of the conductive surface [3-5]. We investigate the surface electronic structure of SmB_6 by means of high resolution angle-resolved photoemission spectroscopy measurements below 1 K. We will present new insights into the surface states that determine the low temperature conductivity of this material.

[1] Dzero et al., PRL 104, 106408 (2010).
[2] Lu et al., PRL 110, 096401 (2013).
[3] Wolgast, PRB 88, 180405 (2013).
[4] Kim, Sci. Rep. 3, 3150 (3013).
[5] Xu et al., Nat. Com. 5, 4566 (2014).

TT 101.12 Thu 18:00 H 3010

Calculation of topological properties of strongly correlated electrons without inversion symmetry using Wannier charge centres. — •Robert Triebl and Markus Aichhorn — Institute of Theoretical Physics and Computational Physics, Graz University of Technology, Petersgasse 16, 8010 Graz, Austria

We study the topological properties of a role model for interacting Z_2 topological insulators, namely the Kane-Mele-Hubbard model including a staggered sublattice potential controlled by a parameter λ_ν, which breaks inversion symmetry. The applicability of a naïve mean field approach was analysed by comparing to a variational cluster approach, employing a two-site dynamical impurity approximation (DIA). The obtained Greens function determines the topological Hamiltonian, which maps the interacting system to an effective free-particle model with the same topological properties. Since inversion symmetry is lost, we calculate the Z_2 invariant for both Mean Field and topological Hamiltonian using Wannier charge centers. We conclude that a two-site DIA in combination with Wannier charge centers is an easy-to-implement and stable method to determine topological invariants for interacting systems. Comparing with mean field results we find that the direction of magnetisation is crucial for topological properties and hence an inherent mean field magnetisation may lead to incorrect results.

TT 101.13 Thu 18:15 H 3010

An analytical study of the entanglement spectrum of graphene bilayers — •Sonja Predin and John Sliemann — Institute for Theoretical Physics, University of Regensburg, D-93040 Regensburg, Germany

We present an analytical study of the entanglement spectrum of graphene bilayers. The entanglement spectrum has been proposed as a ground state property that exhibits characteristic energy excitations[1]. Futhermore, it was claimed that gapless systems possess the same number of Dirac cones as their entanglement spectrum [2]. In addition, it was suggested that the entanglement spectrum is a promising tool to characterize topological phases. In this work we will show that the energy spectrum of an gapless system and its entanglement spectrum can have a different topology. In particular, we will show that Lifshitz transitions change the topology of the energy spectrum of graphene bilayers in a different way than the topology of entanglement spectrum. The topology of the energy spectrum of graphene bilayers for small energies is changed by Lifshitz transitions by changing the connectivity by the appearance of the three additional Dirac cones around every Dirac point [3]. The entanglement spectrum, on the other hand, is changed by deforming a Dirac cone into a neck characterized by vanishing eigenvalues of the entanglement Hamiltonian.

[1] H. Li and F. D. M. Haldane,
Phys. Rev. Lett. 101, 010504 (2008)
[2] A. M. Turner, et al., Phys. Rev. B, 82, 241102R (2010)
[3] J. Cserti, et al., Phys. Rev. Lett. 99, 066802 (2007)

The 19th Symposium on Condensed Matter Physics - SFKM 2015, Belgrade - Serbia
Contributed: 11

The effect of the trigonal warping on the energy and the entanglement spectrum of graphene bilayers

Sonja Predin[a] and John Schliemann[a]

[a]*Institute for Theoretical Physics, University of Regensburg, D-93040 Regensburg, Germany*

Abstract. We present an analytical study of the entanglement spectrum of graphene bilayers. We mainly focus on the influence of the skew parameter, which causes the trigonal warping in the energy spectrum, on the topology of the entanglement spectrum. Furthermore, we explore a connection between two characteristics: the entanglement spectrum of a bilayer structure, given by tracing out one of the layer, and the energy of the resulting monolayer structure, which is shown in many previous analytical and numerical studies. An explicit relation between the entanglement spectrum and the energy spectrum of remaining monolayer graphene is shown when the skew tight binding parameter, which causes the trigonal warping is neglected. However, the trigonal warping of the graphene bilayers is reflected to the topology of the entanglement spectrum and a similarity between the entanglement spectrum of graphene bilayers and the energy spectrum of the monolayer graphene is broken.

REFERENCES

1. Sonja Predin and John Schliemann, in preparation.

European Physical Journal B

Article reference: b170447
Title: [redacted]
Author(s):

Original submission: B170447.PDF
Revision 1: B170447_REPLY.PDF B170447_SOURCE.RAR B170447REV1.PDF

Referee: Predin Sonja

View your previous reports: report1 report2

- **Submit your report**
- **Decline to review/Transfer review to someone else**
- **Update information of professional expertise**
- **Questions and comments to the editor, or deadline extension**

EPJ.org
your physics journal

Sabine Lehr
Springer-Verlag
Tiergartenstraße 17
69121 Heidelberg
Germany
phone: 0049-(0)6221-487-8336
fax: 0049-(0)6221-487-6-8336
e-mail: sabine.lehr@springer.com

24/11/2017

Sonja Predin
Hochweg 56a

93049 Regensburg

Dear Dr. Predin,

We are very pleased to send you a complimentary copy of the book entitled

Problems in Quantum Mechanics

with the compliments of the EPJ publishing consortium (www.epj.org).

We would like to take this opportunity to express our deep gratitude for your support to *The European Physical Journal B* also through the all-important task of refereeing, which is one of the pillars of the acknowledged quality and reputation of this journal.

We hope that you also find *EPJ B* a most satisfactory platform for publishing your own research.

With our best regards,

Sabine Lehr
on behalf of the EPJ Publishers

Enc.

Citation report for 4 results from All Databases between 1980 and 2021 Go

You searched for: **AUTHOR:** (predin s*)

Timespan: All years. **Databases:** WOS, KJD, RSCI, SCIELO.

...Less

This report reflects citations to source items indexed within All Databases.

Export Data: Save to Excel File

Total Publications
4 Analyze

1998 2017

h-index
2

Average citations per item
7.5

Sum of Times Cited
30

Without self citations
28

Citing articles
29 Analyze

Without self citations
28 Analyze

Sum of Times Cited per Year

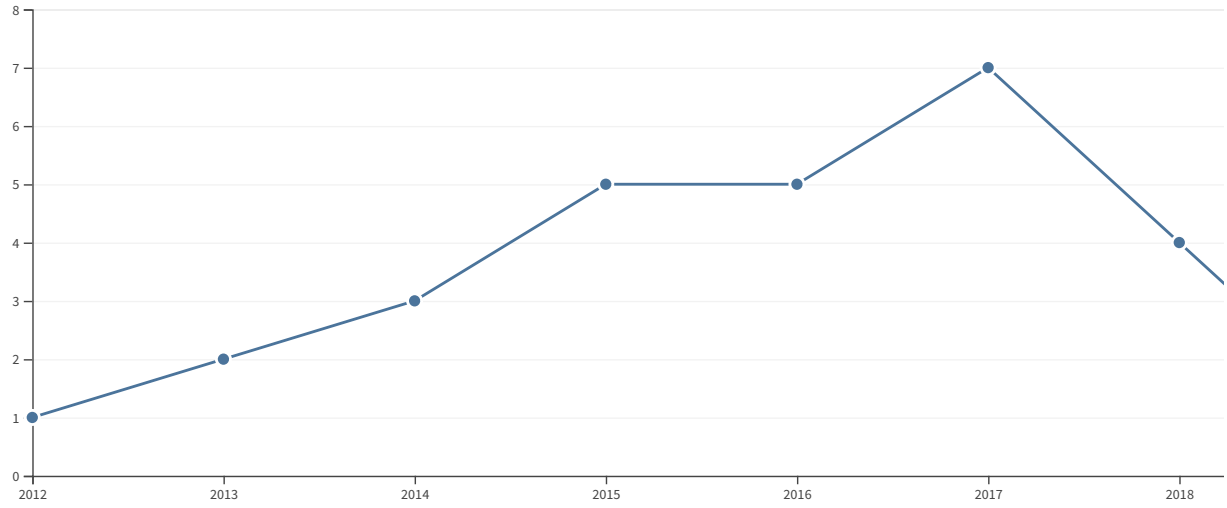

Sort by: Times Cited Date More

1 of 1

How are these totals calculated?

2017	2018	2019	2020	2021	Total	Average Citations per Year
7	4	1	2	0	30	3.33

Use the checkboxes to remove individual items from this Citation Report

or restrict to items published between 1980 and 2021 Go

1. **Coexistence of antiferromagnetism and d plus id superconducting correlations in the graphene bilayer** By: Milovanovic, M. V.; Predin, S. **PHYSICAL REVIEW B** Volume: 86 Issue: 19 Article Number: 195113 Published: NOV 8 2012	2	1	0	0	0	17	1.89
2. **Trigonal warping in bilayer graphene: Energy versus entanglement spectrum** By: Predin, Sonja; Wenk, Paul; Schliemann, John **PHYSICAL REVIEW B** Volume: 93 Issue: 11 Article Number: 115106 Published: MAR 2 2016	5	3	0	1	0	11	2.20
3. **Entanglement spectrum of the degenerative ground state of Heisenberg ladders in a time-dependent magnetic field** By: Predin, Sonja **EPL** Volume: 119 Issue: 5 Article Number: 57003 Published: SEP 2017	0	0	1	1	0	2	0.50
4. **Entanglement spectra of superconductivity ground states on the honeycomb lattice** By: Predin, Sonja; Schliemann, John **EUROPEAN PHYSICAL JOURNAL B** Volume: 90 Issue: 12 Article Number: 239 Published: DEC 11 2017	0	0	0	0	0	0	0.00

Select Page Save to Excel File

Sort by: Times Cited Date More 1 of 1

4 records matched your query of the 51,897,012 in the data limits you selected.

Web of Science

Citing Articles: Most Recent

(from Web of Science Core Collection)

For: Trigonal warping in bilayer graphene: Energy versus entanglement spectrum ...Less

Select Page | Save to EndNote desktop

1. **Phase-space elementary information content of confined Dirac spinors**

   By: Bernardini, Alex E.
   EUROPEAN PHYSICAL JOURNAL PLUS Volume: 135 Issue: 8 Article Number: 675 Published: AUG 25 2020
   Usage Count: 0 (Last 180 Days) 0 (Since 2013)
   View Abstract

   Times Cited: 0 *(from Web of Science Core Collection)*

2. **Trigonal warping and photo-induced effects on zone boundary phonon in monolayer graphene**

   By: Akay, D.
   SUPERLATTICES AND MICROSTRUCTURES Volume: 117 Pages: 18-24 Published: MAY 2018
   Usage Count: 0 (Last 180 Days) 4 (Since 2013)
   View Abstract

   Times Cited: 6 *(from Web of Science Core Collection)*

3. **Valley Hall effect and Nernst effect in strain engineered graphene**

   By: Niu, Zhi Ping; Yao, Jian-ming
   PHYSICS LETTERS A Volume: 382 Issue: 13 Pages: 920-924 Published: APR 5 2018
   Usage Count: 1 (Last 180 Days) 23 (Since 2013)
   View Abstract

   Times Cited: 4 *(from Web of Science Core Collection)*

4. **Bilayer graphene lattice-layer entanglement in the presence of non-Markovian phase noise**

   By: Bittencourt, Victor A. S. V.; Blasone, Massimo; Bernardini, Alex E.
   PHYSICAL REVIEW B Volume: 97 Issue: 12 Article Number: 125435 Published: MAR 30 2018
   Usage Count: 0 (Last 180 Days) 2 (Since 2013)
   View Abstract

   Times Cited: 2 *(from Web of Science Core Collection)*

5. **Entanglement spectra of superconductivity ground states on the honeycomb lattice**

   By: Predin, Sonja; Schliemann, John
   EUROPEAN PHYSICAL JOURNAL B Volume: 90 Issue: 12 Article Number: 239 Published: DEC 11 2017
   Usage Count: 0 (Last 180 Days) 8 (Since 2013)
   View Abstract

   Times Cited: 0 *(from Web of Science Core Collection)*

6. **Velocity renormalization in graphene: The role of trigonal warping and electron-phonon coupling effects**

   By: Kandemir, B. S.; Gokcek, N.

   Times Cited: 2 *(from Web of Science Core Collection)*

INTERNATIONAL JOURNAL OF MODERN PHYSICS B Volume: 31 Issue: 30 Article Number: 1750235 Published: DEC 10 2017
Usage Count: 0 (Last 180 Days) 11 (Since 2013)
View Abstract

7. **Lattice-layer entanglement in Bernal-stacked bilayer graphene**

Times Cited: 10 *(from Web of Science Core Collection)*

By: Bittencourt, Victor A. S. V.; Bernardini, Alex E.
PHYSICAL REVIEW B Volume: 95 Issue: 19 Article Number: 195145 Published: MAY 19 2017
Usage Count: 0 (Last 180 Days) 14 (Since 2013)
View Abstract

8. **Existence of semi-Dirac cones and symmetry of two-dimensional materials**

Times Cited: 5 *(from Web of Science Core Collection)*

By: Damljanovic, V.; Gajic, R.
JOURNAL OF PHYSICS-CONDENSED MATTER Volume: 29 Issue: 18 Article Number: 185503 Published: MAY 10 2017
Usage Count: 4 (Last 180 Days) 38 (Since 2013)
View Abstract

9. **Pairwise entanglement and the Mott transition for correlated electrons in nanochains**

Times Cited: 4 *(from Web of Science Core Collection)*

By: Rycerz, Adam
NEW JOURNAL OF PHYSICS Volume: 19 Article Number: 053025 Published: MAY 2017
Usage Count: 0 (Last 180 Days) 7 (Since 2013)
View Abstract

10. **Entanglement spectrum of fermionic bilayer honeycomb lattice: Hofstadter butterfly**

Times Cited: 3 *(from Web of Science Core Collection)*

By: Moradi, Z.; Abouie, J.
JOURNAL OF STATISTICAL MECHANICS-THEORY AND EXPERIMENT Article Number: 113101 Published: NOV 2016
Usage Count: 1 (Last 180 Days) 4 (Since 2013)
View Abstract

Select Page | Save to EndNote desktop

Web of Science

Citing Articles: Most Recent
(from Web of Science Core Collection)

For: Trigonal warping in bilayer graphene: Energy versus entanglement spectrum ...More

2 of 2

Select Page | Save to EndNote desktop

11. **Entanglement Chern Number of the Kane-Mele Model with Ferromagnetism**

By: Araki, Hiromu; Kariyado, Toshikaze; Fukui, Takahiro; et al.
JOURNAL OF THE PHYSICAL SOCIETY OF JAPAN Volume: 85 Issue: 4 Article Number: 043706 Published: APR 15 2016
Usage Count: 0 (Last 180 Days) 6 (Since 2013)
View Abstract

Times Cited: 4
(from Web of Science Core Collection)

Select Page | Save to EndNote desktop

2 of 2

Web of Science

Citing Articles: Most Recent

(from Web of Science Core Collection)

For: Entanglement spectrum of the degenerative ground state of Heisenberg ladders in a time-dependent magnetic field ...Less

1 of 1

Select Page | Save to EndNote desktop

1. **Distribution of entanglement Hamiltonian spectrum in free fermion models**

   By: Pouranvari, Mohammad
   EUROPEAN PHYSICAL JOURNAL B Volume: 93 Issue: 6
   Published: JUN 22 2020
   Usage Count: 0 (Last 180 Days) 0 (Since 2013)
   View Abstract

   Times Cited: 0
   (from Web of Science Core Collection)

2. **Entanglement conductance as a characterization of a delocalized-localized phase transition in free fermion models**

   By: Pouranvari, Mohammad; Abouie, Jahanfar
   PHYSICAL REVIEW B Volume: 100 Issue: 19 Article Number: 195109 Published: NOV 7 2019
   Usage Count: 0 (Last 180 Days) 0 (Since 2013)
   View Abstract

   Times Cited: 1
   (from Web of Science Core Collection)

Select Page | Save to EndNote desktop

1 of 1

Web of Science

Citing Articles: Most Recent

(from Web of Science Core Collection)

For: Coexistence of antiferromagnetism and d plus id superconducting correlations in the graphene bilayer **...Less**

Select Page | Save to EndNote desktop

1. **Magnetic Properties of a Nano-graphene Monolayer with Higher-Order Exchange Interaction Coupling**

   By: Feraoun, A.; Kerouad, M.
   JOURNAL OF SUPERCONDUCTIVITY AND NOVEL MAGNETISM Volume: 31 Issue: 5 Pages: 1389-1394 Published: MAY 2018
   Usage Count: 0 (Last 180 Days) 2 (Since 2013)
   View Abstract

   Times Cited: 4 *(from Web of Science Core Collection)*

2. **Entanglement spectra of superconductivity ground states on the honeycomb lattice**

   By: Predin, Sonja; Schliemann, John
   EUROPEAN PHYSICAL JOURNAL B Volume: 90 Issue: 12 Article Number: 239 Published: DEC 11 2017
   Usage Count: 0 (Last 180 Days) 8 (Since 2013)
   View Abstract

   Times Cited: 0 *(from Web of Science Core Collection)*

3. **Magnetic properties of bilayer graphene: a Monte Carlo study**

   By: Masrour, R.; Jabar, A.
   JOURNAL OF COMPUTATIONAL ELECTRONICS Volume: 16 Issue: 1 Pages: 12-17 Published: MAR 2017
   Usage Count: 1 (Last 180 Days) 10 (Since 2013)
   View Abstract

   Times Cited: 25 *(from Web of Science Core Collection)*

4. **Dynamic phase transitions and the effects of frequency of oscillating magnetic field on the dynamic phase diagrams in the bilayer honeycomb lattice with AB stacking geometry**

   By: Kantar, Ersin
   PHASE TRANSITIONS Volume: 89 Issue: 10 Pages: 971-985 Published: OCT 2016
   Usage Count: 0 (Last 180 Days) 13 (Since 2013)
   View Abstract

   Times Cited: 10 *(from Web of Science Core Collection)*

5. **Generation of an external magnetic field with the spin orientation effect in a single layer Ising nanographene**

   By: Sarli, Numan
   PHYSICA E-LOW-DIMENSIONAL SYSTEMS & NANOSTRUCTURES Volume: 83 Pages: 22-29 Published: SEP 2016
   Usage Count: 0 (Last 180 Days) 20 (Since 2013)
   View Abstract

   Times Cited: 17 *(from Web of Science Core Collection)*

6. **Phase boundary of spin-polarized-current state of**

   Times Cited: 0

electrons in bilayer graphene

(from Web of Science Core Collection)

By: Yan, Xin-Zhong; Ma, Yinfeng; Ting, C. S.
PHYSICAL REVIEW B Volume: 93 Issue: 24 Article Number: 245158 Published: JUN 29 2016
Usage Count: **0** (Last 180 Days) **9** (Since 2013)
View Abstract

7. **The Dynamic Hysteresis Curves and Compensation Types of Kinetic Bilayer Honeycomb Lattice System with AB Stacking Geometry**

Times Cited: 12
(from Web of Science Core Collection)

By: Kantar, Ersin
JOURNAL OF SUPERCONDUCTIVITY AND NOVEL MAGNETISM Volume: 28 Issue: 11 Pages: 3387-3395 Published: NOV 2015
Usage Count: **2** (Last 180 Days) **15** (Since 2013)
View Abstract

8. **Magnetic hysteresis, compensation behaviors, and phase diagrams of bilayer honeycomb lattices**

Times Cited: 11
(from Web of Science Core Collection)

By: Kantar, Ersin
CHINESE PHYSICS B Volume: 24 Issue: 10 Article Number: 1674-1056(2015)24:10<107501:MHCBAP>2.0.TX;2-D Published: OCT 2015
Usage Count: **2** (Last 180 Days) **19** (Since 2013)
View Abstract

9. **Current orderings of interacting electrons in bilayer graphene**

Times Cited: 3
(from Web of Science Core Collection)

By: Yan, Xin-Zhong; Ting, C. S.
PHYSICAL REVIEW B Volume: 92 Issue: 7 Article Number: 075442 Published: AUG 27 2015
Usage Count: **0** (Last 180 Days) **12** (Since 2013)
View Abstract

10. **Phase diagram of the Kohn-Luttinger superconducting state for bilayer graphene**

Times Cited: 5
(from Web of Science Core Collection)

By: Kagan, Maxim Yu; Mitskan, Vitaly A.; Korovushkin, Maxim M.
EUROPEAN PHYSICAL JOURNAL B Volume: 88 Issue: 6 Article Number: 157 Published: JUN 15 2015
Usage Count: **1** (Last 180 Days) **23** (Since 2013)
View Abstract

11. **Anomalous superconductivity and superfluidity in repulsive fermion systems**

Times Cited: 12
(from Web of Science Core Collection)

By: Kagan, M. Yu; Mitskan, V. A.; Korovushkin, M. M.
PHYSICS-USPEKHI Volume: 58 Issue: 8 Pages: 733-761 Published: 2015
Usage Count: **1** (Last 180 Days) **33** (Since 2013)
View Abstract

12. **The peak effect (PE) region of the antiferromagnetic two layer Ising nanographene**

Times Cited: 31
(from Web of Science Core Collection)

By: Sarli, Numan; Akbudak, Salih; Ellialtioglu, Mehmet Recai
PHYSICA B-CONDENSED MATTER Volume: 452 Pages: 18-22 Published: NOV 1 2014
Usage Count: **0** (Last 180 Days) **41** (Since 2013)
View Abstract

13. **Superconductivity on the Brink of Spin-Charge Order in**

Times Cited: 17
(from Web of Science Core

a Doped Honeycomb Bilayer

By: Vafek, Oskar; Murray, James M.; Cvetkovic, Vladimir
PHYSICAL REVIEW LETTERS Volume: 112 Issue: 14 Article Number: 147002 Published: APR 11 2014
Usage Count: 1 (Last 180 Days) 16 (Since 2013)
View Abstract

Collection)

14. **Superconductivity from weak repulsion in hexagonal lattice systems**

By: Nandkishore, Rahul; Thomale, Ronny; Chubukov, Andrey V.
PHYSICAL REVIEW B Volume: 89 Issue: 14 Article Number: 144501 Published: APR 7 2014
Usage Count: 0 (Last 180 Days) 28 (Since 2013)
View Abstract

Times Cited: 43 *(from Web of Science Core Collection)*

15. **d-wave superconductivity and its coexistence with antiferromagnetism in the t-J-U model: Statistically consistent Gutzwiller approach**

By: Abram, M.; Kaczmarczyk, J.; Jedrak, J.; et al.
PHYSICAL REVIEW B Volume: 88 Issue: 9 Article Number: 094502 Published: SEP 3 2013
Usage Count: 1 (Last 180 Days) 17 (Since 2013)
View Abstract

Times Cited: 25 *(from Web of Science Core Collection)*

16. **Ordered-current state of electrons in bilayer graphene**

By: Yan, Xin-Zhong; Ting, C. S.
PHYSICAL REVIEW B Volume: 88 Issue: 4 Article Number: 045410 Published: JUL 8 2013
Usage Count: 0 (Last 180 Days) 8 (Since 2013)
View Abstract

Times Cited: 5 *(from Web of Science Core Collection)*

17. **Possible broken inversion and time-reversal symmetry state of electrons in bilayer graphene**

By: Yan, Xin-Zhong; Ting, C. S.
PHYSICAL REVIEW B Volume: 86 Issue: 23 Article Number: 235126 Published: DEC 17 2012
Usage Count: 0 (Last 180 Days) 10 (Since 2013)
View Abstract

Times Cited: 10 *(from Web of Science Core Collection)*

Select Page | Save to EndNote desktop

ENTANGLEMENT SPECTRUM OF GRAPHENE SYSTEMS

DISSERTATION ZUR ERLANGUNG DES DOKTORGRADES DER NATURWISSENSCHAFTEN (DR. RER. NAT.) DER FAKULTÄT PHYSIK
DER UNIVERSITÄT REGENSBURG

vorgelegt von Sonja Predin aus Belgrad, Serbien

im Jahr 2017

Promotionsgesuch eingereicht am: 28.10.2016

Die Arbeit wurde angeleitet von: Prof. Dr. John Schliemann

Prüfungsausschuss:
Vorsitz: Prof. Dr. Sergey Ganichev
Erstgutachter: Prof. Dr. John Schliemann
Zweitgutachter: Prof. Dr. Jaroslav Fabian
Weiterer Prüfer: Prof. Dr. Gunnar Bali
Ersatzprüfer: Prof. Dr. Ferdinand Evers

Termin Promotionskolloquium: 25.07.2017

ABSTRACT

In the present thesis, the properties of the entanglement spectra of the ground state of graphene bilayers Bernal-stacked is analytically investigated. In addition, the entanglement spectra of the ground state of the honeycomb lattice in the presence of superconductivity instabilities are analytically studied. We consider not only the eigenvalues of the reduced density matrix that form the entanglement spectrum, but also, its eigenstates. From these eigenstates, we construct topological quantities, such as the Berry phase and the Chern number, in order to investigate the topological properties of the entanglement spectrum.

In the first part of this thesis, we present an analytical study of the graphene bilayers, mainly focusing on the effects of the trigonal warping. When the term causing the trigonal warping is neglected, the entanglement Hamiltonian obtained by tracing out one layer shows a proportionality with the energetic Hamiltonian of the remaining monolayer graphene, in the limit of strongly coupled layers. We demonstrate that this proportionality leads to an agreement of the topological quantities of these Hamiltonians. Moreover, we demonstrate that the entanglement spectrum of graphene bilayers with a trigonal warping spectrum clearly differs in the geometric shape from the energy spectrum of the remaining monolayer graphene. However, there is an agreement of the topological quantities such as Berry phase contributions to Chern numbers.

In the second part of this thesis, we give a detailed study of graphene in the presence of superconductivity instabilities, mainly considering the s-wave and the chiral $d_{x^2-y^2} + id_{xy}$ state. We investigate the relationship between the entanglement and energy spectrum, making use of the concepts of the Chern number constructed from eigenstates of the entanglement Hamiltonian. We demonstrate that the entanglement and remaining subsystem Hamiltonians can have different topologies. These findings are illustrated by considering the entanglement Hamiltonian of the ground state of graphene with $d_{x^2-y^2} + id_{xy}$ superconductivity obtained by tracing out one spin direction.

Our investigations are based on closed analytical expressions for the full eigensystem in the entire Brillouin zone of bilayer graphene with a trigonally warped spectrum and graphene with superconductivity instabilities.

PUBLICATIONS

1. Sonja Predin, Entanglement spectrum of Heisenberg ladders in a time-dependent magnetic field, preprint (submitted to the EuroPhysics Letters), arxiv:1705.08675.

2. Sonja Predin, and John Schliemann, Entanglement spectra of superconductivity ground states on the honeycomb lattice, preprint (submitted to the European Physical Journal B), arxiv:1611.01039.

3. Sonja Predin, Paul Wenk, and John Schliemann, Trigonal Warping in Bilayer Graphene: Energy versus Entanglement Spectrum, Phys. Rev. B **93**, 115106, (2016).

4. M. V. Milovanović, and S. Predin, On the coexistence of antiferromagnetism and d + i d superconducting correlations in the graphene bilayer, Phys. Rev. B **86**, 195113,(2012).

ACKNOWLEDGMENTS

I would like to take this opportunity to thank a number people for their help and support.

- First of all, I would like to express my sincere gratitude to my supervisor, Prof. Dr. John Schliemann for accepting me as a Ph.D. student and giving me the opportunity to work in the exciting field of entanglement. He shared his deep understanding of physical problems with me without limiting my freedom to research and investigate problems I considered interesting. I also thank Prof. Dr. Schliemann for his strong support in scientific matters throughout my Ph.D. studies.

- I would like to thank my diploma thesis advisor Prof. Dr. Milica Milovanović for introducing me to the field of superconductivity instabilities in a honeycomb lattice and for her comments on a draft of article arXiv:1611.01039.

- I appreciate Dr. Paul Wenk for checking my analytical results of the entanglement spectrum of the ground state of graphene bilayers with a trigonal warping and for his discussions and comments.

- I would like to thank Lars Milz for his comments.

- For the pleasant working atmosphere, I would like to thank all the members of Prof. Dr. Milena Grifoni chair, especially our lunch group and my office mates.

- Financial support through the Deutsche Forschungsgemeinschaft via GRK1570 and SFB 631 is gratefully acknowledged.

- I warmly thank my parents Olivera and Saša, and my sister Nina for their endless love and support.

CONTENTS

LIST OF FIGURES

LIST OF TABLES

1 INTRODUCTION

Quantum entanglement is the counterintuitive prediction of quantum mechanics that has no analogous phenomenon in classical physics. The entanglement arises from nonlocal quantum correlations between two or more subsystems of the quantum system. The concept of entanglement was first introduced in 1935 by Einstein, Podolsky, and Rosen in Ref. [Einstein et al., 1935], while the term *entanglement* was first introduced by Schrödinger in Ref. [Schrödinger, 1935]. Two entangled quantum subsystems cannot be described separately. Thus, the wavefunction of the whole system cannot be written as a product of the wavefunctions of the entangled subsystems. A well-known example of an entangled state is the spin singlet state of two spin-1/2 particles $|\psi\rangle = \frac{1}{\sqrt{2}}(|\uparrow\rangle\,|\downarrow\rangle - |\downarrow\rangle\,|\uparrow\rangle)$. After an interaction in which the spin-singlet state is produced, these two particles are separated in different locations. If one measures the spin of one particle and gets the spin direction $|\uparrow\rangle$, then the spin of the second particle is projected on the state $|\downarrow\rangle$. Thus, the measurement of one particle changes the state of the other particle, although the particles are in different locations and cannot communicate with each other. This was a paradox for Einstein, Podolsky, and Rosen, (EPR paradox) since, according to special relativity, the *locality* condition assumes that nothing can travel faster than the speed of light. If we can predict with *certainty* the result of the measurement of a physical quantity then this quantity is an element of *physical reality*. Furthermore, they concluded that the description of the quantum mechanics of physical reality is not complete and proposed hidden local variables as a solution to this problem. This means that each particle possesses all the necessary information, and no information should be transmitted from one particle to another during the measurement. In 1965, John Bell showed that in local realism, the correlations between distant measurements satisfy inequalities. He mathematically proved that the quantum theory predicts a violation of these inequalities [Bell, 2004]. Bell-inequality violations have been

experimentally demonstrated [Freedman and Clauser, 1972,Aspect et al., 1982, Garg and Mermin, 1987, Eberhard, 1993, Weihs et al., 1998, Rowe et al., 2001, Barrett et al., 2002, Matsukevich et al., 2008, Ansmann et al., 2009, Scheidl et al., 2010, Hensen et al., 2015]. Nowadays, we believe that quantum mechanics is an adequate theory for the description of the microscopic world and entanglement can successfully describe nonlocal and nonclassical correlations.

The idea of a quantum computer was proposed by Richard Feynman in 1982. [Feynman, 1982]. A quantum computer based on the quantum mechanical principles of superposition and entanglement would be much more powerful than a classical one. In recent decades, much effort has been invested in experimental and theoretical physics work to develop the quantum computer, owing to its possible uses, mainly in civil, business, and national security applications. The study of the many-body entangled state has recently become a very attractive topic, since it was realized that entanglement could be useful in quantum informatics. In particular, the quantum correlations between entangled states could be a useful resource for communications, because when a system is entangled, measurements of distant subsystems of the system can be much more correlated than is classically allowed [Bell, 2004]. It makes the quantum entanglement an attractive topic of research in various fields of physics.

The entanglement of the bipartite system of the subsystems A and B is defined in terms of the Schmidt decomposition of its ground state because the Hilbert space of the whole system is the direct product of two subsystems: $\mathcal{H} = \mathcal{H}_{\mathcal{A}} \otimes \mathcal{H}_{\mathcal{B}}$. The reduced density matrix for the subsystem A $\rho_A = \mathrm{t}r_B\rho$ is obtained by tracing out all degrees of freedom of the subsystem B. One of the most popular measurements of entanglement is entanglement entropy. The entanglement entropy of the subsystem A can be defined as:

$$S_A = -\mathrm{t}r_B \left(\rho_A \ln \rho_A\right). \tag{1.1}$$

Although first considered a source of quantum corrections to the entropy of black holes [Bombelli et al., 1986], entanglement entropy, in particular, the von Neumann entropy, evolved into a tool in the field of many-body systems. This heralded connections between seemingly unrelated research areas. In condensed matter, entanglement entropy serves, for example, as a geometrical interpretation for the boundary between local quantum many-body sys-

tems. This connection has its origin in the *area laws* [Eisert et al., 2010].

Another common tool for the measurement of entanglement is the entanglement spectrum. Since the reduced density matrix does not have negative eigenvalues, it can be always reformulated:

$$\rho_A = \frac{1}{Z} e^{-\mathcal{H}_\mathcal{A}} \tag{1.2}$$

with the entanglement Hamiltonian $\mathcal{H}_\mathcal{A}$ and the partition function $Z = tr\left(e^{-\mathcal{H}_\mathcal{A}}\right)$. The spectrum of the entanglement Hamiltonian is the entanglement spectrum.

In condensed matter physics, the study of phases of matter and phase transitions is one of the most important topics of research. The phase and phase transitions are usually distinguished by Landau's theory of phase transitions, which involves the existence of a local order parameter, as opposed to the topological phases and topological phase transitions, which cannot be distinguished by a local order parameter. The latter phases possess so-called topological order [Wen, 1990, Wen, 1991]; their ground states might be degenerate and no local measurement can distinguish these degenerate ground states. The significance of the topological phase was underlined in 2016, when the Nobel Prize for Physics was awarded to David J. Thouless, F. Duncan M. Haldane, and J. Michael Kosterlitz "for theoretical discoveries of topological phase transitions and topological phases of matter". The entanglement spectrum is constructed from the ground state, which consists all the correlations that give rise to the various phases of matter. Li and Haldane found that one signature of the Fractional Quantum Hall effect, the low-energy excitations, can be related to the entanglement spectrum and suggested that the entanglement spectrum has information about a given phase [Li and Haldane, 2008]. Further, they concluded that the entanglement spectrum is beyond entanglement entropy, which extracts all the information from the reduced density matrix and proposed it as a new order parameter for distinguishing topological phases. Nowadays, the framework of the entanglement spectrum in condensed matter physics is very broad and is applied to many condensed matter systems, such as Quantum Hall liquids [Regnault et al., 2009, Zozulya et al., 2009, Läuchli et al., 2010, Thomale et al., 2010b, Ardonne and Regnault, 2011, Chandran et al., 2011, Hermanns et al., 2011, Schliemann, 2011, Sterdyniak et al., 2011, Thomale et al., 2011, Alba et al., 2012, Dubail et al., 2012, Liu et al., 2012, Rodriguez et al., 2012, Sterdyniak et al., 2012], topological insulators and superconductors [Fidkowski, 2010, Turner et al., 2010, Bray-Ali et al., 2009,

Prodan et al., 2010, Borchmann et al., 2014, Kim, 2014], the fractional Chern insulator [Regnault and Bernevig, 2011], superfluids [Dubail and Read, 2011], spin systems [Nienhuis et al., 2009, Poilblanc, 2010, Pollmann and Moore, 2010, Pollmann et al., 2010, Yao and Qi, 2010, Cirac et al., 2011, Huang and Lin, 2011, Lou et al., 2011, Peschel and Chung, 2011, Thomale et al., 2010a, De Chiara et al., 2012, Läuchli and Schliemann, 2012, Lundgren et al., 2012, Schliemann and Läuchli, 2012, Tanaka et al., 2012, Chen and Fradkin, 2013, Lundgren et al., 2013, Lundgren et al., 2014, Lundgren, 2016, Predin, 2017], and Hofstadter bilayers [Schliemann, 2013]; for recent reviews, see Ref. [Regnault, 2015, Laflorencie, 2016]. As a result of this study, the entanglement spectrum possesses universal information about a phase and this is reflected to an exact equivalence between the low-lying entanglement spectrum and edge energy spectrum.

The statement that the entanglement spectrum has fundamental and universal information about the phase was criticized in Ref. [Chandran et al., 2014]. These authors have indicated that topological phase transitions can occur in the entanglement Hamiltonian, even though a physical system remains in the same state. The physical reason for this is that they have defined the entanglement Hamiltonian as $\mathcal{H}_{ent} = -\ln(\rho_{red})$, implying $Z \equiv 1$ at a finite effective temperature $T_E = 1/\beta \equiv 1$, with β is a inverse effective temperature. This makes the entanglement thermodynamics an important task of research.

A particular situation arises if the edge comprises the entire remaining subsystem. A typical observation in such a scenario is the proportionality between the entanglement spectrum, given by a traced out subsystem, and the energy spectrum of a remaining subsystem in the limit of strongly coupled subsystems. These findings are illustrated by many important examples, including spin systems [Poilblanc, 2010, Cirac et al., 2011, Peschel and Chung, 2011, Läuchli and Schliemann, 2012, Schliemann and Läuchli, 2012, Tanaka et al., 2012, Lundgren et al., 2013, Chen and Fradkin, 2013, Lundgren, 2016, Predin, 2017], and bilayer systems [Schliemann, 2011, Schliemann, 2013, Schliemann, 2014]. This proportionality can be illustrated by

$$\mathcal{H}_{ent} \sim \lambda \mathcal{H}_A / t \tag{1.3}$$

where λ is inverse proportional to the coupling between subsystems and t has the dimensions of energy. We note that the entanglement Hamiltonian entering the reduced density matrix Eq.(1.2) is only determined up to multiples of the unit operator, which

has consequences regarding the thermodynamic relations between the entanglement entropy and the subsystem energy [Schliemann, 2011, Schliemann, 2013, Schliemann, 2014].

On the other hand, such a close relationship between the energy and entanglement Hamiltonian is not truly general, as shown in Ref. [Lundgren et al., 2012], in which a spin ladder of clearly nonidentical legs was studied.

In the present thesis, we will represent a detailed analytical study of the entanglement spectra of the ground states of graphene systems. This includes considerations of graphene bilayers focusing on trigonal warping [McCann and Koshino, 2013, Rozhkov et al., 2016], and as well graphene in the presence of superconducting instabilities [Black-Schaffer and Doniach, 2007]. Our analytical approach of the entanglement includes the eigenvalues of the reduced density matrix (giving rise to the entanglement spectrum) as well as its eigenvectors. From these eigenvectors, we construct topological quantities, the Berry phase, and the Chern number, in order to study the topological properties of the entanglement Hamiltonian. This ensures that our consideration of the relationship between the energy Hamiltonian of the remaining subsystem and the appropriately defined entanglement Hamiltonian includes not only their geometric but also topological properties. We will show that although the geometric shapes of the entanglement spectrum of an undoped graphene bilayer with a trigonal warped spectrum clearly differ from the energy spectrum of the remaining monolayer, their topological quantities such as the Berry phase contribution to the Chern number agree. On the other hand, the entanglement Hamiltonian of the $d_{x^2-y^2} + id_{xy}$ superconductivity ground states on the honeycomb lattice obtained by tracing out one spin direction and the Hamiltonian of the remaining subsystem have completely different topologies.

Our investigations are based on closed analytical expressions for the full eigensystem in the entire Brillouin zone of bilayer graphene with a trigonally warped spectrum and of graphene in the presence of superconductivity instabilities.

In the following, we give an outline of this thesis:

In Chapter 2, the lattice structure, tight-binding model, and energy description around the Dirac points in graphene are addressed. Here, we derive the tight-binding models assuming that electrons can hop to a nearest-neighbor atom. The topological properties of graphene are also discussed, and the density of states is presented.

Chapter 3 is dedicated to an investigation of Bernal-stacked graphene bilayers, taking into account only the nearest-neighbor

hopping parameter and the hoping parameter between the atoms on opposite sites which are on top of each other. First, we recapitulate the tight-binding model of graphene bilayers. Here, as well as in Chapter 4, the entanglement Hamiltonian of the noninteracting free fermionic system on the graphene bilayers is analytically calculated as a single particle operator [Schliemann, 2013, Peschel, 2003, Cheong and Henley, 2004]. We demonstrate that upon tracing out one layer, in the limit of strongly coupled layers the proportionality between the entanglement Hamiltonian and the energy Hamiltonian of the graphene monolayer leads to the equivalence of their topological and thermodynamic properties. Here, the entanglement spectrum given by tracing out another two of four sublattices is considered, as well as the influence of the bias voltage or the mass term.

In Chapter 4, we analytically study the entanglement and the energy spectrum of the graphene bilayers in a Bernal stacking arrangement when the trigonal warping is present in the energy spectrum. In contrast with all earlier works, our analytical investigations of the energy spectrum of graphene bilayers with the presence of trigonal warping cover the entire Brillouin zone and avoid the Dirac cone approximation and the low-energy description of graphene bilayers. We demonstrate that the entanglement spectrum obtained by tracing out one layer vanishes between points where the energy spectrum possesses three additional Dirac cones caused by the trigonal warping. The topological properties of the entanglement spectrum of graphene bilayers, described by the Berry phase contributions to the Chern number, agree with the topological properties of graphene monolayers. Furthermore, we verify that the entanglement spectrum can be a discontinuous function of the momentum as a consequence of the fact that the trigonal warping produces discontinuities in the eigenvectors of the energetic Hamiltonian from which the entanglement spectrum is constructed. These discontinuities play an important role in both the geometric and topological properties of the entanglement spectrum. When an identical mass term in both layers or bias voltage is introduced, these discontinuities vanish and an entanglement gap opens. We also discuss the geometric and topological properties of the entanglement spectra given by tracing out other two of four sublattices. Technical details of the calculations of the full eigensystem of the Hamiltonian of graphene bilayers are presented in Appendix A. Furthermore, analytical derivations of the entanglement spectra are given in Appendix B.

Chapter 5 is dedicated to the entanglement spectra resulting from the superconductivity ground states on the honeycomb lattice tracing out one spin direction, mainly focusing on the s-wave and $d_{x^2-y^2} + id_{xy}$ -wave superconductivity states. Here, in order to analytically study the entanglement spectrum, we modify the method for analytical calculations of a free fermionic system to a system with superconductivity instabilities. We demonstrate that the topology of the entanglement Hamiltonian can differ from that of the subsystem Hamiltonian. In particular, the topological properties of the entanglement Hamiltonian of the chiral $d_{x^2-y^2} + id_{xy}$ superconductivity state obtained by tracing out one spin direction clearly differ from those of the time-reversal-invariant Hamiltonian of noninteracting fermions on the honeycomb lattice. Some technical details on the analytical derivation of the full eigenstates of the noninteracting fermionic system on the honeycomb lattice in the presence of superconductivity instabilities, as well as the correlation matrix calculations, are presented in Appendices C and D.

2

GRAPHENE: NEW PHYSICS IN TWO-DIMENSION

Graphene is an allotrope of carbon, a nonmetal that is a cornerstone of all organic compounds and thus of life on Earth. Since graphene is one atom thick, it can be considered as a two-dimensional object. Graphite, a three-dimensional crystal, is built of layers of graphene bonding via weak van der Walls bonds and is a well-known material since the 16th century, used in the cores of pencils. Graphene can be wrapped up as zero-dimensional fullerenes and rolled out as one-dimensional carbon nanotubes. The first molecules of fullerenes were fabricated in 1985 by Richard Smalley, Robert Curl, James Heath, Sean O'Brien, and Harold Kroto, while carbon nanotubes were discovered in 1991 by Sumio Iijima. A theoretical description of the band structure of graphene was written down by Wallace in 1947 as an important step in the research of graphite [Wallace, 1947]. Notwithstanding, it was believed that graphene could not exist as a free and stable two-dimensional crystal. Pierls and Landau indicated that two-dimensional crystals are thermodynamically unstable and cannot exist [Peirls, 1934, Landau and Lifshitz, 1980]. Mermin and Wagner amplified their contention, and it was illustrated with many experiments [Mermin and Wagner, 1966, Mermin, 1968]. Meanwhile, it was noticed that two-dimensional crystal structures can be stabilized by three-dimensional structures. Geim and Novoselov developed the method for isolation graphene by using Scotch tape in 2004 [Novoselov et al., 2004]. They were rewarded by the Nobel prize for this simple, groundbreaking, and inspiring discovery in 2010.

Since it was isolated, it has been one of the most intensively studied materials. Graphene is a light, strong, flexible, and conductive two-dimensional material with remarkable optical and electrical properties. This extraordinary combination of properties makes graphene a promising material for a new generation of devices, such as transistors, sensors, solar cells, and smartphones. Apart from the huge interest in investigations of graphene due to its

potential applications in various devices, there is an enormous interest in fundamental research. The low-energy excitations in graphene are massless Dirac fermions, which were believed to be realizable in accelerators. The half-integer Quantum Hall effect and Berry's phase of π are consequences of the existence of the massless Dirac fermions in graphene [Zhang et al., 2005]. The existence of massless Dirac fermions enables measurements of high-energy phenomena, such as the Klein paradox [Katsnelson et al., 2006] and Zitterbewegung [Rusin and Zawadzki, 2008]. Thus, graphene has become a noteworthy bridge between condensed matter and high-energy physics, as quantum entanglement is a bridge between condensed matter physics and quantum informatics.

The electronic structure of graphene rapidly changes with the number of layers and ten layers can already be considered as graphite. Strictly speaking, only graphene and its bilayer have a simple electronic structure: both are either zero-gap semiconductors or zero-overlap semimetals. Furthermore, graphene possesses massless chiral quasiparticles as opposed to the massive ones in its bilayers. In the case of multilayer graphene, which consists of three to ten layers, the valence and conduction bands overlap and there are a few kinds of charge carriers. Monolayer, bilayer, and multilayer graphene can be realized as three different structures.

Carbon belongs to group IV of the periodic system. One carbon atom contains six electrons with the electronic structure $1s_2 2s_2 2p_2$. Two atoms are in the inner shell $1s$ and are more or less inert, while four valence electrons are described by $2s$, $2p_x$, $2p_y$ and $2p_z$, since one electron from the $2s$ orbital excites to the $2p_z$ orbital, in order to build covalent bonds. Three valence electrons in $2s$, $2p_x$ and $2p_y$ hybridize in planar sp^2 bonds, σ bonds. The three sp^2 orbitals lie in the x-y plane with an angle 120° between them. σ bonds are the strongest type of covalent bonds, because of the direct overlap between the orbitals. These bonds are responsible for the robustness of the honeycomb lattice of graphene [Castro Neto et al., 2009]. The remaining delocalized $2p_z$ orbitals are perpendicular to the plane. They are responsible for forming half-filled π-bonds by covalent bonding. The π electrons are responsible for the low-energy excitations, while σ electrons form energy bands far away from the Fermi energy. p_z orbitals allow hopping between carbon atoms and thus can be described by the tight-binding model. Considering p_z orbitals of graphene, Wallace derived the tight-binding model of graphene for the first time in 1947 [Wallace, 1947].

This chapter is organized as follows: The lattice structure of graphene is briefly described in the first section 2.1. In Section

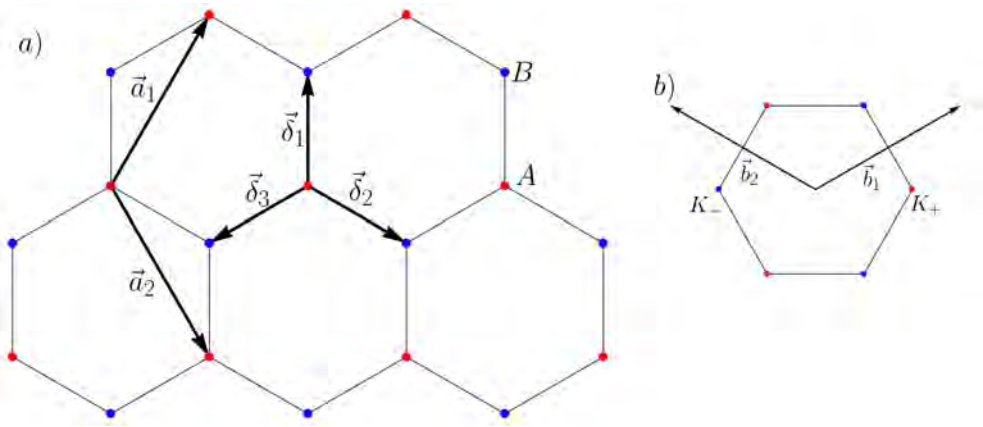

Figure 2.1: a) Lattice of graphene with $\vec{a}_1$ and $\vec{a}_2$ denoting lattice vectors, and $\vec{\delta}_1$, $\vec{\delta}_2$, and $\vec{\delta}_3$ the nearest-neighbor vectors b) first Brillouin zone of graphene with the reciprocal-lattice vectors $\vec{b}_1$ and $\vec{b}_2$ and the Dirac points K_+ and K_-.

2.2, we derive the tight-binding approximation of the valence and conduction band of graphene considering the nearest-neighbor interactions and overlap interactions. The topological properties of graphene are addressed in Section 2.3. Numerical calculations of the density of states are given in Section 2.4.

2.1 LATTICE STRUCTURE

Graphene consists of carbon atoms arranged in honeycomb lattice, as shown in Fig.(2.1). The honeycomb lattice is not a Bravais lattice and can be considered as two triangular Bravais lattices with the basis formed by two atoms, sites A and B.

The span of the triangular Bravais lattice is defined by two lattice vectors $\vec{a}_i$

$$\vec{a}_1 = \frac{a}{2}\left(1, \sqrt{3}\right) \qquad \vec{a}_2 = \frac{a}{2}\left(-1, \sqrt{3}\right) \tag{2.1}$$

where $a = \sqrt{3}a_{C-C}$ with $a_{C-C} \approx 0.142$ nm is the distance between two nearest carbon atoms. Using a Fourier transform of the Brillouin zone Fig.(2.1), the primitive cell in the momentum space is defined by the reciprocal lattice vectors

$$\vec{b}_1 = \frac{2\pi}{\sqrt{3}a}(\sqrt{3}, 1), \qquad \vec{b}_2 = \frac{2\pi}{\sqrt{3}a}(-\sqrt{3}, 1) \tag{2.2}$$

as

$$\vec{a}_i \vec{b}_j = 2\pi\delta_{ij} \tag{2.3}$$

where δ_{ij} denotes the Kronecker delta. The corners of the Brillouin zone are called Dirac points and only two of them are not equivalent

$$K_{\pm} = \pm\frac{4\pi}{3a}\,(1,0)\,. \tag{2.4}$$

Every A atom is connected with three nearest B atoms with nearest–nearest vectors

$$\vec{\delta}_1 = a(0,\frac{1}{\sqrt{3}}), \qquad \vec{\delta}_2 = \frac{a}{2}(1,-\frac{1}{\sqrt{3}}), \qquad \vec{\delta}_3 = \frac{a}{2}(-1,-\frac{1}{\sqrt{3}}). \tag{2.5}$$

2.2 ELECTRONIC STRUCTURE OF GRAPHENE

The tight-binding model is a simple and effective tool to describe the energy bands of a crystal structure. In this model, it is assumed that in the vicinity of every lattice point, the crystal Hamiltonian can be approximated by the Hamiltonian of a single atom $\mathcal{H}_{at}$ [Ashcroft and Mermin, 1976]

$$\mathcal{H}_{at}\psi_n(\vec{r}) = E_j\psi_n(\vec{r}). \tag{2.6}$$

A further assumption is that the bound levels of the Hamiltonian $\mathcal{H}_{at}$ are well localized, i.e. the $\psi_n(\vec{r})$ are very small when $\vec{r}$ is larger than the distance of the lattice spacing. The entire crystal is described by the Hamiltonian

$$\mathcal{H} = \mathcal{H}_{at} + U(\vec{r}) \tag{2.7}$$

which includes the spatially periodic lattice potential $U(\vec{r})$. Because the honeycomb lattice of graphene has two atoms per unit cell, the eigenstates of the Hamiltonian Eq.(2.7) are given as a linear combination of two Bloch functions $\psi^A_{\vec{k}}(\vec{r})$ and $\psi^B_{\vec{k}}(\vec{r})$

$$\begin{aligned}\psi_{\vec{k}}(\vec{r}) =& c_A\psi^A_{\vec{k}}(\vec{r}) + c_B\psi^B_{\vec{k}}(\vec{r}) \\ =& \frac{1}{\sqrt{N}}\sum_j e^{i\vec{k}\vec{R}_j}\left(c_A(\vec{k})\phi(\vec{r}-\vec{R}^A_j) + c_B(\vec{k})\phi(\vec{r}-\vec{R}^B_j)\right)\end{aligned} \tag{2.8}$$

where N is the number of elementary cells, and $c_A(\vec{k})$ and $c_B(\vec{k})$ are complex functions of the momentum $\vec{k}$. The $\phi(\vec{r}-\vec{R}^A_j)(\phi(\vec{r}-\vec{R}^B_j))$ are atomic wavefunctions around the positions of the A (B) atoms at the lattice site, respectively

$$R^A_j = n_1\vec{a}_1 + n_2\vec{a}_2$$

$$R_j^B = R_j^A + \vec{\delta}_1. \tag{2.9}$$

where n_1 and n_2 are integers. By multiplication of the Schrödinger equation $\mathcal{H}\psi_{\vec{k}}(\vec{r}) = \epsilon_{\vec{k}}\psi_{\vec{k}}(\vec{r})$ with $\psi_{\vec{k}}(\vec{r})$, one can obtain

$$(c_A^*(\vec{k}), c_B^*(\vec{k}))\mathcal{H}_{\vec{k}} \begin{pmatrix} c_A(\vec{k}) \\ c_B(\vec{k}) \end{pmatrix} = \epsilon_{\vec{k}}(c_A^*(\vec{k}), c_B^*(\vec{k}))\mathcal{S}_{\vec{k}} \begin{pmatrix} c_A(\vec{k}) \\ c_B(\vec{k}) \end{pmatrix} \tag{2.10}$$

where the $\epsilon_{\vec{k}}$ are the energy bands. Considering only the hopping of the electrons between nearest– sites, the transfer matrix $\mathcal{H}_{\vec{k}}$ and the overlap map $\mathcal{S}_{\vec{k}}$ become

$$\mathcal{H}_{\vec{k}} = \begin{pmatrix} \epsilon_A & -t\gamma(\vec{k}) \\ -t\gamma^*(\vec{k}) & \epsilon_B \end{pmatrix}, \qquad \mathcal{S}_{\vec{k}} = \begin{pmatrix} 1 & s_0\gamma(\vec{k}) \\ s_0\gamma^*(\vec{k}) & 1 \end{pmatrix} \tag{2.11}$$

where t is the nearest– neighbor hopping energy, s_0 is the on-site energy and ϵ_A (ϵ_B) are on-site energies of the A(B) lattice sites, respectively; the function $\gamma(\vec{k}) = \sum_{\vec{\delta}_i} e^{i\vec{k}\vec{\delta}_i}$ is the geometric structural factor and depends up to a phase factor of the choice of the nearest-neighbor vectors $\vec{\delta}_i$. For details of the calculations of the elements of $\mathcal{H}_{\vec{k}}$ and $\mathcal{S}_{\vec{k}}$ we refer the reader to the recent reviews Refs. [McCann and Koshino, 2013, Goerbig, 2011]. Solving the secular equation of the Eq.(2.10), we find the energies for intrinsic graphene when $\epsilon_A = \epsilon_B = 0$

$$E_\pm = \frac{\pm t|\gamma(\vec{k})|}{1 \mp s_0|\gamma(\vec{k})|}. \tag{2.12}$$

The tight-binding parameter values are $t \approx 3.033$eV and $s_0 \approx 0.129$eV [Saito et al., 1998]. The energy description of graphene is visualized over the entire Brillouin zone in Fig.(2.2).

The valence band is completely filled and touches the completely empty conduction band at the Dirac points. Furthermore, $\gamma(\vec{k})$ can be approximated around Dirac points up to linear order of the momentum as

$$\gamma(K_\nu + \vec{k}) \approx \frac{\sqrt{3}a}{2}(-\nu k_x + ik_y) \tag{2.13}$$

where $\nu = \pm 1$ detonates the valley degeneracy. Neglecting the s_0, of which the effects are small and irrelevant at low energies around the Dirac points, see Fig.(2.3), the low-energy excitations have linear dispersion

$$\epsilon(K_\nu + \vec{k}) \approx \nu v_F|k| \tag{2.14}$$

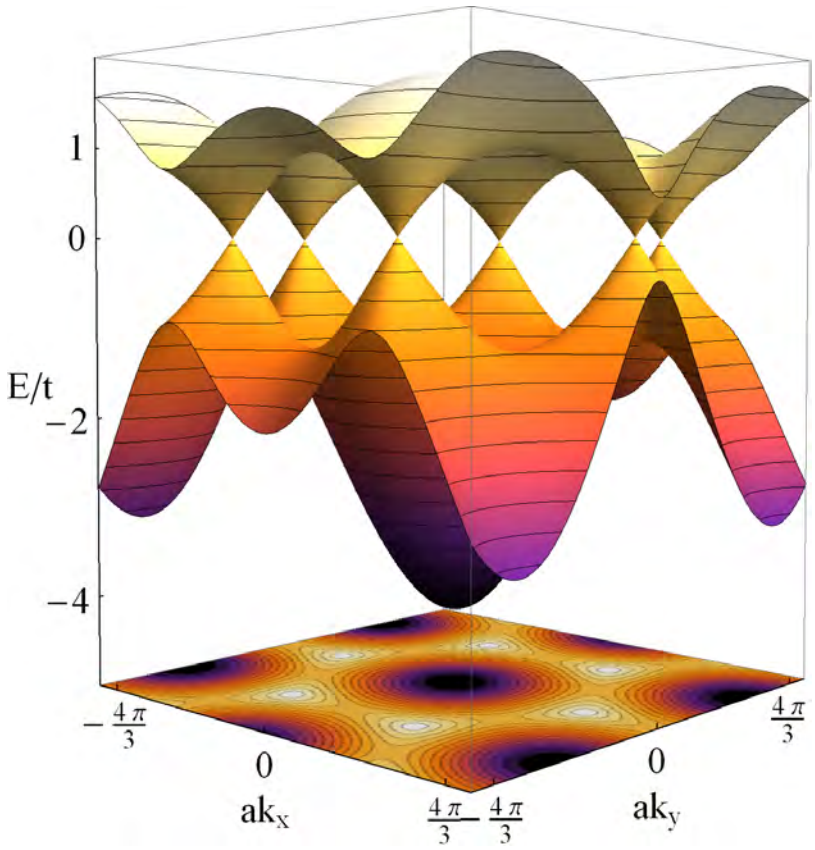

Figure 2.2: Energy description of graphene within the entire Brillioun zone for $t = 3.033$ eV, and $s_0 = 0.129$eV. The dispersions show a linear dispersion relation around every Dirac cone.

and propagate with the Fermi–Dirac velocity $v_F = \sqrt{3}at/2$, which is independent of their momentum $p = \hbar k$ (as photons with the speed of light "v_F"). These kinds of excitations are protected by the symmetry of the honeycomb lattice of graphene and described by the Hamiltonian

$$\mathcal{H}(K_\nu + \vec{k}) = v_F \vec{\sigma}_\nu \vec{k} \tag{2.15}$$

which has essentially the form of the Dirac equation which describes relativistic massless fermions (with velocity v_E). Here, $\vec{\sigma}_\nu = (\nu\sigma_x, \sigma_y)$ are Pauli Matrices, which represent the sublattice pseudospin with valley degeneracy. To summarize, the low-energy excitations are massless chiral Dirac fermions with a linear dispersion relation.

2.3 TOPOLOGICAL INVARIANTS

Among other interesting and fascinating properties, graphene possesses nontrivial topological properties.

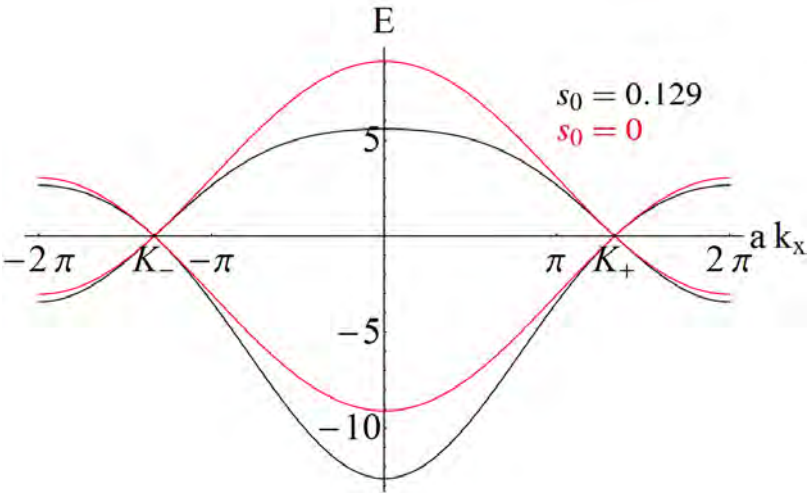

Figure 2.3: Energy bands of graphene plotted along the k_x axis. The effects of the parameter s_0 are small and irrelevant at low energies around the Dirac points.

The space inversion and time-reversal symmetry have essential roles in the topological properties of graphene. The space inversion is defined as

$$I: \quad \mathcal{H}(\vec{k}) = \sigma_x \mathcal{H}(-\vec{k})\sigma_x. \tag{2.16}$$

Whereas, the time-reversal symmetry is defined as

$$T: \quad \mathcal{H}(\vec{k}) = \mathcal{H}^*(-\vec{k}). \tag{2.17}$$

In the context of graphene, the Berry phase is the phase that an eigenstate acquires after the electron wavevector in graphene completes a full cycle at constant energy around a Dirac point. The eigenstates of graphene read

$$\chi_\pm(\vec{k}) = \frac{1}{\sqrt{2}} \begin{pmatrix} 1 \\ \mp e^{i\phi(\vec{k})} \end{pmatrix} \tag{2.18}$$

where the phase $\phi(\vec{k})$ is $\phi(\vec{k}) = \gamma(\vec{k})/|\gamma(\vec{k})|$. The eigenstates are smooth and well-defined functions of the wavevector, except for at the locations of Dirac cones.

The degeneracy points of the eigenstates act as sources of the Berry curvature, defined as

$$F(\vec{k}) = \frac{\partial A_y}{\partial k_x} - \frac{\partial A_x}{\partial k_y} \tag{2.19}$$

where the Berry connection

$$\vec{A}(\vec{k}) = i\langle \chi_\pm(\vec{k}) | \frac{\partial}{\partial \vec{k}} | \chi_\pm(\vec{k}) \rangle. \tag{2.20}$$

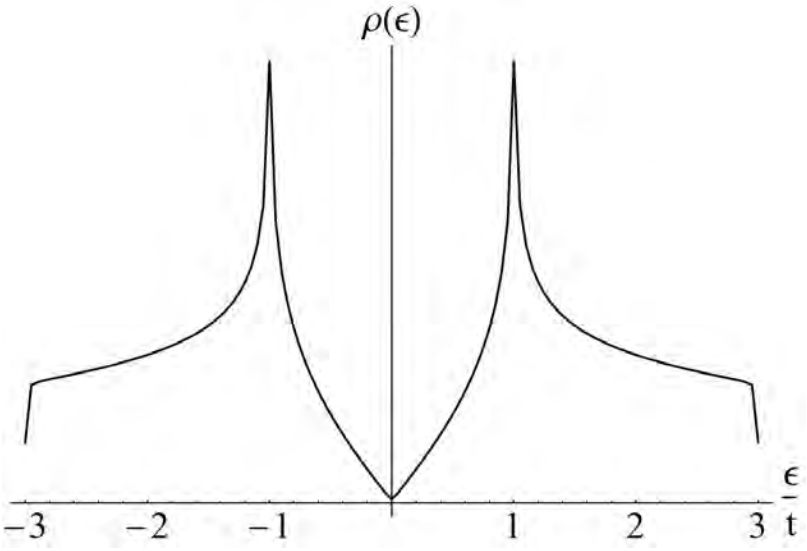

Figure 2.4: Single particle density of states of graphene as a function of energy ϵ in units of t. The van-Hove singularity points occur at $\epsilon/t = \pm 1$.

In graphene, the Berry curvature due to the time-reversal and space inversion symmetry vanishes everywhere outside the Dirac cones where quantized "monopole" sources of the δ-function type exist.

The Berry is defined as an integral over a closed path in $\vec{k}$ space [Xiao et al., 2010]. Thus, integrating over a closed path around one Dirac cone $K_{\pm}$ yields the Berry phase $\pm\pi$. The nontrivial topological quantity, the Berry phase, implies that the Dirac cones are topologically protected.

2.4 DENSITY OF STATES

Fig.(2.4) shows the single particle density of states, obtained by numerically integrating the spectral function [Bena and Kivelson, 2005]

$$\rho(\epsilon) = \int \frac{dk^2}{4\pi^2} A(\vec{k}, \epsilon) \tag{2.21}$$

over first Brillioun zone, where

$$A(\vec{k}, \epsilon) = -2\mathrm{Im}\left(\left(\epsilon - t|\gamma(\vec{k})| + i\eta\right)^{-1} + \left(\epsilon + t|\gamma(\vec{k})| + i\eta\right)^{-1}\right). \tag{2.22}$$

We perform the numerical calculations for a finite inverse lifetime of the quasiparticle $\eta = 0.005$ t. The van-Hove singularity points

are points where the density of states possesses singularities. As can be seen from Fig.(2.4), the van-Hove singularity points occur at $\epsilon/t = \pm 1$. Furthermore, at low energies $|\epsilon|/t < 1$ the density of states has a v-shape, while at energies $|\epsilon|/t > 3$ the density of states goes to zero.

The finite value of the inverse lifetime η, which goes to zero, has two consequences:

1. the density of states at $\epsilon = 0$ has a very small value and goes to zero as $\rho(0) \approx \eta \ln(1/\eta)$,

2. the divergence of the density of states at van-Hove singularity points as $\rho(\pm t) \approx \ln(1/\eta)$.

3

GRAPHENE BILAYERS: ENERGY VERSUS ENTANGLEMENT

Graphene bilayers were isolated soon after the graphene monolayer. The low-energy excitations are massive chiral fermions, which do not exist in high-energy physics. The main consequences of this are the integer Quantum Hall effect without plateau at zero and the non-trivial Berry's phase of 2π [Novoselov et al., 2006].

Quantum entanglement, primarily a source of quantum information, has developed into one of the most studied subfields of many-body physics. In the last decade, quantum entanglement has mainly been used to study phase structure in condensed matter physics [Amico et al., 2008]. The entanglement spectrum of a bipartite system of subsystems A and B is defined in terms of the Schmidt decomposition of its ground state $|\psi\rangle$ as

$$|\psi\rangle = \sum_n e^{-\frac{\xi_n}{2}} |\psi_n^A\rangle |\psi_n^B\rangle \tag{3.1}$$

where the states $|\psi_n^A\rangle$ ($|\psi_n^B\rangle$) are orthonormal states of the subsystem A (B), respectively, and the non-negative quantities ξ_n represent the levels of the entanglement spectrum. In many previous studies, the proportionality between the energetic Hamiltonian of the subsystem A $\mathcal{H}_A$ and the entanglement Hamiltonian $\mathcal{H}_{ent}$ in the strong coupling regime between rungs [Poilblanc, 2010, Cirac et al., 2011, Schliemann, 2011, Peschel and Chung, 2011, Läuchli and Schliemann, 2012, Schliemann and Läuchli, 2012, Schliemann, 2013, Predin, 2017] has been observed.

The starting point of this chapter is to recapture the energy description of graphene bilayers considering only the hopping parameter between nearest neighbors on honeycomb lattice and the hopping parameter between neighbor sites that are on top of each other. The effects of the term that causes the trigonal warping [McCann and Koshino, 2013, Rozhkov et al., 2016] in graphene bilayers will be a central point of Chapter 4. Furthermore, we will neglect the term breaking the particle–hole symmetry. In this chapter,

we analytically consider the entanglement spectrum of the free fermionic system on a graphene bilayers in a Bernal stacking arrangement. In the limit of strongly coupled layers, there is a proportionality between the entanglement Hamiltonian of graphene bilayers obtained by tracing out one layer, and the energetic Hamiltonian of the graphene monolayer. Then, we place a special focus on the effects of this proportionality on thermodynamic and topological properties of the entanglement Hamiltonian. We also study the entanglement spectrum of graphene bilayers in the presence of the bias voltage and the mass term.

The tight-binding description of graphene bilayers is studied in Section 3.1. In Section 3.2, we start with a brief review of the method for analytical derivation of the entanglement spectrum of the free fermionic system given in Refs. [Peschel, 2003, Cheong and Henley, 2004, Schliemann, 2013]. Then, we analyze the entanglement spectrum of graphene bilayers obtained by tracing out one layer and applied the concept of the entanglement thermodynamics. Furthermore, we also stress here an agreement in the topology of the entanglement Hamiltonian of graphene bilayers and the energy Hamiltonian of a graphene monolayer, due to the proportionality between these Hamiltonians. Then, we study the entanglement spectrum of graphene bilayers obtained by tracing out other two of possible four sublattices. In Section 3.3, we give an explicit equation for entanglement levels when the bias voltage or mass term are included. Finally, we close this chapter with a brief conclusion and an outlook in Section 3.4.

3.1 ELECTRONIC STRUCTURE OF GRAPHENE BILAYERS

Graphene bilayers consist of two coupled layers via Van der Walls forces. The unit cell of graphene bilayers has four carbon atoms, A1, B1 on the lower layer and A2, B2 on the upper layer. The layers are arranged in the Bernal stacking [McCann and Koshino, 2013, Rozhkov et al., 2016], where one atom at the B1 site is directly below an atom at the A2 site Fig.(3.1).

Then, the integral matrix of the graphene bilayers has the following form [McCann and Koshino, 2013]

$$\mathcal{H}_{\vec{k}} = \begin{pmatrix} \epsilon_{A1} & -t\gamma(\vec{k}) & t_4\gamma(\vec{k}) & -t_3\gamma^*(\vec{k}) \\ -t\gamma^*(\vec{k}) & \epsilon_{B1} & t_\perp & t_4\gamma(\vec{k}) \\ t_4\gamma^*(\vec{k}) & t_\perp & \epsilon_{A2} & -t\gamma(\vec{k}) \\ -t_3\gamma(\vec{k}) & t_4\gamma^*(\vec{k}) & -t\gamma^*(\vec{k}) & \epsilon_{B2} \end{pmatrix} \tag{3.2}$$

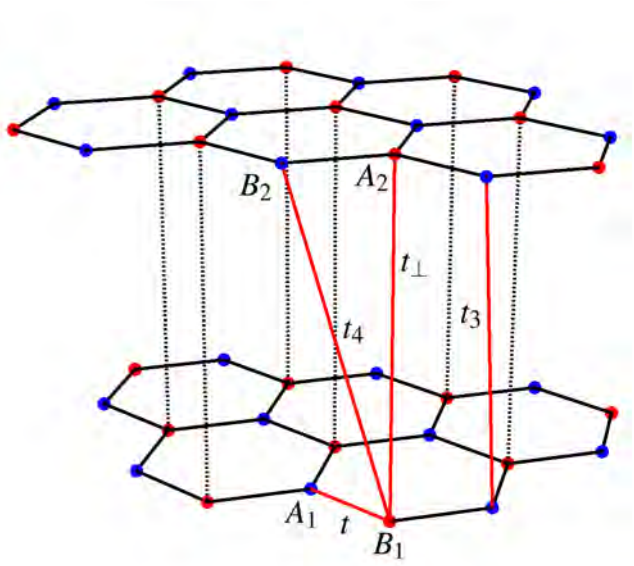

Figure 3.1: Schematic representation of Bernal-stacked bilayer graphene. Two sublattices of each layer are represented by red and blue spheres. The intralayer hopping parameter t between nearest electrons and also interlayer hopping parameters t, t_3, and t_4 are represented by red lines.

in the basis $\left(a^\dagger_{1\vec{k}}, b^\dagger_{1\vec{k}}, a^\dagger_{2\vec{k}}, b^\dagger_{2\vec{k}}\right)|0\rangle$ where $a^\dagger_{i\vec{k}}$ $(a_{i\vec{k}})$ and $b^\dagger_{i\vec{k}}$ $(b_{i\vec{k}})$ create (annihilate) electrons layers $i = 1, 2$ on sublattice A and B, respectively.. Here, $\gamma(\vec{k}) = \sum_{\vec{\delta}} \exp(i\vec{k}\cdot\vec{\delta})$ with $\vec{\delta}$ being nearest–neighbor vectors on a graphene monolayer, defined by Eq.(2.5). ϵ_{A1}, ϵ_{B1}, ϵ_{A2} and ϵ_{B2} are on-site energies. The parameter t is the hopping parameter between nearest-neighbor atoms within each layer, while $t_\perp$ describes coupling between atoms at the sites B1 and A2. The parameter t_3 is the interlayer hopping parameter between atoms A1 and B2 and causes trigonal warping. Whereas the parameter t_4 is the interlayer hoping parameter between A1 and A2 and B1 and B2 and leads to the electron–hole asymmetry. Hopping parameters are represented in Fig.(3.1). Effects of the parameters t_3 on the energy, and as well entanglement spectrum will be discussed in Chapter 4. Since, the eigenvalues and eigenstates of the Hamiltonian Eq.(3.2) cannot be obtained in closed analytical form when the hopping parameter t_4 is included, we will neglect it in this thesis. The experimentally established values [Kuzmenko et al., 2009] for these parameters are $t = 3.16$eV, $t_\perp = 0.381$eV, $t_3 = 0.38$eV, and $t_4 = 0.14$eV.

Furthermore, we will neglect the overlap matrix, since it has only a small and irrelevant influence around the Dirac cones. For

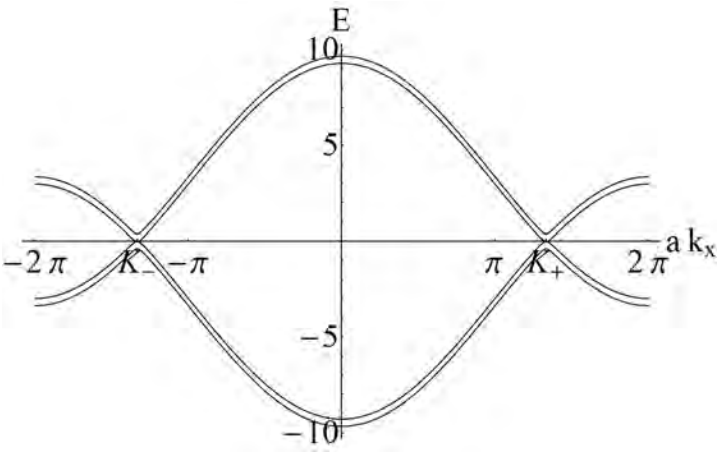

Figure 3.2: The energy bands of graphene bilayers plotted along the k_x axis for $t = 3.16$eV, and $t_\perp = 0.381$eV. The dispersions show a quadratic dispersion relation around every Dirac cone.

intrinsic graphene bilayers when $\epsilon_{A1} = \epsilon_{A2} = \epsilon_{B1} = \epsilon_{B2} = 0$ solving the eigenproblem of the Hamiltonian Eq.(3.2) we obtain the symmetric energy spectrum with four bands $\pm E_1(\vec{k})$ and $\pm E_2(\vec{k})$

$$E_{1,2}(\vec{k}) = \pm\frac{1}{2}t_\perp + \sqrt{\frac{t_\perp^2}{4} + t^2|\gamma(\vec{k})|^2}, \tag{3.3}$$

a pair of conduction bands and a pair of the valence bands. The energy bands structure of graphene bilayers is plotted along the k_x axis in the momentum space in Fig.(3.2).

The Hamiltonian that describes the properties of electrons in the vicinity of the Dirac points $\vec{k} + K_\nu$ ($\nu = \pm 1$ detonates the valley degeneracy) can be approximated within the Dirac cone approximation

$$\mathcal{H}_{\vec{k}+K_\nu} = \begin{pmatrix} 0 & v_F\pi^\dagger & 0 & 0 \\ v_F\pi & 0 & t_\perp & 0 \\ 0 & t_\perp & 0 & v_F\pi^\dagger \\ 0 & 0 & v_F\pi & 0 \end{pmatrix} \tag{3.4}$$

where v_F is the Fermi-Dirac velocity, and $\pi = \nu p_x + ip_y$ and $\pi^\dagger = \nu p_x - ip_y$. Energy bands Eq.(3.3) can be approximated around Dirac points

$$E_{1,2} = \nu m^* v_F^2 + \sqrt{(m^* v_F^2)^2 + p^2 v_F^2} \tag{3.5}$$

where m^* is the effective mass of the quasiparticles $m^* = \frac{t_\perp}{2v_F^2}$ and it is directly proportional to the hopping parameter $t_\perp$. Thus,

the mass of the quasiparticles directly arises from the interaction between the layers. Even more, at small momentum, the energy band Eq.(3.3)

$$E_1 = \frac{p^2}{2m^*} \tag{3.6}$$

shows the quadratic dispersion. However, these excitations are not classical massive quasiparticles, which are the most common in the condensed matter physics. Similar to the case of graphene, we will prove the chirality of the quasiparticle in graphene bilayers by showing that they can be described by the generalized Dirac Hamiltonian with elements $\frac{p^2}{2m^*}$. In this sense, it is necessary to rewrite the Hamiltonian Eq.(3.4), which possesses information about the high-energy bands $\pm E_1$ as the low-energy effective Hamiltonian which possesses the information only about the low-energy bands $\pm E_2$ [McCann and Fal'ko, 2006]. Keeping only terms up to linear in $t_\perp$ we find

$$\mathcal{H}^{(eff)}_{\vec{k}} = -\begin{pmatrix} 0 & \frac{t^2}{t_\perp}\left(\gamma^*(\vec{k})\right)^2 \\ \frac{t^2}{t_\perp}\left(\gamma(\vec{k})\right)^2 & 0 \end{pmatrix} \tag{3.7}$$

in the basis $\left(b^\dagger_{2\vec{k}}, a^\dagger_{1\vec{k}}\right)|0\rangle$ and it is good approximation in the energy range $|E_2| < \frac{1}{4}t_\perp$. It the vicinity of the Dirac point K_ν the effective Hamiltonian Eq.(3.7) can be approximated by the Dirac cone approximation to

$$\mathcal{H}^{(eff)}_{\vec{k}+K_\nu} = -\nu\frac{\hbar^2 v_F^2}{t_\perp}\begin{pmatrix} 0 & (\pi^\dagger)^2 \\ \pi^2 & 0 \end{pmatrix} \tag{3.8}$$

It is more convenient to write this Hamiltonian in the following form

$$\mathcal{H}^{(eff)}_{\vec{k}+K_\nu} = -\nu\frac{\hbar^2 k^2}{2m^*}\vec{\sigma}\vec{n} \tag{3.9}$$

where $\vec{k} = (k\cos(\phi_{\vec{k}}), k\sin(\phi_{\vec{k}}))$ and $\vec{n} = (n\cos(2\phi_{\vec{k}}), n\sin(2\phi_{\vec{k}}))$. $\vec{\sigma}$ denote Pauli matrices. To conclude, the low-energy excitations are massive chiral particles with the quadratic dispersion. In quantum electrodynamics, only massless particles are chiral and thus graphene bilayers become an exciting playground for studying properties of massive chiral quasiparticles that do not exist in quantum electrodynamics.

3.1.1 *Topological invariants*

The Hamiltonian Eq.(3.2) of intrinsic graphene fulfills the time-reversal symmetry

$$\mathcal{H}^*(\vec{k}) = \mathcal{H}(-\vec{k}) \tag{3.10}$$

and the space inversion symmetry

$$(\sigma_x \otimes \sigma_x)\, \mathcal{H}(\vec{k})\, (\sigma_x \otimes \sigma_x) = \mathcal{H}(-\vec{k}). \tag{3.11}$$

The eigenstates of the effective Hamiltonian Eq.(3.7)

$$|\chi_\pm\rangle = \frac{1}{\sqrt{2}} \begin{pmatrix} 1 \\ \mp \mathrm{e}^{2i\phi(\vec{k})} \end{pmatrix} \tag{3.12}$$

with $\phi(\vec{k}) = \gamma(\vec{k})/|\gamma(\vec{k})|$. The singularities of these eigenstates at the Dirac points act as the sources of the Berry curvature flux

$$F(\vec{k}) = \frac{\partial A_y}{\partial k_x} - \frac{\partial A_x}{\partial k_y} \tag{3.13}$$

where the Berry connection

$$\vec{A}(\vec{k}) = i\langle\chi_\pm(\vec{k})|\frac{\partial}{\partial \vec{k}}|\chi_\pm(\vec{k})\rangle. \tag{3.14}$$

Integrating the Berry connection $\vec{A}$ over a closed path, it is found that the Dirac cone $K_\pm$ contributes $\pm 2\pi$ to the Berry phase.

3.2 ENTANGLEMENT SPECTRUM

3.2.1 *Method*

For systems of free fermions as studied here, the entanglement Hamiltonian can be formulated as a single-particle operator [Peschel, 2003, Cheong and Henley, 2004, Schliemann, 2013].

Consider first a system of free fermions described by Hamiltonian

$$\mathcal{H} = \sum_{i,j} t_{ij} c_i^\dagger c_j \tag{3.15}$$

where t_{ij}-hopping parameter, and $c_i^\dagger$ (c_i) creates (annihilates) an electron on the i-th site.

The one-particle function determined by the ground state $|\psi\rangle$ of the previous Hamiltonian Eq. (3.15) reads

$$C_{ij} = \langle\psi|c_i^\dagger c_j|\psi\rangle = \mathrm{tr}\left(\rho c_i^\dagger c_j\right) \tag{3.16}$$

where ρ is the density matrix.

In this thesis, we restrict our considerations to a bipartite system, which consists of two subsystems A and B. Since the reduced density ρ_A, obtained by tracing out subsystem B, does not have any negative eigenvalues, it can be always reformulated as

$$\rho_A = \frac{1}{Z} e^{-\mathcal{H}_A} \tag{3.17}$$

with the entanglement spectrum $\mathcal{H}_A$ and the partition function $Z = \mathrm{tr}\left(e^{-\mathcal{H}_A}\right)$.

Now, we will consider only the subsystem A, which has L sides. It is clear that the correlation matrix in this subsystem has the following form

$$C_{\alpha\beta} = \mathrm{tr}_A(\rho_A c_\alpha^\dagger c_\beta) = \langle\psi|c_\alpha^\dagger c_\beta|\psi\rangle \tag{3.18}$$

where $|\psi\rangle$ is the ground state of the composite system, and single-particle operators c_α, c_β act on its remaining part after tracing out a subsystem.

In order to represent all correlation functions in the free fermion subsystem A, the entanglement Hamiltonian $\mathcal{H}_A$ of the non-interacting system must have the following form

$$\mathcal{H}_A = \sum_{\alpha,\beta\in A} \mathcal{H}_{\alpha\beta} c_\alpha^\dagger c_\beta. \tag{3.19}$$

Furthermore, every Hamiltonian of free fermions Eq. (3.15) can be diagonalized using the unitary matrix U as

$$\mathcal{H} = UDU^\dagger \tag{3.20}$$

where $D = \mathrm{diag}\left(E_1, E_2, ..., E_{N/2}, -E_1, -E_2, ..., -E_{N/2}\right)$, with E_i are eigenenergies. We use a new kind fermion operations a_α

$$a_\alpha = \sum_\beta U_{\beta\alpha} c_\beta \tag{3.21}$$

to calculate the correlation function in the set $\{|\lambda\rangle\}$ of many-body eigenstates of $\mathcal{H}_A$

$$C_{\alpha\beta} = \langle c_\alpha^\dagger c_\beta\rangle_A$$

$$= \frac{\sum_\lambda \langle\lambda| c_\alpha^\dagger c_\beta e^{-\mathcal{H}_A} |\lambda\rangle}{\sum_{\lambda'} \langle\lambda'| e^{-\mathcal{H}_A} |\lambda'\rangle}$$
$$= \frac{\sum_\lambda \langle\lambda| \sum_{mn} a_m^\dagger U_{\alpha m} U_{\beta n} a_n e^{-\mathcal{H}_A} |\lambda\rangle}{\sum_{\lambda'} \langle\lambda'| e^{-\mathcal{H}_A} |\lambda'\rangle}. \tag{3.22}$$

where

$$\sum_{\lambda'} \langle\lambda^{'}| e^{-\mathcal{H}_A} |\lambda^{'}\rangle = \sum_{\{n_\alpha\}} \langle\{n_\alpha\}| e^{-\sum_\alpha \xi_\alpha n_\alpha} |\{n_\alpha\}\rangle = \prod_\alpha \sum_{n_\alpha = \{0,1\}} e^{-\xi_\alpha n_\alpha}$$

and

$$\sum_\lambda \langle\lambda| \sum_{mn} a_m^\dagger U_{\alpha m} U_{\beta n} a_n e^{-\mathcal{H}_A} |\lambda\rangle = \sum_{mn} U_{\alpha m} U_{\beta n} \sum_\lambda \langle\lambda| a_m^\dagger a_n e^{-\mathcal{H}_A} |\lambda\rangle$$
$$= \sum_l U_{\alpha l} U_{\beta l} \sum_\lambda \langle\lambda| n_l e^{-\mathcal{H}_A} |\lambda\rangle$$
$$= \sum_l U_{\alpha l} U_{\beta l} \sum_{\{n_\alpha\}} \langle\{n_\alpha\}| n_l e^{-\sum_\alpha \xi_\alpha n_\alpha} |\{n_\alpha\}\rangle$$
$$= \sum_l U_{\alpha l} U_{\beta l} \left(\prod_{\alpha \neq l} \sum_{n_\alpha = \{0,1\}} e^{-\xi_\alpha n_\alpha} \right) \sum_{n_l = \{0,1\}} e^{-\xi_l n_l} n_l$$
$$= \sum_l U_{\alpha l} U_{\beta l} \left(\prod_\alpha \left(1 + e^{-\xi_\alpha n_\alpha} \right) \right) \frac{e^{-\xi_l}}{1 + e^{-\xi_l}}.$$

Finally, we get

$$C_{\alpha\beta} = \sum_l U_{\alpha l} U_{\beta l} \frac{e^{-\xi_l}}{1 + e^{-\xi_l}} \tag{3.23}$$

where we sum only over states with negative energies, because only these states are occupied. The eigenvalues ξ_α of the entanglement Hamiltonian, known as entanglement levels. The entanglement Hamiltonian then can be reformulated as a single particle operator

$$\mathcal{H}_A = \sum_{\alpha=1}^{L} \xi_\alpha a_\alpha^\dagger a_\alpha. \tag{3.24}$$

The eigenvalues ξ_α are related to the eigenvalues η_α of the correlation matrix via

$$\xi_\alpha = \ln \left(\frac{1 - \eta_\alpha}{\eta_\alpha} \right) = 2\text{artanh} \left(1 - 2\eta_\alpha \right) . \tag{3.25}$$

The entanglement levels form the entanglement spectrum. In particular, the entanglement Hamiltonian and the correlation matrix share the same system of eigenvectors.

Here, the only condition is that the eigenvalues of the correlation matrix lie between 0 and 1, which is always the case because they can be written in the form $\langle a_\alpha^\dagger a_\alpha \rangle$.

3.2.2 *Tracing out one layer*

Here, we will analytically obtain the entanglement spectrum by tracing out layer 1 from the ground state of the undoped graphene bilayers where all states with negative energies $(-E_1(\vec{k}))$, $(-E_2(\vec{k}))$ are occupied, while all others are empty. Then, the correlation matrix has the following form

$$\begin{aligned} C(\vec{k}) &= \begin{pmatrix} \langle a^\dagger_{2\vec{k}} a_{2\vec{k}} \rangle & \langle a^\dagger_{2\vec{k}} b_{2\vec{k}} \rangle \\ \langle b^\dagger_{2\vec{k}} a_{2\vec{k}} \rangle & \langle b^\dagger_{2\vec{k}} b_{2\vec{k}} \rangle \end{pmatrix} \\ &= \begin{pmatrix} \frac{1}{2} & u(\vec{k}) \\ u^*(\vec{k}) & \frac{1}{2} \end{pmatrix} \end{aligned} \tag{3.26}$$

where $u(\vec{k}) = \frac{1}{2} e^{i\phi(\vec{k})} \frac{t|\gamma(\vec{k})|}{\sqrt{t^2|\gamma(\vec{k})|^2 + \frac{1}{4}t_\perp^2}}$.

The eigenvalues of the correlation matrix

$$\eta_\pm(\vec{k}) = \frac{1}{2}\left(1 \mp \frac{t|\gamma(\vec{k})|}{\sqrt{t^2|\gamma(\vec{k})|^2 + \frac{1}{4}t_\perp^2}}\right) \tag{3.27}$$

lead to the entanglement levels

$$\xi_\pm(\vec{k}) = \pm 2\text{arcsinh}\left(\frac{2t|\gamma(\vec{k})|}{t_\perp}\right). \tag{3.28}$$

These entanglement levels get into the entanglement Hamiltonian as

$$\mathcal{H}_{ent} = \sum_{n=\pm} \xi_n c^\dagger_{\vec{k}n} c_{\vec{k}n}. \tag{3.29}$$

Here, the operators $c_{\vec{k}n}$ diagonalize the energetic Hamiltonian.

The entanglement levels $\xi_\pm$ are represented in Fig. (3.3) in the entire Brilloun zone. At every Dirac point, two layers are maximally entangled $(1/t_\perp = 0)$ and the entanglement spectrum vanishes $\xi_\pm = 0$.

One can notice that the entanglement spectrum Eq. (3.28) for a given energy spectrum of a graphene monolayer depends only on the coupling parameter $t_\perp$. Furthermore, the entanglement spectrum $\xi_\pm$ in the limit of strongly coupled layers $t_\perp >> t|\gamma(\vec{k})|$ can be approximated as

$$\xi_\pm \approx \pm\frac{4t|\gamma(\vec{k})|}{t_\perp} \mp \frac{8t^3|\gamma(\vec{k})|^3}{3t_\perp^3} + \mathcal{O}\left(\frac{1}{t_\perp^5}\right). \tag{3.30}$$

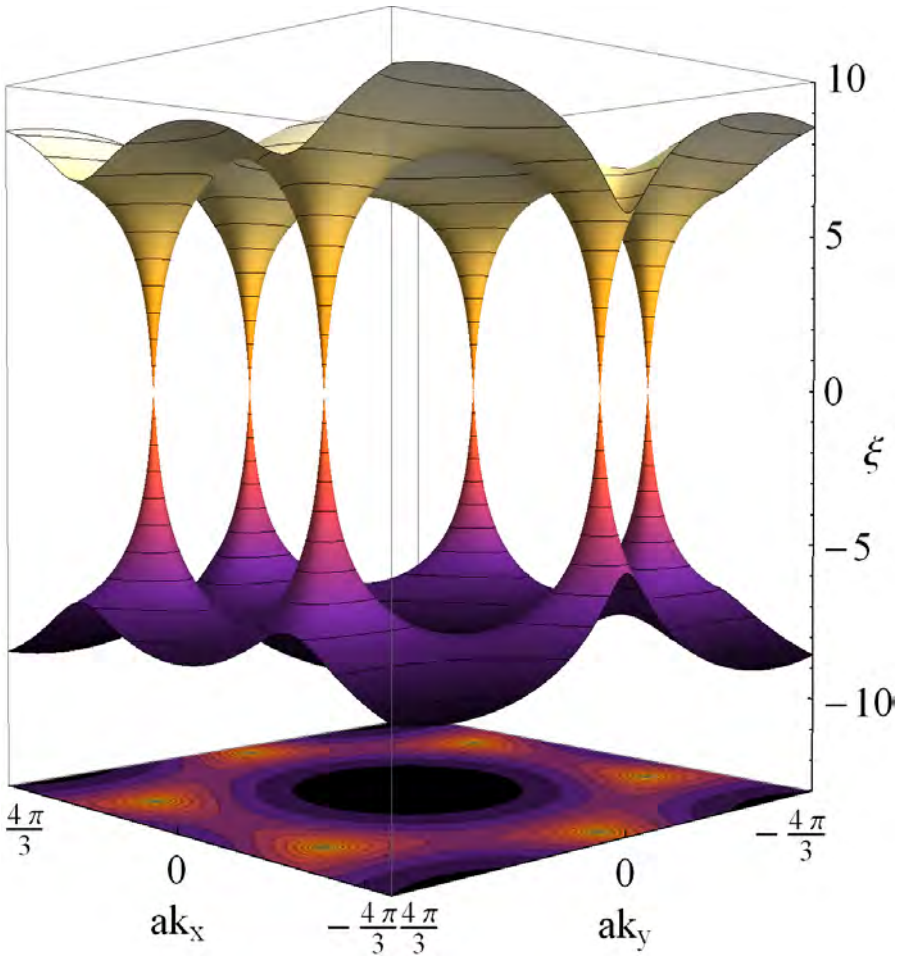

Figure 3.3: The entanglement spectrum $\xi_{\pm}(\vec{k})$ plotted for $t = 3.16$eV, $t_{\perp} = 0.381$eV over entire Brillouin zone. The contour plot represents the lower entanglement level ξ_{-}.

This implies the direct proportionality, in the limit of the strong coupling layers, between the entanglement spectrum $\xi_{\pm}$ of graphene bilayers and the energy spectrum $t|\gamma(\vec{k})|$ of a graphene monolayer

$$\xi_{\pm} \approx \frac{4}{t_{\perp}} t|\gamma(\vec{k})| \tag{3.31}$$

with the proportionality factor $\lambda = 4/t_{\perp}$, which is indeed the phenomenological inverse temperature [Schliemann, 2014]. As we shall see in the following, this proportionality has crucial consequences on the topological quantities of the entanglement Hamiltonian [Predin et al., 2016] and the entanglement thermodynamics [Schliemann, 2011, Schliemann, 2013, Schliemann, 2014].

Topological invariants

The entanglement Hamiltonian and the correlation matrix share the same eigenstates. Integrating the Berry connection constructed from the eigenstates of the correlation matrix over a closed path around the Dirac cone $K_\pm$, we find a Berry phase of $\pm\pi$. This result agrees with the Berry phase around the Dirac cones in monolayer graphene.

Entanglement thermodynamics

The entanglement entropy and entanglement energy are defined as functions of the reduced density matrix [Schliemann, 2011, Schliemann, 2013, Schliemann, 2014]

$$S = \langle -\ln \rho_{red} \rangle \tag{3.32}$$

$$\overline{E} = \langle \mathcal{H}_{ent} \rangle \tag{3.33}$$

where $\langle \cdot \rangle = \mathrm{tr}\,(\rho_{red} \cdot)$. Since the reduced density matrix can be rewritten as

$$\rho_{red}(\lambda) = \frac{\mathrm{e}^{-\mathcal{H}_{ent}(\lambda)}}{Z(\lambda)} = \sum_n \frac{\mathrm{e}^{-\xi_n(\lambda) c_n^\dagger c_n}}{1 + \mathrm{e}^{-\xi_n(\lambda)}}. \tag{3.34}$$

the entanglement entropy and energy have the following forms

$$\begin{aligned} S(\lambda) &= \sum_n \left(\frac{\ln\left(1 + \mathrm{e}^{-\xi_n(\lambda)}\right)}{1 + \mathrm{e}^{-\xi_n(\lambda)}} + \frac{\ln\left(1 + \mathrm{e}^{\xi_n(\lambda)}\right)}{1 + \mathrm{e}^{\xi_n(\lambda)}} \right) \\ &= \sum_n \left(\ln\left(1 + \mathrm{e}^{-\xi_n(\lambda)}\right) + \frac{\xi_n(\lambda)}{1 + \mathrm{e}^{\xi_n(\lambda)}} \right) \end{aligned} \tag{3.35}$$

$$\overline{E}(\lambda) = \sum_n \frac{\xi_n(\lambda)}{1 + \mathrm{e}^{\xi_n(\lambda)}}, \tag{3.36}$$

respectively. This leads to the expression for the entanglement free energy defined as

$$\overline{F} = \overline{E} - S. \tag{3.37}$$

Here, the thermodynamic relation

$$\frac{\partial S}{\partial E} = \frac{\partial S}{\partial \lambda} \frac{\partial \lambda}{\partial E} = \beta(\lambda) \tag{3.38}$$

holds, where $\beta(\lambda)$ is the inverse thermodynamic temperature. Furthermore, the connection between the entanglement Hamiltonian and canonical entanglement Hamiltonian $\mathcal{H}_{can}$ is

$$\mathcal{H}_{ent} = \beta(\lambda) \mathcal{H}_{can} \tag{3.39}$$

and allows us to define the entanglement inner energy as

$$E(\lambda) = \langle \mathcal{H}_{can} \rangle \tag{3.40}$$

and the free energy as

$$F(\lambda) = E(\lambda) - S(\lambda)/\beta(\lambda). \tag{3.41}$$

It is easy to obtain from Eq.(3.38)

$$\beta \frac{\partial \overline{F}}{\partial \beta} = \overline{E}. \tag{3.42}$$

Thus, the connection between the inverse thermodynamic temperature $\beta(\lambda)$ and the phenomenological inverse temperature λ is given by

$$\frac{\partial \beta(\lambda)}{\partial \lambda} = \frac{1}{\overline{E}} \frac{\partial \overline{F}}{\partial \lambda} = \frac{1}{\overline{E}} \frac{\partial \left(\overline{E} - S \right)}{\partial \lambda}. \tag{3.43}$$

Here, the entanglement entropy and entanglement energy is

$$\begin{aligned} S(\lambda) &= 2\ln\left(1 + \lambda t|\gamma(\vec{k})|\right) - \lambda t|\gamma(\vec{k})| \left(1 + \tanh\left(\frac{1}{2}\lambda t|\gamma(\vec{k})|\right)\right), \\ \overline{E}(\lambda) &= -\lambda t|\gamma(\vec{k})| \tanh\left(\frac{1}{2}\lambda t|\gamma(\vec{k})|\right), \end{aligned} \tag{3.44}$$

respectively. This leads to

$$\frac{\partial \left(\overline{E} - S \right)}{\partial \lambda} = -t|\gamma(\vec{k})| \tanh\left(\frac{1}{2}\lambda t|\gamma(\vec{k})|\right) \tag{3.45}$$

and further to

$$\frac{\partial \beta(\lambda)}{\partial \lambda} = \frac{1}{\lambda}. \tag{3.46}$$

The inverse thermodynamic temperature is proportional the phenomenological inverse temperature

$$\beta(\lambda) = k_E \lambda \tag{3.47}$$

where k_E is a constant. Finally, the canonical entanglement Hamiltonian is independent of the inverse temperature $\beta = 4k_E/t_\perp$, such that

$$\mathcal{H}_{can} = \frac{1}{k_E} \left(c^\dagger_{\vec{k},+} c_{\vec{k},+} - c^\dagger_{\vec{k},-} c_{\vec{k},-} \right). \tag{3.48}$$

3.2.3 *Tracing out A1 and B2 (or A2 and B1) sublattices*

The correlation matrix obtained by tracing out sublattices A1 and B2 lying in opposite layers has the following form

$$C(\vec{k}) = \begin{pmatrix} \langle a^\dagger_{2\vec{k}} a_{2\vec{k}} \rangle & \langle a^\dagger_{2\vec{k}} b_{1\vec{k}} \rangle \\ \langle b^\dagger_{1\vec{k}} a_{2\vec{k}} \rangle & \langle b^\dagger_{1\vec{k}} b_{1\vec{k}} \rangle \end{pmatrix} = \begin{pmatrix} \frac{1}{2} & -v(\vec{k}) \\ -v(\vec{k}) & \frac{1}{2} \end{pmatrix} \tag{3.49}$$

where $v(\vec{k}) = \frac{1}{4} \frac{t_\perp}{\sqrt{t^2|\gamma(\vec{k})|^2 + \frac{1}{4}t_\perp^2}}$.

One can notice that the off-diagonal terms of the correlation matrix Eq.(3.26) and the correlation matrix Eq.(3.49) satisfy the relation

$$|u(\vec{k})|^2 + |v(\vec{k})|^2 = \frac{1}{4}. \tag{3.50}$$

The eigenvalues $\eta_\pm$ of this correlation matrix

$$\eta_\pm = \frac{1}{2}\left(1 \pm \frac{\frac{1}{2}t_\perp}{\sqrt{t^2|\gamma(\vec{k})|^2 + \frac{1}{4}t_\perp^2}}\right) \tag{3.51}$$

escort the entanglement levels

$$\xi_\pm = \pm 2\text{arsinh}\left(\frac{t_\perp}{2t|\gamma(\vec{k})|}\right). \tag{3.52}$$

In Fig.(3.4) we visualize the eigenvalue η_- of the correlation matrix around a given K-point.

In the Dirac points, the eigenvalues of the correlation matrix become $\eta_+ = 1$ and $\eta_- = 0$ and thus, the remaining subsystem is not entangled with the subsystem which is traced out.

Topological invariant

The entanglement gap is always opened, because the off-diagonal elements $v(\vec{k})$ of the correlation matrix do not vanish anywhere. This implies that the Berry curvature and all Berry phases are zero in entire Brillouin zone.

3.2.4 *Tracing out A1 and A2 (or B1 and B2) sublattices*

The correlation matrix given by tracing out A1 and A2 sublatties

$$C(\vec{k}) = \begin{pmatrix} \langle b^\dagger_{1\vec{k}} b_{1\vec{k}} \rangle & \langle b^\dagger_{1\vec{k}} b_{2\vec{k}} \rangle \\ \langle b^\dagger_{2\vec{k}} b_{1\vec{k}} \rangle & \langle b^\dagger_{2\vec{k}} b_{2\vec{k}} \rangle \end{pmatrix}$$

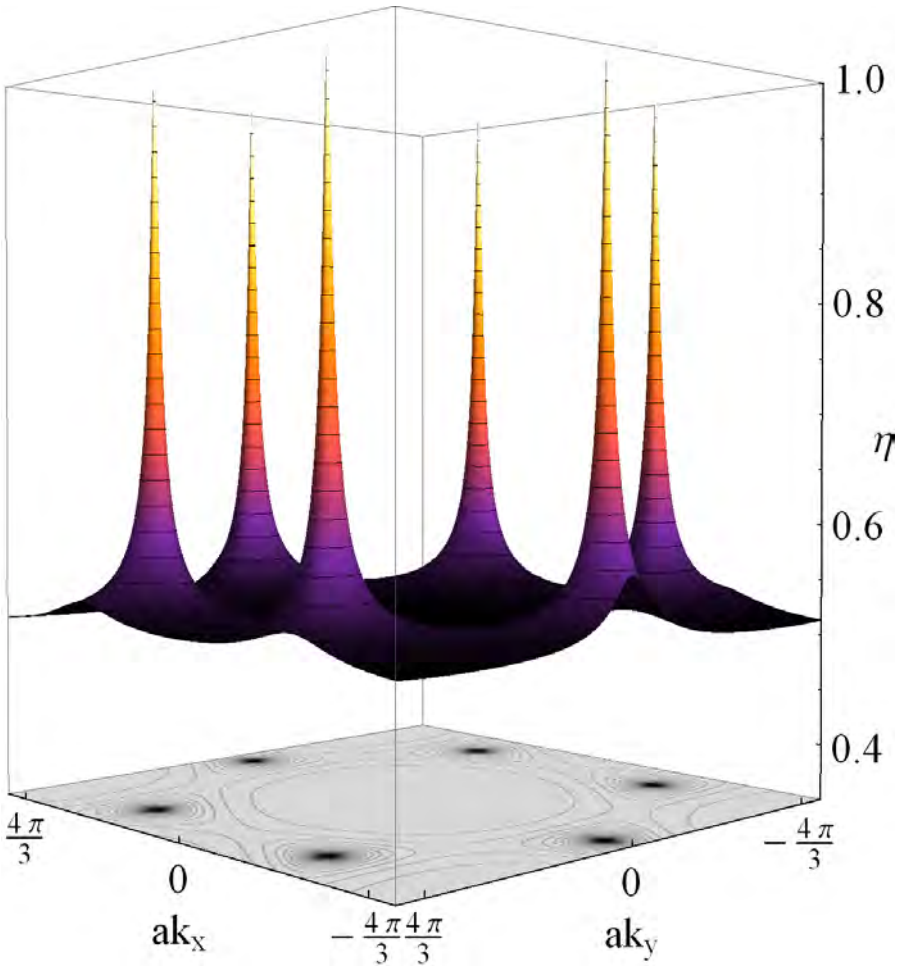

Figure 3.4: The eigenvalue $\eta_- = 1/2 + |v(\vec{k})|$ of the correlation matrix plotted over entire Brillouin zone for the same value of parameters as Fig.(3.2).

$$= \begin{pmatrix} \frac{1}{2} & 0 \\ 0 & \frac{1}{2} \end{pmatrix} \tag{3.53}$$

is proportional to the unit matrix. Thus, the remaining subsystem is maximally entangled with the traced out subsystem.

3.3 EFFECTS OF BIAS VOLTAGE AND MASS TERM

3.3.1 *Energy spectrum*

Bias voltage

Applying the bias voltage makes the difference of on-site energies Λ of different layers, thus the lower layer 1 of graphene bilayers is

on the energy $\epsilon_{A1} = \epsilon_{B1} = -\frac{\Lambda}{2}$ and the upper layer 2 is on the energy $\epsilon_{A2} = \epsilon_{B2} = \frac{\Lambda}{2}$. Then the Hamiltonian Eq.(3.2) becomes

$$\mathcal{H}_{\vec{k}} = \begin{pmatrix} -\frac{\Lambda}{2} & -t\gamma(\vec{k}) & 0 & 0 \\ -t\gamma^*(\vec{k}) & -\frac{\Lambda}{2} & t_\perp & 0 \\ 0 & t_\perp & \frac{\Lambda}{2} & -t\gamma(\vec{k}) \\ 0 & 0 & -t\gamma^*(\vec{k}) & \frac{\Lambda}{2} \end{pmatrix}. \tag{3.54}$$

The energy bands of this Hamiltonian are given by $\pm\varepsilon_{1,2}$ where

$$\varepsilon_{1,2} = \sqrt{t^2|\gamma(\vec{k})|^2 + \frac{t_\perp^2}{2} + \left(\frac{\Lambda}{2}\right)^2 \pm 2\sqrt{t^2|\gamma(\vec{k})|^2\left(\Lambda^2 + t_\perp^2\right) + \left(\frac{t_\perp}{2}\right)^4}}. \tag{3.55}$$

Thus, the changing of the bias voltage opens the band gap Λ between central energy bands ($\pm E_2$). The energy bands are plotted over entire Brillouin zone for $t = t_\perp$ and $\Lambda = 0.2t_\perp$ in Fig. 3.5.

Mass term

The mass term m makes the difference between the A and B sublattices. The Hamiltonian reads

$$\mathcal{H}_{\vec{k}} = \begin{pmatrix} m & -t\gamma(\vec{k}) & 0 & 0 \\ -t\gamma^*(\vec{k}) & -m & t_\perp & 0 \\ 0 & t_\perp & m & -t\gamma(\vec{k}) \\ 0 & 0 & -t\gamma^*(\vec{k}) & -m \end{pmatrix}. \tag{3.56}$$

The eigenenergies of the Hamiltonian Eq.(3.56) are given by $\pm\bar{\varepsilon}_{1,2}$ where

$$\bar{\varepsilon}_{1,2} = \sqrt{\left(\frac{1}{2}t_\perp \pm \sqrt{t^2|\gamma(\vec{k})|^2 + \frac{1}{4}t_\perp^2}\right)^2 + m^2}. \tag{3.57}$$

. The energy difference between two central bands ($\pm\bar{\varepsilon}_2$) is $2m$.

In Fig.(3.6), we plot these eigenergies throughout Brillouin zone for $t = t_\perp$ and $m = 0.1t_\perp$.

3.3.2 *Entanglement spectrum*

Bias voltage

Tracing out one layer 1 of ground state of bilayer graphene in the presence of the bias voltage leads to the correlation matrix

$$C(\vec{k}) = \begin{pmatrix} C_{11} & C_{12} \\ C_{12}^* & C_{22} \end{pmatrix} \tag{3.58}$$

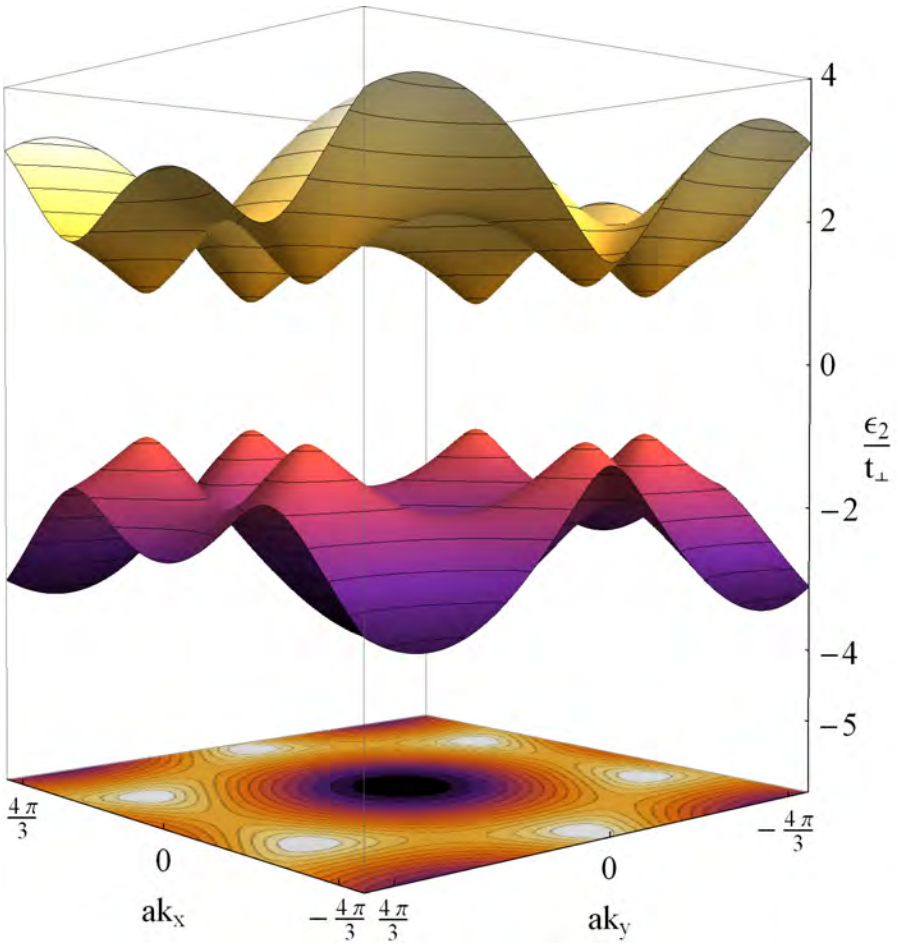

Figure 3.5: The central energy bands $\pm\varepsilon_2$ plotted over entire Brillouin zone for $t = t_\perp$ and $\Lambda = 0.2t_\perp$. The contour plot represents the energy band (ε_2).

where

$$C_{11}(\vec{k}) = \langle a^\dagger_{2\vec{k}} a_{2\vec{k}} \rangle$$
$$= \frac{1}{2} - \frac{1}{4}\left(1 - \frac{\frac{1}{2}t_\perp^2}{\sqrt{t^2|\gamma(\vec{k})|^2(t_\perp^2+\Lambda^2)+\frac{1}{4}t_\perp^4}}\right)\frac{\Lambda}{\sqrt{\Lambda^2+t_\perp^2}}\frac{1}{\varepsilon_2}\left(e_2 - \frac{t_1^2}{\sqrt{\Lambda^2+t_\perp^2}}\right)$$
$$+ \frac{1}{4}\left(1 + \frac{\frac{1}{2}t_\perp^2}{\sqrt{t^2|\gamma(\vec{k})|^2(t_\perp^2+\Lambda^2)+\frac{1}{4}t_\perp^4}}\right)\frac{\Lambda}{\sqrt{\Lambda^2+t_\perp^2}}\frac{1}{\varepsilon_1}\left(e_1 - \frac{t_1^2}{\sqrt{\Lambda^2+t_\perp^2}}\right)$$
$$C_{22} = \langle b^\dagger_{2\vec{k}} b_{2\vec{k}} \rangle$$
$$= \frac{1}{2} - \frac{1}{4}\left(1 + \frac{\frac{1}{2}t_\perp^2}{\sqrt{t^2|\gamma(\vec{k})|^2(t_\perp^2+\Lambda^2)+\frac{1}{4}t_\perp^4}}\right)\frac{\Lambda}{\sqrt{\Lambda^2+t_\perp^2}}\frac{1}{\varepsilon_2}\left(e_2 + \frac{t_1^2}{\sqrt{\Lambda^2+t_\perp^2}}\right)$$
$$+ \frac{1}{4}\left(1 - \frac{\frac{1}{2}t_\perp^2}{\sqrt{t^2|\gamma(\vec{k})|^2(t_\perp^2+\Lambda^2)+\frac{1}{4}t_\perp^4}}\right)\frac{\Lambda}{\sqrt{\Lambda^2+t_\perp^2}}\frac{1}{\varepsilon_1}\left(e_1 + \frac{t_1^2}{\sqrt{\Lambda^2+t_\perp^2}}\right)$$

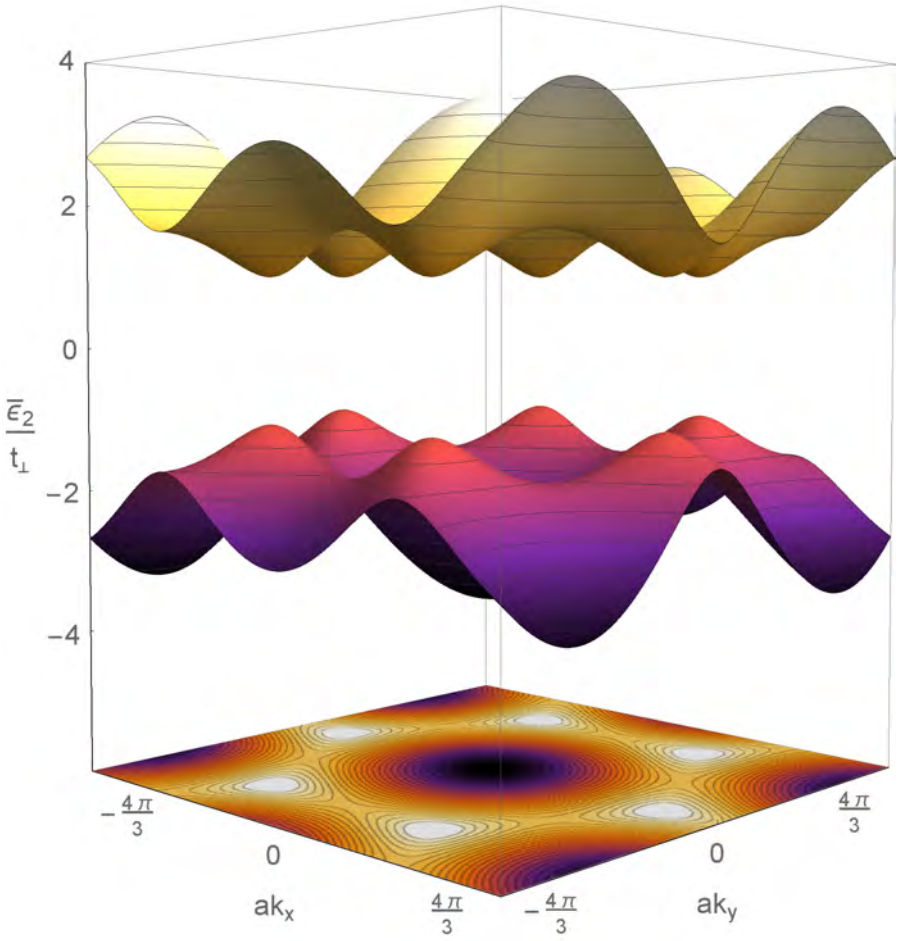

Figure 3.6: The central energy bands $\pm\bar{\varepsilon}_2$ plotted over entire Brillouin zone for $t = t_\perp$ and $m = 0.1t_\perp$. The contour plot represents the energy band ($\bar{\varepsilon}_2$).

$$C_{12} = \langle a^\dagger_{2\vec{k}} b_{2\vec{k}} \rangle$$
$$= \frac{1}{2} e^{i\phi(\vec{k})} \frac{t|\gamma(\vec{k})|}{\sqrt{t^2|\gamma(\vec{k})|^2 + \frac{1}{4}\frac{t_\perp^4}{t_\perp^2+\Lambda^2}}} \left(\frac{e_1}{\varepsilon_1} - \frac{e_2}{\varepsilon_2}\right) \tag{3.59}$$

with

$$e_{1,2} = \frac{1}{2}\left(\sqrt{\Lambda^2 + t_\perp^2} \pm \sqrt{4t^2|\gamma(\vec{k})|^2 + \frac{t_\perp^4}{t_\perp^2 + \Lambda^2}}\right) \tag{3.60}$$

The entanglement levels analytically obtained from this correlation matrix will be discussed later in 3.3.2.

Mass term

The correlation matrix of ground state of graphene bilayers in the presence of the mass term m given by tracing out one layer 1 reads

$$C(\vec{k}) = \begin{pmatrix} C_{11} & C_{12} \\ C_{12}^{*} & C_{22} \end{pmatrix} \tag{3.61}$$

where

$$\begin{aligned}
C_{11}(\vec{k}) &= \langle a_{2\vec{k}}^{\dagger} a_{2\vec{k}} \rangle \\
&= \frac{1}{2} - \frac{1}{4}\left(1 - \frac{\frac{1}{2}t_{\perp}}{\sqrt{t^2|\gamma(\vec{k})|^2 + \frac{1}{4}t_{\perp}^2}}\right)\frac{m}{\overline{\varepsilon}_2} + \left(1 + \frac{\frac{1}{2}t_{\perp}}{\sqrt{t^2|\gamma(\vec{k})|^2 + \frac{1}{4}t_{\perp}^2}}\right)\frac{m}{\overline{\varepsilon}_1} \\
C_{22}(\vec{k}) &= \langle b_{2\vec{k}}^{\dagger} b_{2\vec{k}} \rangle \\
&= \frac{1}{2} + \frac{1}{4}\left(1 + \frac{\frac{1}{2}t_{\perp}}{\sqrt{t^2|\gamma(\vec{k})|^2 + \frac{1}{4}t_{\perp}^2}}\right)\frac{m}{\overline{\varepsilon}_2} + \left(1 - \frac{\frac{1}{2}t_{\perp}}{\sqrt{t^2|\gamma(\vec{k})|^2 + \frac{1}{4}t_{\perp}^2}}\right)\frac{m}{\overline{\varepsilon}_1} \\
C_{12}(\vec{k}) &= \langle a_{2\vec{k}}^{\dagger} b_{2\vec{k}} \rangle \\
&= \frac{1}{2}\mathrm{e}^{i\phi(\vec{k})}\frac{t|\gamma(\vec{k})|}{\sqrt{t^2|\gamma(\vec{k})|^2 + \frac{1}{4}t_{\perp}^2}}\left(\frac{\overline{e}_1}{\overline{\varepsilon}_1} - \frac{\overline{e}_2}{\overline{\varepsilon}_2}\right)
\end{aligned} \tag{3.62}$$

with

$$\overline{e}_{1,2} = \frac{1}{2}t_{\perp} \pm \sqrt{t^2|\gamma(\vec{k})|^2 + \frac{1}{4}t_{\perp}^2}. \tag{3.63}$$

Analytical results

The entanglement levels obtained from the correlation matrices Eq.(3.58) and Eq.(3.61) have the following form

$$\xi_{\pm} = -2\mathrm{arctanh}\left(C_{11} + C_{22} - 1 \pm \sqrt{(C_{11} - C_{22})^2 + |C_{12}|^2}\right). \tag{3.64}$$

Our analytically obtained entanglement levels Eq.(3.64) are visualized in the Fig.(3.7) of graphene bilayers in the presence of the bias voltage along the axis k_x for $t/t_{\perp} = 1$ and $U/t_{\perp} = 0.2$. Meanwhile, the entanglement levels of graphene bilayers in the presence of mass term are represented in Fig. (3.8) along the axis k_x.

When the bias voltage or mass term are included, the average occupancy number at site A, $C_{11}(\vec{k})$, and the average occupancy number at site B, $C_{22}(\vec{k})$ are not equal and differ from the 1/2. This leads to the remaining layer 2 not being half-filled obtained

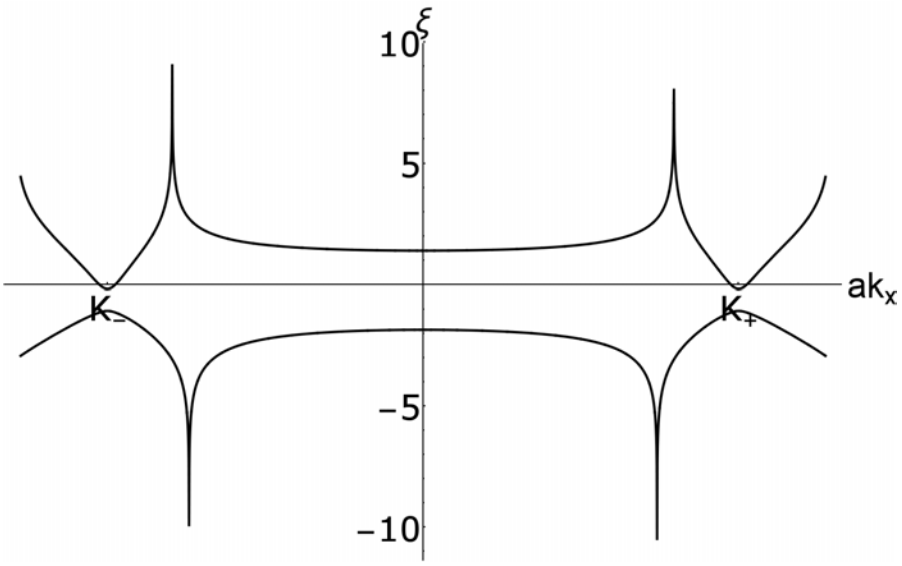

Figure 3.7: The central energy bands $\pm\varepsilon_2$ plotted over entire Brillouin zone along the k_x axis for $t = t_\perp$ and $\Lambda = 0.2t_\perp$.

from ground state of half-filed graphene bilayers, and the entanglement gap between entanglement levels is opened. In this context, there is no the relation of the entanglement spectrum of undoped graphene bilayers and the energy of doped graphene monolayer. All this is just a consequence of the hopping parameter $t_\perp$ couples A1 and B2 sites which have different sign.

3.4 CONCLUSION AND OUTLOOK

We have analytically derived the entanglement Hamiltonian of ground state of Bernal stacked graphene bilayers. When the entanglement Hamiltonian is obtained by tracing out one layer, there is a proportionality between it and the energetic Hamiltonian of the remaining monolayer of graphene in the limit of strong coupling layers. The proportionality factor represents the phenomenological inverse temperature, and there is an exact relation between this phenomenological scale and the inverse temperature. Furthermore, this relation leads to that the canonical Hamiltonian being independent of temperature.

The proportionality between the entanglement Hamiltonian of graphene bilayers and the energetic Hamiltonian of monolayer graphene also leads to the equivalence of their topological quantities. In this case, this is the Berry phase contribution to the Chern number.

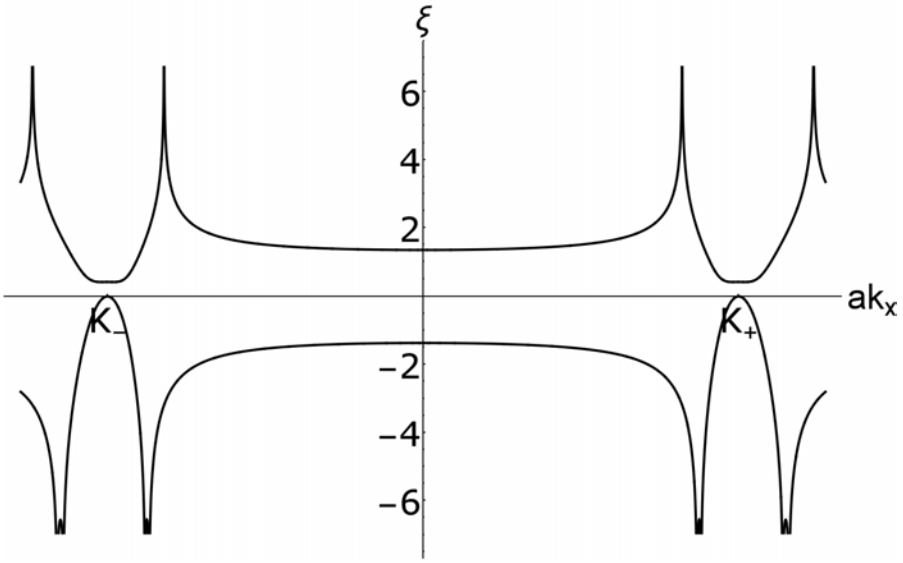

Figure 3.8: The entanglement spectrum of graphene bilayers in the presence the mass term plotted along the k_x axis for $t/t_\perp = 1$ and $m/t_\perp = 0.1$.

In the presence of the on-site energy or the mass term, the remaining layer is doped which is obtained by tracing other layer from ground state of undoped graphene bilayers. In such a way, there is no relation between the entanglement Hamiltonian of graphene bilayers and the energetic Hamiltonian of graphene monolayer.

The relation between the phenomenological inverse temperature and the inverse thermodynamic temperature given by Eq.(3.43), depends on the lattice geometry, Ref. [Schliemann, 2013]. Thus, one possible extension of this is to consider other lattice geometry.

4

TRIGONAL WARPING IN BILAYER GRAPHENE: ENERGY VERSUS ENTANGLEMENT SPECTRUM

Most of the work presented in this chapter has been published to the Physical Review Journal B.
Sonja Predin, Paul Wenk and John Schliemann, Trigonal Warping in Bilayer Graphene: Energy versus Entanglement Spectrum, Phys. Rev. B ***93****, 115106, (2016).* [Predin et al., 2016]

In the previous Chapter 3, we have shown that upon tracing out one layer, the entanglement Hamiltonian of ground state of free fermions in graphene bilayers arranged in Bernal stacking is proportional to the energetic Hamiltonian of graphene monolayer in the strong coupling limit. However, this does not hold in general even in the strong coupling limit what is illustrated by counterexamples in Ref. [Lundgren et al., 2012] where a spin ladders of clearly nonidentical legs were considered and in Ref. [Schliemann and Läuchli, 2012] where the anisotropic spin ladders of the arbitrary spin length were considered, while then even the unperturbed non-degenerate ground state has a nontrivial entanglement spectrum. In this Chapter we provide another counter example given by graphene bilayers in the presence of trigonal warping [McCann and Koshino, 2013,Rozhkov et al., 2016]. As we shall see in the following, the geometric properties of the entanglement spectrum of an undoped graphene bilayer and the energy spectrum of a monolayer clearly differ qualitatively. However, certain topological quantities such as Berry phase type contributions to Chern numbers agree. After we had made our work available as an arXiv preprint and submitted to the journal, we became aware of a little bit earlier study Ref. [Fukui and Hatsugai, 2014], where also Chern numbers calculated from the eigenstates of entanglement Hamiltonians are studied.

This Chapter is organized as follows. In Section 4.1 we discuss the full eigensystem of the tight-binding model of bilayer graphene in the presence of trigonal warping. To enable analytical progress we neglect here terms breaking particle-hole symmetry. On the other hand, our calculation considers the entire first Brillouin zone and avoids the Dirac cone approximation usually employed in studies of trigonal warping in graphene bilayers [McCann and Fal'ko, 2006, Nilsson et al., 2006, Koshino and Ando, 2006, Kechedzhi et al., 2007, Manes et al., 2007, Cserti et al., 2007, Mikitik and Sharlai, 2008, Mariani et al., 2012, Cosma and Fal'ko, 2015]. We compare our results for the full four-band model with an effective Hamiltonian acting on the two central bands [McCann and Fal'ko, 2006, Mariani et al., 2012, Cosma and Fal'ko, 2015]. The entanglement spectrum obtained from the ground state of undoped graphene bilayers is analyzed in Section 4.2. We discuss the case of one layer being traced out as well as the situation where the trace is performed over two other out of four sublattices. In Section 4.3 we will show that discontinuities of wave vector in eigenvectors of the Hamiltonian are reflected on the entanglement Hamiltonian and have a large influence on the geometric and topological properties of the entanglement Hamiltonian. We close with a conclusion and an outlook in Section 4.4.

4.1 ENERGY SPECTRUM OF GRAPHENE BILAYERS: TRIGONAL WARPING AND TOPOLOGICAL INVARIANTS

The standard tight-binding Hamiltonian for graphene bilayers in Bernal stacking can be formulated as [McCann and Koshino, 2013, Rozhkov et al., 2016]

$$\begin{aligned} H = & -t \sum_{\vec{k}} \left(\gamma(\vec{k}) a^\dagger_{1\vec{k}} b_{1\vec{k}} + \gamma(\vec{k}) a^\dagger_{2\vec{k}} b_{2\vec{k}} + \text{h.}c. \right) \\ & + t_\perp \sum_{\vec{k}} \left(b^\dagger_{1\vec{k}} a_{2\vec{k}} + a^\dagger_{2\vec{k}} b_{1\vec{k}} \right) \\ & - t_3 \sum_{\vec{k}} \left(\gamma(\vec{k}) b^\dagger_{2\vec{k}} a_{1\vec{k}} + \gamma^*(\vec{k}) a^\dagger_{1\vec{k}} b_{2\vec{k}} \right) \\ & + t_4 \sum_{\vec{k}} \left(\gamma(\vec{k}) \left(a^\dagger_{1\vec{k}} a_{2\vec{k}} + b^\dagger_{1\vec{k}} b_{2\vec{k}} \right) + \text{h.}c. \right) , \end{aligned} \tag{4.1}$$

where $a^\dagger_{i\vec{k}}$ ($a_{i\vec{k}}$) and $b^\dagger_{i\vec{k}}$ ($b_{i\vec{k}}$) create (annihilate) electrons with wave vector $\vec{k}$ in layers $i = 1, 2$ on sublattice A and B, respectively. Moreover, $\gamma(\vec{k}) = \sum_{l=1}^{3} \exp(i\vec{k} \cdot \vec{\delta}_l)$ where the $\vec{\delta}_l$ are the vectors connecting a given carbon atom with its nearest neighbors on the

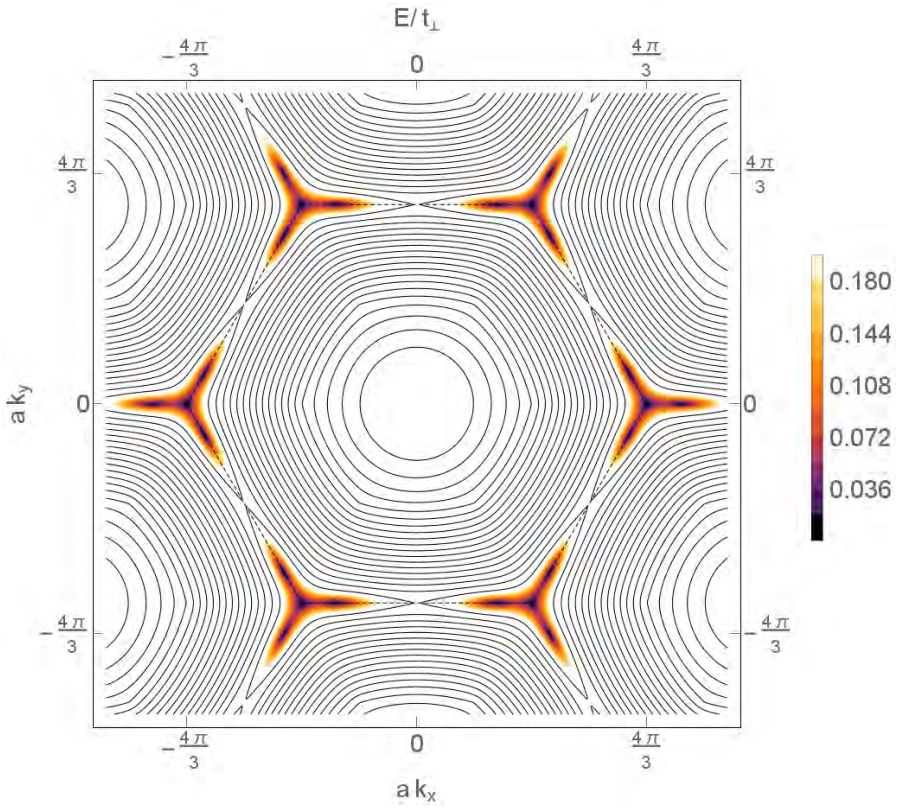

Figure 4.1: Contour plot of the energy band $(+E_2(\vec{k}))$ plotted for $t_\perp = t$, $t_3 = 0.5t$. The contour of the colored region indicates $E = 0.2/t_\perp$. The edge of the first Brillouin zone is marked by dashed lines.

other sublattice in a graphene monolayer defined by Eq(2.5). The hopping parameters $t, t_\perp, t_3, t_4$ are plotted at Fig(3.1).

The presence of all four couplings in the Hamiltonian Eq. (4.1) makes its explicit diagonalization in terms of analytical expressions a particularly cumbersome task. As the present study chiefly relies on analytical calculations rather than resorts to numerics, we will drop the contributions proportional to the smallest parameter t_4 in order to achieve an analytically manageable situation.

Putting $t_4 = 0$ the full eigensystem of the Hamiltonian (4.1) can be obtained in a closed analytical fashion as detailed in appendix A. The four dispersion branches $(\pm E_1(\vec{k}))$, $(\pm E_2(\vec{k}))$ form a symmetric spectrum with

$$E_{1/2}(\vec{k}) = \left[\frac{1}{2}\left(t_\perp^2 + t_3^2|\gamma(\vec{k})|^2 + 2t^2|\gamma(\vec{k})|^2\right) \pm \frac{1}{2}\sqrt{4t^2|\gamma(\vec{k})|^2\left(t_\perp^2 + t_3^2|\gamma(\vec{k})|^2 - 2t_\perp t_3|\gamma(\vec{k})|\cos\left(3\phi_{\vec{k}}\right)\right) + \left(t_\perp^2 - t_3^2|\gamma(\vec{k})|^2\right)^2}\right]^{1/2} \tag{4.2}$$

and $\gamma(\vec{k}) = |\gamma(\vec{k})|e^{i\phi_{\vec{k}}}$. The two outer branches ($\pm E_1(\vec{k})$) are separated from the inner ones ($\pm E_2(\vec{k})$) by gaps determined essentially by the hopping parameter $t_\perp$. The result Eq. (4.2) generalizes the energy spectrum given in Ref. [McCann and Fal'ko, 2006] within the Dirac cone approximation to the full Brillouin zone. Moreover, in appendix A we also give the complete data of the corresponding eigenvectors. Fig. 4.2 concentrates on the vicinity of a given K-point using realistic parameters.

The inner branches ($\pm E_2(\vec{k})$) dominate the low-energy physics of the system near half filling and meet at zero energy for

$$\gamma(\vec{k}) = 0 \tag{4.3}$$

corresponding to the two inequivalent corners $K_\pm$ of the first Brillouin zone, and for

$$\cos\left(3\phi_{\vec{k}}\right) = -1 \quad \wedge \quad |\gamma(\vec{k})| = \frac{t_\perp t_3}{t^2}\,. \tag{4.4}$$

The latter condition defines three additional satellite Dirac cones around each K-point two of which lying on the edges (faces) of the Brillouin zone connecting $K_\pm$. The third satellite Dirac cone lies formally outside the Brillouin zone but is equivalent to a satellite cone on the edge around an equivalent K-point. Indeed, the quantity $\gamma(\vec{k})$ has a constant phase $\phi_{\vec{k}} \in \{-\pi/3, \pi/3, \pi\}$ on each face: As an example, consider the edge connecting the two inequivalent K-points given by $\vec{K}_\pm = \frac{2\pi}{\sqrt{3}a}\left(\pm\frac{1}{\sqrt{3}}, 1\right)$ where one finds

$$\gamma\left(k_x, \frac{2\pi}{\sqrt{3}a}\right) = e^{-i\pi/3}\left(2\cos\left(\frac{a}{2}k_x\right) - 1\right) \tag{4.5}$$

with the parenthesis being nonnegative for k_x ranging between $(\pm 2\pi/(3a))$. Thus, solving for k_x the satellite Dirac cones on that edge lie at

$$\vec{k} = \left(\pm\frac{2}{a}\arccos\left(\frac{1}{2}\left(1 + \frac{t_\perp t_3}{t^2}\right)\right), \frac{2\pi}{\sqrt{3}a}\right), \tag{4.6}$$

and the other satellite cones are located at positions being equivalent under reciprocal lattice translation and/or hexagonal rotation. Note that for $t_\perp t_3/t^2 = 1$ the satellite cones merge in the M-points (centers of the faces) and they vanish for even larger values of that ratio. In Fig. 4.1 we give a sketch of the situation in the entire Brillouin zone for moderate values of $t_\perp$ and t_3. As

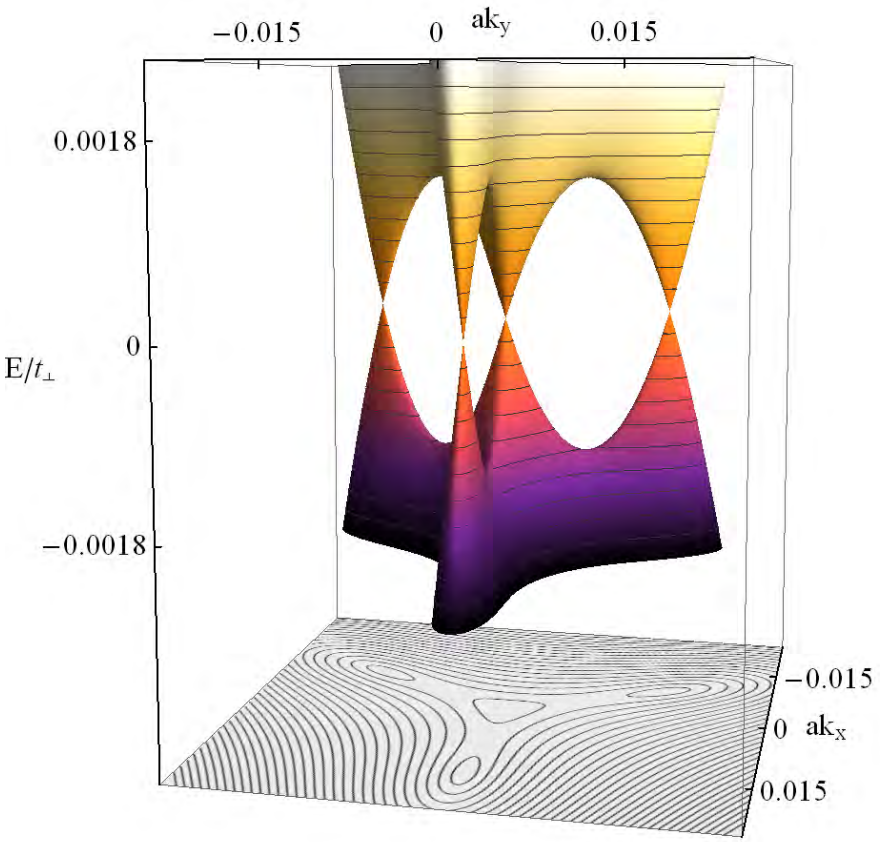

Figure 4.2: The central energy bands ($\pm E_2(\vec{k})$) plotted around a given K-point for $t_\perp = 0.1t$, $t_3 = 0.15t$. The dispersions show a central Dirac cone accompanied by three satellites. The components of the wave vector are measured relatively to the K-point.

we have already seen in Chapter 3, for $t_3 = 0$ the two energy bands ($\pm E_2(\vec{k})$) touch only at the K-points where they have a quadratic dispersion. Finite $t_3 \neq 0$ causes a splitting into in total four Dirac cones with linear dispersion, an effect known as trigonal warping [McCann and Koshino, 2013, Mariani et al., 2012].

As a further important property, the eigenvectors corresponding to ($\pm E_2(\vec{k})$) are discontinuous as a function of wave vector at the degeneracy points defined by Eq. (4.4); for more technical details we refer to chapter 4.3. As a simplistic toy model mimicking such an effect one can consider the Hamiltonian $H = -k\sigma^z$ with a one-dimensional wave number k and the Pauli matrix σ^z describing some internal degree of freedom: In the many-body ground state

of zero Fermi energy all occupied states with $k > 0$ have spin up while for all states with $k < 0$ the spin points downwards, resulting in a discontinuity of the occupied eigenvectors at $k = 0$. As we shall see below, in the present case of graphene bilayers this discontinuity is also reflected in the entanglement spectrum.

An effective Hamiltonian in the presence of the trigonal warping providing an approximate description of the central bands ($\pm E_2(\vec{k})$) can be given following Ref. [McCann and Fal'ko, 2006]. In up to linear order in $1/t_\perp$ one finds

$$H = -\begin{pmatrix} 0 & \frac{t^2}{t_\perp}\left(\gamma^*(\vec{k})\right)^2 + t_3\gamma(\vec{k}) \\ \frac{t^2}{t_\perp}\left(\gamma(\vec{k})\right)^2 + t_3\gamma^*(\vec{k}) & 0 \end{pmatrix} \tag{4.7}$$

with respect to the basis $\left(b^\dagger_{2\vec{k}}, a^\dagger_{1\vec{k}}\right)|0\rangle$. The eigenstates read

$$|\chi_\pm\rangle = \frac{1}{\sqrt{2}}\begin{pmatrix} 1 \\ \mp e^{i\psi_{\vec{k}}} \end{pmatrix} \tag{4.8}$$

with

$$e^{i\psi_{\vec{k}}} = \frac{\frac{t^2}{t_\perp}\left(\gamma(\vec{k})\right)^2 + t_3\gamma^*(\vec{k})}{\left|\frac{t^2}{t_\perp}\left(\gamma(\vec{k})\right)^2 + t_3\gamma^*(\vec{k})\right|}. \tag{4.9}$$

Note that the Hamiltonian (4.7) vanishes if and only if the conditions (4.3) or (4.4) are fulfilled implying that the positions of the central and satellite Dirac cones are the same as for the full Hamiltonian (4.1). Moreover , $\psi_{\vec{k}}$ is a smooth and well-defined function of the wave vector except for the locations of Dirac cones. Accordingly, the Berry curvature

$$F(\vec{k}) = \frac{\partial A_y}{\partial k_x} - \frac{\partial A_x}{\partial k_y} \tag{4.10}$$

arising from the Berry connection

$$\vec{A}(\vec{k}) = i\langle\chi_\pm(\vec{k})|\frac{\partial}{\partial\vec{k}}|\chi_\pm(\vec{k})\rangle = -\frac{1}{2}\frac{\partial\psi_{\vec{k}}}{\partial\vec{k}} \tag{4.11}$$

vanishes everywhere outside the Dirac cones where contributions in terms of δ-functions arise. Integrating the Berry connection along closed path in $\vec{k}$-space leads to geometrical quantities often referred to as Berry phases, although no contact to adiabaticity is made here. Moreover, if the Berry curvature has only nonzero contributions in terms of δ-functions (as it is the case here and in the following) these geometrical phases are indeed topological, i.e. they are invariant under continuous variations of the paths as long as the support of the δ-functions is not touched.

As discussed in Refs. [Manes et al., 2007, Mikitik and Sharlai, 2008, Mariani et al., 2012], integrating along a closed path around the central Dirac cones at $K_\pm$ yields a Berry phase of $(\mp\pi)$, while each of the accompanying satellite cones gives a contribution of $(\pm\pi)$. Thus, the total Berry phase arising at and around each K-point is, as in the absence of trigonal warping, $(\pm 2\pi)$, and the integral over the whole Brillouin zone of the Berry connection (i.e. the Chern number) vanishes. Naturally, our present analysis going beyond the Dirac cone approximation confirms these results.

4.2 ENTANGLEMENT SPECTRA

Here we analytically derive the entanglement Hamiltonian of free fermions on bilayer honeycomb lattice in the presence of trigonal warping by using the method described in Chapter 3. In particular, we formulate the entanglement Hamiltonian for systems of free fermions as a single-particle operator [Peschel, 2003, Cheong and Henley, 2004, Schliemann, 2013].

4.2.1 *Tracing out one layer*

We now consider the ground state of the undoped graphene bilayer such that all states with negative energies $(-E_1(\vec{k}))$, $(-E_2(\vec{k}))$ are occupied while all others are empty. Tracing out layer 1 leads to the correlation matrix

$$C(\vec{k}) = \begin{pmatrix} \frac{1}{2} & u(\vec{k}) \\ u^*(\vec{k}) & \frac{1}{2} \end{pmatrix} \tag{4.12}$$

where an explicit expression for $u(\vec{k})$ is given in appendix B. The entanglement levels corresponding to the eigenvalues $\eta_\pm(\vec{k}) = 1/2 \mp |u(\vec{k})|$ are

$$\xi_\pm(\vec{k}) = \pm\, 2\,\mathrm{artanh}\left(2|u(\vec{k})|\right) . \tag{4.13}$$

The modulus $|u|$ can be formulated as

$$|u| = \frac{1/2}{\sqrt{1+(d/(t|\gamma(\vec{k})|))^2}} \sqrt{\frac{1}{2}\left(1 - \frac{\epsilon_1\epsilon_2 + b^2}{E_1 E_2}\right)} \tag{4.14}$$

with (cf. Eqs. (A.14),(A.15))

$$d = \frac{\left(t_\perp^2 - t_3^2|\gamma(\vec{k})|^2\right)/2}{\sqrt{t_\perp^2 + t_3^2|\gamma(\vec{k})|^2 - 2t_\perp t_3|\gamma(\vec{k})|\cos\left(3\phi_{\vec{k}}\right)}} , \tag{4.15}$$

$$b = \frac{t_\perp t_3 |\gamma(\vec{k})| |\sin\left(3\phi_{\vec{k}}\right)|}{\sqrt{t_\perp^2 + t_3^2|\gamma(\vec{k})|^2 - 2t_\perp t_3|\gamma(\vec{k})|\cos\left(3\phi_{\vec{k}}\right)}}, \quad (4.16)$$

and (cf. Eq. (A.21))

$$\epsilon_{1,2} = t|\gamma(\vec{k})| \pm\sqrt{\left(t_\perp^2 + t_3^2|\gamma(\vec{k})|^2 - 2t_\perp t_3|\gamma(\vec{k})|\cos\left(3\phi_{\vec{k}}\right)\right)^2/4 + d^2} \quad (4.17)$$

implying

$$E_{1,2} = \sqrt{\epsilon_{1,2}^2 + b^2}\,. \quad (4.18)$$

The r.h.s of Eq. (4.14) becomes zero if the radicand vanishes. According to the discussion in Section 4.3 and Appendix B this is the case when $\cos\left(3\phi_{\vec{k}}\right) = -1$ leading to $b = 0$ and $E_1 = \epsilon_1 \geq 0$, $E_2 = |\epsilon_2|$ such that

$$|u| \propto \sqrt{\frac{1}{2}\left(1 - \frac{\epsilon_2}{|\epsilon_2|}\right)} \quad (4.19)$$

Now equation (4.27) shows that $|u(\vec{k})| = 0$ is equivalent to

$$\cos\left(3\phi_{\vec{k}}\right) = -1 \quad \wedge \quad |\gamma(\vec{k})| \in \left[0, t_\perp t_3/t^2\right], \quad (4.20)$$

where the endpoint of the above interval defines according to condition (4.4) the location of the satellite Dirac cones. As a result, the entanglement levels (4.13) vanish along segments of the faces of the first Brillouin zone bounded by the positions of the central Dirac cones and their satellites. At the satellite Dirac cones the entanglement spectrum is discontinuous as a function of wave vector. In Fig. 4.3 we plotted the entanglement spectrum $\xi_+(\vec{k})$ for the whole Brillouin zone. For a better visualization large hopping parameters have been chosen. The contour of the colored region connects all three satellite Dirac cones. As discussed in chapter 4.3, this discontinuity is inherited from a discontinuity in the eigenvectors of the occupied single-particle states. The entanglement spectrum in the entire Brillouin zone is illustrated in Fig. 4.3, whereas Fig. 4.4 focuses on a given K-point.

Moreover, apart from the eigenvalues of the entanglement Hamiltonian, let us also consider its eigenvector which coincide with the eigenvectors of the correlation matrix (D.8). As discussed in appendix B, the complex function $u(\vec{k})$ entering the correlation matrix becomes singular at the K-points and the positions of the accompanying satellite Dirac cones of the energy spectrum,

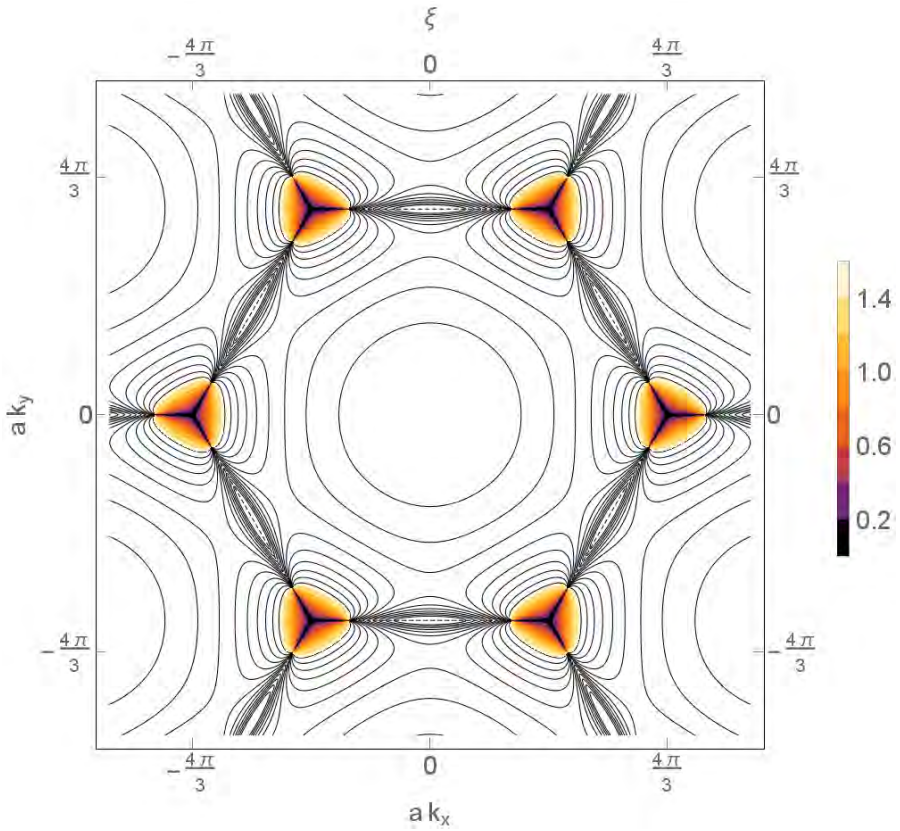

Figure 4.3: Contour plot of the entanglement spectrum $\xi_+(\vec{k})$ plotted for $t_\perp = t$, $t_3 = 0.5t$. The contour of the colored region indicates $\xi = 1.5$. The dashed line delineates the first Brillouin zone.

leading again to δ-function-type contributions to the Berry curvature which vanishes otherwise. Combining symbolic computer algebra techniques and numerical calculations we find here a Berry phase of $(\mp\pi/2)$ around the corners $K_\pm$ of the Brillouin zone, and $(\pm\pi/2)$ for the corresponding satellite positions. For the central positions the above calculations can also be done fully analytically by expanding the eigensystem data around $K_\pm$. For the satellite locations such an expansion is not possible due to the discontinuity of the eigenvectors.

Thus, the total Berry phase contribution from each K-point $K_\pm$ is $(\pm\pi)$ and agrees with the Berry phase around the Dirac cones in monolayer graphene. As a result, although the entanglement spectrum of graphene bilayers generated by tracing out one layer shows obvious differences to the energy spectrum of monolayer graphene regarding qualitative geometrical properties, the topological Berry phases obtained from the corresponding eigenvectors still coincide at each K-point.

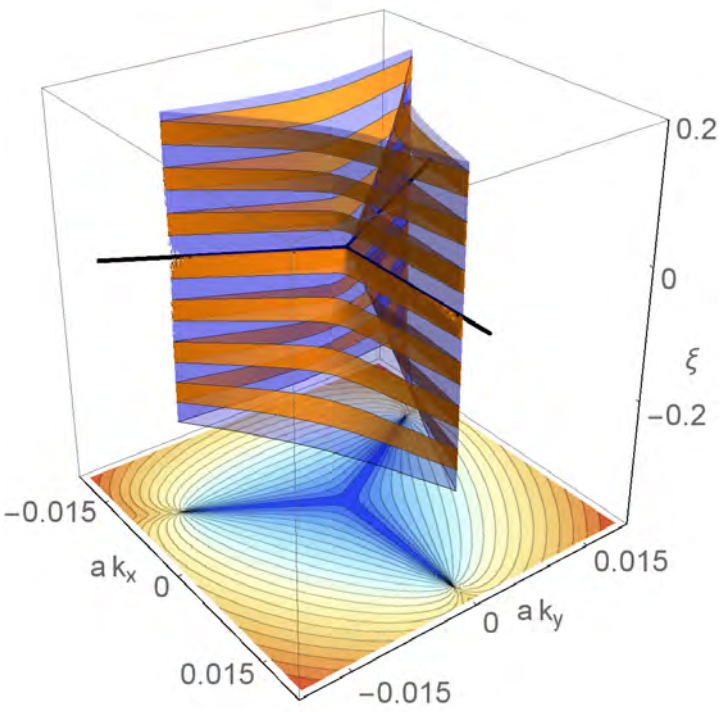

Figure 4.4: The entanglement spectrum (4.13) plotted around a given K-point for the same parameters as in Fig. 4.2. The density plot shows the upper entanglement level. Zero eigenvalues of the entanglement Hamiltonian occur along lines connecting the K-point with the locations of satellite Dirac cones of the energy spectrum (thick black lines). The components of the wave vector are measured relatively to the K-point.

4.2.2 *Tracing out other sublattices*

Now, we will consider the entanglement spectrum obtained by tracing out sublattices A1 and B2 (or A2 and B1) lying in different layers. In the former case one finds

$$C(\vec{k}) = \begin{pmatrix} \frac{1}{2} & v(\vec{k}) \\ v^*(\vec{k}) & \frac{1}{2} \end{pmatrix} \tag{4.21}$$

where an explicit expression for $v(\vec{k})$ is given in appendix B. The above correlation matrix has eigenvalues $\eta_\pm(\vec{k}) = 1/2 \mp |v(\vec{k})|$ leading to the entanglement levels

$$\xi_\pm(\vec{k}) = \pm 2\,\mathrm{artanh}\left(2|v(\vec{k})|\right) . \tag{4.22}$$

In Fig. 4.5 we plotted the eigenvalues $\eta_-(\vec{k}) = 1/2 + |v(\vec{k})|$ of the correlation matrix around a given K-point. The modulus $|v(\vec{k})|$ reads more explicitly

$$|v(\vec{k})| = \frac{1}{2}\sqrt{1 - \frac{t^2|\gamma(\vec{k})|^2}{t^2|\gamma(\vec{k})|^2 + d^2}\frac{1}{2}\left(1 - \frac{\epsilon_1\epsilon_2 + b^2}{E_1E_2}\right)} \tag{4.23}$$

$$= \frac{1}{2}\sqrt{1 - 4|u(\vec{k})|^2} \tag{4.24}$$

and has a similar structure as $|u(\vec{k})|$ given in Eq. (4.14). In particular, $|v(\vec{k})| = 1/2 \Leftrightarrow |u(\vec{k})| = 0$ if the conditions (4.20) are fulfilled. In this case $\eta_+ = 0$ and $\eta_- = 1$ indicating that the remaining subsystem is unentangled with the system traced out.

Regarding Berry phases generated from the eigenstates of the correlation matrix (4.21) we note that the off-diagonal element $v(\vec{k})$ nowhere vanishes. As a consequence the Berry curvature is zero throughout the Brillouin zone, which in turn holds for all Berry phases. The nonvanishing of $v(\vec{k})$ follows from the fact that $|v(\vec{k})| = 0$ would require $|u(\vec{k})| = 1/2$ such that the entanglement (4.13) would diverge which is, as seen in section 4.2.1, not the case.

Finally, the correlation matrix obtained by tracing over the sublattices A1, A2 (or B1, B2) is proportional to the unit matrix,

$$C(\vec{k}) = \begin{pmatrix} \frac{1}{2} & 0 \\ 0 & \frac{1}{2} \end{pmatrix}, \tag{4.25}$$

indicating that these sublattices are maximally entangled with the part traced out.

4.3 CONTINUITY PROPERTIES

The eigenvectors corresponding to the energy branches $(\pm E_2(\vec{k}))$ are discontinuous at wave vectors determined by the condition (4.4). This comes about as follows: The matrix elements $U_{2,n}(\vec{k})$, $U_{3,n}(\vec{k})$, $n \in \{1,2,3,4\}$ contain the quantities $\gamma_\pm^{(2)}$ defined in Eqs. (C.25) whereas the $U_{1,n}(\vec{k})$, $U_{4,n}(\vec{k})$ corresponding to $(\pm E_1(\vec{k}))$ involve $\gamma_\pm^{(1)}$. Fixing now $\cos\left(\phi_{\vec{k}}\right) = -1$ we have $b = 0$ such that $E_1 = \epsilon_1 \geq 0$ and $E_2 = |\epsilon_2|$ such that $\gamma_\pm^{(1)}$ remain continuous while $\gamma_\pm^{(2)}$ become

$$\gamma_\pm^{(2)} = \sqrt{\frac{1}{2}\left(1 \pm \frac{\epsilon_2}{|\epsilon_2|}\right)}. \tag{4.26}$$

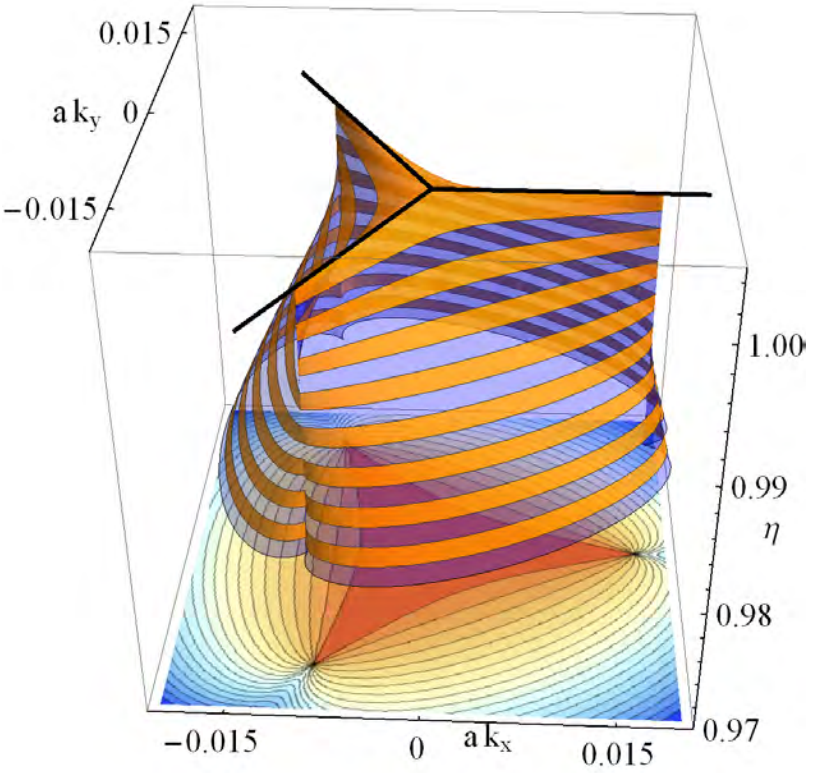

Figure 4.5: Eigenvalues $\eta_-(\vec{k}) = 1/2 + |v(\vec{k})|$ of the correlation matrix plotted around a given K-point for $t_\perp = 0.1t$, $t_3 = 0.15t$. The thick black lines correspond to the one in Fig. 4.4, and the components of the wave vector are again measured relatively to the K-point.

Inspection of Eq. (A.21) now shows that for $\cos\left(\phi_{\vec{k}}\right) = -1$

$$\epsilon_2(\vec{k}) \begin{cases} > 0 & |\gamma(\vec{k})| < t_\perp t_3/t^2 \\ < 0 & |\gamma(\vec{k})| > t_\perp t_3/t^2 \end{cases} \tag{4.27}$$

such that $\epsilon_2(\vec{k})$ changes sign for $|\gamma(\vec{k})| = t_\perp t_3/t^2$, i.e. $\gamma_\pm^{(2)}$ is discontinuous at wave vectors given by the condition (4.4). This discontinuity is inherited by the correlation matrix and, in turn, by the entanglement spectrum.

The technical reason for this discontinuity in the eigenvectors is of course the fact that the dispersions $(\pm E_2(\vec{k}))$ become degenerate at wave vectors fulfilling (4.4). In fact the eigenvectors can also be considered as continuous functions of the wave vector by appropriately relabeling the dispersion branches. In the ground state of the undoped bilayer system, however, only the lower branch $(-E_2(\vec{k}))$ is occupied, which makes the discontinuity unavoidable.

To circumvent this discontinuity one can open an energy gap between the upper and lower central band such that the corresponding eigenstates are necessarily continuous for all wave vectors. Among the various mechanisms producing such a gap only few allow for a still halfway convenient analytical treatment of the Hamiltonian. These include introducing identical mass terms in both layers, i.e. $H \mapsto H + H'$ with

$$H' = \operatorname{diag}(m, -m, -m, m) \ , \tag{4.28}$$

or applying a bias voltage Λ between the layers,

$$H' = \operatorname{diag}(-\Lambda/2, \Lambda/2, -\Lambda/2, \Lambda/2) \ . \tag{4.29}$$

In the former case the four dispersion branches $(\pm E_1(\vec{k}))$, $(\pm E_2(\vec{k}))$ are given by

$$E_{1/2}(\vec{k}) = \Bigg[m^2 + \frac{1}{2}\left(t_\perp^2 + t_3^2|\gamma(\vec{k})|^2 + 2t^2|\gamma(\vec{k})|^2\right) \pm \frac{1}{2}\sqrt{4t^2|\gamma(\vec{k})|^2\left(t_\perp^2 + t_3^2|\gamma(\vec{k})|^2 - 2t_\perp t_3|\gamma(\vec{k})|\cos\left(3\phi_{\vec{k}}\right)\right) + \left(t_\perp^2 - t_3^2|\gamma(\vec{k})|^2\right)^2}\Bigg]^{1/2} \tag{4.30}$$

while for a bias voltage one finds [McCann and Fal'ko, 2006]

$$E_{1/2}(\vec{k}) = \Bigg[\frac{\Lambda^2}{4} + \frac{1}{2}\left(t_\perp^2 + t_3^2|\gamma(\vec{k})|^2 + 2t^2|\gamma(\vec{k})|^2\right) \pm \frac{1}{2}\sqrt{4t^2|\gamma(\vec{k})|^2\left(t_\perp^2 + t_3^2|\gamma(\vec{k})|^2 - 2t_\perp t_3|\gamma(\vec{k})|\cos\left(3\phi_{\vec{k}}\right) + \Lambda^2\right) + \left(t_\perp^2 - t_3^2|\gamma(\vec{k})|^2\right)^2}\Bigg]^{1/2} . \tag{4.31}$$

In both cases the central energy bands $(\pm E_2(\vec{k}))$ are separated by a gap, and the spectrum can still be given in terms of comparably simple closed expressions since the characteristic polynomial of the 4×4 Hamiltonian matrix is a second-order polynomial in the energy squared leading to a spectrum being symmetric around zero. Also the corresponding eigenvectors can be obtained in closed analytical forms by procedures analogous to (but in detail somewhat more complicated than).

Note that applying a bias voltage as well as introducing a mass term in each layer discriminates the layers against each other. As we have shown in previous Chapter 3, the latter circumstance is due to the fact that $t_\perp$ couples sublattices in different layers for which the mass term has different sign.

4.4 CONCLUSION AND OUTLOOK

We have studied entanglement properties of the ground state of Bernal stacked graphene bilayers in the presence of trigonal warping. Our analysis includes both the eigenvalues of the reduced density matrix (giving rise to the entanglement spectrum) as well as its eigenvectors. When tracing out one layer, the entanglement spectrum shows qualitative geometric differences to the energy spectrum of a graphene monolayer while topological quantities such as Berry phase type contributions to Chern numbers agree. The latter finding is in contrast to the reduced density matrix resulting from tracing out other sublattices of the bilayer system. Here, all corresponding Berry phase integrals yield trivially zero. Thus, our study provides an example for common topological properties of the eigensystem of the energy Hamiltonian of a subsystem (here a graphene monolayer) and the entanglement Hamiltonian, while the geometrical shape of both spectra grossly differs. Our investigations are based on closed analytical expressions for the full eigensystem of bilayer graphene in the entire Brillouin zone with a trigonally warped spectrum.

Future work might address bilayer systems of other geometrical structures such as the Kagome lattice.

Furthermore, the graphene monolayer under a circularly polarized light exhibits ten different topological phases and high-Chern number behaviour is found in Ref. [Wang and Li, 2016]. The understanding of the topological phases of driven graphene bilayers under polarized light, especially in the presence of the trigonal warping in the energy and entanglement spectrum might be an extension of the present study. Moreover, the combination of influences of a static perpendicular magnetic field [Schliemann, 2013, Nemec and Cuniberti, 2007] and a circularly polarized light on the energy and entanglement spectrum of graphene bilayers could be an interesting research task.

5

ENTANGLEMENT SPECTRA OF SUPERCONDUCTIVITY GROUND STATES ON THE HONEYCOMB LATTICE

Most of the work presented in this chapter has been submitted to the European Physical Journal B.
Sonja Predin, and John Schliemann, Entanglement spectra of superconductivity ground states on the honeycomb lattice, preprint (submitted to the European Physical Journal B), arxiv:1611.01039. [Predin and Schliemann, 2016]

Soon after the birth of graphene has begun the searching for its complex electronic phases and phase transitions, such as superconductivity or exciton condensation [Sorella and Tosatti, 1992, Khveshchenko, 2001, Herbut, 2006, Hou et al., 2007, Honerkamp, 2008, Raghu et al., 2008, Liu et al., 2009, Drut and Lähde, 2009, Herbut et al., 2009, Gamayun et al., 2010, Meng et al., 2010, Sorella and Yunoki, 2012, Ulybyshev et al., 2013]. First searches were done in the vicinity of the Dirac point using the Dirac cone approximations. However, nowadays investigations of possible superconductivity states in graphene are in opposite limit, far away from the Dirac points.

In graphene, the sixfold symmetry of the honeycomb lattice favors the degenerate $d_{x^2-y^2}$- and d_{xy}-wave superconductivity states. Recent theoretical studies have shown that an s-wave superconductivity state [Uchoa and Castro Neto, 2007] and a chiral $d_{x^2-y^2} \pm id_{xy}$ superconducting state emerge from electron-electron interactions in graphene doped to the vicinity of the van-Hove singularity point [Black-Schaffer and Doniach, 2007, Honerkamp, 2008, Pathak et al., 2010, Nandkishore et al., 2011, Kiesel et al., 2012, Wang et al., 2012], and in lower doped bilayer graphene [Milovanović and Predin, 2012, Vučićević et al., 2012] (for a recent review, see Ref. [Black-Schaffer and Honerkamp, 2014]). Below the superconducting transition temperature T_C, this degeneracy yields

the time-reversal symmetry-breaking $d_{x^2-y^2} \pm id_{xy}$ state [Platt et al., 2013, Black-Schaffer and Honerkamp, 2014]. In the past two years, considerable experimental progress has been made regarding the observation of superconductivity in graphene. Evidence of superconductivity has been experimentally observed on Ca-intercalated bilayer graphene and graphene laminates at 4 [Ichinokura et al., 2016] and 6.4 K [Chapman et al., 2016], respectively. Furthermore, additional experimental progress has been made regarding evidence of superconductivity in Li-decorated monolayer graphene with a transition temperature of approximately 5.9 K [Ludbrook et al., 2015].

In this Chapter, we present an analytical study of the entanglement spectrum of the fermionic ground state on a graphene honeycomb lattice, in the presence of superconductivity instability and as obtained by tracing out a single spin direction. We investigate the relationship between the entanglement and energy spectra of the remaining noninteracting part, placing a special focus on the correlation between their topologies. We show that the entanglement Hamiltonian obtained by tracing out one of the subsystems and the Hamiltonian of the remaining subsystem can have completely different topologies. This difference is due to the fact that the entanglement Hamiltonian is a ground-state property. That is, the $d_{x^2-y^2} + id_{xy}$ superconductivity state breaks the time-reversal symmetry of the superconductivity Hamiltonian; this behaviour is reflected in the ground state of the composite superconductivity Hamiltonian. Further, the entanglement Hamiltonian is constructed from that ground state.

In the next section, the topological phases of the superconductivity states on the honeycomb lattice are classified based on their different symmetries. In Section 5.2, we introduced the model Hamiltonian and discuss the different superconductivity paired states that can arise from the electron–electron interaction on the honeycomb lattice. The renormalized mean-field treatment of self-consistent order parameter is given in Section 5.3. Then, we discuss classification of topological superconductors on a honeycomb lattice based on symmetry of systems in Section 5.4. The entanglement spectrum obtained from the Bardeen-Cooper-Schrieffer ground state by tracing out a single spin direction is analyzed in Section 5.5. Our primary interest in this section is to explore the relationship between the geometrical and topological properties of the entanglement Hamiltonian and the remaining noninteracting Hamiltonian. We close with a conclusion and an outlook, which are presented in Section 5.6.

C_{6v}	E	C_2	2 C_3	2 C_6	3 σ_v	3 σ_d	form
A_1	+1	+1	+1	+1	+1	+1	s-wave
A_2	+1	+1	+1	+1	-1	-1	
B_1	+1	-1	+1	-1	+1	-1	f-wave
B_2	+1	-1	+1	-1	-1	+1	f-wave
E_1	+2	-2	-1	+1	0	0	p_x, p_y
E_2	+2	+2	-1	-1	0	0	$d_{x^2-y^2}$, d_{xy}

Table 5.1: Character table of C_{6v} point groups. The identity operator is given by E. C_2 is the trace of a 180^0 rotation matrix. C_3 and C_6 are 120^0 and 60^0 rotation, respectively. σ_v and σ_d denote reflections at distinct lattice axis.

5.1 SYMMETRY GROUP REPRESENTATION

An understanding of the symmetry of the hexagonal lattice of graphene is essential for its physical properties. Possible superconductivity states and their symmetries are determined by the symmetry of the lattice and can be characterized by group theory. Furthermore, the form of the superconductivity order parameter is denoted by the symmetry group, as we shall see in 5.2.2. The crystal symmetry group for the hexagonal lattice of graphene is C_{6v} and it is presented in Table 5.1.

The fully isotropic A_1 is the fully gapped s-wave superconductivity state. The superconductivity state that breaks additional symmetries (except global $U(1)$ symmetry) in respect of the normal state is called an unconventional superconductivity state. These additional broken symmetries include time-reversal symmetry, crystal lattice symmetry, and spin-rotation symmetry, among others. In this sense, since the s-wave superconductivity state does not break any additional symmetry, is a conventional superconducting state.

The B_1 and B_2 states are spin-triplet f-wave states.

Any linear combination of the elements of the two-dimensional representations of E_1 and E_2 are possible from symmetry requirements. For the two-dimensional representation, E_2 are $d_{x^2-y^2}$ and d_{xy} superconductivity states and are degenerate at T_C according to group theory. However, below T_C, the complex combination, chiral $d_{x^2-y^2} + id_{xy}$ superconductivity states are a fully gapped for graphene doped at and beyond the van Hove singularity point, and minimize the free energy [Black-Schaffer and Honerkamp, 2014].

Recently, it was predicted that the graphene doped to the van Hove singularity point is a chiral d-wave superconductor [Nandkishore et al., 2011,Kiesel et al., 2012,Wang et al., 2012]. The chiral $d_{x^2-y^2} + id_{xy}$ superconductivity states breaks time-reversal symmetry and in this sense, is an unconventional superconductivity state.

Finally, a chiral $p_x + ip_y$ combination that belongs to the E_1, is characterized for the square lattice.

5.2 MODEL HAMILTONIAN

The tight-binding Hamiltonian for free fermions on a graphene honeycomb lattice with a single $2p_z$ orbital per carbon (C) atom is

$$\begin{aligned} H_0 = & -t \sum_{\langle ij \rangle} \sum_{\sigma=\uparrow,\downarrow} \left(a^\dagger_{i,\sigma} b_{j,\sigma} + h.c. \right) \\ & - \mu \sum_{i,\sigma} \left(a^\dagger_{i,\sigma} a_{i,\sigma} + b^\dagger_{i,\sigma} b_{i,\sigma} \right), \end{aligned} \tag{5.1}$$

where t is the hopping energy between the nearest-neighbor C atoms, μ is the chemical potential and $a_{i,\sigma}$ ($a^\dagger_{i,\sigma}$), and $b_{i,\sigma}$ ($b^\dagger_{i,\sigma}$) are the on-site annihilation (creation) operators for electrons on sublattices A and B, respectively, with spin $\sigma =\uparrow,\downarrow$. Diagonalization of Eq. (5.1) yields the energy spectrum $\pm E_\pm$, with

$$E_\pm = \pm t|\gamma(\vec{k})| - \mu, \tag{5.2}$$

where $\gamma(\vec{k}) = \sum_{\vec{\delta}} \exp\left(i\vec{k}\cdot\vec{\delta}\right)$ and $\vec{\delta}$ is a nearest-neighbor vector defined by Eq. (2.5). The energy spectrum of the free fermions over the first Brillouin zone is visualized in Fig. 5.1.

5.2.1 *Effective t-J model*

The interaction effects and the symmetry of the lattice are very important for the physics of superconductivity, and condensed matter physics in general. In the presence of the strong Coulomb repulsion, d-wave superconductivity state is the most favorable superconductivity state of the high-temperature cuprate superconductors. Using quantum Monte Carlo simulations, it is found that undoped graphene in the presence of the Coulomb repulsion $U > 3.9t$ could exhibit the order of the antiferromagnetic ground state [Wehling et al., 2011].

In the following, we will consider a simple effective model that gives superconductivity instabilities.

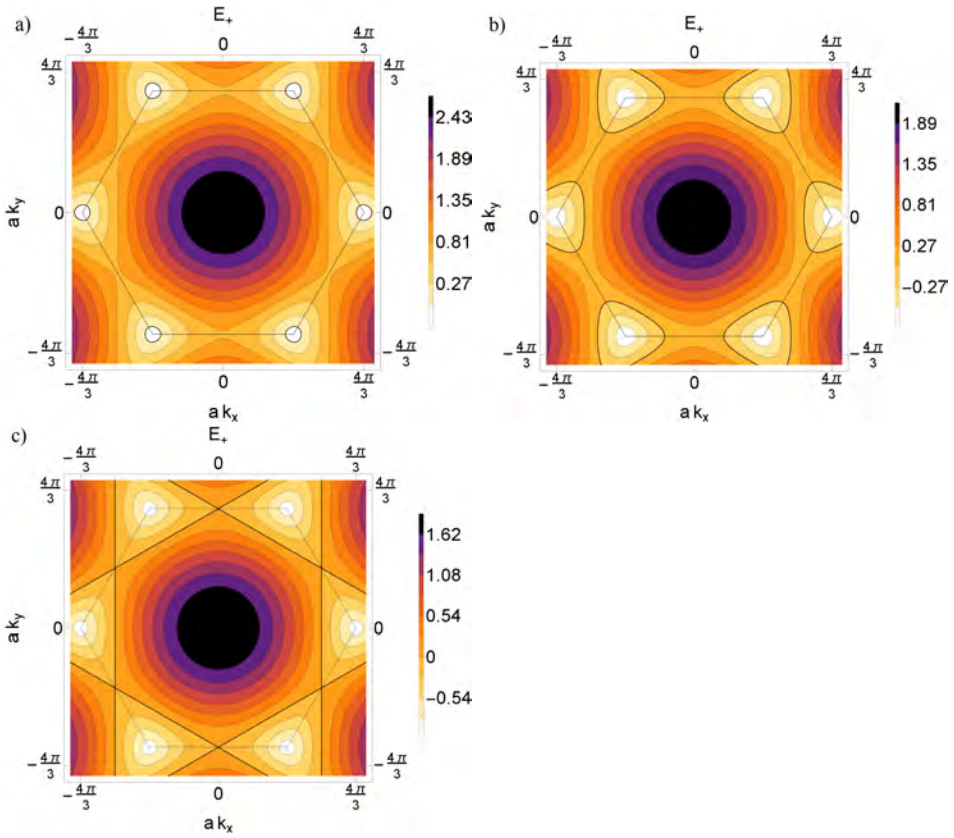

Figure 5.1: Brillouin zone with density plot of $|\gamma(\vec{k})| - \frac{\mu}{t}$ for: (a) $\frac{\mu}{t} = 0.2$; (b) $\frac{\mu}{t} = 0.8$; and (c) $\frac{\mu}{t} = 1$. The edge of the first Brillouin zone is marked by dashed black lines.

The repulsive Hubbard model has the following form in the half-filled case:

$$\mathcal{H}_U = -t \sum_{\langle ij \rangle} \sum_{\sigma} \left(a^{\dagger}_{i,\sigma} b_{j,\sigma} + h.c. \right) + U \sum_{i} n_{i\uparrow} n_{i\downarrow} \tag{5.3}$$

where U is the on-site Coulomb repulsion and n_i is the number operator on the site i. Wehling et al. determined the strength of the on-site Coulomb repulsion to be $U = 3.3t$ by first-principles calculations [Wehling et al., 2011]. The Hubbard Hamiltonian Eq.(5.3) consists of the kinetic part $T = -t \sum_{\langle ij \rangle} \sum_{\sigma} \left(a^{\dagger}_{i,\sigma} b_{j,\sigma} + h.c. \right)$ and the on-site interaction $U = U \sum_i n_{i\uparrow} n_{i\downarrow}$. The on-site interaction has a tendency to localize electrons, while the kinetic part resists this localization. We will consider the limit $U >> t$. Hopping of one electron to a neighbor site would cost energy of the order U. While the potential energy is much higher than the kinetic energy, the motion of electrons is frozen.

The Fock space can be divided into two subspaces:

1. subspace spanned by the sites that are maximally occupied by at most one electron per site: $S = \{|n_{1,\uparrow}, n_{1,\downarrow}, n_{2,\uparrow}, n_{2,\downarrow}\rangle : \forall i, n_{i,\uparrow} + n_{i,\downarrow} \leq 1\}$,

2. subspace spanned by at least one site that is double-occupied $D = \{|n_{1,\uparrow}, n_{1,\downarrow}, n_{2,\uparrow}, n_{2,\downarrow}\rangle : \exists i, n_{i,\uparrow} + n_{i,\downarrow} = 2\}$.

Thus, the kinetic part T of the Hubbard Hamiltonian Eq.(5.3) connects subspaces S and D.

We use the projector P, which projects on the subsystem S in order to find the effective Hubbard model Eq.(5.3) in this subspace [Auerbach, 1994]

$$G_{SS}(E) = P\left(E - \mathcal{H}_U\right)^{-1} P = \left(E - \mathcal{H}_{eff}\right)^{-1} \tag{5.4}$$

where we define the effective Hamiltonian $\mathcal{H}_{eff}$. Furthermore, the decomposition of the Hubbard Hamiltonian Eq.(5.3) obtained by the projector P is

$$\mathcal{H}_U = \begin{pmatrix} P\left(U+T\right)P & PT(I-P) \\ (I-P)PT & (I-P)(U+T)(I-P) \end{pmatrix} \tag{5.5}$$

where I is a unitary matrix. Thus, using

$$\begin{pmatrix} A & B \\ C & D \end{pmatrix}^{-1} = \left(A - BD^{-1}C\right)^{-1} \tag{5.6}$$

we obtain the following form of the effective Hamiltonian

$$\begin{aligned} \mathcal{H}_{eff} &= P\left(U+T\right)P \\ &\quad + PT(I-P)\left[(I-P)(E-(U+T))(I+P)\right]^{-1}(I-P)TP. \end{aligned} \tag{5.7}$$

Further approximations $\frac{E}{U} << 1$ and $\frac{I}{U} << 1$ lead to

$$\begin{aligned} \mathcal{H}_{eff} &= PTP - PTU^{-1}TP \\ &= P\left(T - \frac{t^2}{U}\sum_{i,j,k}\sum_{\sigma,\sigma'} c^{\dagger}_{i\sigma}c_{j\sigma}n_{j\uparrow}n_{j\downarrow}c^{\dagger}_{j\sigma'}c_{k\sigma'}\right)P \end{aligned} \tag{5.8}$$

Finally, when $i = k$, we are able to rewrite the effective Hamiltonian in the following form

$$\mathcal{H}_{eff} = -t\sum_{\langle ij\rangle}\sum_{\sigma}\left(a^{\dagger}_{i,\sigma}b_{j,\sigma} + h.c.\right) + J\sum_{\langle ij\rangle}\sum_{\sigma}\left(\vec{S}_i\vec{S}_j - \frac{1}{4}n_in_j\right) \tag{5.9}$$

with an antifferomagnetic exchange constant $J = 2t^2/U$, the spin operator $\vec{S}_i = \frac{1}{2}\sum_{\sigma,\sigma'} c^\dagger_{i\sigma}\vec{\sigma}c_{i\sigma'}$ on the site i. The Heisenberg antiferromagnetism part of the effective Hamiltonian Eq.(5.9) can be seen as a consequence of virtual hopping processes, where an electron with a certain spin direction hops to its neighbor site with opposite spin direction, builds a virtual double occupied site and hops back to the empty site. Thus, the electron reduces its kinetic energy in such a way and electrons are organized in antiferromagnetic order. This process is called a *"super-exchange"* process.

According to the above considerations, in the large-U limit, the Hubbard model can be rewritten as a t-J Hamiltonian:

$$\begin{aligned} H_{t-J} = &- t\sum_{\langle ij\rangle}\sum_{\sigma}\left(a^\dagger_{i,\sigma}b_{j,\sigma} + h.c.\right) + \mu\sum_{i,\sigma}\left(a^\dagger_{i,\sigma}a_{i,\sigma} + b^\dagger_{i,\sigma}b_{i,\sigma}\right) \\ &+ J\sum_{\langle ij\rangle}\sum_{\sigma}\left(\vec{S}_i\vec{S}_j - \frac{1}{4}n_in_j\right). \end{aligned} \tag{5.10}$$

The interaction term can be rewritten as a spin-singlet nearest neighbor attraction

$$J\sum_{\langle ij\rangle}\sum_{\sigma}\left(\vec{S}_i\vec{S}_j - \frac{1}{4}n_in_j\right) = -J\sum_{\langle i,j\rangle} g^\dagger_{ij}g_{ij} \tag{5.11}$$

with $g^\dagger_{ij} = \frac{1}{\sqrt{2}}\left(a^\dagger_{i\uparrow}b^\dagger_{j\downarrow} - a^\dagger_{i\downarrow}b^\dagger_{j\uparrow}\right)$ when $i \in A$ site and the same with $a \leftrightarrow b$ when $i \in B$. Thus, the interaction term in Eq.(5.11) is an effective resonance valence bond interaction term emphasized by Pauling [Pauling, 1960]. Baskaran estimated the parameter J as $J = \frac{1}{2}\left(\sqrt{U^2 + 16t^2} - U\right)$ which in graphite with $t \approx 2.5eV$ and $U \approx 6eV$ gives $\frac{J}{t} \sim 1$ [Baskaran and Jafari, 2002]. This model predicts that T_c vanishes for the undoped graphene, while the density of states vanishes at the Dirac points. The doped graphene has a finite density of states and it can be a superconductor.

5.2.2 *Mean-field superconductivity order parameter*

In order to apply the mean-field approximation, we define the superconductivity order parameter as a three-component complex vector

$$\overrightarrow{\Delta} \equiv \left(\Delta_{\vec{\delta}_1}, \Delta_{\vec{\delta}_2}, \Delta_{\vec{\delta}_3}\right), \tag{5.12}$$

where the components are defined by

$$\Delta_{\vec{\delta}} = \left\langle a_{i\uparrow}b_{i+\vec{\delta}\downarrow} - a_{i\downarrow}b_{i+\vec{\delta}\uparrow}\right\rangle. \tag{5.13}$$

We study the superconductivity pairing arising from the nearest-nearest neighbor attractive interaction

$$H_{int} = J \sum_{i,\vec{\delta}} \Delta_{\vec{\delta}} \left(a^{\dagger}_{i\uparrow} b^{\dagger}_{i+\vec{\delta}\downarrow} - a^{\dagger}_{i\downarrow} b^{\dagger}_{i+\vec{\delta}\uparrow} \right). \tag{5.14}$$

The resulting mean-field Hamiltonian can be expressed in momentum space as

$$\begin{aligned} H_{MF} = & -t \sum_{\vec{k}\sigma} \left(\gamma(\vec{k}) a^{\dagger}_{\vec{k}\sigma} b_{\vec{k}\sigma} + h.c. \right) \\ & - \mu \sum_{\vec{k}\sigma} \left(a^{\dagger}_{\vec{k}\sigma} a_{\vec{k}\sigma} + b^{\dagger}_{\vec{k}\sigma} b_{\vec{k}\sigma} \right) \\ & - J \sum_{\vec{k},\vec{\delta}} \left(\Delta_{\vec{\delta}} e^{i\vec{k}\vec{\delta}} \left(a^{\dagger}_{\vec{k}\uparrow} b^{\dagger}_{-\vec{k}\downarrow} - a^{\dagger}_{\vec{k}\downarrow} b^{\dagger}_{-\vec{k}\uparrow} \right) + h.c. \right), \end{aligned} \tag{5.15}$$

where J is the effective pairing potential arising from the electron-electron interaction.

The corresponding span of the superconducting order parameter is

$$\overrightarrow{\Delta} = \begin{cases} \Delta(1,1,1), \\ \Delta(2,-1,-1), \\ \Delta(0,-1,1), \end{cases} \tag{5.16}$$

where Δ is the self-consistent superconductivity order parameter. The first solution corresponds to the s-wave, $\overrightarrow{\Delta} = \Delta(1,1,1)$, belonging to the natural A1 irreducible representation of the C_{6v} group of the honeycomb lattice. The A1 irreducible representation is spanned by the vector $\vec{u}_1 = (1,1,1)$. The final two solutions, $\overrightarrow{\Delta} = \Delta(2,-1,-1)$ and $\overrightarrow{\Delta} = \Delta(0,-1,1)$, belong to the two-dimensional representation E_2, the span of which is $\vec{u}_2 = (2,-1,-1)$ and $\vec{u}_3 = (0,-1,1)$. The second solution corresponds to the $d_{x^2-y^2}$ wave, while the third corresponds to the d_{xy} wave, respectively. From the symmetry perspective, it is noteworthy that every combination of the $d_{x^2-y^2}$ and d_{xy} waves is possible. However, the $d_{x^2-y^2} \pm i d_{xy}$-wave superconductivity state with an order parameter

$$\overrightarrow{\Delta}_{d_{x^2-y^2} \pm i d_{xy}} = \Delta \begin{pmatrix} 1 \\ e^{\mp \frac{2i\pi}{3}} \\ e^{\pm \frac{2i\pi}{3}} \end{pmatrix} \tag{5.17}$$

is energetically preferred.

The resulting order parameters obtained in correspondence to the symmetry group representation have the following analytical forms

$$\Delta_s(\vec{k}) = \Delta \left(\mathrm{e}^{i\vec{k}\vec{\delta}_1} + \mathrm{e}^{i\vec{k}\vec{\delta}_2} + \mathrm{e}^{i\vec{k}\vec{\delta}_3} \right),$$

$$\Delta_s(\vec{k}) = \Delta\left(\mathrm{e}^{ia\frac{1}{\sqrt{3}}k_y} + 2\cos\left(\frac{a}{2}k_x\right)\mathrm{e}^{-ia\frac{1}{2\sqrt{3}}k_y}\right), \tag{5.18}$$

for the s-wave with $\overrightarrow{\Delta} = \Delta(1,1,1)$,

$$\begin{aligned}\Delta_{d_{x^2-y^2}}(\vec{k}) &= \Delta\left(2\mathrm{e}^{i\vec{k}\vec{\delta}_1} - \mathrm{e}^{i\vec{k}\vec{\delta}_2} - \mathrm{e}^{i\vec{k}\vec{\delta}_3}\right),\\ \Delta_{d_{x^2-y^2}}(\vec{k}) &= 2\Delta\left(e^{i\frac{a}{\sqrt{3}}k_y} - e^{-i\frac{a}{2\sqrt{3}}k_y}\cos(\frac{a}{2}k_x)\right),\end{aligned} \tag{5.19}$$

for the $d_{x^2-y^2}$-wave order parameter with $\overrightarrow{\Delta} = \Delta(2,-1,-1)$, and

$$\begin{aligned}\Delta_{d_{xy}}(\vec{k}) &= \Delta\left(-\mathrm{e}^{i\vec{k}\vec{\delta}_2} + \mathrm{e}^{i\vec{k}\vec{\delta}_3}\right),\\ \Delta_{d_{xy}}(\vec{k}) &= -2i\Delta\sin\left(\frac{a}{2}k_x\right)e^{-i\frac{a}{2\sqrt{3}}k_y},\end{aligned} \tag{5.20}$$

for the d_{xy}-wave order parameter with $\overrightarrow{\Delta} = \Delta(0,-1,1)$.

Whereas, the $d_{x^2-y^2} + id_{xy}$-wave superconductivity order parameter is

$$\Delta_{d\pm id}(\vec{k}) = \cos\left(\frac{\pi}{3}\right)\Delta_{d_{x^2-y^2}}(\vec{k}) \pm \sin\left(\frac{\pi}{3}\right)\Delta_{d_{xy}}(\vec{k}). \tag{5.21}$$

5.2.3 *Energy band basis*

The kinetic part of the Hamiltonian Eq.(5.15) can be diagonalized by introducing the following transformations

$$\begin{aligned}c_{\vec{k},\sigma} &= \frac{1}{\sqrt{2}}(a_{\vec{k},\sigma} - e^{i\cdot\phi_{\vec{k}}}b_{\vec{k},\sigma}),\\ d_{\vec{k},\sigma} &= \frac{1}{\sqrt{2}}(a_{\vec{k},\sigma} + e^{i\cdot\phi_{\vec{k}}}b_{\vec{k},\sigma}),\end{aligned} \tag{5.22}$$

where the phase $\phi_{\vec{k}}$ is defined as $\phi_{\vec{k}} = \arg(\gamma_{\vec{k}})$. Note that $c^{\dagger}_{\vec{k},\vec{\sigma}}$ and $d^{\dagger}_{\vec{k},\vec{\sigma}}$ create an electron in the upper and lower Bogoliubov bands, respectively. Thus, introducing the energy basis, the Hamiltonian becomes

$$\begin{aligned}H_{MF} &= -t\sum_{\vec{k},\sigma}|\gamma_{\vec{k}}|(d^{\dagger}_{\vec{k},\sigma}d_{\vec{k},\sigma} - c^{\dagger}_{\vec{k},\sigma}c_{\vec{k},\sigma})\\ &- \mu\sum_{\vec{k},\sigma}(d^{\dagger}_{\vec{k},\sigma}d_{\vec{k},\sigma} + c^{\dagger}_{\vec{k},\sigma}c_{\vec{k},\sigma})\\ &- J\sum_{\vec{k}}\sum_{\vec{\delta}}\Big(\Delta_{\vec{\delta}}\Big(\cos(\vec{k}\vec{\delta} - \phi_{\vec{k}})(d^{\dagger}_{\vec{k},\uparrow}d^{\dagger}_{-\vec{k},\downarrow} - c^{\dagger}_{\vec{k},\uparrow}c^{\dagger}_{-\vec{k},\downarrow})\\ &+ i\sin(\vec{k}\vec{\delta} - \phi_{\vec{k}})(c^{\dagger}_{\vec{k},\uparrow}d^{\dagger}_{-\vec{k},\downarrow} - d^{\dagger}_{\vec{k},\uparrow}c^{\dagger}_{-\vec{k},\downarrow})\Big) + h.c.\Big).\end{aligned} \tag{5.23}$$

The third line in this Hamiltonian is the intraband pairing, containing an order parameter that is even in k-space and corresponding to the spin-singlet pairing. The fourth line is the interband pairing, containing an order parameter that is odd in k-space and corresponding to the spin-triplet pairing. We use the definitions

$$C_{\vec{k}} = \sum_{\vec{\delta}} \Delta_{\vec{\delta}} \cos(\vec{k}\vec{\delta} - \phi_{\vec{k}}), \tag{5.24}$$

and

$$S_{\vec{k}} = \sum_{\vec{\delta}} \Delta_{\vec{\delta}} \sin(\vec{k}\vec{\delta} - \phi_{\vec{k}}). \tag{5.25}$$

In a small-momentum expansion $k << a$ around Dirac points $K_\pm$ for the $d_{x^2-y^2}$-wave yields

$$\begin{aligned} C_{K_\pm+\vec{k}}(d_{x^2-y^2}) &\approx \mp 3\Delta \frac{k_x}{\sqrt{k_x^2+k_y^2}}, \\ S_{K_\pm+\vec{k}}(d_{x^2-y^2}) &\approx -3\Delta \frac{k_y}{\sqrt{k_x^2+k_y^2}}. \end{aligned} \tag{5.26}$$

Here, near Dirac points p_x (p_y) symmetries are found for $C_{\vec{k}}$ ($S_{\vec{k}}$), respectively. For the d_{xy}-wave we obtain

$$\begin{aligned} C_{K_\pm+\vec{k}}(d_{xy}) &\approx \pm\sqrt{3}\Delta \frac{k_y}{\sqrt{k_x^2+k_y^2}}, \\ S_{K_\pm+\vec{k}}(d_{xy}) &\approx -\sqrt{3}\Delta \frac{k_x}{\sqrt{k_x^2+k_y^2}}. \end{aligned} \tag{5.27}$$

The combination of $d_{x^2-y^2} + id_{xy}$ in the small-momentum expansion has the following form

$$\begin{aligned} C_{K_\pm+\vec{k}}(d_{x^2-y^2}+id_{xy}) &\approx \mp\frac{3}{2}\Delta \frac{k_x - ik_y}{\sqrt{k_x^2+k_y^2}}, \\ iS_{K_\pm+\vec{k}}(d_{x^2-y^2}+id_{xy}) &\approx \frac{3}{2}\Delta \frac{k_x - ik_y}{\sqrt{k_x^2+k_y^2}}. \end{aligned} \tag{5.28}$$

This is effectively a $p_x - ip_y$ pairing.

Furthermore, for the s-wave we find the following a small-momentum expansion

$$\begin{aligned} C_{K_\pm+\vec{k}} &\approx \mp\frac{a\sqrt{3}}{2}\Delta\sqrt{k_x^2+k_y^2}, \\ S_{K_\pm+\vec{k}} &= 0. \end{aligned} \tag{5.29}$$

$C_{\vec{k}}$ in the first Brillouin zone are plotted in Fig. (5.2).

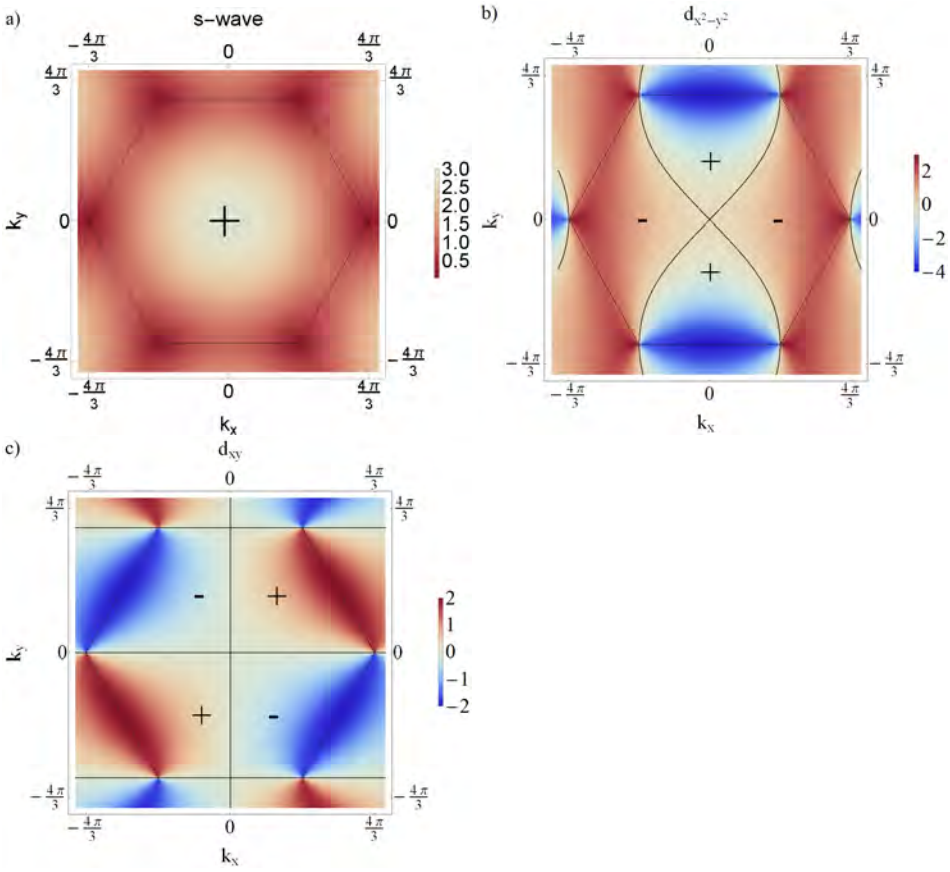

Figure 5.2: The interband order parameter $C_{\vec{k}}$ plotted over Brillouin zone for a) the s-wave with symmetry $\vec{\Delta} = \Delta(1,1,1)$, b) the $d_{x^2-y^2}$-wave with symmetry $\vec{\Delta} = \Delta(2,-1,-1)$, and c) the d_{xy}-wave with symmetry $\vec{\Delta} = \Delta(0,-1,1)$. The thick black line indicates zero values, while plus indicates positive values, and minus indicates negative values. The dashed black line delineates the first Brillouin zone.

5.3 RENORMALIZED MEAN-FIELD THEORY

As we have seen in 5.2.1, the Gutzwiller projector reduced the space of t-J Hamiltonian Eq.(5.10) by excluding double occupied sites. However, within the renormalized mean-field theory the condition of the exclusion of doubly occupied sites is relaxed by replacing the tight-binding parameters by statistical weights $t \to g_t t$ where $g_t = \frac{2\delta}{1+\delta}$ and $J \to g_s J$, where $g_s = \frac{4}{(1+\delta^2)}$ with $\delta = 1 - n$ is the doping away from half-filling per site, where $\delta = 0$ corresponds to the undoped graphene [Vollhardt, 1984]. The numerical approach for solving of the self-consistency equations for the superconducting bond order in order to get the superconductivity critical temperature T_c and the order parameter Δ has already

been preformed in Refs. [Wu et al., 2013, Black-Schaffer et al., 2014].

5.3.1 *s-wave scenario*

The Hamiltonian Eq.(5.23) for s-wave superconductivity state can be diagonalized by Bogoliubov transformations

$$\begin{aligned}\mathcal{H} =& E_0^{(1)} + \sum_{\vec{k}} E_\alpha (e_{\vec{k}\dagger} e_{\vec{k}} + e^\dagger_{-\vec{k}} e_{-\vec{k}}) \\ &+ E_0^{(2)} + \sum_{\vec{k}} E_\beta (f^\dagger_{\vec{k}} f_{\vec{k}} + f^\dagger_{-\vec{k}} f_{-\vec{k}}) + \frac{N_s |\Delta|^2}{g_s J}\end{aligned} \tag{5.30}$$

where

$$E_0^{(1)} = -\sum_{\vec{k}} \Big(t|\gamma(\vec{k})| - \mu \Big) - \sum_{\vec{k}} E_\alpha, \tag{5.31}$$

$$E_0^{(2)} = \sum_{\vec{k}} \Big(t|\gamma(\vec{k})| + \mu \Big) - \sum_{\vec{k}} E_\beta. \tag{5.32}$$

The energies of Bogoliubov quasi-particles are

$$E_\alpha = \sqrt{\Big(t\gamma(\vec{k})| - \mu \Big)^2 + J^2 |C_{\vec{k}}|^2} \tag{5.33}$$

$$E_\beta = \sqrt{\Big(t\gamma(\vec{k})| + \mu \Big)^2 + J^2 |C_{\vec{k}}|^2}. \tag{5.34}$$

The Bogoliubov transformations $e_{\vec{k},+}$ and $f_{\vec{k},+}$ are given in Appendix D by Eqs.(D.1, D.2). The total number of unit cells is N_s.

The free energy then becomes

$$\begin{aligned}F = &-\frac{2}{\beta} \sum_{\vec{k}} \ln \left(2 \cosh \left(\frac{\beta E_\alpha}{2} \right) \right) \\ &-\frac{2}{\beta} \sum_{\vec{k}} \ln \left(2 \cosh \left(\frac{\beta E_\beta}{2} \right) \right) \\ &- N_s \mu + \frac{N_s |\Delta|^2}{g_s J}\end{aligned} \tag{5.35}$$

where $\beta = \frac{1}{k_B T}$ denotes the inverse temperature, with k_B is the Bolztmann constant.

The conditions for the minimum of the free energy are given by

$$\frac{\partial F}{\partial \delta} = 0, \quad \frac{\partial F}{\partial \Delta} = 0. \tag{5.36}$$

The superconductivity critical temperature T_c and the order parameter Δ can be found by solving the self-consistence equations

$$\begin{aligned}\delta =&\frac{1}{N_s}\sum_{\vec{k}}\frac{t|\gamma(\vec{k})|-\mu}{E_\alpha}\tanh\left(\frac{\beta E_\alpha}{2}\right)\\ &-\frac{1}{N_s}\sum_{\vec{k}}\frac{t|\gamma(\vec{k})|+\mu}{E_\beta}\tanh\left(\frac{\beta E_\beta}{2}\right) \qquad (5.37)\\ \Delta =&\frac{Jg_s}{8N_s}\sum_{\vec{k}}\frac{\Delta|\gamma(\vec{k})|}{E_\alpha}\tanh\left(\frac{\beta E_\alpha}{2}\right)\\ &+\frac{Jg_s}{4N_s}\sum_{\vec{k}}\frac{\Delta|\gamma(\vec{k})|}{E_\beta}\tanh\left(\frac{\beta E_\beta}{2}\right). \qquad (5.38)\end{aligned}$$

We solve the self-consistence equations Eq.(5.38) in two opposite limits, close to the T_c when the order parameter Δ is very small and when temperature is $T = 0$. The numerical solutions of these equations will be discussed in 5.3.3.

5.3.2 *d-wave scenario*

To enable further calculations, we diagonalize the Hamiltonian Eq.(5.55) for the chiral d-wave superconductivity state

$$\begin{aligned}H_{MF} =&\sum_{\vec{k}}E_\alpha(o^\dagger_{\vec{k},+}o_{\vec{k},+}+o^\dagger_{-\vec{k},-}o_{-\vec{k},-})\\ &+\sum_{\vec{k}}E_\beta(p^\dagger_{\vec{k},+}p_{\vec{k},+}+p^\dagger_{-\vec{k},-}p_{-\vec{k},-}) \qquad (5.39)\end{aligned}$$

by the Bogoliubov quasiparticles $o_{\vec{k},+}, o_{-\vec{k},-}, p_{\vec{k},+}$ and $p_{-\vec{k},-}$ given in Appendix (C) with Eqs.(C.30)-Eq.(C.31). The energies of the Bogoliubov quasiparticles are $\pm E_\alpha$ and $\pm E_\beta$, where

$$E_\alpha=\sqrt{t^2|\gamma(\vec{k})|^2+\mu^2+\left(|S_{\vec{k}}|^2+|C_{\vec{k}}|^2\right)+2\sqrt{u+v}}, \qquad (5.40)$$

and

$$E_\beta=\sqrt{t^2|\gamma(\vec{k})|^2+\mu^2+\left(|S_{\vec{k}}|^2+|C_{\vec{k}}|^2\right)-2\sqrt{u+v}} \qquad (5.41)$$

with

$$u=\left(\mu^2+|S_{\vec{k}}|^2\right)t^2|\gamma(\vec{k})|^2, \qquad (5.42)$$

and

$$v=\left(\mathrm{Re}(C_{\vec{k}})\mathrm{Im}(S_{\vec{k}})-\mathrm{Re}(S_{\vec{k}})\mathrm{Im}(C_{\vec{k}})\right)^2. \qquad (5.43)$$

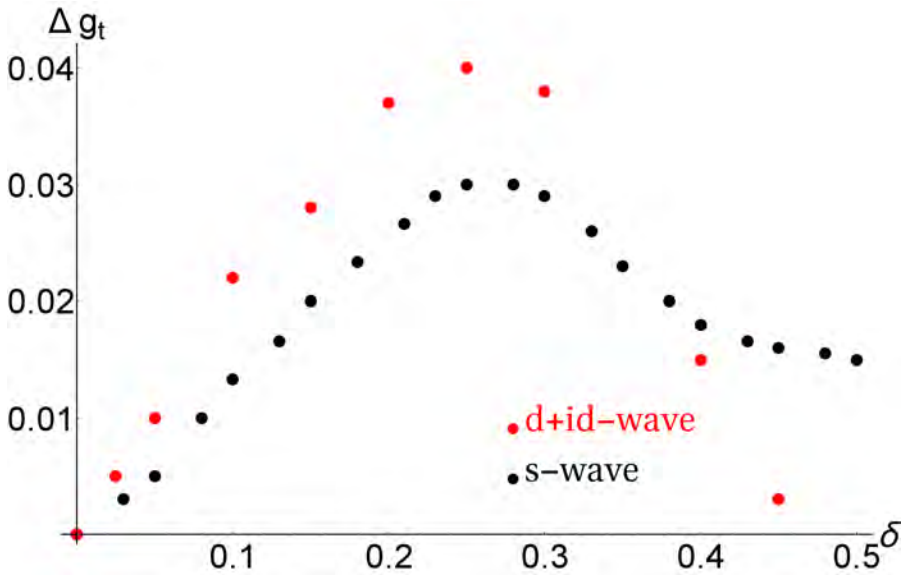

Figure 5.3: The superconductivity transition temperature T_C ($T_C \sim g_t\Delta$) for the s-wave and the $d_{x^2-y^2} + id_{xy}$-wave as a function of doping δ and for $J/t = 0.8$. The superconductivity order parameter Δ is given units $\frac{3}{4}g_s J$.

When the superconductivity order parameters $\Delta_{\vec{\delta}}$ are purely real, i.e., when no time-reversal symmetry breaking occurs, v vanishes.

We obtain the following self-consistence equations

$$\frac{\partial E_\alpha}{\partial \Delta} = \frac{|C_{\vec{k}}|^2}{\Delta E_\alpha} + \frac{|S_{\vec{k}}|^2}{\Delta E_\alpha} + \frac{1}{2\Delta E_\alpha}\frac{|S_{\vec{k}}|^2 t^2 |\gamma(\vec{k})|^2 + 2v^2}{\sqrt{u^2+v^2}} \tag{5.44}$$

$$\frac{\partial E_\beta}{\partial \Delta} = \frac{|C_{\vec{k}}|^2}{\Delta E_\beta} + \frac{|S_{\vec{k}}|^2}{\Delta E_\beta} - \frac{1}{\Delta E_\beta}\frac{|S_{\vec{k}}|^2 t^2 |\gamma(\vec{k})|^2 + 2v^2}{\sqrt{u^2+v^2}} \tag{5.45}$$

$$\frac{\partial E_\alpha}{\partial \mu} = \frac{\mu}{E_\alpha} + \frac{1}{2\Delta E_\alpha}\frac{\mu t^2 |\gamma(\vec{k})|^2}{\sqrt{u^2+v^2}} \tag{5.46}$$

$$\frac{\partial E_\beta}{\partial \mu} = \frac{\mu}{E_\beta} - \frac{1}{2\Delta E_\beta}\frac{\mu t^2 |\gamma(\vec{k})|^2}{\sqrt{u^2+v^2}}. \tag{5.47}$$

5.3.3 *Numerical results*

The value of T_C and the superconductivity order parameter Δ are obtained as solutions of the self-consistence equations to fix the values of t, J, and the finite electron doping or hole doping, δ (chemical potential is a function of the doping). In Fig.(5.3), we plot Δg_t for the s-wave and chiral $d_{x^2-y^2} + id_{xy}$-wave superconductivity state for a fixed value $J/t = 0.8$ as a function of doping δ. Δg_t is an approximation for T_C within renormalized mean-field theory.

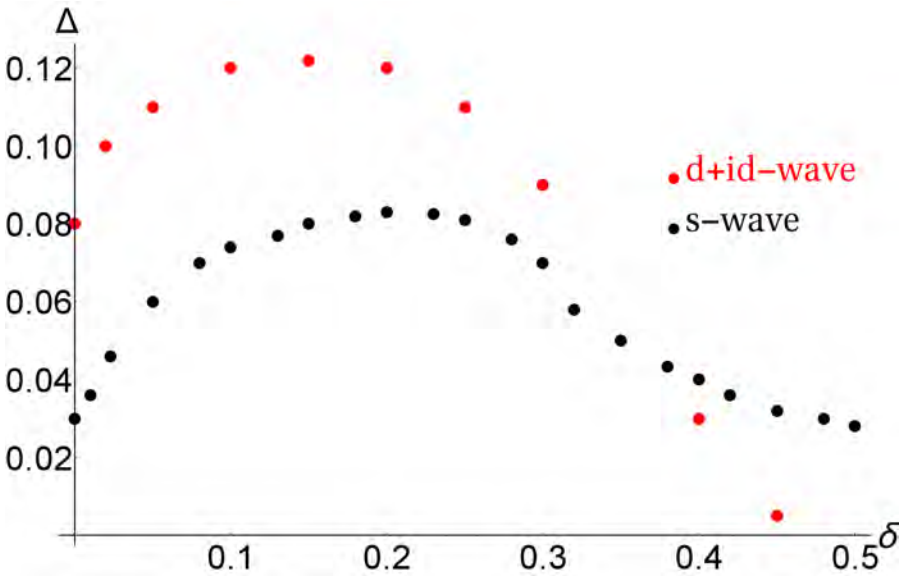

Figure 5.4: The-self consistent superconductivity order parameter Δ for the s-wave and the $d_{x^2-y^2}+id_{xy}$ as a function of doping δ and for $J/t=0.8$ in units $\frac{3}{4}g_sJ$.

In this work, we will consider graphene doped below and around the van-Hove singularity point, which corresponds to $\delta = 1/4$. For this doping, T_C for the chiral $d_{x^2-y^2}+id_{xy}$-wave is much higher than for the s-wave and is preferred. As we have pointed out in 5.1, any combination of the $d_{x^2-y^2}$- and d_{xy}-wave is allowed from a symmetry point of view. Black-Schaffer and Doniach numerically solved the self-consistence equations to obtain that the chiral $d_{x^2-y^2}+id_{xy}$-wave with $\vec{\Delta}=\Delta(1,e^{\mp\frac{2i\pi}{3}},e^{\pm\frac{2i\pi}{3}})$ is energetically favored. We present our numerical results for the superconductivity order parameter Δ for s-wave and chiral $d_{x^2-y^2}+id_{xy}$- wave at $T=0$ in Fig. (5.4).

5.4 SYMMETRY ANALYSIS

Introducing the spinor

$$\varphi^\dagger_{\vec{k}}=\left(a^\dagger_{\vec{k}\uparrow},b^\dagger_{\vec{k}\uparrow},a^\dagger_{\vec{k}\downarrow},b^\dagger_{\vec{k}\downarrow},a_{-\vec{k}\uparrow},b_{-\vec{k}\uparrow},a_{-\vec{k}\downarrow},b_{-\vec{k}\downarrow}\right), \tag{5.48}$$

the Hamiltonian of Eq. (5.15) can be expressed as

$$H_{MF}=\frac{1}{2}\sum_{\vec{k}}\varphi^\dagger_{\vec{k}}\mathcal{M}_{\vec{k}}\varphi_{\vec{k}}, \tag{5.49}$$

where

$$\mathcal{M}_{\vec{k}} = \begin{pmatrix} \zeta(\vec{k}) & 0 & 0 & -\overline{\Delta}(\vec{k}) \\ 0 & \zeta(\vec{k}) & \overline{\Delta}(\vec{k}) & 0 \\ 0 & \overline{\Delta}^*(-\vec{k}) & -\zeta^*(-\vec{k}) & 0 \\ -\overline{\Delta}^*(-\vec{k}) & 0 & 0 & -\zeta^*(-\vec{k}) \end{pmatrix}, \quad (5.50)$$

with

$$\zeta(\vec{k}) = \begin{pmatrix} -\mu & -t\gamma(\vec{k}) \\ -t\gamma^*(\vec{k}) & -\mu \end{pmatrix}, \quad (5.51)$$

$$\overline{\Delta}(\vec{k}) = \begin{pmatrix} 0 & \Delta(\vec{k}) \\ \Delta(-\vec{k}) & 0 \end{pmatrix}. \quad (5.52)$$

The resultant Hamiltonian indicates that the spin-singlet superconductivity state without spin-orbit coupling is invariant under the spin SU(2) rotation. Hence, we obtain the condition

$$\left[J_i, \mathcal{M}(\vec{k})\right] = 0, \qquad J_i = \begin{pmatrix} s_i & 0 \\ 0 & -s_i^* \end{pmatrix}, \qquad (i = x, y, z). \quad (5.53)$$

As a result of the spin SU(2) rotation, it is sufficient to use the spinor $\Psi_{\vec{k}}^\dagger = (a_{\vec{k}\uparrow}^\dagger, b_{\vec{k}\uparrow}^\dagger, a_{-\vec{k}\downarrow}, b_{-\vec{k}\downarrow})$ in order to express the Hamiltonian of the superconductivity state on the honeycomb lattice in the form

$$H_{MF} = \sum_{\vec{k}} \Psi_{\vec{k}}^\dagger h(\vec{k}) \Psi_{\vec{k}}, \quad (5.54)$$

where

$$h(\vec{k}) = \begin{pmatrix} -\mu & -t\gamma(\vec{k}) & 0 & -\Delta(\vec{k}) \\ -t\gamma^*(\vec{k}) & -\mu & -\Delta(-\vec{k}) & 0 \\ 0 & -\Delta^*(-\vec{k}) & \mu & t\gamma^*(-\vec{k}) \\ -\Delta^*(\vec{k}) & 0 & t\gamma(-\vec{k}) & \mu \end{pmatrix}. \quad (5.55)$$

When the superconductivity order parameter is purely real, the Hamiltonian $h(\vec{k})$ satisfies

$$Th(\vec{k})T^{-1} = h(-\vec{k}), \quad (5.56)$$

where $T = K$ mimics time-reversal symmetry. The condition given in Eq. (5.56) can satisfy a real superconductivity order parameter only. The $d_{x^2-y^2} + id_{xy}$-wave superconductivity order parameter given in Eq. (5.21) breaks the time-reversal symmetry. It appertains to the CI-class in the Altland-Zirnbauer classification of

topological insulators and superconductors [Sato and Fujimoto, 2016, Altland and Zirnbauer, 1997, Schnyder et al., 2008]. Furthermore, it is possible to classify two-dimensional C-class superconductors using the Chern number C. Note that the nontrivial topology of the $d_{x^2-y^2} + id_{xy}$-wave superconductivity state is denoted by the Chern number $C = 2$.

5.5 ENTANGLEMENT SPECTRA

A method for analytically calculating the entanglement spectrum of a free-fermion system is given in Refs. [Peschel, 2003, Cheong and Henley, 2004,Schliemann, 2013]. Here, we generalize this method to superconductivity systems, using an approach similar to that described in Refs. [Borchmann et al., 2014, Kim, 2014].

The entanglement Hamiltonian can be constructed as a single-particle operator in a quadratic matrix [Peschel, 2003,Cheong and Henley, 2004,Schliemann, 2013], as it is completely determined by any correlation matrix of operators acting on the remaining part after the subsystem has been traced out. Our system consists of two subsystems, A and B. The reduced density matrix for subsystem A, defined as $\rho_A = \mathrm{tr}_B\, \rho$, can be formulated as in the free fermion case, such that $\rho_A = \frac{1}{Z} e^{-H_{ent}}$, using the entanglement spectrum H_{ent} and the partition function $Z = \mathrm{t}r\left(e^{-H_{ent}}\right)$. Furthermore, the average $\langle \mathcal{O} \rangle$ of a local operator in subsystem A can be calculated as $\langle \mathcal{O} \rangle = \mathrm{tr}(\rho_A \mathcal{O}_A)$.

By tracing out a single spin direction, e.g., the negative spin $\downarrow$, from the ground state on the honeycomb lattice in the presence of the s-wave and chiral $d + id$-wave superconductivity, the correlation matrix can be formulated as

$$C(\vec{k}) = \begin{pmatrix} \langle a^\dagger_{\vec{k}\uparrow} a_{\vec{k}\uparrow} \rangle & \langle a^\dagger_{\vec{k}\uparrow} b_{\vec{k}\uparrow} \rangle \\ \langle b^\dagger_{\vec{k}\uparrow} a_{\vec{k}\uparrow} \rangle & \langle b^\dagger_{\vec{k}\uparrow} b_{\vec{k}\uparrow} \rangle \end{pmatrix}. \tag{5.57}$$

For more technical details of the analytical calculations of the correlation matrix, we refer the reader to Appendix (D). Here, one can show that the eigenvalues of the correlation matrix η_l are related to the entanglement spectrum ξ_l, such that

$$\xi_l = \ln\left(\frac{1-\eta_l}{\eta_l}\right). \tag{5.58}$$

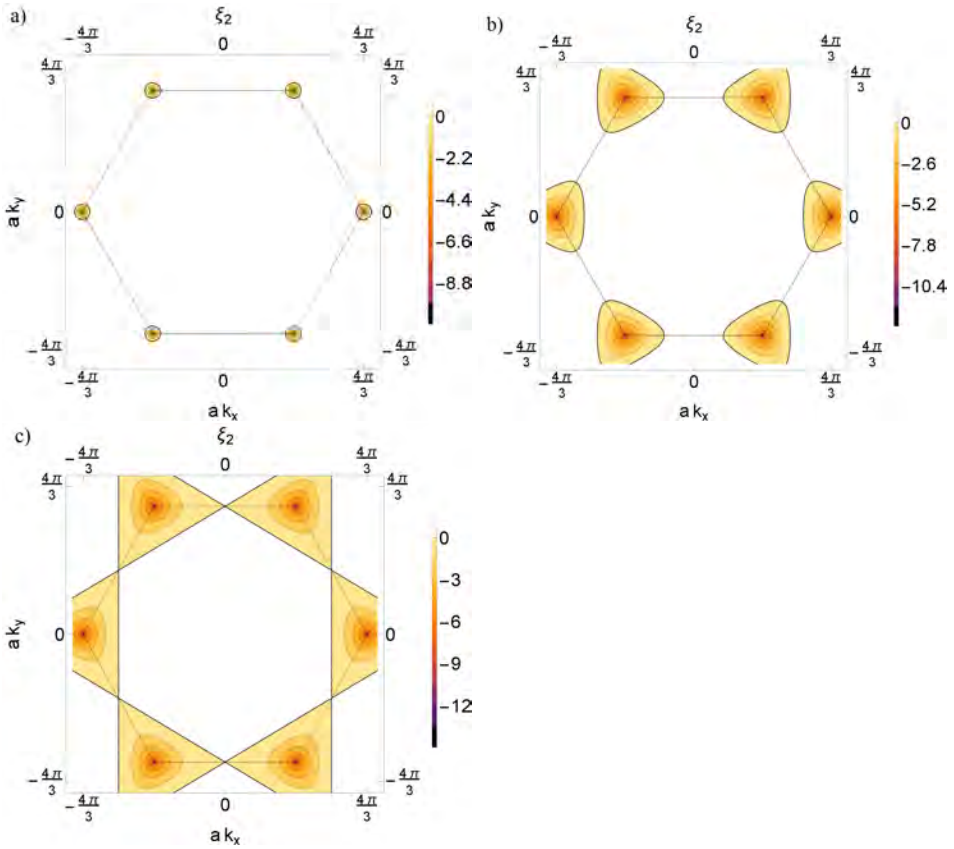

Figure 5.5: Contour plot of entanglement level $\xi_1(\vec{k})$ of s-wave superconductivity state on honeycomb lattice plotted for $\frac{J}{t} = 3$ and: (a) $\frac{\mu}{t} = 0.2$; (b) $\frac{\mu}{t} = 0.8$; and (c) $\frac{\mu}{t} = 1$. The thin dashed and thick black lines represent the first Brillouin zone and connect the zero energy states, respectively.

5.5.1 *s-wave scenario*

The s-wave superconductivity order parameter corresponds to the bond-independent superconductivity state; thus, $S_{\vec{k}}$ is identically zero.

We analytically obtain the entanglement levels (Eq. (5.58))

$$\xi_1(\vec{k}) = -2\,\mathrm{arsinh}\left(\frac{t|\gamma(\vec{k})| + \mu}{|C_{\vec{k}}|}\right) \tag{5.59}$$

and

$$\xi_2(\vec{k}) = 2\,\mathrm{arsinh}\left(\frac{t|\gamma(\vec{k})| - \mu}{|C_{\vec{k}}|}\right). \tag{5.60}$$

The entanglement Hamiltonian has the form

$$\mathcal{H}_{ent} = \sum_{\vec{k}} \left(\xi_1 e^{\dagger}_{\vec{k},+} e_{\vec{k},+} + \xi_2 f^{\dagger}_{\vec{k},+} f_{\vec{k},+}\right), \tag{5.61}$$

where $e_{\vec{k},+}$ and $f_{\vec{k},+}$ are Bogoliubov transformations given in Appendix D by Eqs.(D.1)- (D.2). The entanglement levels for different values of μ, with $t = 2.5eV$, and $\Delta = 3eV$, are shown in Fig. 5.5.

In general, there is no proportionality between the entanglement Hamiltonian and the energy Hamiltonian of free fermions, because the coupling between subsystems $C_{\vec{k}}$ is $\vec{k}$-dependent in the Brillouin zone. When $C_{\vec{k}} = 0$, at the Dirac points, the entanglement levels are not entangled. However, at finite doping, the maximally entangled states, when the entanglement levels are zero, correspond to the zero energy state of the noninteracting fermions. To provide a superior visualization, a thick black line is used to connect the zero-energy states in Fig. 5.1 and the maximally entangled states in Fig. 5.5.

Entanglement thermodynamic

The undoped graphene is a gapless semi-metal and is not a superconductor at low temperatures. However, when the system is at half-filling (with $\mu = 0$), the entanglement levels are

$$\xi_{1,2}(\vec{k}) = \pm 2 \operatorname{arsinh}\left(\frac{t}{\Delta}\right), \tag{5.62}$$

being constant over the entire Brillouin zone. In the strong coupling regime between subsystems, when $\Delta \gg t$, one finds

$$\xi_{1,2}(\vec{k}) \approx \pm 2\frac{t}{\Delta}. \tag{5.63}$$

In what follows we will use the redefinition $\lambda \equiv \frac{1}{\Delta}$ for the phenomenological scale.

The concept of the entanglement thermodynamics given in Ref. [Schliemann, 2011,Schliemann, 2013,Schliemann, 2014] have been already discussed in Chapter 3.

Here, the entanglement entropy and energy are

$$\begin{aligned} S =& 2\ln\left(1 + \mathrm{e}^{2t\lambda}\right) - 2t\lambda\left(1 + \tanh\left(t\lambda\right)\right) \\ \overline{E} =& -2t\lambda\tanh\left(t\lambda\right), \end{aligned} \tag{5.64}$$

respectively. This leads

$$\frac{\partial\left(\overline{E} - S\right)}{\partial\lambda} = -2t\tanh\left(t\lambda\right) \tag{5.65}$$

and further to

$$\frac{\partial\beta(\lambda)}{\partial\lambda} = \frac{1}{\lambda}. \tag{5.66}$$

The inverse thermodynamic temperature is proportional the phenomenological inverse temperature

$$\beta(\lambda) = k_E \lambda \tag{5.67}$$

where k_E is a constant. Finally, the canonical entanglement Hamiltonian at half-filling is independent of the inverse temperature $\beta = k_E/\Delta$, such that

$$\mathcal{H}_{can} = \frac{1}{k_E}\left(e^{\dagger}_{\vec{k},+} e_{\vec{k},+} - f^{\dagger}_{\vec{k},+} f_{\vec{k},+}\right) \tag{5.68}$$

where operators $e_{\vec{k},+}$ and $f_{\vec{k},+}$ are given in the Appendix D with Eqs.(D.1)-(D.2), respectively.

5.5.2 *chiral d-wave scenario*

From analytical calculations, one obtains the correlation matrix at $T = 0$

$$C(\vec{k}) = \begin{pmatrix} C_{11}(\vec{k}) & C_{12}(\vec{k}) \\ C^{*}_{12}(\vec{k}) & C_{22}(\vec{k}) \end{pmatrix}, \tag{5.69}$$

where

$$\begin{aligned} C_{11} &= \langle a^{\dagger}_{\vec{k}\uparrow} a_{\vec{k}\uparrow}\rangle \\ &= \frac{1}{2} + \frac{1}{4}\frac{\mu}{\sqrt{\mu^2 + |S_{\vec{k}}|^2}}(\epsilon_1 + m)\frac{1}{E_\alpha}\left(1 - \frac{m}{\sqrt{t^2|\gamma(\vec{k})|^2 + m^2}}\right) \\ &+ \frac{1}{4}\frac{\mu}{\sqrt{\mu^2 + |S_{\vec{k}}|^2}}(\epsilon_2 + m)\frac{1}{E_\beta}\left(1 + \frac{m}{\sqrt{t^2|\gamma(\vec{k})|^2 + m^2}}\right), \end{aligned} \tag{5.70}$$

$$\begin{aligned} C_{22} &= \langle b^{\dagger}_{\vec{k}\uparrow} b_{\vec{k}\uparrow}\rangle \\ &= \frac{1}{2} + \frac{1}{4}\frac{\mu}{\sqrt{\mu^2 + |S_{\vec{k}}|^2}}(\epsilon_1 - m)\frac{1}{E_\alpha}\left(1 + \frac{m}{\sqrt{t^2|\gamma(\vec{k})|^2 + m^2}}\right) \\ &+ \frac{1}{4}\frac{\mu}{\sqrt{\mu^2 + |S_{\vec{k}}|^2}}(\epsilon_2 - m)\frac{1}{E_\beta}\left(1 - \frac{m}{\sqrt{t^2|\gamma(\vec{k})|^2 + m^2}}\right), \end{aligned} \tag{5.71}$$

$$\begin{aligned} C_{12} &= \langle a^{\dagger}_{\vec{k}\uparrow} b_{\vec{k}\uparrow}\rangle \\ &= \frac{1}{4} e^{-i\phi_{\vec{k}}}\left(\left(\frac{\epsilon_1}{E_\alpha} - \frac{\epsilon_2}{E_\beta}\right) - in\left(\frac{1}{E_\alpha} - \frac{1}{E_\beta}\right)\right)\frac{t|\gamma(\vec{k})|}{\sqrt{t^2|\gamma(\vec{k})|^2 + m^2}} \end{aligned} \tag{5.72}$$

with

$$\epsilon_{1,2} = \sqrt{\mu^2 + |S_{\vec{k}}|^2} \pm \sqrt{t^2|\gamma(\vec{k})|^2 + m^2}, \tag{5.73}$$

while

$$m = \frac{\mathrm{Re}(C_{\vec{k}}) \cdot \mathrm{Im}(S_{\vec{k}}) - \mathrm{Im}(C_{\vec{k}}) \cdot \mathrm{Re}(S_{\vec{k}})}{\sqrt{\mu^2 + |S_{\vec{k}}|^2}}, \tag{5.74}$$

and

$$n = \frac{\mathrm{Re}(C_{\vec{k}})\mathrm{Re}(S_{\vec{k}}) + \mathrm{Im}(C_{\vec{k}})\mathrm{Im}(S_{\vec{k}})}{\sqrt{\mu^2 + |S_{\vec{k}}|^2}}. \tag{5.75}$$

Thus, the entanglement spectrum obtained from the eigenvalues of the correlation matrix given in Eq. (5.58) consists of entanglement levels ξ_1 and ξ_2 where

$$\xi_{1,2} = -2\,\mathrm{artanh}(C_{11} + C_{22} - 1 \pm \sqrt{(C_{11} - C_{22})^2 + 4|C_{12}|^2}). \tag{5.76}$$

As the d-wave spin-singlet superconductivity order parameter involves both $C_{\vec{k}}$ and $S_{\vec{k}}$, there is no relationship between states with the zero-value states of the entanglement spectrum and the zero-energy states of the free fermions. At the van-Hove singularity point, i.e., when $\mu = t$, both the entanglement spectrum and the energy spectrum of the free fermions are zero at the M point. The results of our analytical calculations of the entanglement spectrum of the $d_{x^2-y^2} + id_{xy}$-wave superconductivity on the honeycomb lattice are presented in Fig. 5.6.

As we have discussed above, the $d_{x^2-y^2}$- and d_{xy}-wave superconductivity order parameters preserve the time-reversal symmetry (Eq. (5.56)). Based on the time-reversal symmetry and provided $\mathbf{\Psi}_{\vec{k}}$ are the eigenstates of the Hamiltonian given in Eq.(5.55), we can state that

$$\mathbf{\Psi}^*_{\vec{k}} = \mathbf{\Psi}_{-\vec{k}}, \tag{5.77}$$

where the $\mathbf{\Psi}^*_{-\vec{k}}$ are also eigenstates of the Hamiltonian of Eq. (5.55). This yields

$$\mathbf{\Phi}^*_{\vec{k}} = \mathbf{\Phi}_{-\vec{k}}. \tag{5.78}$$

Hence, the real d-wave superconductivity order parameter preserves the time-reversal symmetry in the correlation matrix, which is constructed from the $\mathbf{\Phi}_{\vec{k}}$ as $C(\vec{k}) = \langle \mathbf{\Phi}^\dagger_{\vec{k}} \mathbf{\Phi}_{\vec{k}} \rangle$. The entanglement Hamiltonian satisfies:

$$T_E \mathcal{H}_{ent}(\vec{k}) T_E^{-1} = \mathcal{H}_{ent}(-\vec{k}), \tag{5.79}$$

with $T_E = K$.

When the $d_{x^2-y^2} + id_{xy}$-wave superconductivity order parameter is considered, $C_{\vec{k}}$ and $S_{\vec{k}}$ are complex functions. Then, the m and n terms are non-zero. Hence, the average occupancy number at site A, $C_{11}(\vec{k})$, and the average occupancy number at site B,

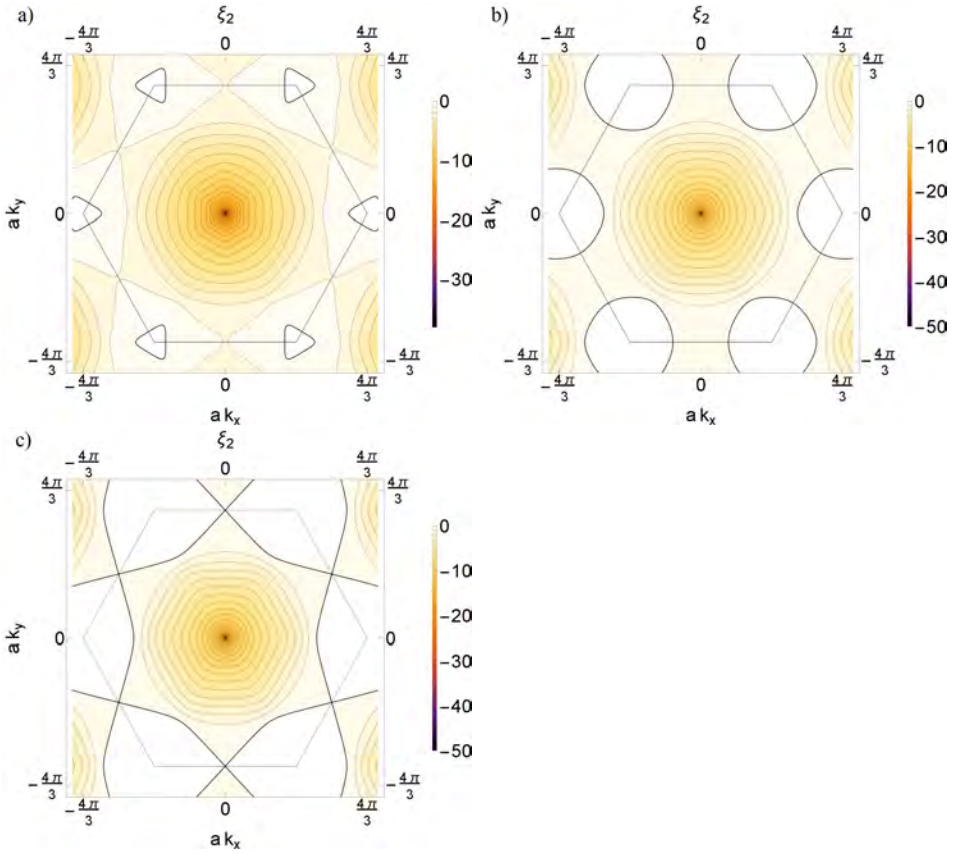

Figure 5.6: Contour plot of entanglement level $\xi_1(\vec{k})$ of $d_{x^2-y^2} + id_{xy}$ -wave superconductivity state on honeycomb lattice plotted for $\frac{J}{t} = 3$, and a) $\frac{\mu}{t} = 0.2$, b) $\frac{\mu}{t} = 0.8$ and c) $\frac{\mu}{t} = 1$. The dashed black line delineates the first Brillouin zone, while the thick black line shows maximally entangled states.

$C_{22}(\vec{k})$, are inequivalent and the off-diagonal element of the correlation matrix $C_{12}(\vec{k})$ is complex. Because $S_{\vec{k}}$ is an odd function in the momentum space, while $C_{\vec{k}}$ is a even function, it can be shown that elements of the correlation matrix $C_{11}(\vec{k})$, $C_{22}(\vec{k})$, and $C_{12}(\vec{k})$ are constrained as $C_{11}(-\vec{k}) = C_{22}(\vec{k})$ and $C^*_{12}(-\vec{k}) = C_{12}(\vec{k})$. Therefore, it follows that the complex $d_{x^2-y^2} + id_{xy}$-wave superconductivity order parameter breaks the time-reversal symmetry in the entanglement Hamiltonian. The topology of the entanglement Hamiltonian in two-dimension with broken time-reversal symmetry is characterized by the entanglement Chern number.

For further analysis of the topological properties of the entanglement Hamiltonian, we require not only its eigenvalues, but also its eigenstates. The eigenstates of the correlation matrix are identical to the eigenstates of the entanglement Hamiltonian and can be expressed as

$$q_{\vec{k}\uparrow} = \delta_+(\vec{k}) a_{\vec{k}\uparrow} + \delta_-(\vec{k}) b_{\vec{k}\uparrow} \tag{5.80}$$

$$r_{\vec{k}\uparrow} = \delta_+(-\vec{k}) a_{\vec{k}\uparrow} - \delta^*_-(-\vec{k}) b_{\vec{k}\uparrow} \tag{5.81}$$

where explicit expressions for $\delta_+(\vec{k})$ and $\delta_-(\vec{k})$ are given in Appendix (D) by Eq.(D.21). Using these eigenstates, we can calculate the Berry curvature

$$F(\vec{k}) = \frac{\partial A_y}{\partial k_x} - \frac{\partial A_x}{\partial k_y}, \tag{5.82}$$

and the Berry connection

$$\vec{A}(\vec{k}) = i\langle r(\vec{k})| \frac{\partial}{\partial \vec{k}} |r(\vec{k})\rangle. \tag{5.83}$$

Through numerical integrations of the Berry curvature along the Brillouin zone, we find that the entanglement Chern number is $C = 1$, in the case of the chiral $d_{x^2-y^2} + id_{xy}$-wave superconductivity state. In the presence of $SU(2)$ rotation and broken time-reversal symmetry, as in the case of an energetic Hamiltonian, the Chern number C can have even values only. For the entanglement Hamiltonian, it is possible to obtain an odd value for the Chern number, as it is not invariant to the $SU(2)$ rotation. As a result, the topology of the entanglement Hamiltonian, which is obtained by tracing out the spin-down subsystem of the ground state of the chiral $d_{x^2-y^2} + id_{xy}$-wave superconductivity state on the honeycomb lattice, clearly differs from the topology of the energetic Hamiltonian of free fermions without the superconductivity instabilities.

5.6 CONCLUSION AND OUTLOOK

We analytically evaluated the entanglement spectra of the superconductivity states on the graphene honeycomb lattice, primarily focusing on the s-wave and chiral $d_{x^2-y^2} + id_{xy}$ superconductivity states. When one spin direction was traced out, exact correspondence between the maximally entangled states of the s-wave superconductor and the zero energies of the noninteracting fermionic honeycomb lattice at finite doping was observed. The relationship between the topologies of the entanglement and subsystem Hamiltonians was found to depend on the coupling between the subsystems. Further, the chiral $d_{x^2-y^2} + id_{xy}$ superconductivity order parameter breaks the time-reversal symmetry in the entanglement Hamiltonian. The topological properties of the entanglement Hamiltonian, characterized by the topological nontrivial entanglement Chern number $C = 1$, clearly differ from those of the time-reversal invariant Hamiltonian of the noninteracting fermions on the honeycomb lattice.

The investigations presented herein are based on closed analytical expressions for the full eigensystems of the s- and d-wave superconductivity states on the honeycomb lattice over the entire Brillouin zone. The method used to examine these eigensystems may constitute a useful tool for new studies of superconductivity in graphene.

Future work may investigate the relationship between the topologies of the entanglement and subsystem Hamiltonians through the topological phase transition; for example, in the coexistence region between antiferromagnetism and $d_{x^2-y^2} + id_{xy}$ superconducting correlations in graphene [Black-Schaffer and Hur, 2015] and graphene bilayers [Milovanović and Predin, 2012].

Superconducting states possess particle-hole symmetry for fermionic excitations. A particle can become a hole by creating a Cooper pair. Hence, the fermionic excitations are expressed by $c_\sigma(\epsilon)$ ($c_\sigma^\dagger(\epsilon)$) being the annihilation (creation) operator of a quasiparticle with energy ϵ and the spin σ. From particle-hole symmetry, we obtain

$$c_\sigma(\epsilon) = c_\sigma^\dagger(-\epsilon) \tag{5.84}$$

$$\lim_{\epsilon\to 0}\left(c_\sigma(\epsilon)\right) = \lim_{\epsilon\to 0}\left(c_\sigma^\dagger(-\epsilon)\right) \tag{5.85}$$

$$c_\sigma(0) = c_\sigma^\dagger(0) \tag{5.86}$$

$$\gamma = \gamma^\dagger. \tag{5.87}$$

Thus, because of the particle-hole symmetry of the superconductivity state, the quasi-particle and its antiparticle are equal at zero

energy. This self-conjugate condition is called the Majorana condition, which is satisfied by a class of fermions called Majorana fermions [Sato and Ando, 2017]. A fascinating feature of the Majorana fermions is that they obey non-Abelian statistics, which differs from Abelian statistics. Particles that obey Abelian statistics satisfy the anticommutation relation $\langle \Psi_1 \Psi_2 \rangle = \langle \Psi_2 \Psi_1 \rangle e^{i\phi}$, where $\phi = 0$ denotes bosons and $\phi = \pi$ denotes fermions. Let us now consider N Majorana zero energy modes given by $\gamma_1, \gamma_2, \gamma_3, ..., \gamma_N$. Then, all Majorana fields satisfy

$$\gamma_i^2 = 1, \tag{5.88}$$

$$\gamma_i \gamma_j = -\gamma_j \gamma_i \quad \text{for} \quad i \neq j. \tag{5.89}$$

The non-Abelian statistics is reflected by branding of any pair of Majorana fields.

$$\gamma_i \to \gamma_j, \qquad \gamma_j \to -\gamma_i. \tag{5.90}$$

As we have already seen in this Chapter, the doped graphene can be a chiral $d_{x^2-y^2} + id_{xy}$ superconductor. Graphene, in the presence of the spin-singlet $d_{x^2-y^2} + id_{xy}$ state, could exhibit incredibly rich physics. Because graphene is a two-dimensional material, the possibility of tuning of the Rashba spin-orbit coupling is remarkable and its manipulation could be easier than that in other materials [Min et al., 2006]. For realistic values of the Rashba spin-orbit, in the possible $d_{x^2-y^2} + id_{xy}$ state in doped graphene to the van-Hove singularity point, Majorana fermions could appear at edges by tuning a Zeeman field [Black-Schaffer, 2012]. Furthermore, by increasing the spin-orbit coupling, the $d_{x^2-y^2} + d_{xy}$ superconductor undergoes a topological phase transition from a chiral superconductor to a helical superconductor. In the region where the energy gap is closed, the low energy excitations are Majorana fermions [Sun et al., 2016, Huang et al., 2016]. The Majorana fermion of this system obeys non-Abelian statistics, which is at the heart of the idea of the quantum computer [Nayak et al., 2008]. The Majorana fermions reduce the probability of a random change of the ground state, and this state is very stable to thermal fluctuations. The state obtained by the exchange of two Majorana fermions does not take a simple phase due to the non-Abelian statistics. This corresponds to the manipulations of qubits, which are superposition of $|0\rangle$ and $|1\rangle$. The superposition and entanglement can make a quantum computer operate much faster than a classical one.

The above makes further research on the spin-singlet $d_{x^2-y^2} + id_{xy}$ state, particularly with the Rashba spin-orbit coupling and entanglement, quite interesting.

A

DIAGONALIZATION OF THE BILAYER HAMILTONIAN

Putting $t_4 = 0$ and fixing a wave vector $\vec{k}$ the Hamiltonian (4.1) reads with respect to the basis $\left(a^\dagger_{2\vec{k}}, b^\dagger_{1\vec{k}}, b^\dagger_{2\vec{k}}, a^\dagger_{1\vec{k}}\right)|0\rangle$

$$H = \begin{pmatrix} 0 & t_\perp & -t\gamma(\vec{k}) & 0 \\ t_\perp & 0 & 0 & -t\gamma^*(\vec{k}) \\ -t\gamma^*(\vec{k}) & 0 & 0 & -t_3\gamma(\vec{k}) \\ 0 & -t\gamma(\vec{k}) & -t_3\gamma^*(\vec{k}) & 0 \end{pmatrix}. \tag{A.1}$$

Using $\gamma(\vec{k}) = |\gamma(\vec{k})|e^{i\phi_{\vec{k}}}$ we apply the transformation

$$U_1 = \frac{1}{\sqrt{2}} \begin{pmatrix} 1 & 1 & 0 & 0 \\ 0 & 0 & e^{i\phi_{\vec{k}}} & e^{-i\phi_{\vec{k}}} \\ 0 & 0 & e^{i\phi_{\vec{k}}} & -e^{-i\phi_{\vec{k}}} \\ 1 & -1 & 0 & 0 \end{pmatrix} \tag{A.2}$$

such that in

$$\begin{aligned} H_1 =& U_1 H U_1^\dagger \\ =& \begin{pmatrix} t_\perp & -t|\gamma(\vec{k})| & 0 & 0 \\ -t|\gamma(\vec{k})| & -t_3|\gamma(\vec{k})|\cos\left(3\phi_{\vec{k}}\right) & it_3|\gamma(\vec{k})|\sin\left(3\phi_{\vec{k}}\right) & 0 \\ 0 & -it_3|\gamma(\vec{k})|\sin\left(3\phi_{\vec{k}}\right) & t_3|\gamma(\vec{k})|\cos\left(3\phi_{\vec{k}}\right) & -t|\gamma(\vec{k})| \\ 0 & 0 & -t|\gamma(\vec{k})| & -t_\perp \end{pmatrix} \end{aligned} \tag{A.3}$$

all information on the phase $\phi_{\vec{k}}$ is contained in the matrix elements being proportional to the skew parameter t_3. Proceeding now with the transformation

$$U_2 = \frac{1}{\sqrt{2}} \begin{pmatrix} 1 & -1 & 0 & 0 \\ 1 & 1 & 0 & 0 \\ 0 & 0 & 1 & -1 \\ 0 & 0 & 1 & 1 \end{pmatrix} \tag{A.4}$$

we find

$$H_2 = U_2 H_1 U_2^\dagger = \frac{1}{2} \begin{pmatrix} e_1 & c & -is & -is \\ c & e_2 & is & is \\ is & -is & -e_2 & c \\ is & -is & c & -e_1 \end{pmatrix} \tag{A.5}$$

with

$$e_1 = 2t|\gamma(\vec{k})| + t_\perp - t_3|\gamma(\vec{k})|\cos\left(3\phi_{\vec{k}}\right), \quad (A.6)$$

$$e_2 = -2t|\gamma(\vec{k})| + t_\perp - t_3|\gamma(\vec{k})|\cos\left(3\phi_{\vec{k}}\right), \quad (A.7)$$

$$c = t_\perp + t_3|\gamma(\vec{k})|\cos\left(3\phi_{\vec{k}}\right), \quad (A.8)$$

$$s = t_3|\gamma(\vec{k})|\sin\left(3\phi_{\vec{k}}\right). \quad (A.9)$$

Here it is useful to split the above matrix as $H_2 = H_2^{'} + H_2^{''}$ where

$$H_2^{'} = \frac{1}{2}\begin{pmatrix} e_1 & 0 & -is & 0 \\ 0 & e_2 & 0 & is \\ is & 0 & -e_2 & 0 \\ 0 & -is & 0 & -e_1 \end{pmatrix}$$

$$H_2^{''} = \frac{1}{2}\begin{pmatrix} 0 & c & 0 & -is \\ c & 0 & is & 0 \\ 0 & -is & 0 & c \\ is & 0 & c & 0 \end{pmatrix}. \quad (A.10)$$

$H_2^{'}$ is diagonalized by

$$U_3 = \begin{pmatrix} \alpha_+ & 0 & -i\sigma\alpha_- & 0 \\ 0 & -i\sigma\alpha_+ & 0 & \alpha_- \\ -i\sigma\alpha_- & 0 & \alpha_+ & 0 \\ 0 & \alpha_- & 0 & -i\sigma\alpha_+ \end{pmatrix} \quad (A.11)$$

with $\sigma = \text{sign}\left(\sin(3\phi(\vec{k}))\right)$ and

$$\alpha_\pm = \sqrt{\frac{1}{2}\left(1 \pm \frac{t_\perp - t_3|\gamma(\vec{k})|\cos\left(3\phi_{\vec{k}}\right)}{\sqrt{t_\perp^2 + t_3^2|\gamma(\vec{k})|^2 - 2t_\perp t_3|\gamma(\vec{k})|\cos\left(3\phi_{\vec{k}}\right)}}\right)} \quad (A.12)$$

such that

$$H_3 = U_3 H_2 U_3^\dagger = \begin{pmatrix} \zeta_1 & id\sigma & 0 & b \\ -id\sigma & \zeta_2 & b & 0 \\ 0 & b & -\zeta_2 & id\sigma \\ b & 0 & -id\sigma & -\zeta_1 \end{pmatrix} \quad (A.13)$$

where

$$d = \frac{\left(t_\perp^2 - t_3^2|\gamma(\vec{k})|^2\right)/2}{\sqrt{t_\perp^2 + t_3^2|\gamma(\vec{k})|^2 - 2t_\perp t_3|\gamma(\vec{k})|\cos\left(3\phi_{\vec{k}}\right)}}, \quad (A.14)$$

$$b = \frac{t_\perp t_3 |\gamma(\vec{k})| |\sin\left(3\phi_{\vec{k}}\right)|}{\sqrt{t_\perp^2 + t_3^2|\gamma(\vec{k})|^2 - 2t_\perp t_3|\gamma(\vec{k})|\cos\left(3\phi_{\vec{k}}\right)}}, \quad \text{(A.15)}$$

and $\pm\zeta_1$ and $\pm\zeta_2$ are eigenvalues of $H_2^{'}$ given by

$$\zeta_{1/2} = \frac{1}{2}\left(\pm 2t|\gamma(\vec{k})| + \sqrt{t_\perp^2 + t_3^2|\gamma(\vec{k})|^2 - 2t_\perp t_3|\gamma(\vec{k})|\cos\left(3\phi_{\vec{k}}\right)}\right). \quad \text{(A.16)}$$

Splitting now H_3 in the form

$$H_3 = \begin{pmatrix} \zeta_1 & id & 0 & 0 \\ -id & \zeta_2 & 0 & 0 \\ 0 & 0 & -\zeta_2 & id \\ 0 & 0 & -id & -\zeta_1 \end{pmatrix} + \begin{pmatrix} 0 & 0 & 0 & b \\ 0 & 0 & b & 0 \\ 0 & b & 0 & 0 \\ b & 0 & 0 & 0 \end{pmatrix} \quad \text{(A.17)}$$

the first part is diagonalized by

$$U_4 = \begin{pmatrix} -i\sigma\tau\beta_+ & \beta_- & 0 & 0 \\ \beta_- & -i\sigma\tau\beta_+ & 0 & 0 \\ 0 & 0 & -i\sigma\tau\beta_+ & \beta_- \\ 0 & 0 & \beta_- & -i\sigma\tau\beta_+ \end{pmatrix} \quad \text{(A.18)}$$

with $\tau = \text{sign}(d)$ and

$$\beta_\pm = \sqrt{\frac{1}{2}\left(1 \pm \frac{\zeta_1 - \zeta_2}{\sqrt{(\zeta_1 - \zeta_2)^2 + 4d^2}}\right)} \quad \text{(A.19)}$$

while the second part is left unchanged by U_4 resulting in

$$H_4 = U_4 H_3 U_4^\dagger = \begin{pmatrix} \epsilon_1 & 0 & 0 & b \\ 0 & \epsilon_2 & b & 0 \\ 0 & b & -\epsilon_2 & 0 \\ b & 0 & 0 & -\epsilon_1 \end{pmatrix} \quad \text{(A.20)}$$

with the diagonal elements are given in terms of

$$\epsilon_{1/2} = \frac{1}{2}\left(\zeta_1 + \zeta_2 \pm \sqrt{(\zeta_1 - \zeta_2)^2 + 4d^2}\right). \quad \text{(A.21)}$$

Finally, H_4 is brought into diagonal form via

$$U_5 = \begin{pmatrix} \gamma_+^{(1)} & 0 & 0 & \gamma_-^{(1)} \\ 0 & \gamma_+^{(2)} & \gamma_-^{(2)} & 0 \\ 0 & \gamma_-^{(2)} & -\gamma_+^{(2)} & 0 \\ \gamma_-^{(1)} & 0 & 0 & -\gamma_+^{(1)} \end{pmatrix} \quad \text{(A.22)}$$

with

$$\gamma_{\pm}^{(1)} = \sqrt{\frac{1}{2}\left(1 \pm \frac{\epsilon_1}{E_2}\right)} \quad , \quad \gamma_{\pm}^{(2)} = \sqrt{\frac{1}{2}\left(1 \pm \frac{\epsilon_2}{E_2}\right)} \tag{A.23}$$

and

$$E_{1/2} = \sqrt{\epsilon_{1,2}^2 + b^2} \tag{A.24}$$

$$= \frac{1}{2}\Bigg[t_\perp^2 + t_3^2|\gamma(\vec{k})|^2 + 2t^2|\gamma(\vec{k})|^2$$

$$\pm \sqrt{4t^2|\gamma(\vec{k})|^2\left(t_\perp^2 + t_3^2|\gamma(\vec{k})|^2 - 2t_\perp t_3|\gamma(\vec{k})|\cos\left(3\phi_{\vec{k}}\right)\right) + \left(t_\perp^2 - t_3^2|\gamma(\vec{k})|^2\right)^2}\Bigg]. \tag{A.25}$$

Thus,

$$U_5 H_4 U_5^\dagger = \text{ diag}\left(E_1, E_2, -E_2, -E_1\right) , \tag{A.26}$$

and the matrix elements of the corresponding total transformation $U = U_5U_4U_3U_2U_1$ can be expressed as

$$U_{11} = \frac{1}{2}\left(\alpha_- - i\sigma\alpha_+\right)\left(\tau\beta_+ + \beta_-\right)\left(\gamma_+^{(1)} - i\sigma\gamma_-^{(1)}\right) \tag{A.27}$$

$$U_{12} = \frac{1}{2}\left(\alpha_+ - i\sigma\alpha_-\right)\left(\tau\beta_+ + \beta_-\right)\left(\gamma_-^{(1)} - i\sigma\gamma_+^{(1)}\right) \tag{A.28}$$

$$U_{13} = -\frac{e^{i\phi_{\vec{k}}}}{2}\left(\alpha_- - i\sigma\alpha_+\right)\left(\tau\beta_+ - \beta_-\right)\left(\gamma_+^{(1)} + i\sigma\gamma_-^{(1)}\right) \tag{A.29}$$

$$U_{14} = \frac{e^{-i\phi_{\vec{k}}}}{2}\left(\alpha_- + i\sigma\alpha_+\right)\left(\tau\beta_+ - \beta_-\right)\left(\gamma_+^{(1)} - i\sigma\gamma_-^{(1)}\right) \tag{A.30}$$

and

$$U_{21} = -\frac{1}{2}\left(\alpha_+ + i\sigma\alpha_-\right)\left(\tau\beta_+ - \beta_-\right)\left(\gamma_+^{(2)} - i\sigma\gamma_-^{(2)}\right) \tag{A.31}$$

$$U_{22} = -\frac{1}{2}\left(\alpha_+ - i\sigma\alpha_-\right)\left(\tau\beta_+ - \beta_-\right)\left(\gamma_+^{(2)} + i\sigma\gamma_-^{(2)}\right) \tag{A.32}$$

$$U_{23} = -\frac{e^{i\phi_{\vec{k}}}}{2}\left(\alpha_+ + i\sigma\alpha_-\right)\left(\tau\beta_+ + \beta_-\right)\left(\gamma_+^{(2)} + i\sigma\gamma_-^{(2)}\right) \tag{A.33}$$

$$U_{24} = -\frac{e^{-i\phi_{\vec{k}}}}{2}\left(\alpha_+ - i\sigma\alpha_-\right)\left(\tau\beta_+ + \beta_-\right)\left(\gamma_+^{(2)} - i\sigma\gamma_-^{(2)}\right) \tag{A.34}$$

which are the complex conjugates of the components of the eigenvectors of the conduction-band states with positive energies $E_1(\vec{k})$, $E_2(\vec{k})$, while

$$U_{31} = \frac{1}{2}\left(\alpha_- - i\sigma\alpha_+\right)\left(\tau\beta_+ - \beta_-\right)\left(\gamma_+^{(2)} - i\sigma\gamma_-^{(2)}\right) \tag{A.35}$$

$$U_{32} = \frac{1}{2}\left(\alpha_- + i\sigma\alpha_+\right)\left(\tau\beta_+ - \beta_-\right)\left(\gamma_+^{(2)} + i\sigma\gamma_-^{(2)}\right) \tag{A.36}$$

$$U_{33} = -\frac{e^{i\phi_{\vec{k}}}}{2}\left(\alpha_+ + i\sigma\alpha_-\right)\left(\tau\beta_+ + \beta_-\right)\left(\gamma_-^{(2)} - i\sigma\gamma_+^{(2)}\right) \tag{A.37}$$

$$U_{34} = -\frac{e^{-i\phi_{\vec{k}}}}{2}\left(\alpha_+ - i\sigma\alpha_-\right)\left(\tau\beta_+ + \beta_-\right)\left(\gamma_-^{(2)} + i\sigma\gamma_+^{(2)}\right) \tag{A.38}$$

and

$$U_{41} = \frac{1}{2}\left(\alpha_+ + i\sigma\alpha_-\right)\left(\tau\beta_+ + \beta_-\right)\left(\gamma_+^{(1)} - i\sigma\gamma_-^{(1)}\right) \tag{A.39}$$

$$U_{42} = -\frac{1}{2}\left(\alpha_- + i\sigma\alpha_+\right)\left(\tau\beta_+ + \beta_-\right)\left(\gamma_-^{(1)} - i\sigma\gamma_+^{(1)}\right) \tag{A.40}$$

$$U_{43} = \frac{e^{i\phi_{\vec{k}}}}{2}\left(\alpha_+ + i\sigma\alpha_-\right)\left(\tau\beta_+ - \beta_-\right)\left(\gamma_+^{(1)} + i\sigma\gamma_-^{(1)}\right) \tag{A.41}$$

$$U_{44} = \frac{e^{-i\phi_{\vec{k}}}}{2}\left(\alpha_- + i\sigma\alpha_+\right)\left(\tau\beta_+ - \beta_-\right)\left(\gamma_-^{(1)} + i\sigma\gamma_+^{(1)}\right) \tag{A.42}$$

correspond to the valence-band states with negative energies $(-E_2(\vec{k}))$, $(-E_1(\vec{k}))$. Note that all factors involving $\alpha_\pm$, $\gamma_\pm^{(1)}$, $\gamma_\pm^{(2)}$ in the above expressions have modulus one, i.e. they are phase factors.

B

CORRELATION MATRICES

Upon tracing out layer 1 from the ground state of the undoped bilayer system the correlation matrix reads in the basis $\left(a^\dagger_{2\vec{k}}, b^\dagger_{2\vec{k}}\right)|0\rangle$

$$\begin{aligned} C(\vec{k}) &= \begin{pmatrix} U_{31}U_{31}^* + U_{41}U_{41}^* & U_{31}U_{33}^* + U_{41}U_{43}^* \\ U_{33}U_{31}^* + U_{43}U_{41}^* & U_{33}U_{33}^* + U_{43}U_{43}^* \end{pmatrix} \\ &= \begin{pmatrix} \frac{1}{2} & u(\vec{k}) \\ u^*(\vec{k}) & \frac{1}{2} \end{pmatrix} \end{aligned} \tag{B.1}$$

with

$$u(\vec{k}) = \frac{e^{-i\phi_{\vec{k}}}}{4}\left(\beta_+^2 - \beta_-^2\right)\left(\left(\gamma_+^{(1)} - i\sigma\gamma_-^{(1)}\right)^2 - \left(\gamma_+^{(2)} - i\sigma\gamma_-^{(2)}\right)^2\right). \tag{B.2}$$

This quantity becomes singular at the corners of the Brillouin zone where $\gamma(\vec{k})$ is zero such that its phase is ill-defined, and at the positions of the satellite Dirac cones of the energy spectrum where, as discussed in appendix 4.3, $\gamma_\pm^{(2)}$ is discontinuous.

Tracing out the sublattices A1 and B2 one finds in the basis $\left(a^\dagger_{2\vec{k}}, b^\dagger_{1\vec{k}}\right)|0\rangle$

$$\begin{aligned} C(\vec{k}) &= \begin{pmatrix} U_{31}U_{31}^* + U_{41}U_{41}^* & U_{31}U_{32}^* + U_{41}U_{42}^* \\ U_{32}U_{31}^* + U_{42}U_{41}^* & U_{32}U_{32}^* + U_{42}U_{42}^* \end{pmatrix} \\ &= \begin{pmatrix} \frac{1}{2} & v(\vec{k}) \\ v^*(\vec{k}) & \frac{1}{2} \end{pmatrix} \end{aligned} \tag{B.3}$$

with

$$\begin{aligned} v(\vec{k}) =& \frac{\left(\alpha_- - i\sigma\alpha_+\right)^2}{4}\left(\left(\tau\beta_+ - \beta_-\right)^2\left(\gamma_+^{(2)} - i\sigma\gamma_-^{(2)}\right)^2\right. \\ &\left. + \left(\tau\beta_+ + \beta_-\right)^2\left(\gamma_+^{(1)} - i\sigma\gamma_-^{(1)}\right)^2\right). \end{aligned} \tag{B.4}$$

Note that the expressions (B.2),(B.4) obey the interesting sum rule

$$|u(\vec{k})|^2 + |v(\vec{k})|^2 = \frac{1}{4} \tag{B.5}$$

which s fulfilled whenever the coefficients involved satisfy

$$\alpha_+^2 + \alpha_-^2 = \beta_+^2 + \beta_-^2 = \left(\gamma_+^{(1/2)}\right)^2 + \left(\gamma_-^{(1/2)}\right)^2 = 1\,, \tag{B.6}$$

which is the case here by construction.

Finally, the correlation matrix obtained by tracing out the sublattices A1, A2 is proportional to the unit matrix,

$$\begin{aligned} C(\vec{k}) &= \begin{pmatrix} U_{32}U_{32}^* + U_{42}U_{42}^* & U_{32}U_{33}^* + U_{42}U_{43}^* \\ U_{33}U_{32}^* + U_{43}U_{42}^* & U_{33}U_{33}^* + U_{43}U_{43}^* \end{pmatrix} \\ &= \begin{pmatrix} \frac{1}{2} & 0 \\ 0 & \frac{1}{2} \end{pmatrix} \end{aligned} \tag{B.7}$$

implying that the remaining subsystem is maximally entangled with the subsystem traced out.

C

DIAGONALIZATION OF THE $d + id$-WAVE SUPERCONDUCTIVITY STATE ON THE HONEYCOMB LATTICE

In this Appendix we present analytical diagolazation of the Hamiltonian of the chiral $d + id$-wave superconductivity state on the honeycomb lattice. Complexity of the order parameter makes the analytical approach more difficult. The starting point of our analysis is the Bardeen-Cooper-Schrieffer mean-field Hamiltonian in momentum space is

$$\begin{aligned} H_{MF}(\vec{k}) = & -t\sum_{\vec{k}}\left(\gamma(\vec{k})a^{\dagger}_{\vec{k}\sigma}b_{\vec{k}\sigma}+h.c.\right) \\ & -\mu\sum_{\vec{k}}\left(a^{\dagger}_{\vec{k}\sigma}a_{\vec{k}\sigma}+b^{\dagger}_{\vec{k}\sigma}b_{\vec{k}\sigma}\right) \\ & -J\sum_{\vec{k},\vec{\delta}}\left(\Delta_{\vec{\delta}}e^{i\vec{k}\vec{\delta}}\left(a^{\dagger}_{\vec{k}\uparrow}b^{\dagger}_{-\vec{k}\downarrow}-a^{\dagger}_{\vec{k}\downarrow}b^{\dagger}_{-\vec{k}\uparrow}\right)+h.c.\right) \end{aligned} \tag{C.1}$$

where we define the superconductivity order parameter

$$\Delta(\vec{k}) = \sum_{\vec{\delta}}\Delta_{\vec{\delta}}e^{i\vec{k}\vec{\delta}} \tag{C.2}$$

as a combination of the $d_{x^2-y^2}$ and d_{xy}-wave superconductivity state $\Delta_{d\pm id}(\vec{k}) = \cos\left(\frac{\pi}{3}\right)\Delta_{d_x^2-y^2}(\vec{k}) \pm \sin\left(\frac{\pi}{3}\right)\Delta_{d_{xy}}(\vec{k})$ which minimalizes a free energy.

We apply the transformations

$$\begin{aligned} c_{\vec{k},\sigma} &= \frac{1}{\sqrt{2}}(a_{\vec{k},\sigma} - e^{i\cdot\phi_{\vec{k}}}b_{\vec{k},\sigma}), \\ d_{\vec{k},\sigma} &= \frac{1}{\sqrt{2}}(a_{\vec{k},\sigma} + e^{i\cdot\phi_{\vec{k}}}b_{\vec{k},\sigma}) \end{aligned} \tag{C.3}$$

such that in

$$H_1(\vec{k}) = \begin{pmatrix} t|\gamma(\vec{k})|-\mu & 0 & C_{\vec{k}} & -iS_{\vec{k}} \\ 0 & -t|\gamma(\vec{k})|-\mu & iS_{\vec{k}} & -C_{\vec{k}} \\ C^*_{\vec{k}} & -iS^*_{\vec{k}} & -t|\gamma(\vec{k})|+\mu & 0 \\ iS^*_{\vec{k}} & -C^*_{\vec{k}} & 0 & t|\gamma(\vec{k})|+\mu \end{pmatrix}. \tag{C.4}$$

diagonalize the kinetic part of the Hamiltonian. $C_{\vec{k}} = J\sum_{\vec{\delta}}\vec{\Delta}_{\vec{\delta}}\cos(\vec{k}\vec{\delta} - \phi_{\vec{k}})$ and $S_{\vec{k}} = J\sum_{\vec{\delta}}\vec{\Delta}_{\vec{\delta}}\sin(\vec{k}\vec{\delta} - \phi_{\vec{k}})$ are complex functions.

Here it is useful to split this Hamiltonian as $H_1 = H_1^{'} + H_1^{''}$ where

$$H_1^{'}(\vec{k}) = \begin{pmatrix} t|\gamma(\vec{k})| - \mu & 0 & 0 & -iS_{\vec{k}} \\ 0 & -t|\gamma(\vec{k})| - \mu & iS_{\vec{k}} & 0 \\ 0 & -iS_{\vec{k}}^{*} & -t|\gamma(\vec{k})| + \mu & 0 \\ iS_{\vec{k}}^{*} & 0 & 0 & t|\gamma(\vec{k})| + \mu \end{pmatrix}. \tag{C.5}$$

and

$$H_1^{''}(\vec{k}) = \begin{pmatrix} 0 & 0 & C_{\vec{k}} & 0 \\ 0 & 0 & 0 & -C_{\vec{k}} \\ C_{\vec{k}}^{*} & 0 & 0 & 0 \\ 0 & -C_{\vec{k}}^{*} & 0 & 0 \end{pmatrix}. \tag{C.6}$$

$H_1^{'}$ is diagonalized by

$$e_{\vec{k}+} = i\alpha_{-}^{*} c_{\vec{k}\uparrow} + \alpha_{+} d_{-\vec{k}\downarrow}^{\dagger} \tag{C.7}$$

$$f_{\vec{k}+} = -i\alpha_{-}^{*} d_{\vec{k}\uparrow} + \alpha_{+} c_{-\vec{k}\downarrow}^{\dagger} \tag{C.8}$$

with

$$\begin{aligned} \alpha_{+} &= \sqrt{\frac{1}{2}\left(1 + \frac{\mu}{\sqrt{\mu^2 + |S_{\vec{k}}|^2}}\right)} \\ \alpha_{-} &= \frac{S_{\vec{k}}}{\sqrt{2\sqrt{\mu^2 + |S_{\vec{k}}|^2}\left(\mu + \sqrt{\mu^2 + |S_{\vec{k}}|^2}\right)}}. \end{aligned} \tag{C.9}$$

This leads to

$$H_2 = U_2 H_1 U_2^{\dagger} = \begin{pmatrix} e_1 & m & -l & 0 \\ m & e_2 & 0 & l \\ -l^{*} & 0 & -e_1 & m \\ 0 & l^{*} & m & -e_2 \end{pmatrix} \tag{C.10}$$

with

$$m = \frac{\mathrm{R}e(C_{\vec{k}}) \cdot \mathrm{I}m(S_{\vec{k}}) - \mathrm{I}m(C_{\vec{k}}) \cdot \mathrm{R}e(S_{\vec{k}})}{\sqrt{\mu^2 + |S_{\vec{k}}|^2}} \tag{C.11}$$

and

$$l = \alpha_{+}^{2} C_{\vec{k}}^{*} + (\alpha_{-}^{*})^2 C_{\vec{k}} \tag{C.12}$$

and $\pm e_1$ and $\pm e_2$ are eigenenergies of the Hamiltonian $H_1^{'}$ given by

$$e_1 = t|\gamma(\vec{k})| + \sqrt{\mu^2 + |S_{\vec{k}}|^2} \tag{C.13}$$

and

$$e_2 = -t|\gamma(\vec{k})| + \sqrt{\mu^2 + |S_{\vec{k}}|^2}. \tag{C.14}$$

We can now split this Hamiltonian as $H_2 = H_2^{'} + H_2^{''}$ where

$$H_2^{'} = \begin{pmatrix} e_1 & m & 0 & 0 \\ m & e_2 & 0 & 0 \\ 0 & 0 & -e_1 & m \\ 0 & 0 & m & -e_2 \end{pmatrix} \quad , \quad H_2^{''} = \begin{pmatrix} 0 & 0 & -l & 0 \\ 0 & 0 & 0 & l \\ -l^* & 0 & 0 & 0 \\ 0 & l^* & 0 & 0 \end{pmatrix}. \tag{C.15}$$

Proceeding now with the transformations

$$g_{\vec{k}+} = \beta_+ e_{\vec{k}+} + \sigma\beta_- f_{\vec{k}+} \tag{C.16}$$

$$h_{\vec{k}+} = \sigma\beta_- e_{\vec{k}+} - \beta_+ f_{\vec{k}+} \tag{C.17}$$

where $\sigma = \text{sign}(m)$ and

$$\beta_\pm = \sqrt{\frac{1}{2}\left(1 \pm \frac{t|\gamma(\vec{k})|}{\sqrt{t^2|\gamma(\vec{k})|^2 + m^2}}\right)} \tag{C.18}$$

we diagonalize first part of the Hamiltonian $H_2^{'}$ and we get

$$H_3 = U_3 H_2 U_3^\dagger = \begin{pmatrix} \epsilon_1 & 0 & 0 & -l \\ 0 & \epsilon_2 & -l & 0 \\ 0 & -l^* & -\epsilon_2 & 0 \\ -l^* & 0 & 0 & -\epsilon_1 \end{pmatrix} \tag{C.19}$$

where $\pm\epsilon_1$ and $\pm\epsilon_2$ are eigenenergies of the Hamiltonian $H_2^{'}$

$$\epsilon_1 = \sqrt{\mu^2 + |S_{\vec{k}}|^2} + \sqrt{t^2|\gamma(\vec{k})|^2 + m^2} \tag{C.20}$$

and

$$\epsilon_2 = \sqrt{\mu^2 + |S_{\vec{k}}|^2} - \sqrt{t^2|\gamma(\vec{k})|^2 + m^2}. \tag{C.21}$$

Finally, this Hamiltonian is brought to the diagonalized form with transformations

$$o_{\vec{k}+} = \gamma_+^{(1)} g_{\vec{k}+} - \gamma_-^{(1)} g_{\vec{k}-}^\dagger \tag{C.22}$$

$$p_{\vec{k}+} = \gamma_+^{(2)} h_{\vec{k}+} - \gamma_-^{(2)} h_{\vec{k}-}^\dagger \tag{C.23}$$

with

$$\gamma_+^{(1)} = \sqrt{\frac{1}{2}\left(1 + \frac{\epsilon_1}{E_\alpha}\right)} \quad , \quad \gamma_-^{(1)} = \frac{l}{\sqrt{2E_\alpha\left(E_\alpha + \epsilon_1\right)}} \tag{C.24}$$

and

$$\gamma_{+}^{(2)}=\sqrt{\frac{1}{2}\left(1+\frac{\epsilon_2}{E_\beta}\right)}\quad,\quad\gamma_{-}^{(2)}=\frac{l}{\sqrt{2E_\beta\left(E_\beta+\epsilon_2\right)}}\tag{C.25}$$

and

$$E_\alpha=\sqrt{t^2|\gamma(\vec{k})|^2+\mu^2+|S_{\vec{k}}|^2+|C_{\vec{k}}|^2+2\sqrt{u+v}}\tag{C.26}$$

and

$$E_\beta=\sqrt{t^2|\gamma(\vec{k})|^2+\mu^2+|S_{\vec{k}}|^2+|C_{\vec{k}}|^2-2\sqrt{u+v}}.\tag{C.27}$$

where

$$u=\left(\mu^2+|S_{\vec{k}}|^2\right)t^2|\gamma(\vec{k})|^2\tag{C.28}$$

and

$$v=\left(\mathrm{Re}C_{\vec{k}}\mathrm{Im}S_{\vec{k}}-\mathrm{Re}S_{\vec{k}}\mathrm{Im}C_{\vec{k}}\right)^2.\tag{C.29}$$

Bogoliubov transformations $o_{\vec{k}+}$ and $p_{\vec{k}+}$ in the basis $a_{\vec{k}\uparrow},b_{\vec{k},\uparrow}$

$$\begin{aligned}
o_{\vec{k}+}=&-\frac{1}{\sqrt{2}}\left(\alpha_+\gamma_{-}^{(1)}-i\alpha_{-}^{*}\gamma_{+}^{(1)}\right)\left(\beta_+-\sigma\beta_-\right)a_{\vec{k}\uparrow}\\
&-\frac{1}{\sqrt{2}}e^{i\phi_{\vec{k}}}\left(\alpha_+\gamma_{-}^{(1)}+i\alpha_{-}^{*}\gamma_{+}^{(1)}\right)\left(\beta_++\sigma\beta_-\right)b_{\vec{k}\uparrow}\\
&+\frac{1}{\sqrt{2}}\left(\alpha_+\gamma_{+}^{(1)}+i\alpha_-\gamma_{-}^{(1)}\right)\left(\beta_++\sigma\beta_-\right)a^{\dagger}_{-\vec{k}\downarrow}\\
&+\frac{1}{\sqrt{2}}e^{i\phi_{\vec{k}}}\left(\alpha_+\gamma_{+}^{(1)}-i\alpha_-\gamma_{-}^{(1)}\right)\left(\beta_+-\sigma\beta_-\right)b^{\dagger}_{-\vec{k}\downarrow}
\end{aligned}\tag{C.30}$$

$$\begin{aligned}
p_{\vec{k}+}=&-\frac{1}{\sqrt{2}}\left(\alpha_+\gamma_{-}^{(2)}+i\alpha_{-}^{*}\gamma_{+}^{(2)}\right)\left(\beta_++\sigma\beta_-\right)a_{\vec{k}\uparrow}\\
&+\frac{1}{\sqrt{2}}e^{i\phi_{\vec{k}}}\left(\alpha_+\gamma_{-}^{(2)}-i\alpha_{-}^{*}\gamma_{+}^{(2)}\right)\left(\beta_+-\sigma\beta_-\right)b_{\vec{k}\uparrow}\\
&\frac{1}{\sqrt{2}}\left(\alpha_+\gamma_{+}^{(2)}-i\alpha_-\gamma_{-}^{(2)}\right)\left(\beta_+-\sigma\beta_-\right)a^{\dagger}_{-\vec{k}\downarrow}\\
&-\frac{1}{\sqrt{2}}e^{i\phi_{\vec{k}}}\left(\alpha_+\gamma_{+}^{(2)}+i\alpha_-\gamma_{-}^{(2)}\right)\left(\beta_++\sigma\beta_-\right)a^{\dagger}_{-\vec{k}\downarrow}
\end{aligned}\tag{C.31}$$

D

CORRELATION MARTIX

D.1 S-WAVE SCENARIO

The Hamiltonian Eq.(5.55) for s-wave superconductivity state in graphene can be diagonalized by using Bogoluibov transformations

$$e_{\vec{k}+} = \alpha_+ \frac{1}{\sqrt{2}}(a_{\vec{k},\uparrow} - e^{i\cdot\phi_{\vec{k}}} b_{\vec{k},\uparrow}) + \alpha_- \frac{1}{\sqrt{2}}(a^\dagger_{-\vec{k},\downarrow} - e^{i\cdot\phi_{\vec{k}}} b^\dagger_{-\vec{k},\downarrow}) \quad \text{(D.1)}$$

$$f_{\vec{k}+} = \beta_- \frac{1}{\sqrt{2}}(a_{\vec{k},\uparrow} + e^{i\cdot\phi_{\vec{k}}} b_{\vec{k},\uparrow}) - \beta_+ \frac{1}{\sqrt{2}}(a^\dagger_{-\vec{k},\downarrow} + e^{i\cdot\phi_{\vec{k}}} b^\dagger_{-\vec{k},\downarrow}) \quad \text{(D.2)}$$

where $\alpha_+ = \sqrt{\frac{1}{2}\left(1 + \frac{t|\gamma(\vec{k})|-\mu}{\sqrt{\left(t|\gamma(\vec{k})|-\mu\right)^2+|C_{\vec{k}}|^2}}\right)}$, $\alpha_- = \frac{C_{\vec{k}}}{\sqrt{2E_\alpha\left(E_\alpha+t|\gamma(\vec{k})|-\mu\right)}}$, $\beta_+ = \sqrt{\frac{1}{2}\left(1 + \frac{t|\gamma(\vec{k})|+\mu}{\sqrt{\left(t|\gamma(\vec{k})|+\mu\right)^2+|C_{\vec{k}}|^2}}\right)}$, and $\beta_- = \frac{C_{\vec{k}}}{\sqrt{2E_\beta\left(E_\beta+t|\gamma(\vec{k})|+\mu\right)}}$ with E_α and E_β are energies of Bogoliubov quasi-particles

$$E_\alpha = \sqrt{\left(t|\gamma(\vec{k})| - \mu\right)^2 + |C_{\vec{k}}|^2} \quad \text{(D.3)}$$

and

$$E_\beta = \sqrt{\left(t|\gamma(\vec{k})| + \mu\right)^2 + |C_{\vec{k}}|^2}. \quad \text{(D.4)}$$

The e (f) sections are determined by Eq. (D.1) (Eq. (D.2)), respectively. These sections are decoupled in Bogoliubov description and we are allowed than to obtain their contributions to the ground state separative. We can demand $e_{\vec{k}+}|G\rangle = 0$ and $e^\dagger_{\vec{k}-}|G\rangle = 0$ where $|G\rangle$ is the ground state. The e section contributes to the ground state as:

$$\prod_{\vec{k}\in IBZ} \left(\alpha_+(\vec{k}) - \alpha_-(\vec{k}) c^\dagger_{\vec{k}\uparrow} c^\dagger_{-\vec{k}\downarrow}\right)|0\rangle \quad \text{(D.5)}$$

where $|0\rangle$ is the vacuum state. Similar, the contribution of the f section to the ground state:

$$\prod_{\vec{k}\in IBZ} \left(\beta_-(\vec{k}) + \beta_+(\vec{k}) d^\dagger_{\vec{k}\uparrow} d^\dagger_{-\vec{k}\downarrow}\right)|0\rangle \quad \text{(D.6)}$$

the ground state $|G\rangle$ is determined by conditions: $f_{\vec{k}+}|G\rangle = 0$ and $f^{\dagger}_{\vec{k}-}|G\rangle = 0$. This leads to the complete ground state vector:

$$\prod_{\vec{k}\in IBZ}\left(\alpha_{+}(\vec{k}) - \alpha_{-}(\vec{k})c^{\dagger}_{\vec{k}\uparrow}c^{\dagger}_{-\vec{k}\downarrow}\right) \prod_{\vec{q}\in IBZ}\left(\beta_{-}(\vec{q}) + \beta_{+}(\vec{q})d^{\dagger}_{\vec{q}\uparrow}d^{\dagger}_{-\vec{q}\downarrow}\right)|0\rangle. \tag{D.7}$$

Similar findings are obtained for the ground state of the p-wave superconductivity state in graphene.

This ground state leads to the correlation matrix when spin $\downarrow$ is traced out:

$$C(\vec{k}) = \begin{pmatrix} \frac{1}{2}\left(|\alpha_{-}|^2 + |\beta_{+}|^2\right) & \frac{1}{2}e^{-i\phi_{\vec{k}}}\left(|\beta_{+}|^2 - |\alpha_{-}|^2\right) \\ \frac{1}{2}e^{i\phi_{\vec{k}}}\left(|\beta_{+}|^2 - |\alpha_{-}|^2\right) & \frac{1}{2}\left(|\alpha_{-}|^2 + |\beta_{+}|^2\right) \end{pmatrix}. \tag{D.8}$$

D.2 CHIRAL D-WAVE SCENARIO

Here, o section is defined by Eq. (C.30), while p section is defined by Eq. (C.31). We can consider o and p sections separative. Thus, the o section contributes to the ground state as

$$\prod_{\vec{k}\in IBZ}\left(\gamma^{(1)}_{+}(\vec{k}) + \gamma^{(1)}_{-}(\vec{k})g^{\dagger}_{\vec{k}+}g^{\dagger}_{-\vec{k}-}\right)|0\rangle \tag{D.9}$$

where $|0\rangle$ is the vacuum state. While, the p section contributes to the ground state

$$\prod_{\vec{k}\in IBZ}\left(\gamma^{(2)}_{+}(\vec{k}) + \gamma^{(2)}_{-}(\vec{k})h^{\dagger}_{\vec{k}+}h^{\dagger}_{-\vec{k}-}\right)|0\rangle. \tag{D.10}$$

The complete ground state vector $|G\rangle$ can be determined by conditions $g_{\vec{k}+}|G\rangle = 0$ and $g^{\dagger}_{\vec{k}-}|G\rangle = 0$ and $h_{\vec{k}+}|G\rangle = 0$ and $h^{\dagger}_{\vec{k}-}|G\rangle = 0$, which leads to the following form

$$\prod_{\vec{k}\in IBZ}\left(\gamma^{(1)}_{+}(\vec{k}) + \gamma^{(1)}_{-}(\vec{k})g^{\dagger}_{\vec{k}+}g^{\dagger}_{-\vec{k}-}\right)\prod_{\vec{q}\in IBZ}\left(\gamma^{(2)}_{+}(\vec{q}) + \gamma^{(2)}_{-}(\vec{q})h^{\dagger}_{\vec{q}+}h^{\dagger}_{-\vec{q}-}\right)|0\rangle. \tag{D.11}$$

Using

$$a_{\vec{k}\uparrow} = -\frac{1}{\sqrt{2}}\left(\alpha_{+}\left(\gamma^{(1)}_{-}\right)^{*} + i\alpha_{-}\gamma^{(1)}_{+}\right)\left(\beta_{+} - \sigma\beta_{-}\right)o_{\vec{k},+}$$

$$
\begin{aligned}
&- \frac{1}{\sqrt{2}} \left(\alpha_+ \left(\gamma_-^{(2)} \right)^* + i\alpha_- \gamma_+^{(2)} \right) \left(\beta_+ + \sigma\beta_- \right) p_{\vec{k},+} \\
&+ \frac{1}{\sqrt{2}} \left(\alpha_+ \gamma_+^{(2)} - i\alpha_- \gamma_-^{(2)} \right) \left(\beta_+ + \sigma\beta_- \right) p^\dagger_{-\vec{k},-} \\
&+ \frac{1}{\sqrt{2}} \left(\alpha_+ \gamma_+^{(1)} - i\alpha_- \gamma_-^{(1)} \right) \left(\beta_+ - \sigma\beta_- \right) o^\dagger_{-\vec{k},-} \qquad \text{(D.12)}
\end{aligned}
$$

we can calculate the mean occupancy at cite A:

$$
\begin{aligned}
\langle a^\dagger_{\vec{k}\uparrow} a_{\vec{k}\uparrow} \rangle = & \\
&\frac{1}{2} \left(\alpha_+^2 |\gamma_-^{(1)}|^2 + |\alpha_-|^2 \left(\gamma_+^{(1)} \right)^2 + i\alpha_+ \gamma_+^{(1)} \left(\alpha_- \gamma_-^{(1)} - \alpha_-^* \left(\gamma_-^{(1)} \right)^* \right) \right) \\
&\left(\beta_+ - \sigma\beta_- \right)^2 n_{\vec{k}}^{(0)} \\
&+ \frac{1}{2} \left(\alpha_+^2 |\gamma_-^{(2)}|^2 + |\alpha_-|^2 \left(\gamma_+^{(2)} \right)^2 + i\alpha_+ \gamma_+^{(2)} \left(\alpha_- \gamma_-^{(2)} - \alpha_-^* \left(\gamma_-^{(2)} \right)^* \right) \right) \\
&\left(\beta_+ + \sigma\beta_- \right)^2 n_{\vec{k}}^{(0)} \\
&+ \frac{1}{2} \left(\alpha_+^2 (\gamma_+^{(1)})^2 + |\alpha_-|^2 |\gamma_-^{(1)}|^2 - i\alpha_+ \gamma_+^{(1)} \left(\alpha_- \gamma_-^{(1)} - \alpha_-^* \left(\gamma_-^{(1)} \right)^* \right) \right) \\
&\left(\beta_+ - \sigma\beta_- \right)^2 (1 - n_{\vec{k}}^{(0)}) \\
&+ \frac{1}{2} \left(\alpha_+^2 (\gamma_+^{(2)})^2 + |\alpha_-|^2 |\gamma_-^{(2)}|^2 - i\alpha_+ \gamma_+^{(2)} \left(\alpha_- \gamma_-^{(2)} - \alpha_-^* \left(\gamma_-^{(2)} \right)^* \right) \right) \\
&\left(\beta_+ + \sigma\beta_- \right)^2 (1 - n_{\vec{k}}^{(0)}). \qquad \text{(D.13)}
\end{aligned}
$$

The average number $n_{\vec{k}}^{(0)}$ of fermions with momentum k at temperature $T = 0$ is $n_{\vec{k}}^{(0)} = 0$.

Further, we get the mean occupancy at the cite A

$$
\begin{aligned}
\langle a^\dagger_{\vec{k}\uparrow} a_{\vec{k}\uparrow} \rangle = & \frac{1}{2} \left(\alpha_+^2 (\gamma_+^{(1)})^2 + |\alpha_-|^2 |\gamma_-^{(1)}|^2 - i\alpha_+ \gamma_+^{(1)} \left(\alpha_- \gamma_-^{(1)} - \alpha_-^* \left(\gamma_-^{(1)} \right)^* \right) \right) \\
&\left(\beta_+ - \sigma\beta_- \right)^2 \\
&+ \frac{1}{2} \left(\alpha_+^2 (\gamma_+^{(2)})^2 + |\alpha_-|^2 |\gamma_-^{(2)}|^2 - i\alpha_+ \gamma_+^{(2)} \left(\alpha_- \gamma_-^{(2)} - \alpha_-^* \left(\gamma_-^{(2)} \right)^* \right) \right) \\
&\left(\beta_+ + \sigma\beta_- \right)^2 . \qquad \text{(D.14)}
\end{aligned}
$$

After basic algebra we find that the correlation matrix obtained by tracing out spin $\downarrow$ at $T = 0$ reads

$$
C(\vec{k}) = \begin{pmatrix} C_{11}(\vec{k}) & C_{12}(\vec{k}) \\ C_{12}^*(\vec{k}) & C_{22}(\vec{k}) \end{pmatrix} \qquad \text{(D.15)}
$$

with

$$
\begin{aligned}
&C_{11}(\vec{k}) = \frac{1}{2}\left(\alpha_+^2(\gamma_+^{(1)})^2 + |\alpha_-|^2|\gamma_-^{(1)}|^2 - i\alpha_+\gamma_+^{(1)}\left(\alpha_-\gamma_-^{(1)} - \alpha_-^*\left(\gamma_-^{(1)}\right)^*\right)\right)\\
&(\beta_+ - \sigma\beta_-)^2\\
&+\frac{1}{2}\left(\alpha_+^2(\gamma_+^{(2)})^2 + |\alpha_-|^2|\gamma_-^{(2)}|^2 - i\alpha_+\gamma_+^{(2)}\left(\alpha_-\gamma_-^{(2)} - \alpha_-^*\left(\gamma_-^{(2)}\right)^*\right)\right)\\
&(\beta_+ + \sigma\beta_-)^2\\
&=\frac{1}{2} + \frac{1}{4}\frac{\mu}{\sqrt{\mu^2+|S_{\vec{k}}|^2}}(\epsilon_1+m)\frac{1}{E_\alpha}\left(1 - \frac{m}{\sqrt{t^2|\gamma(\vec{k})|^2+m^2}}\right)\\
&+\frac{1}{4}\frac{\mu}{\sqrt{\mu^2+|S_{\vec{k}}|^2}}(\epsilon_2+m)\frac{1}{E_\beta}\left(1 + \frac{m}{\sqrt{t^2|\gamma(\vec{k})|^2+m^2}}\right), \qquad \text{(D.16)}
\end{aligned}
$$

$$
\begin{aligned}
&C_{22}(\vec{k}) = \frac{1}{2}\left(\alpha_+^2(\gamma_+^{(1)})^2 + |\alpha_-|^2|\gamma_-^{(1)}|^2 + i\alpha_+\gamma_+^{(1)}\left(\alpha_-\gamma_-^{(1)} - \alpha_-^*\left(\gamma_-^{(1)}\right)^*\right)\right)\\
&(\beta_+ + \sigma\beta_-)^2\\
&+\frac{1}{2}\left(\alpha_+^2(\gamma_+^{(2)})^2 + |\alpha_-|^2|\gamma_-^{(2)}|^2 + i\alpha_+\gamma_+^{(2)}\left(\alpha_-\gamma_-^{(2)} - \alpha_-^*\left(\gamma_-^{(2)}\right)^*\right)\right)\\
&(\beta_+ - \sigma\beta_-)^2\\
&=\frac{1}{2} + \frac{1}{4}\frac{\mu}{\sqrt{\mu^2+|S_{\vec{k}}|^2}}(\epsilon_1-m)\frac{1}{E_\alpha}\left(1 + \frac{m}{\sqrt{t^2|\gamma(\vec{k})|^2+m^2}}\right)\\
&+\frac{1}{4}\frac{\mu}{\sqrt{\mu^2+|S_{\vec{k}}|^2}}(\epsilon_2-m)\frac{1}{E_\beta}\left(1 - \frac{m}{\sqrt{t^2|\gamma(\vec{k})|^2+m^2}}\right), \qquad \text{(D.17)}
\end{aligned}
$$

and

$$
\begin{aligned}
&C_{12}(\vec{k}) =\\
&\frac{1}{2}e^{-i\phi_{\vec{k}}}\left(\alpha_+^2(\gamma_+^{(1)})^2 - |\alpha_-|^2|\gamma_-^{(1)}|^2 - i\alpha_+\gamma_+^{(1)}\left(\alpha_-^{(1)}\gamma_-^{(1)} + \left(\alpha_-^{(1)}\right)^*\left(\gamma_-^{(1)}\right)^*\right)\right)\\
&\left(\beta_+^2 - \beta_-^2\right)\\
&-\frac{1}{2}e^{-i\phi_{\vec{k}}}\left(\alpha_+^2(\gamma_+^{(2)})^2 - |\alpha_-|^2|\gamma_+^{(2)}|^2 - i\alpha_+\gamma_+^{(2)}\left(\alpha_-^{(1)}\gamma_-^{(2)} + \left(\alpha_-^{(1)}\right)^*\left(\gamma_-^{(2)}\right)^*\right)\right)\\
&\left(\beta_+^2 - \beta_-^2\right)\\
&=\frac{1}{4}e^{-i\phi_{\vec{k}}}\left(\left(\frac{\epsilon_1}{E_\alpha} - \frac{\epsilon_2}{E_\beta}\right) - i\frac{\mathrm{Re}(C_{\vec{k}})\mathrm{Re}(S_{\vec{k}}) + \mathrm{Im}(C_{\vec{k}})\mathrm{Im}(S_{\vec{k}})}{\sqrt{\mu^2 + \ |S_{\vec{k}}|^2}}\left(\frac{1}{E_\alpha} - \frac{1}{E_\beta}\right)\right)\\
&\frac{t|\gamma(\vec{k})|}{\sqrt{t^2|\gamma(\vec{k})|^2+m^2}}. \qquad \text{(D.18)}
\end{aligned}
$$

Here, one should notice that $C_{11}(-\vec{k}) = C_{22}(\vec{k})$ and $C_{12}(\vec{k}) = \left(C_{12}(-\vec{k})\right)^*$.

Eigenvectors of the correlation matrix

$$q_{\vec{k}\uparrow} = \delta_+(\vec{k}) a_{\vec{k}\uparrow} + \delta_-(\vec{k}) b_{\vec{k}\uparrow} \tag{D.19}$$

$$r_{\vec{k}\uparrow} = \delta_+(-\vec{k}) a_{\vec{k}\uparrow} - \delta_-^*(-\vec{k}) b_{\vec{k}\uparrow} \tag{D.20}$$

where:

$$\begin{aligned}
\delta_+(\vec{k}) &= \sqrt{\frac{1}{2}\left(1 + \frac{C_{11} - C_{22}}{\sqrt{(C_{11} - C_{22})^2 + 4|C_{12}|^2}}\right)} \\
\delta_-(\vec{k}) &= \frac{2C_{12}}{\sqrt{2\sqrt{(C_{11} - C_{22})^2 + 4|C_{12}|^2}(C_{11} - C_{22} + \sqrt{d})}}.
\end{aligned} \tag{D.21}$$

BIBLIOGRAPHY

[Alba et al., 2012] Alba, V., Haque, M., and Läuchli, A. M. (2012). Boundary-locality and perturbative structure of entanglement spectra in gapped systems. *Phys. Rev. Lett.*, 108:227201. (Cited on page 3.)

[Altland and Zirnbauer, 1997] Altland, A. and Zirnbauer, M. R. (1997). Nonstandard symmetry classes in mesoscopic normal-superconducting hybrid structures. *Phys. Rev. B*, 55:1142–1161. (Cited on page 69.)

[Amico et al., 2008] Amico, L., Fazio, R., Osterloh, A., and Vedral, V. (2008). Entanglement in many-body systems. *Rev. Mod. Phys.*, 80:517–576. (Cited on page 19.)

[Ansmann et al., 2009] Ansmann, M., Wang, H., Bialczak, R. C., Hofheinz, M., Lucero, E., Neeley, M., O'Connell, A. D., Sank, D., Weides, M., Wenner, J., Cleland, A. N., and Martinis, J. M. (2009). Violation of bell's inequality in josephson phase qubits. *Nature*, 461:504. (Cited on page 2.)

[Ardonne and Regnault, 2011] Ardonne, E. and Regnault, N. (2011). Structure of spinful quantum hall states: A squeezing perspective. *Phys. Rev. B*, 84:205134. (Cited on page 3.)

[Ashcroft and Mermin, 1976] Ashcroft, N. and Mermin, D. (1976). *Solid State Physics*. Harcourt College Publishers. (Cited on page 12.)

[Aspect et al., 1982] Aspect, A., Dalibard, J., and Roger, G. (1982). Experimental test of bell's inequalities using time-varying analyzers. *Phys. Rev. Lett.*, 49:1804. (Cited on page 2.)

[Auerbach, 1994] Auerbach, A. (1994). *Interacting Electrons and Quantum Magnetism*. Springer. (Cited on page 58.)

[Barrett et al., 2002] Barrett, J., Collins, D., Hardy, L., Kent, A., and Popescu, S. (2002). Quantum nonlocality, bell inequalities, and the memory loophole. *Phys. Rev. A*, 66:042111. (Cited on page 2.)

[Baskaran and Jafari, 2002] Baskaran, G. and Jafari, S. A. (2002). Gapless spin-1 neutral collective mode branch for graphite. *Phys. Rev. Lett.*, 89:016402. (Cited on page 59.)

[Bell, 2004] Bell, J. S. (2004). *Speakable and Unspeakable in Quantum Mechanics: Collected Papers on Quantum Philosophy*. Cambridge University Press. (Cited on pages 1 and 2.)

[Bena and Kivelson, 2005] Bena, C. and Kivelson, S. A. (2005). Quasiparticle scattering and local density of states in graphite. *Phys. Rev. B*, 72:125432. (Cited on page 16.)

[Black-Schaffer, 2012] Black-Schaffer, A. M. (2012). Edge properties and majorana fermions in the proposed chiral *d*-wave superconducting state of doped graphene. *Phys. Rev. Lett.*, 109:197001. (Cited on page 77.)

[Black-Schaffer and Doniach, 2007] Black-Schaffer, A. M. and Doniach, S. (2007). Resonating valence bonds and mean-field *d*-wave superconductivity in graphite. *Phys. Rev. B*, 75:134512. (Cited on pages 5 and 53.)

[Black-Schaffer and Honerkamp, 2014] Black-Schaffer, A. M. and Honerkamp, C. (2014). Chiral d -wave superconductivity in doped graphene. *Journal of Physics: Condensed Matter*, 26:423201. (Cited on pages 53, 54, and 55.)

[Black-Schaffer and Hur, 2015] Black-Schaffer, A. M. and Hur, K. L. (2015). Topological superconductivity in two dimensions with mixed chirality. *Phys. Rev. B*, 32:140503(R). (Cited on page 76.)

[Black-Schaffer et al., 2014] Black-Schaffer, A. M., Wu, W., and Le Hur, K. (2014). Chiral *d*-wave superconductivity on the honeycomb lattice close to the mott state. *Phys. Rev. B*, 90:054521. (Cited on page 64.)

[Bombelli et al., 1986] Bombelli, L., Koul, R. K., Lee, J., and Sorkin, R. D. (1986). Quantum source of entropy for black holes. *Phys. Rev. D*, 34:373–383. (Cited on page 2.)

[Borchmann et al., 2014] Borchmann, J., Farrell, A., Matsuura, S., and Pereg-Barnea, T. (2014). Entanglement spectrum as a probe for the topology of a spin-orbit-coupled superconductor. *Phys. Rev. B*, 90:235150. (Cited on pages 3 and 69.)

[Bray-Ali et al., 2009] Bray-Ali, N., Ding, L., and Haas, S. (2009). Topological order in paired states of fermions in two-dimensions with breaking of parity and time-reversal symmetries. *Phys. Rev. B*, 80:180504. (Cited on page 3.)

[Castro Neto et al., 2009] Castro Neto, A. H., Guinea, F., Peres, N. M. R., Novoselov, K. S., and Geim, A. K. (2009). The electronic properties of graphene. *Rev. Mod. Phys.*, 81:109–162. (Cited on page 10.)

[Chandran et al., 2011] Chandran, A., Hermanns, M., Regnault, N., and Bernevig, B. A. (2011). Bulk-edge correspondence in entanglement spectra. *Phys. Rev. B*, 84:205136. (Cited on page 3.)

[Chandran et al., 2014] Chandran, A., Khemani, V., and Sondhi, S. L. (2014). How universal is the entanglement spectrum? *Phys. Rev. Lett.*, 113:060501. (Cited on page 4.)

[Chapman et al., 2016] Chapman, J., Su, Y., Howard, C. A., Kundys, D., Grigorenko, A. N., Guinea, F., Geim, A. K., Grigorieva, I. V., and Nair, R. R. (2016). Superconductivity in ca-doped graphene laminates. *Scientific Reports*, 6:23254. (Cited on page 54.)

[Chen and Fradkin, 2013] Chen, X. and Fradkin, E. (2013). Quantum entanglement and thermal reduced density matrices in fermion and spin systems on ladders. *Journal of Statistical Mechanics: Theory and Experiment*, 2013(08):P08013. (Cited on page 4.)

[Cheong and Henley, 2004] Cheong, S.-A. and Henley, C. L. (2004). Many-body density matrices for free fermions. *Phys. Rev. B*, 69:075111. (Cited on pages 6, 20, 24, 45, and 69.)

[Cirac et al., 2011] Cirac, J. I., Poilblanc, D., Schuch, N., and Verstraete, F. (2011). Entanglement spectrum and boundary theories with projected entangled-pair states. *Phys. Rev. B*, 83:245134. (Cited on pages 4 and 19.)

[Cosma and Fal'ko, 2015] Cosma, D. A. and Fal'ko, V. I. (2015). Trigonal warping effect on velocity and transverse confinement length of topologically confined states in bilayer graphene. *Phys. Rev. B*, 92:165412. (Cited on page 40.)

[Cserti et al., 2007] Cserti, J., Csordás, A., and Dávid, G. (2007). Role of the trigonal warping on the minimal conductivity of

bilayer graphene. *Phys. Rev. Lett.*, 99:066802. (Cited on page 40.)

[De Chiara et al., 2012] De Chiara, G., Lepori, L., Lewenstein, M., and Sanpera, A. (2012). Entanglement spectrum, critical exponents, and order parameters in quantum spin chains. *Phys. Rev. Lett.*, 109:237208. (Cited on page 4.)

[Drut and Lähde, 2009] Drut, J. E. and Lähde, T. A. (2009). Is graphene in vacuum an insulator? *Phys. Rev. Lett.*, 102:026802. (Cited on page 53.)

[Dubail and Read, 2011] Dubail, J. and Read, N. (2011). Entanglement spectra of complex paired superfluids. *Phys. Rev. Lett.*, 107:157001. (Cited on page 4.)

[Dubail et al., 2012] Dubail, J., Read, N., and Rezayi, E. H. (2012). Real-space entanglement spectrum of quantum hall systems. *Phys. Rev. B*, 85:115321. (Cited on page 3.)

[Eberhard, 1993] Eberhard, P. (1993). Background level and counter efficiencies required for a loophole-free einstein-podolsky-rosen experiment. *Phys. Rev. A*, 47:747. (Cited on page 2.)

[Einstein et al., 1935] Einstein, A., Podolsky, B., and N.Rosen (1935). Can quantum-mechanical description of physical reality be considered complete? *Phys. Rev.*, 47:777. (Cited on page 1.)

[Eisert et al., 2010] Eisert, J., Cramer, M., and Plenio, M. B. (2010). *Colloquium* : Area laws for the entanglement entropy. *Rev. Mod. Phys.*, 82:277. (Cited on page 3.)

[Feynman, 1982] Feynman, R. (1982). Simulating physics with computers. *International Journal of Theoretical Physics*, 21:467–488. (Cited on page 2.)

[Fidkowski, 2010] Fidkowski, L. (2010). Entanglement spectrum of topological insulators and superconductors. *Phys. Rev. Lett.*, 104:130502. (Cited on page 3.)

[Freedman and Clauser, 1972] Freedman, S. J. and Clauser, J. F. (1972). Experimental test of local hidden-variable theories. *Phys. Rev. Lett.*, 28:938. (Cited on page 2.)

[Fukui and Hatsugai, 2014] Fukui, T. and Hatsugai, Y. (2014). Entanglement chern number for an extensive partition of a topological ground state. *Journal of the Physical Society of Japan*, 83:113705. (Cited on page 39.)

[Gamayun et al., 2010] Gamayun, O. V., Gorbar, E. V., and Gusynin, V. P. (2010). Gap generation and semimetal-insulator phase transition in graphene. *Phys. Rev. B*, 81:075429. (Cited on page 53.)

[Garg and Mermin, 1987] Garg, A. and Mermin, N. D. (1987). Detector inefficiencies in the einstein-podolsky-rosen experiment. *Phys. Rev. D*, 35:3831. (Cited on page 2.)

[Goerbig, 2011] Goerbig, M. O. (2011). Electronic properties of graphene in a strong magnetic field. *Rev. Mod. Phys.*, 83:1193–1243. (Cited on page 13.)

[Hensen et al., 2015] Hensen, B., Bernien, H., Dreau, A. E., Reiserer, A., Kalb, N., Blok, M. S., Ruitenberg, J., Vermeulen, R. F. L., Schouten, R. N., Abellan, C., Amaya, W., Pruneri, V., Mitchell, M. W., Markham, M., Twitchen, D. J., Elkouss, D., Wehner, S., Taminiau, T. H., and Hanson, R. (2015). Loophole-free bell inequality violation using electron spins separated by 1.3 kilometres. *Nature*, 526:682. (Cited on page 2.)

[Herbut, 2006] Herbut, I. F. (2006). Interactions and phase transitions on graphene's honeycomb lattice. *Phys. Rev. Lett.*, 97:146401. (Cited on page 53.)

[Herbut et al., 2009] Herbut, I. F., Juričić, V., and Roy, B. (2009). Theory of interacting electrons on the honeycomb lattice. *Phys. Rev. B*, 79:085116. (Cited on page 53.)

[Hermanns et al., 2011] Hermanns, M., Chandran, A., Regnault, N., and Bernevig, B. A. (2011). Haldane statistics in the finite-size entanglement spectra of 1/m fractional quantum hall states. *Phys. Rev. B*, 84:121309. (Cited on page 3.)

[Honerkamp, 2008] Honerkamp, C. (2008). Density waves and cooper pairing on the honeycomb lattice. *Phys. Rev. Lett.*, 100:146404. (Cited on page 53.)

[Hou et al., 2007] Hou, C.-Y., Chamon, C., and Mudry, C. (2007). Electron fractionalization in two-dimensional graphene-like structures. *Phys. Rev. Lett.*, 98:186809. (Cited on page 53.)

[Huang and Lin, 2011] Huang, C.-Y. and Lin, F.-L. (2011). Topological order and degenerate singular value spectrum in two-dimensional dimerized quantum heisenberg model. *Phys. Rev. B*, 84:125110. (Cited on page 4.)

[Huang et al., 2016] Huang, S.-M., Tsai, W.-F., Chung, C.-H., and Mou, C.-Y. (2016). Duality in topological superconductors and topological ferromagnetic insulators in a honeycomb lattice. *Phys. Rev. B*, 93:054518. (Cited on page 77.)

[Ichinokura et al., 2016] Ichinokura, S., Sugawara, K., Takayama, A., Takahashi, T., and Hasegawa, S. (2016). Superconducting calcium-intercalated bilayer graphene. *ACS Nano*, 10:2761–2765. (Cited on page 54.)

[Katsnelson et al., 2006] Katsnelson, M. I., Novoselov, K. S., and Geim, A. K. (2006). Chiral tunnelling and the klein paradox in graphene. *Nature Physics*, 2:620–625. (Cited on page 10.)

[Kechedzhi et al., 2007] Kechedzhi, K., Fal'ko, V. I., McCann, E., and Altshuler, B. L. (2007). Influence of trigonal warping on interference effects in bilayer graphene. *Phys. Rev. Lett.*, 98:176806. (Cited on page 40.)

[Khveshchenko, 2001] Khveshchenko, D. V. (2001). Ghost excitonic insulator transition in layered graphite. *Phys. Rev. Lett.*, 87:246802. (Cited on page 53.)

[Kiesel et al., 2012] Kiesel, M., Platt, C., Hanke, W., Abanin, D. A., and Thomale, R. (2012). Competing many-body instabilities and unconventional superconductivity in graphene. *Phys. Rev. B*, 86:020507(R). (Cited on pages 53 and 56.)

[Kim, 2014] Kim, E. H. (2014). Characterizing topological order in superconductors via entanglement. *Journal of Physics: Condensed Matter*, 26:205602. (Cited on pages 3 and 69.)

[Koshino and Ando, 2006] Koshino, M. and Ando, T. (2006). Transport in bilayer graphene: Calculations within a self-consistent born approximation. *Phys. Rev. B*, 73:245403. (Cited on page 40.)

[Kuzmenko et al., 2009] Kuzmenko, A. B., Crassee, I., van der Marel, D., Blake, P., and Novoselov, K. S. (2009). Determination of the gate-tunable band gap and tight-binding parameters in bilayer graphene using infrared spectroscopy. *Phys. Rev. B*, 80:165406. (Cited on page 21.)

[Laflorencie, 2016] Laflorencie, N. (2016). Quantum entanglement in condensed matter systems. *Physics Reports*, 646:1 – 59. (Cited on page 4.)

[Landau and Lifshitz, 1980] Landau, L. D. and Lifshitz, E. M. (1980). *Statistical Physics*. Pergamon, Oxford. (Cited on page 9.)

[Läuchli et al., 2010] Läuchli, A. M., Bergholtz, E. J., Suorsa, J., and Haque, M. (2010). Disentangling entanglement spectra of fractional quantum hall states on torus geometries. *Phys. Rev. Lett.*, 104:156404. (Cited on page 3.)

[Läuchli and Schliemann, 2012] Läuchli, A. M. and Schliemann, J. (2012). Entanglement spectra of coupled $s = \frac{1}{2}$ spin chains in a ladder geometry. *Phys. Rev. B*, 85:054403. (Cited on pages 4 and 19.)

[Li and Haldane, 2008] Li, H. and Haldane, F. D. M. (2008). Entanglement spectrum as a generalization of entanglement entropy: Identification of topological order in non-abelian fractional quantum hall effect states. *Phys. Rev. Lett.*, 101:010504. (Cited on page 3.)

[Liu et al., 2009] Liu, G.-Z., Li, W., and Cheng, G. (2009). Interaction and excitonic insulating transition in graphene. *Phys. Rev. B*, 79:205429. (Cited on page 53.)

[Liu et al., 2012] Liu, Z., Bergholtz, E. J., Fan, H., and Läuchli, A. M. (2012). Edge-mode combinations in the entanglement spectra of non-abelian fractional quantum hall states on the torus. *Phys. Rev. B*, 85:045119. (Cited on page 3.)

[Lou et al., 2011] Lou, J., Tanaka, S., Katsura, H., and Kawashima, N. (2011). Entanglement spectra of the two-dimensional affleck-kennedy-lieb-tasaki model: Correspondence between the valence-bond-solid state and conformal field theory. *Phys. Rev. B*, 84:245128. (Cited on page 4.)

[Ludbrook et al., 2015] Ludbrook, B. M., Levy, G., Nigge, P., Zonno, M., Schneider, M., Dvorak, D. J., Veenstra, C. N., Zhdanovich, S., Wong, D., Dosanjh, P., Straßer, C., Stöhr, A., Forti, S., Ast, C. R., Starke, U., and Damascelli, A. (2015). Evidence for superconductivity in li-decorated monolayer graphene. *Proceedings of the National Academy of Sciences*, 112:11795–11799. (Cited on page 54.)

[Lundgren, 2016] Lundgren, R. (2016). Momentum-space entanglement in heisenberg spin-half ladders. *Phys. Rev. B*, 93:125107. (Cited on page 4.)

[Lundgren et al., 2014] Lundgren, R., Blair, J., Greiter, M., Läuchli, A., Fiete, G. A., and Thomale, R. (2014). Momentum-space entanglement spectrum of bosons and fermions with interactions. *Phys. Rev. Lett.*, 113:256404. (Cited on page 4.)

[Lundgren et al., 2012] Lundgren, R., Chua, V., and Fiete, G. A. (2012). Entanglement entropy and spectra of the one-dimensional kugel-khomskii model. *Phys. Rev. B*, 86:224422. (Cited on pages 4, 5, and 39.)

[Lundgren et al., 2013] Lundgren, R., Fuji, Y., Furukawa, S., and Oshikawa, M. (2013). Entanglement spectra between coupled tomonaga-luttinger liquids: Applications to ladder systems and topological phases. *Phys. Rev. B*, 88:245137. (Cited on page 4.)

[Manes et al., 2007] Manes, J. L., Guinea, F., and Vozmediano, M. A. H. (2007). Existence and topological stability of fermi points in multilayered graphene. *Phys. Rev. B*, 75:155424. (Cited on pages 40 and 45.)

[Mariani et al., 2012] Mariani, E., Pearce, A. J., and von Oppen, F. (2012). Fictitious gauge fields in bilayer graphene. *Phys. Rev. B*, 86:165448. (Cited on pages 40, 43, and 45.)

[Matsukevich et al., 2008] Matsukevich, N. D., Maunz, P., Moehring, D. L., Olmschenk, S., and Monroe, C. (2008). Bell inequality violation with two remote atomic qubits. *Phys. Rev. Lett.*, 100:150404. (Cited on page 2.)

[McCann and Fal'ko, 2006] McCann, E. and Fal'ko, V. I. (2006). Landau-level degeneracy and quantum hall effect in a graphite bilayer. *Phys. Rev. Lett.*, 96:086805. (Cited on pages 23, 40, 42, 44, and 51.)

[McCann and Koshino, 2013] McCann, E. and Koshino, M. (2013). The electronic properties of bilayer graphene. *Reports on Progress in Physics*, 76:056503. (Cited on pages 5, 13, 19, 20, 39, 40, and 43.)

[Meng et al., 2010] Meng, Z. Y., Lang, T. C., Wessel, S., Assaad, F. F., and Muramatsu, A. (2010). Quantum spin liquid emerging in two-dimensional correlated dirac fermion. *Nature*, 464:847. (Cited on page 53.)

[Mermin, 1968] Mermin, N. D. (1968). Crystalline order in two dimensions. *Phys. Rev.*, 176:250. (Cited on page 9.)

[Mermin and Wagner, 1966] Mermin, N. D. and Wagner, H. (1966). Absence of ferromagnetism or antiferromagnetism in one - or two dimensional isotropic heisenberg model. *Phys. Rev. Lett.*, 17:1133. (Cited on page 9.)

[Mikitik and Sharlai, 2008] Mikitik, G. P. and Sharlai, Y. V. (2008). Electron energy spectrum and the berry phase in a graphite bilayer. *Phys. Rev. B*, 77:113407. (Cited on pages 40 and 45.)

[Milovanović and Predin, 2012] Milovanović, M. V. and Predin, S. (2012). On the coexistence of antiferromagnetism and d + i d superconducting correlations in the graphene bilayer. *Phys. Rev. B*, 86:195113. (Cited on pages 53 and 76.)

[Min et al., 2006] Min, H., Hill, J. E., Sinitsyn, N. A., Sahu, B. R., Kleinman, L., and MacDonald, A. H. (2006). Intrinsic and rashba spin-orbit interactions in graphene sheets. *Phys. Rev. B*, 74:165310. (Cited on page 77.)

[Nandkishore et al., 2011] Nandkishore, R., Levitov, L. S., and Chubukov, A. V. (2011). Chiral superconductivity from repulsive interactions in doped graphene. *Nature Physics*, 8:158. (Cited on pages 53 and 56.)

[Nayak et al., 2008] Nayak, C., Simon, S. H., Stern, A., Freedman, M., and Das Sarma, S. (2008). Non-abelian anyons and topological quantum computation. *Rev. Mod. Phys.*, 80:1083–1159. (Cited on page 77.)

[Nemec and Cuniberti, 2007] Nemec, N. and Cuniberti, G. (2007). Hofstadter butterflies of bilayer graphene. *Phys. Rev. B*, 75:201404. (Cited on page 52.)

[Nienhuis et al., 2009] Nienhuis, B., Campostrini, M., and Calabrese, P. (2009). Entanglement, combinatorics and finite-size effects in spin chains. *Journal of Statistical Mechanics: Theory and Experiment*, 2009(02):P02063. (Cited on page 4.)

[Nilsson et al., 2006] Nilsson, J., Castro Neto, A. H., Peres, N. M. R., and Guinea, F. (2006). Electron-electron interactions and the phase diagram of a graphene bilayer. *Phys. Rev. B*, 73:214418. (Cited on page 40.)

[Novoselov et al., 2004] Novoselov, K. S., Geim, A. K., Morozov, S. V., Jiang, D., Zhang, Y., Dubonos, S. V., Grigorieva, I. V., and Firsov, A. A. (2004). Electric field effect in atomically thin carbon films. *Science*, 306:666. (Cited on page 9.)

[Novoselov et al., 2006] Novoselov, K. S., McCann, E., Morozov, S. V., Fal'ko, V. I., Katsnelson, M. I., Zeitler, U., Jiang, D., Schedin, F., and Geim, A. K. (2006). Unconventional quantum hall effect and berry's phase of 2π in bilayer graphene. *Nature Physics*, 2:177. (Cited on page 19.)

[Pathak et al., 2010] Pathak, S., Shenoy, V. B., and Baskaran, G. (2010). Possible high-temperature superconducting state with a $d + id$ pairing symmetry in doped graphene. *Phys. Rev. B*, 81:085431. (Cited on page 53.)

[Pauling, 1960] Pauling, L. (1960). Nature of the chemical bond. *NY:Cornell University Press*. (Cited on page 59.)

[Peirls, 1934] Peirls, R. E. (1934). Bemerkungen uber umwandlungs temperature. *Helv. Phys. Acta*, 7:81. (Cited on page 9.)

[Peschel, 2003] Peschel, I. (2003). Calculation of reduced density matrices from correlation functions. *Journal of Physics A: Mathematical and General*, 36(14):L205. (Cited on pages 6, 20, 24, 45, and 69.)

[Peschel and Chung, 2011] Peschel, I. and Chung, M.-C. (2011). On the relation between entanglement and subsystem hamiltonians. *EPL (Europhysics Letters)*, 96:50006. (Cited on pages 4 and 19.)

[Platt et al., 2013] Platt, C., Hanke, W., and Thomale, R. (2013). Functional renormalization group for multi-orbital fermi surface instabilities. *Advances in Physics*, 62(4-6):453–562. (Cited on page 54.)

[Poilblanc, 2010] Poilblanc, D. (2010). Entanglement spectra of quantum heisenberg ladders. *Phys. Rev. Lett.*, 105:077202. (Cited on pages 4 and 19.)

[Pollmann and Moore, 2010] Pollmann, F. and Moore, J. E. (2010). Entanglement spectra of critical and near-critical systems in one dimension. *New Journal of Physics*, 12:025006. (Cited on page 4.)

[Pollmann et al., 2010] Pollmann, F., Turner, A. M., Berg, E., and Oshikawa, M. (2010). Entanglement spectrum of a topological phase in one dimension. *Phys. Rev. B*, 81:064439. (Cited on page 4.)

[Predin, 2017] Predin, S. (2017). Entanglement spectrum of heisenberg ladders in a time-dependent magnetic field. *arxiv:1705.08675*. (Cited on pages 4 and 19.)

[Predin and Schliemann, 2016] Predin, S. and Schliemann, J. (2016). Entanglement spectra of superconductivity ground states on the honeycomb lattice. *arxiv:1611.01039*. (Cited on page 53.)

[Predin et al., 2016] Predin, S., Wenk, P., and Schliemann, J. (2016). Trigonal warping in bilayer graphene: Energy versus entanglement spectrum. *Phys. Rev. B*, 93:115106. (Cited on pages 28 and 39.)

[Prodan et al., 2010] Prodan, N., Hughes, T. L., and Bernevig, B. A. (2010). Entanglement spectrum of a disordered topological chern insulator. *Phys. Rev. Lett.*, 105:115501. (Cited on page 3.)

[Raghu et al., 2008] Raghu, S., Qi, X.-L., Honerkamp, C., and Zhang, S.-C. (2008). Topological mott insulators. *Phys. Rev. Lett.*, 100:156401. (Cited on page 53.)

[Regnault, 2015] Regnault, N. (2015). Entanglement spectroscopy and its application to the quantum hall effects. *arxiv:1510.07670*. (Cited on page 4.)

[Regnault and Bernevig, 2011] Regnault, N. and Bernevig, B. A. (2011). Fractional chern insulator. *Phys. Rev. X*, 1:021014. (Cited on page 4.)

[Regnault et al., 2009] Regnault, N., Bernevig, B. A., and Haldane, F. D. M. (2009). Topological entanglement and clustering of jain hierarchy states. *Phys. Rev. Lett.*, 103:016801. (Cited on page 3.)

[Rodriguez et al., 2012] Rodriguez, I. D., Simon, S. H., and Slingerland, J. K. (2012). Evaluation of ranks of real space and particle entanglement spectra for large systems. *Phys. Rev. Lett.*, 108:256806. (Cited on page 3.)

[Rowe et al., 2001] Rowe, M. A., Kielpinski, D., Meyer, V., Sackett, C. A., Itano, W. M., Monroe, C., and Wineland, D. J. (2001). Experimental violation of a bell's inequality with efficient detection. *Nature*, 409:791. (Cited on page 2.)

[Rozhkov et al., 2016] Rozhkov, A., Sboychakov, A., Rakhmanov, A., and Nori, F. (2016). Electronic properties of graphene-based bilayer systems. *Physics Reports*, 648:1. (Cited on pages 5, 19, 20, 39, and 40.)

[Rusin and Zawadzki, 2008] Rusin, T. M. and Zawadzki, W. (2008). Zitterbewegung of electrons in graphene in a magnetic field. *Phys. Rev. B*, 78:125419. (Cited on page 10.)

[Saito et al., 1998] Saito, R., Dresselhaus, M. S., and Dresselhaus, G. (1998). *Physical Properties of Carbon Nanotubes*. Imperial College Press, UK. (Cited on page 13.)

[Sato and Ando, 2017] Sato, M. and Ando, Y. (2017). Topological superconductors: a review. *Reports on Progress in Physics*, 80(7):076501. (Cited on page 77.)

[Sato and Fujimoto, 2016] Sato, M. and Fujimoto, S. (2016). Majorana fermions and topology in superconductors. *Journal of the Physical Society of Japan*, 85:072001. (Cited on page 69.)

[Scheidl et al., 2010] Scheidl, T., Ursin, R., Kofler, J., Ramelow, S., Ma, X.-S., Herbst, T., Ratschbacher, L., Fedrizzi, A., Langford, N. K., Jennewein, T., and Zeilinger, A. (2010). Violation of local realism with freedom of choice. *Proc. Natl. Acad. Sci.*, 107:19708. (Cited on page 2.)

[Schliemann, 2011] Schliemann, J. (2011). Entanglement spectrum and entanglement thermodynamics of quantum hall bilayers at $\nu = 1$. *Phys. Rev. B*, 83:115322. (Cited on pages 3, 4, 5, 19, 28, 29, and 71.)

[Schliemann, 2013] Schliemann, J. (2013). Entanglement spectra and entanglement thermodynamics of hofstadter bilayers. *New Journal of Physics*, 15:053017. (Cited on pages 4, 5, 6, 19, 20, 24, 28, 29, 38, 45, 52, 69, and 71.)

[Schliemann, 2014] Schliemann, J. (2014). Entanglement thermodynamics. *Journal of Statistical Mechanics: Theory and Experiment*, 2014:P09011. (Cited on pages 4, 5, 28, 29, and 71.)

[Schliemann and Läuchli, 2012] Schliemann, J. and Läuchli, A. M. (2012). Entanglement spectra of heisenberg ladders of higher spin. *Journal of Statistical Mechanics: Theory and Experiment*, 2012:P11021. (Cited on pages 4, 19, and 39.)

[Schnyder et al., 2008] Schnyder, A. P., Ryu, S., Furusaki, A., and Ludwig, A. W. W. (2008). Classification of topological insulators and superconductors in three spatial dimensions. *Phys. Rev. B*, 78:195125. (Cited on page 69.)

[Schrödinger, 1935] Schrödinger, E. (1935). Discussion of probability relations between separated systems. *Mathematical Proceedings of the Cambridge Philosophical Society*, 31:555. (Cited on page 1.)

[Sorella and Yunoki, 2012] Sorella, Sandro, a. O. Y. and Yunoki, S. (2012). Absence of a spin liquid phase in the hubbard model on the honeycomb lattice. *Scientific Reports*, 2:992. (Cited on page 53.)

[Sorella and Tosatti, 1992] Sorella, S. and Tosatti, E. (1992). Semi-metal-insulator transition of the hubbard model in the honeycomb lattice. *EPL (Europhysics Letters)*, 19:699. (Cited on page 53.)

[Sterdyniak et al., 2011] Sterdyniak, A., Bernevig, B. A., Regnault, N., and Haldane, F. D. M. (2011). The hierarchical structure in the orbital entanglement spectrum of fractional quantum hall systems. *New Journal of Physics*, 13:105001. (Cited on page 3.)

[Sterdyniak et al., 2012] Sterdyniak, A., Chandran, A., Regnault, N., Bernevig, B. A., and Bonderson, P. (2012). Real-space entanglement spectrum of quantum hall states. *Phys. Rev. B*, 85:125308. (Cited on page 3.)

[Sun et al., 2016] Sun, S.-J., Chung, C.-H., Chang, Y.-Y., Tsai, W.-F., and Zhang, F.-C. (2016). Helical majorana fermions in $d_{x^2-y^2} + id_{xy}$-wave topological superconductivity of doped correlated quantum spin hall insulators. *Nature Scientific Reports*, 6:24102. (Cited on page 77.)

[Tanaka et al., 2012] Tanaka, S., Tamura, R., and Katsura, H. (2012). Entanglement spectra of the quantum hard-square model: Holographic minimal models. *Phys. Rev. A*, 86:032326. (Cited on page 4.)

[Thomale et al., 2010a] Thomale, R., Arovas, D. P., and Bernevig, B. A. (2010a). Nonlocal order in gapless systems: Entanglement spectrum in spin chains. *Phys. Rev. Lett.*, 105:116805. (Cited on page 4.)

[Thomale et al., 2011] Thomale, R., Estienne, B., Regnault, N., and Bernevig, B. A. (2011). Decomposition of fractional quantum hall model states: Product rule symmetries and approximations. *Phys. Rev. B*, 84:045127. (Cited on page 3.)

[Thomale et al., 2010b] Thomale, R., Sterdyniak, A., Regnault, N., and Bernevig, B. A. (2010b). Entanglement gap and a new principle of adiabatic continuity. *Phys. Rev. Lett.*, 104:180502. (Cited on page 3.)

[Turner et al., 2010] Turner, A. M., Zhang, Y., and Vishwanath, A. (2010). Entanglement and inversion symmetry in topological insulators. *Phys. Rev. Lett.*, 82:241102(R). (Cited on page 3.)

[Uchoa and Castro Neto, 2007] Uchoa, B. and Castro Neto, A. H. (2007). Superconducting states of pure and doped graphene. *Phys. Rev. Lett.*, 98:146801. (Cited on page 53.)

[Ulybyshev et al., 2013] Ulybyshev, M. V., Buividovich, P. V., Katsnelson, M. I., and Polikarpov, M. I. (2013). Monte carlo study of the semimetal-insulator phase transition in monolayer graphene with a realistic interelectron interaction potential. *Phys. Rev. Lett.*, 111:056801. (Cited on page 53.)

[Vollhardt, 1984] Vollhardt, D. (1984). Normal ^{3}He: an almost localized fermi liquid. *Rev. Mod. Phys.*, 56:99–120. (Cited on page 63.)

[Vučićević et al., 2012] Vučićević, J., Goerbig, M. O., and Milovanović, M. V. (2012). *d*-wave superconductivity on the honeycomb bilayer. *Phys. Rev. B*, 86:214505. (Cited on page 53.)

[Wallace, 1947] Wallace, P. R. (1947). The band theory of graphite. *Phys. Rev.*, 71:622–634. (Cited on pages 9 and 10.)

[Wang et al., 2012] Wang, W. S., Xiang, Y. Y., Wang, Q.-H., Wang, F., Yang, F., and Lee, D.-H. (2012). Functional renormalization group and variational monte carlo studies of the electronic instabilities in graphene near $\frac{1}{4}$ doping. *Phys. Rev. B*, 85:035414. (Cited on pages 53 and 56.)

[Wang and Li, 2016] Wang, Y.-X. and Li, F. (2016). Edge states and phase diagram for graphene under polarized light. *Physica B: Condensed Matter*, 492:1 – 6. (Cited on page 52.)

[Wehling et al., 2011] Wehling, T. O., Sasioglu, E., Friedrich, C., Lichtenstein, A. I., Katsnelson, M. I., and Blügel, S. (2011). Strength of effective coulomb interactions in graphene and graphite. *Phys. Rev. Lett.*, 106:236805. (Cited on pages 56 and 57.)

[Weihs et al., 1998] Weihs, G., Jennewein, T., Simon, C., Weinfurter, H., and Zeilinger, A. (1998). Violation of bell's inequality under strict einstein locality conditions. *Phys. Rev. Lett.*, 81:5039. (Cited on page 2.)

[Wen, 1990] Wen, X. G. (1990). Topological orders in rigid states. *International Journal of Modern Physics B*, 04(02):239–271. (Cited on page 3.)

[Wen, 1991] Wen, X. G. (1991). Mean-field theory of spin-liquid states with finite energy gap and topological orders. *Phys. Rev. B*, 44:2664–2672. (Cited on page 3.)

[Wu et al., 2013] Wu, W., Scherer, M. M., Honerkamp, C., and Le Hur, K. (2013). Correlated dirac particles and superconductivity on the honeycomb lattice. *Phys. Rev. B*, 87:094521. (Cited on page 64.)

[Xiao et al., 2010] Xiao, D., Chang, M.-C., and Niu, Q. (2010). Berry phase effects on electronic properties. *Rev. Mod. Phys.*, 82:1959–2007. (Cited on page 16.)

[Yao and Qi, 2010] Yao, H. and Qi, X.-L. (2010). Entanglement entropy and entanglement spectrum of the kitaev model. *Phys. Rev. Lett.*, 105:080501. (Cited on page 4.)

[Zhang et al., 2005] Zhang, Y., Tan, Y.-W., Stormer, H. L., and Kim, P. (2005). Experimental observation of the quantum hall effect and berry's phase in graphene. *Nature*, 438:201. (Cited on page 10.)

[Zozulya et al., 2009] Zozulya, O. S., Haque, M., and Regnault, N. (2009). Entanglement signatures of quantum hall phase transitions. *Phys. Rev. B*, 79:045409. (Cited on page 3.)

COLOPHON

This document was typeset using the typographical look-and-feel `classicthesis` developed by André Miede. The style was inspired by Robert Bringhurst's seminal book on typography "*The Elements of Typographic Style*". `classicthesis` is available for both LaTeX and LyX:

`http://code.google.com/p/classicthesis/`

Happy users of `classicthesis` usually send a real postcard to the author, a collection of postcards received so far is featured here:

`http://postcards.miede.de/`

Final Version as of August 25, 2017 (`classicthesis` version 1.0).